



**HAL**  
open science

# Mottness scenario for the non-Fermi liquid phase in heavy fermions

Amaricci Adriano

► **To cite this version:**

Amaricci Adriano. Mottness scenario for the non-Fermi liquid phase in heavy fermions. Condensed Matter [cond-mat]. Université Paris Sud - Paris XI, 2009. English. NNT: . tel-00419947

**HAL Id: tel-00419947**

**<https://theses.hal.science/tel-00419947v1>**

Submitted on 25 Sep 2009

**HAL** is a multi-disciplinary open access archive for the deposit and dissemination of scientific research documents, whether they are published or not. The documents may come from teaching and research institutions in France or abroad, or from public or private research centers.

L'archive ouverte pluridisciplinaire **HAL**, est destinée au dépôt et à la diffusion de documents scientifiques de niveau recherche, publiés ou non, émanant des établissements d'enseignement et de recherche français ou étrangers, des laboratoires publics ou privés.

Université de Paris XI - Laboratoire de Physique des Solides



# Mottness scenario for non-Fermi liquid phase in heavy fermions.

Thèse présentée pour obtenir le grade de  
Docteur en Sciences de l'Université de Paris 11, Orsay

**Discipline : PHYSIQUE**

Candidat: **Adriano Amaricci**

*Directeur :* M.J.ROZENBERG

*Rapporteur :* D. POILBLANC

E. MIRANDA

*Jury :* B. COQBLIN

C. PÉPIN

M. CAPONE

©2009 - [Adriano Amaricci]

All rights reserved.

a V.

*"...la differenza tra bufalo e locomotiva salta agli occhi:  
la locomotiva ha la strada segnata, mentre il bufalo può scartare di lato...  
...e cadere..."*

FdG

*"Los amigos son como las estrellas  
No siempre los ves pero siempre están ahí"*

Anonimous



# Contents

<b>Acknowledgements</b>	<b>1</b>
<b>Introduction</b>	<b>3</b>
<b>1 Non-Fermi liquid behavior in <math>d/f</math>-electrons metals</b>	<b>7</b>
1.1 A (brief) introduction to the Fermi liquid theory . . . . .	8
1.2 The heavy fermions problem . . . . .	13
1.2.1 Introduction . . . . .	13
1.2.2 Phenomenology of the heavy fermions . . . . .	15
1.3 Fermi or non-Fermi? Some experimental facts . . . . .	18
1.4 Schematic overview on NFL phase description . . . . .	23
1.4.1 Multi-channel Kondo model . . . . .	23
1.4.2 Kondo disorder . . . . .	24
1.4.3 Quantum criticality . . . . .	25
<b>2 Theoretical framework: DMFT</b>	<b>29</b>
2.1 Insights from mean-field theory: the Ising model . . . . .	30
2.2 Dynamical Mean Field Theory . . . . .	33
2.2.1 Effective action . . . . .	33
2.2.2 Limit of infinite coordination number . . . . .	36
2.2.3 Self-consistency . . . . .	37
2.3 Connection with quantum impurity problem . . . . .	41
2.4 Solution of DMFT equations . . . . .	42
2.4.1 Iterated perturbation theory . . . . .	44
2.4.2 Quantum Monte Carlo . . . . .	45
2.4.3 Exact diagonalization . . . . .	47

2.4.4	Density Matrix Renormalization group . . . . .	52
2.5	Conclusions . . . . .	57
<b>3</b>	<b>Periodic Anderson Model</b>	<b>59</b>
3.1	PAM and solvable limits . . . . .	60
3.1.1	Non-interacting limit . . . . .	63
3.1.2	Atomic limit . . . . .	63
3.2	DMFT solution of PAM . . . . .	69
3.3	Internal energy . . . . .	72
3.4	Long range order DMFT equations . . . . .	74
3.4.1	Antiferromagnetic order . . . . .	74
3.4.2	AFM order and homogeneous magnetic field . . . . .	76
3.5	Conclusions . . . . .	78
<b>4</b>	<b>Mott insulators and metal-insulator transitions in the PAM</b>	<b>79</b>
4.1	PAM description of Mott insulators . . . . .	81
4.1.1	Zaanen-Sawatzky-Allen diagram . . . . .	81
4.1.2	Mott insulator within PAM . . . . .	84
4.1.2.1	Mott-Hubbard regime . . . . .	85
4.1.2.2	Charge-Transfer regime . . . . .	91
4.1.2.3	Mott gap size . . . . .	93
4.2	Doping driven MIT . . . . .	94
4.2.1	Type I metal insulator transition: $\delta < 0$ . . . . .	95
4.2.2	Type II metal insulator transition: $\delta > 0$ . . . . .	98
4.3	Conclusions . . . . .	103
<b>5</b>	<b>Non-Fermi liquid phase and Mottness scenario for Heavy Fermions</b>	<b>105</b>
5.1	Correlated metallic state: a liquid of singlets . . . . .	109
5.2	Non-Fermi liquid state . . . . .	116
5.3	Temperature crossover to Fermi liquid . . . . .	120
5.4	Spin susceptibility . . . . .	124
5.4.1	Enhanced spin susceptibility . . . . .	124
5.4.2	Exhaustion and coherence scale . . . . .	126
5.5	Magnetic properties . . . . .	129
5.5.1	External magnetic field . . . . .	129
5.5.2	Antiferromagnetic ordering . . . . .	132
5.6	Thermodynamics . . . . .	134

---

5.6.1	Specific heat and effective mass . . . . .	134
5.6.2	Entropy . . . . .	138
5.7	Mottness scenario . . . . .	141
5.7.1	T - $\delta$ phase diagram . . . . .	141
5.7.2	Competing magnetic interactions: T - $B_{ext}$ phase diagram . . . . .	144
5.8	Conclusions . . . . .	147
<b>Concluding remarks and perspectives</b>		<b>149</b>
<b>Bibliography</b>		<b>151</b>

# Acknowledgements



# Introduction

In this thesis we describe a new theoretical approach to the problem of non-Fermi liquid behavior in heavy fermion systems.

For almost forty years our comprehension of the metallic behavior in many materials has been founded on the Landau physical intuition about interacting Fermi systems [6, 69]. The idea of Landau, that interacting fermions could be regarded as free particles with renormalized parameters, is at the basis of the standard picture of the solids in terms of single independent electrons delocalized throughout the systems. The extraordinary success of this scenario is demonstrated by the impressive number of predictions and results, on which has root a large part of the actual technology.

The Fermi-liquid concept has been also extended to systems showing a strong electron-electron interaction, *i.e.* strongly correlated electrons systems. Under suitable conditions the low temperature metallic properties of these systems can be interpreted in terms of renormalized quasiparticles.

Nevertheless, recent experiments on some strongly correlated materials have shown remarkable deviations from the Fermi liquid predictions concerning different physical observables, such as specific heat  $C$ , resistivity  $\rho$  or susceptibility  $\chi$  [94].

The theoretical understanding of the breakdown of the Fermi liquid paradigm observed heavy fermion systems or in high  $T_c$  superconductors is one of the open challenges in the correlated electrons physics.

Many ideas have been put forward to explain the observed non-Fermi liquid behavior, without finding an absolute consensus so far. Among them we can distinguish three main directions: overscreening in Kondo models, Kondo disorder and quantum criticality [70, 62, 94].

A common feature can be recognized among some of these ideas, namely the existence of a physical mechanism pushing to zero the coherence temperature below which the Fermi liquid forms. In one case (Kondo disorder) this mechanism is associated to the presence of a certain degree of disorder [62]. However, a more widely accepted mechanism for the formation of a

non-Fermi liquid state is the proximity to a quantum phase transition (QPT) or to a quantum critical point (QCP) [14].

Within this scenario the breakdown of the Fermi liquid properties occurs in the neighborhood of  $T = 0$  transition between a magnetically ordered phase (*e.g.* antiferromagnetic) and a paramagnetic one. In this regime the strong coupling between the fluctuations of the order parameter and the electrons may prevent the formation of a Fermi liquid phase with long-lived quasiparticles.

Among the different approach to non-Fermi liquid problem based on quantum criticality we can mention the Hertz-Millis theory, where the paramagnons of the ordered phase “dress” the conduction electrons to produce the NFL behavior [35, 61]. Another approach is the local quantum critical theory [88, 87], in which the competition between local Kondo screening and long wavelength magnetic fluctuations drives the system into a critical regime where non-Fermi liquid properties can arise. This approach is based on a suitable extension of the dynamical mean-field theory. However, local quantum criticality, even providing useful insights to the non-Fermi liquid problem, requires some simplifying approximations to solve the mean-field equations, spoiling DMFT approach of many of its benefits.

Dynamical Mean Field Theory is a powerful theoretical tool to investigate strongly correlated electrons systems [31, 52]. Among other things, this method has permitted to obtain a satisfactory description of the Mott metal-insulator transition in simplified models, such as Hubbard [75, 76, 78, 100]. Lately, the application to realistic calculations, thru an ab-initio plus DMFT algorithm, has greatly increased our knowledge about real materials [51].

At the heart of the DMFT approach are the simplifications on the lattice quantum many-body problem arising in the limit of infinite dimension [60, 59]. These simplifications permit to map the lattice problem onto an effective single impurity problem, that has to be solved in a self-consistent way. In this respect DMFT can be considered as the quantum generalization of the classic mean-field theory, introduced so far to deal with spin models.

In this thesis we shall show that a new approach to the heavy fermions physics can be based on the DMFT solution of one of the canonical model of this area, namely the periodic Anderson model. In particular we demonstrate that, contrary to conventional expectations, a non-Fermi liquid state is readily obtained from this model within the DMFT framework. In agreement with the quantum criticality scenario, this novel NFL state is located in the neighborhood of a quantum phase transition, but unlike the standard quantum criticality scenario sketched before, the relevant quantum transition here is a Mott transition. Thus, the present study sheds a different light onto the NFL problem, showing that the coupling to long wavelength magnetic fluctuations (absent in DMFT) is not a prerequisite for the realization of a NFL scenario. *Local* temporal magnetic fluctuations alone can provide sufficient scattering to produce an incoherent

metallic state. The presence of such large local magnetic fluctuations in our model has origin in the competition between magnetic interactions, namely the super-exchange antiferromagnetic interaction between the correlated electrons and the ferromagnetic interaction indirectly driven by the delocalization of the doped charges.

Thus, we are able to obtain a DMFT description of the non-Fermi liquid phase in heavy fermion systems which is based on the proximity to a Mott point, *i.e.* Mottness scenario. Our study shows that the PAM, solved within DMFT, may be considered as a “bare bones” or minimal approach able to capture the physical scenario for the formation of a NFL state and that is in qualitative agreement with some observed phenomenology in heavy fermion systems.

The entire thesis is structured as follows.

- In the **first** chapter we review briefly the Landau theory of Fermi liquid and we give an overview on the heavy fermion phenomenology under both the theoretical and the experimental point of view. In particular, we present briefly some experimental evidences for the non-Fermi liquid phase in heavy fermions materials. Finally we discuss the main theoretical ideas proposed to explain the breakdown of the Fermi liquid paradigm.
- In the **second** chapter we introduce the theoretical tool used throughout this thesis, namely the DMFT. We derive the basic equations of the theory, step by step comparing with the well known classical mean-field theory (reviewed in the first part of the same chapter). An overview of the main techniques used to solve the DMFT equations is presented at the end of the chapter.
- In the **third** chapter we introduce the periodic Anderson model. After having studied the solvable limits of the model we proceed by deriving the related DMFT equations and briefly discuss the algorithm used to obtain their solution. Next, we illustrate the derivation of the internal energy expression for the PAM in the framework of DMFT. This will be used later on to obtain the thermodynamical properties of the model. Finally, we extend the DMFT equations to deal with long range magnetically ordered phases.
- In the **fourth** chapter we discuss the various parameter regimes of the model respect to the so-called ZSA diagram. We will demonstrate numerically the existence of a Mott insulating state for large values of the correlation, in two physically relevant regimes. Then we will study the Mott metal-insulator transitions driven by doping. In particular we show the existence of two different transition scenarios, each of which will be discussed. One of the two transitions will constitute the framework for the derivation of the Mottness scenario, that is the subject of the next chapter.
- In the **fifth** chapter we shall demonstrate the existence of a non-Fermi liquid state in the

neighborhood of a Mott point. Then, we show the existence of a crossover regime towards a Fermi liquid phase for temperatures exponentially small in the doping. This coherence temperature scale is estimated and discussed in terms of the exhaustion problem [68, 67]. Next, we study the magnetic properties of the non-Fermi liquid regime. The main finding being the stability of this phase respect to the magnetic order. We present a study of the thermodynamical properties of the system, such as entropy of specific heat, finding for this latter remarkable evidences of logarithmic divergences, in agreement with experimental observations [94]. Finally we shall summarize the results in two phase diagrams that are in qualitatively accord with the observed phenomenology of heavy fermions systems.

# Non-Fermi liquid behavior in *d/f*-electrons metals

## Contents

---

<b>1.1 A (brief) introduction to the Fermi liquid theory</b> . . . . .	8
<b>1.2 The heavy fermions problem</b> . . . . .	13
1.2.1 Introduction . . . . .	13
1.2.2 Phenomenology of the heavy fermions . . . . .	15
<b>1.3 Fermi or non-Fermi? Some experimental facts</b> . . . . .	18
<b>1.4 Schematic overview on NFL phase description</b> . . . . .	23
1.4.1 Multi-channel Kondo model . . . . .	23
1.4.2 Kondo disorder . . . . .	24
1.4.3 Quantum criticality . . . . .	25

---

Deviations from Fermi liquid theory predictions, as observed in many *d*- or *f*-electrons compounds, have recently attracted a great deal of attention [94]. These systems show metallic phases with anomalous low temperature properties, characterized by some critical power law behavior of physical observables such as resistivity or specific heat. The large variety of physical regimes and situations in which non-Fermi liquids are observed, is one of the reasons making this area of research particular appealing for both the theoretical and experimental condensed matter physics community.

After the precursor works of Hertz [35] and Nozières-Blandin [70], many different ideas have been proposed over recent years of intense work, without finding a general consensus, so that a model accounting for the different aspects of this interesting subject is still lacking. Recently, has been proposed that non-Fermi liquid behavior can be associated to “nearness” to

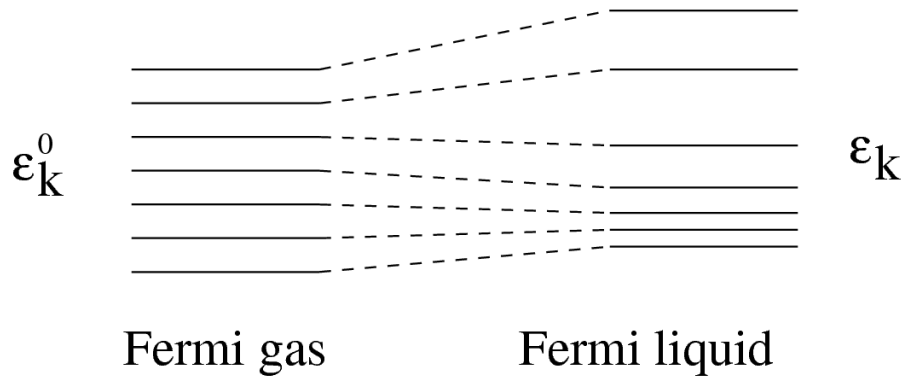
some magnetic instabilities in the phase diagram [94, 14]. Many ideas along this line have as a central point the proximity to a Quantum Phase Transition (QPT) or to a Quantum Critical Point (QCP) [80]. The main reason is that due to some competing mechanism the critical temperature of a magnetic transition can be pushed to zero, preventing the formation of a Fermi liquid phase. The presence of such a zero temperature phase transition is rather usual in heavy fermion systems. These compounds are in fact highly magnetic or can be driven into magnetic phases by tuning some external parameters, such as pressure, doping or magnetic field. This characteristic is related to the strong correlation effects originated from the local nature of the  $d/f$ -orbital electrons.

The chapter is organized as follows: in Sec. 1.1 we will briefly introduce the main ideas of Landau's Fermi liquid theory, that is the standard underlying physical theory for a large class of metals. In Sec. 1.2 we give an overview of the heavy fermion phenomenology. Then, in Sec. 1.3 we review some experimental results about heavy fermions, focusing on the many different aspects these compounds show. In particular we discuss the evidences for the non-Fermi liquid behavior in some heavy fermion compounds. Finally, in Sec. 1.3 we discuss the main theoretical ideas proposed to explain the breakdown of the Fermi liquid paradigm.

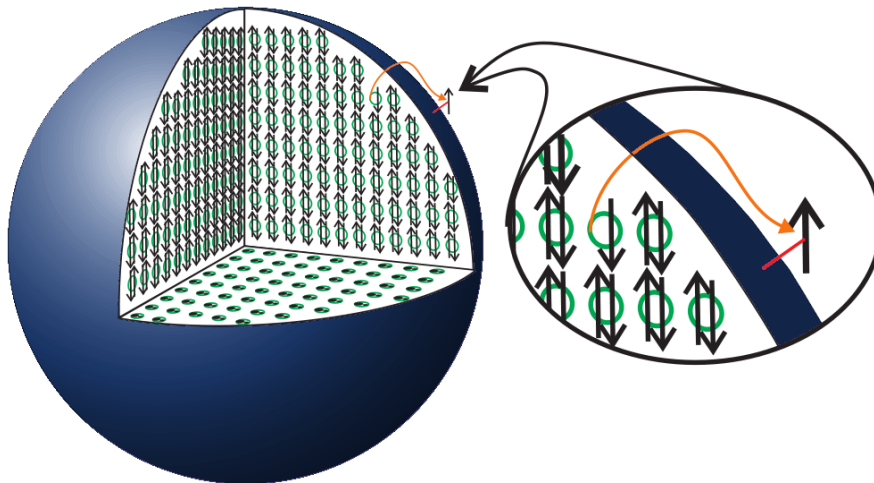
### 1.1 A (brief) introduction to the Fermi liquid theory

Since its introduction [53, 54] (!), Landau's phenomenological theory of interacting Fermi systems has been used as the paradigm for the understanding of metallic behavior. At the heart of this theory is the rather simple, but strong, idea of adiabatic continuity between the non-interacting and the interacting system. Landau's argument was that it is possible to construct a one-to-one correspondence between the states of the non-interacting system and the states of the interacting one, upon adiabatic turning on of the interaction itself Fig. 1.1. Moreover Landau guessed that the interacting states can be labelled with roughly the same quantum numbers of the non-interacting ones. This assumption, to be justified *a posteriori*, may be naively rephrased by saying that the label of the states, *i.e.* the quantum numbers used to classify the states, are stronger than the eigenstates themselves with respect to the presence of an interaction. Although its apparent simplicity the adiabatic continuity hypothesis is in reality a strong constraint on the interaction. For example attractive interactions, even very weak, leading to the formation of composite objects should be excluded.

As a direct consequence of the Landau's assumption it follows that the interacting system can be described, near the ground state, in terms of elementary electronic excitations, having well defined physical properties, *i.e.* the so-called "quasi-particles". This concept is intimately connected with the quantum mechanical nature of the interacting system, being related to the



(a) adiabatic correspondence of the electronic levels



(b) Fermi sphere in momentum space

Figure 1.1: (a) States of the interacting Fermi liquid may be put in one-to-one correspondence with the non-interacting Fermi gas, in the limit of adiabatic turning on of the interaction. (b) The Fermi sphere in momentum space for the free (isotropic homogeneous) Fermi gas.

## 1. Non-Fermi liquid behavior in $d/f$ -electrons metals

---

possibility of the liquid to form resonances that are not eigenstates of the system, but that can live for a sufficiently long time to be regarded as single-particle states. So, one can readily convince oneself that the momentum distribution function of the quasi-particles has the same *functional* form of that of the non-interacting system  $n_F(\mathbf{k})$  [69]. Similarly to the ground state distribution of the ideal Fermi gas, this function is characterized by a (renormalized) jump at the Fermi level, making possible to give a meaning to the Fermi surface even in the interacting system, Fig. 1.3.

For the Landau adiabatic correspondence to work it is necessary that the rate  $R$  at which the interactions is turned on, fulfills the following two conditions [3]:

- Considering low energy excitation (of order  $T$ ) from the Fermi surface, *i.e.* particle or hole excitation with  $\delta E \sim T$ , then

$$R \ll T$$

will ensure the correct energy resolution for the quasi-particle picture to be valid.

- If  $\tau$  is the life-time of the quasi-particle, *i.e.* the time it takes to decay into exact eigenstates, then  $R$  should be such that:

$$R \gg 1/\tau \quad .$$

Thus for sufficiently low temperature:

$$\tau \gg \frac{1}{T}$$

This condition fixes the validity of Landau's theory of Fermi liquids by asserting that quasi-particles are well defined only near the Fermi surface (being excitations with respect to the Fermi energy) and that they have infinite life-time only at the Fermi surface. The justification of the previous condition rely on some phase-space restrictions on scattering processes in interacting Fermi systems. Using these constraints it is possible to show that the life-time of the quasiparticles decay as the inverse of the square of the temperature:  $\tau \propto T^{-2}$ .

the previous condition is satisfied for low enough temperatures.

To demonstrate this it is sufficient to study the simplest scattering process (cf. Fig. 1.2), namely that in which a particle 1 with momentum  $\mathbf{k}$  excite a particle 2 out of the Fermi sea, into an empty state 4, being itself scattered to a state 3. If  $\mathbf{q}$  is the transferred momentum and the energies are all measured from the Fermi surface  $\varepsilon_{\mathbf{k}} = E_{\mathbf{k}} - E_f$ , then we have the following relation for this process:

$$\begin{aligned} \varepsilon_{\mathbf{k}_1} + \varepsilon_{\mathbf{k}_2} &= \varepsilon_{\mathbf{k}_3} + \varepsilon_{\mathbf{k}_4} \\ \mathbf{k}_1 - \mathbf{k}_3 &= \mathbf{k}_4 - \mathbf{k}_2 = \mathbf{q} \end{aligned} \tag{1.1}$$

The scattering rate of this second order process can be evaluated as follow. The total contribution includes the square of the scattering potential (*i.e.* two vertices in the related Feynman

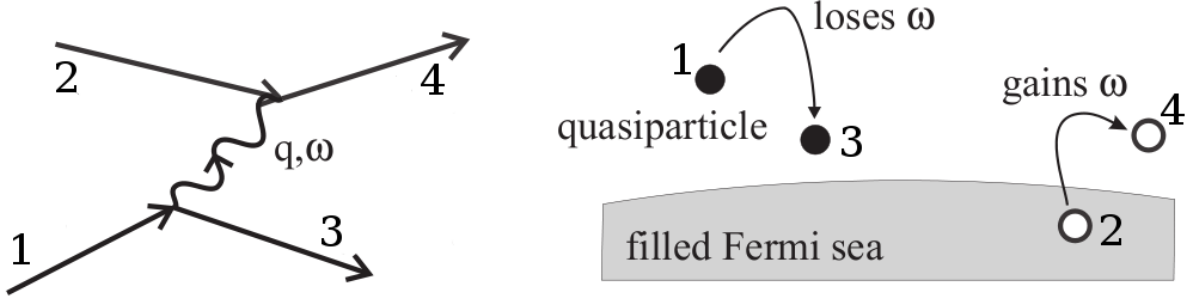


Figure 1.2: The scattering process of a quasiparticle with energy  $\varepsilon$  above the Fermi surface. The process involve the formation of a particle-hole excitation.

diagrams), one integral over the internal momentum  $\mathbf{q}$  and, by means of momentum conservation, one other integral over momentum  $\mathbf{k}_2$  of the inverse of the energy change  $\omega$ , with:

$$\omega = \varepsilon_4 + \varepsilon_3 - \varepsilon_1 - \varepsilon_2$$

such that:

$$\begin{aligned} \frac{1}{\tau} &= \lim_{\eta \rightarrow 0} \int d^3\mathbf{q} d^3\mathbf{k}_2 |V(q)|^2 \text{Im} \left( \frac{1}{\omega - i\eta} \right) \\ &= \int d^3\mathbf{q} d^3\mathbf{k}_2 |V(q)|^2 \delta(\omega) \end{aligned} \quad (1.2)$$

corresponding to the Fermi golden rule for this process. The delta function under the integral will give a finite contribution only if the three excitations energy  $\varepsilon_{\mathbf{k}_4}$ ,  $\varepsilon_{\mathbf{k}_3}$  and  $-\varepsilon_{\mathbf{k}_2}$  will be less than  $\varepsilon_{\mathbf{k}_1}$ . The accessible part of the energy space is thus of the order  $\varepsilon_{\mathbf{k}_1}$ , which also restrict the available momentum space for the previous integrations. With this restriction the integral will contribute to the inverse scattering rate with an  $\varepsilon^2$ . Then supposing the scattering potential to be, in the liquid phase, smaller than the Fermi energy, one finds the following expression for the inverse life-time:

$$\frac{1}{\tau} = C_1 \left( \frac{\varepsilon}{\varepsilon_F} \right)^2$$

with  $C_1$  an unessential constant. For excitations of the order  $T$  this expression imply the previous  $T^{-2}$  behavior for the quasiparticles life-time. The inverse scattering rate decreases faster than the excitation itself.

An important parameter of interacting Fermi system that can be obtained from Landau's theory is the quasiparticle weight  $Z$  [69]. This constant, bounded between zero and one, describes the previously discussed discontinuity at the Fermi level in the momentum distribution function Fig. 1.3(b). The physical meaning of  $Z$  can be understood as describing the fraction of bare electronic states that are "contained" in the quasiparticle, *i.e.* the resonating states in which the quasiparticles eventually decays.

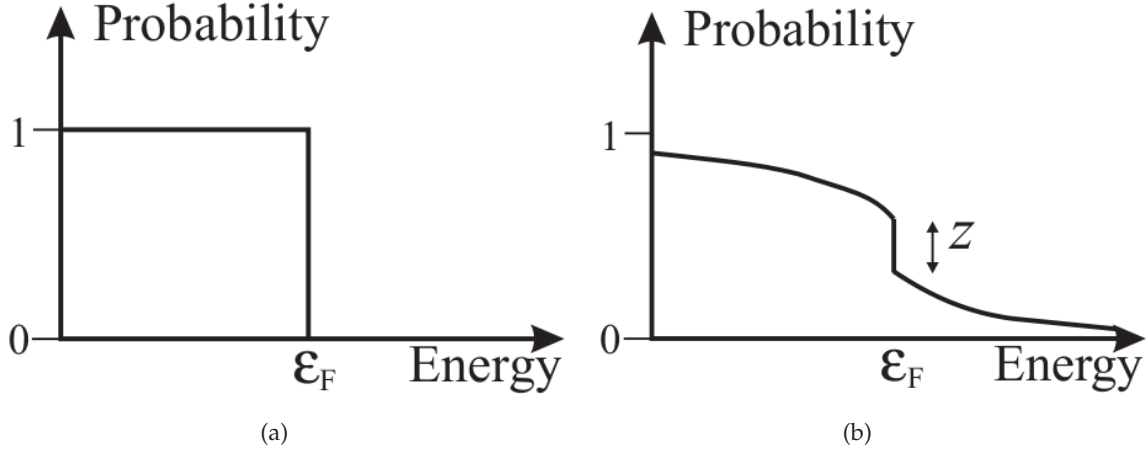


Figure 1.3: Momentum distribution function at  $T = 0$  for (a) non-interacting electrons or Landau quasiparticles in a Fermi liquid, (b) electrons in the interacting Fermi liquid. The discontinuity at the Fermi level  $\epsilon_F$  remains in the interacting systems though with a reduced size  $Z$ .

The analogy between the non-interacting Fermi system and the Fermi liquid can be pushed forward by introducing one of the key concept of the Landau's theory, namely the *effective mass*  $m^*$ . This is intimately connected with the quasiparticle energy  $\epsilon_{\mathbf{k}}$ , that can be written as a linearization of the quadratic dispersion near the Fermi surface, namely:

$$\begin{aligned}
 \epsilon_{\mathbf{k}} &= \epsilon_F + \frac{(\hbar\mathbf{k})^2}{2m} - \frac{(\hbar\mathbf{k}_F)^2}{2m} \\
 &= \epsilon_F + v_F(\mathbf{k} - \mathbf{k}_F) \\
 &= \frac{\hbar\mathbf{k}_F}{m^*}(\mathbf{k} - \mathbf{k}_F)
 \end{aligned} \tag{1.3}$$

where we have defined the effective mass  $m^*$  as the mass of the quasiparticle *at* the Fermi surface. In terms of the density of quasiparticles at the Fermi level (fixing the Fermi energy)  $N(\epsilon_F)$  the effective mass can be rewritten as:

$$m^* = \frac{\pi^2 N(\epsilon_F)}{\hbar}$$

The knowledge of the effective mass is sufficient to determine the behavior of some of the most important macroscopic functions, such as the specific heat, the entropy or the spin susceptibility. Regarding the first it is sufficient to recall that  $C_v = \delta E / \delta T$ , where  $\delta E$  is the variation of the liquid energy. If  $n_0(\mathbf{k})$  is the zero temperature Fermi distribution (*i.e.* the step function at  $\mathbf{k}_F$ ),  $\delta E$  can be written to the first order in  $\delta n = n(\mathbf{k}) - n_0(\mathbf{k})$  as:

$$\delta E = \sum_{\mathbf{k}} \epsilon_{\mathbf{k}} \delta n(\mathbf{k})$$

Then with straightforward calculations (making use of chain property of derivatives and Sommerfeld expansion [1]) one obtains the following expression of the specific heat in terms of the quasiparticles density of states  $\nu(\varepsilon)$ :

$$C_v = \frac{1}{3}\pi^2 T \nu(\mu)$$

where  $\mu$  is the chemical potential. In the case of the isotropic Fermi liquid the previous relation reads [38]:

$$C_v = T \frac{\mathbf{k}_F m^*}{3\hbar^3}$$

Thus, the specific heat coefficient  $\gamma = C_v/T$  is proportional to the effective mass of the charge carriers in the metals. It is worth to observe that while the Fermi energy is almost of the same order of magnitude in many metals, changes in the effective mass can strongly influence the specific heat behavior. Landau's theory can explain experimental observations of large specific heat in some correlated metals. A similar calculation permits to derive an expression for the spin susceptibility:

$$\chi = \frac{m^* \kappa_F}{4\pi^2(1 + F_0)}$$

where  $F_0$  is one Landau's parameter measuring the "polarizability" of the system. Thus, the spin susceptibility of interacting Fermi systems at low enough temperature is fixed by a constant depending on the value of the effective mass  $m^*$ .

Finally, another particularly important quantity can be obtained within Landau theory: the resistivity  $\rho(T)$ . In particular it is possible to show, integrating the inverse scattering time expression over the incoming energy  $\varepsilon_1$ , that the resistivity has a characteristic  $T^2$  behavior, namely:

$$\rho(T) = C_2 \left( \frac{T}{\varepsilon_F} \right)^2$$

where  $C_2$  is a given constant.

The Landau theory predictions about Fermi liquids have been the corner stone of solid state theory of metals, establishing a paradigmatic behavior for many thermodynamical and transport quantities. Roughly speaking the main result of the Fermi liquid theory has been that of explaining how a single particle picture comes out from a quantum many body system with rather strong interactions.

## 1.2 The heavy fermions problem

### 1.2.1 Introduction

Most of the metals are extraordinarily well described by the independent particle approximation, despite the strong electron-electron interactions that are expected to be present in these

## 1. Non-Fermi liquid behavior in $d/f$ -electrons metals

---

materials. As we have seen in the previous section, the underlying justification for this highly non trivial result rely on Landau's description of Fermi liquids. The standard picture of metals is that of single particles carrying charge and moving in a periodic potential induced by the ions (band theory) [6].

Nevertheless, there is a class of materials in which the strong Coulomb interaction is not sufficiently screened, so that single particles may feel a strong interaction between themselves, making the previous picture not applicable to any purpose. The great interest around these *strongly correlated systems* rely on the several new physical effects they show and that puzzle the condensed matter physics community. Significant examples are either the transition induced by correlation from metallic to insulating state in systems with half-filled valence band (Mott transition), or the large critical temperature below which some materials enter a superconductive state, that is (paradoxally) originated from the strong electronic repulsion. None of these effects can be explained by the standard one-particle picture of metals. The origin of the strong correlation is related to the presence in these materials of electrons from transition metals, rare-earth or actinides. These electrons, in the incomplete  $d/f$ -orbitals, are extremely localized and, under particular circumstances, not well screened, so that the Coulomb interaction between them becomes important.

A rather wide class of metallic compounds showing strong correlation is represented by the so-called *heavy fermion systems* [15]. These systems are alloys containing rare-earths or actinides such as *Ce*, *U* or *Yb*. Recently there have been strong indications for heavy fermion behavior also in some early transition metal oxides, such as  $LiV_2O_4$  [5, 46, 86]. Historically the first observed compound showing such heavy fermion behavior has been  $CeAl_3$  [15, 36]. Other examples are  $CeCu_2Si_2$ ,  $UPt_3$ ,  $U_2Zn_{17}$ ,  $YbCuAl$ . In Fig. 1.4 other heavy fermion compounds are reported together with some of their characteristic parameters.

Many of these compounds show ordinary Fermi liquid metallic behavior for temperatures smaller than a characteristic scale. Nevertheless, the electronic specific heat  $\gamma$  and the spin susceptibility  $\chi$  correspond to values of the effective mass of the charge carriers much larger than that of the free electrons:  $m^*/m \simeq 10^2 - 10^3$ . This fact justifies the terminology "heavy fermions" used to indicate these compounds.

Rare-earths in heavy fermion materials tend to donate some electrons to the conduction bands, remaining with  $f$ -orbital valence electrons only. Because of the small extension of the  $f$ -orbital and as a result of screening effects of outer electrons, the  $f$ -orbital electrons are highly localized and may feel a large local Coulomb repulsion, giving rise to strong correlation effects. Thus, in heavy fermion systems delocalized conduction band electrons coexist with large magnetic moments from  $f$ -orbital electrons. The interplay between the itinerant character of the conduction band electrons and the more localized nature of the correlated  $f$ -orbital electrons,

Compound	Crystal Structure	CF (in K)	T <sub>N</sub> (in K)	$\gamma$ (mJ/moleK <sup>2</sup> )
<i>CeAl<sub>3</sub></i>	Hexagonal	60-90	-	1600
<i>CeCu<sub>2</sub>Si<sub>2</sub></i>	Tetragonal	140-360	-	1000
<i>CeCu<sub>6</sub></i>	Orthorhombic	100-240	-	1500
<i>CeRu<sub>2</sub>Si<sub>2</sub></i>	Tetragonal	220	-	350
<i>CeInCu<sub>2</sub></i>	Cubic ( $\Gamma_7$ )	90	-	1200
<i>CeCu<sub>4</sub>Ga</i>	Hexagonal	100	-	1800
<i>CeAl<sub>2</sub></i>	Cubic ( $\Gamma_7$ )	100	3.85	135
<i>CeB<sub>6</sub></i>	Cubic ( $\Gamma_8$ )	500	3.2	300
<i>CeRh<sub>2</sub>Si<sub>2</sub></i>	Tetragonal	150	36	23
<i>Ce<sub>3</sub>Al<sub>11</sub></i>	Orthorhombic	100	6.2*	120
<i>CeIn<sub>3</sub></i>	Cubic ( $\Gamma_7$ )	100	10	140
<i>CeAl<sub>2</sub>Ga<sub>2</sub></i>	Tetragonal	65-120	8.5	80
<i>CeCu<sub>2</sub></i>	Orthorhombic	200	3.5	82
<i>CeCu<sub>2</sub>Ge<sub>2</sub></i>	Tetragonal	200	4.15	100
<i>Ce<sub>2</sub>Sn<sub>5</sub></i>	Orthorhombic	70-155	2.9	380
<i>YbCu<sub>4</sub>Ag</i>	Cubic	45	-	245
<i>YbBiPt</i>	Cubic	-	-	8000
<i>YbNi<sub>2</sub>B<sub>2</sub>C</i>	Tetragonal	40-200	-	530
<i>YbCu<sub>2</sub>Si<sub>2</sub></i>	Tetragonal	216	-	135
<i>YbNiAl</i>	Hexagonal	35	2.9	350
<i>U(Pt<sub>0.95</sub>Pd<sub>0.05</sub>)<sub>3</sub></i>	Hexagonal	-	6	500
<i>UPd<sub>2</sub>Al<sub>3</sub></i>	Hexagonal	-	14.3	150
<i>UNi<sub>2</sub>Al<sub>3</sub></i>	Hexagonal	-	4.6	120
<i>NpSn<sub>3</sub></i>	Cubic	-	9.5	240

Figure 1.4: Examples of heavy fermion compounds. For each entry it has been reported crystal structure (2<sup>nd</sup> column), crystalline field (3<sup>rd</sup>), Néel temperature for magnetic ordering (4<sup>th</sup>) and Sommerfeld specific heat constant (5<sup>th</sup>) [15].

is considered to be at the origin of the unusual low temperature behavior of the heavy fermion systems.

### 1.2.2 Phenomenology of the heavy fermions

In this scenario it is natural to expect the Kondo physics to play a major role. At high temperature heavy fermion systems show a “decoupling” between the conduction electrons and the local moments. The former propagate in the systems with normal values of the electronic mass, corresponding to a small Fermi volume. Nevertheless, the presence of local moments is evident from the Curie-Weiss behavior of the susceptibility. At lower temperature the two electronic species start interacting via standard magnetic exchanges. At low enough temperatures magnetic interactions may lead to the compensation of the local moments from the conduction band electrons, that gain energy by a local binding mechanism (Kondo effect). This permits the *f*-orbital electrons to participate in the conduction process, with the consequent formation of heavy quasiparticles masses and large Fermi volume. In this latter regime the heavy fermions present peculiar metallic properties.

The resistivity has a slowly decreasing behavior upon cooling down the system from high temperature down to a characteristic value, where a minimum is attained. The increasing be-

## 1. Non-Fermi liquid behavior in *df*-electrons metals

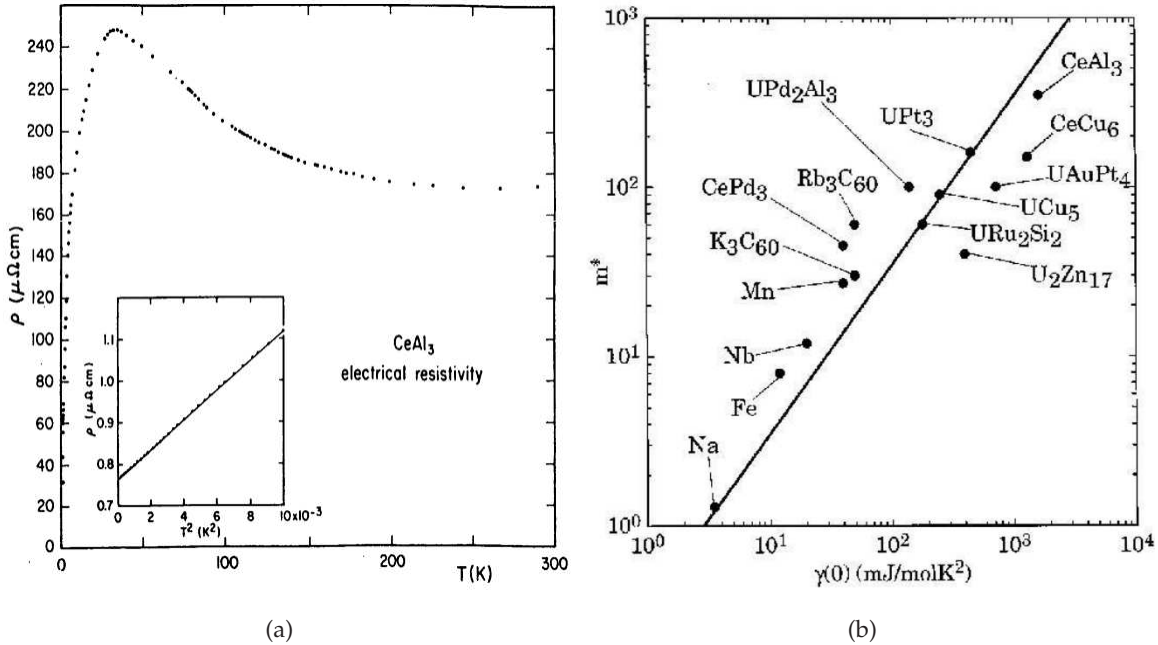


Figure 1.5: (a) Resistivity of  $\text{CeAl}_3$  heavy fermion systems as a function of the temperature. Inset: low temperature quadratic behavior. [71] (b) Effective mass  $m^*$  as a function of the electronic specific heat  $\gamma$  [19, 20]

havior is inverted only upon further lowering the temperature down to a critical value  $T^*$ , where Fermi liquid behavior is reached:  $\rho(T) = \rho_0 + AT^2$  (cf. Fig. 1.5(a)).

The specific heat behavior is non universal among the heavy fermion class till a temperature of the order  $T^*$  is reached. For temperatures lower than this value  $T < T^*$  the specific heat becomes linear, as predicted by Fermi liquid theory. However, the Sommerfeld coefficient  $\gamma = C(T)/T$  has values of the order  $1\text{J/molK}^2$ , that is at least  $10^3$  times bigger than ordinary metals Fig. 1.5(b). On the very same line the spin susceptibility, which has Curie-Weiss behavior at high temperature, saturates at low temperature  $T < T^*$  taking the expected Fermi-liquid Pauli behavior. The existence of a minimum in the resistivity behavior as a function of the temperature and of a “coherence” temperature scale below which a compensation mechanism seems to take place, are two main features of Kondo physics.

The Kondo problem goes back to the discovery of a minimum in the resistivity of metallic systems hosting dilute magnetic impurities. One of the models originally introduced to explain this behavior is the Kondo (or *s-d*) model, describing a single magnetic impurity interacting thru magnetic exchange with electrons in a conduction band. Using a third order perturbation theory Kondo was able to explain the existence of a minimum in the resistivity. A slightly more general model has been proposed by Anderson, *i.e.* the single impurity An-

derson model. This latter describes an impurity that is localized as effect of the correlation  $U$  and that hybridize with conduction band electrons. A canonical transformation permits to obtain the Kondo model from the Anderson model in the large  $U$  limit (Schrieffer-Wolff) [84]. The properties of the Anderson model have been investigated during almost 30 years of intense work, culminated with the introduction of the Wilson's Renormalization Group and the solution of the model [36]. The standard scenario that bears out from this solution, describes the formation of singlet states between the conduction band electrons and the local spin of the impurity for temperatures smaller than a critical value  $T_K$ , *i.e.* the Kondo temperature. The key point to underline and that made so difficult to achieve a solution of this model, is the non-perturbative nature of the Kondo problem (asymptotic freedom). The Kondo perturbative calculation is plagued by a logarithmic divergence at zero temperature. The coupling  $J$  between the magnetic impurity and the conduction band electrons becomes non-perturbatively large upon decreasing the temperature/energy (IR limit), such that perturbation theory breaks down at a scale corresponding to the Kondo temperature  $T_K \simeq C e^{-1/\rho(E_F)J}$ . In this IR limit the conduction electrons magnetic moment is tightly bounded to the impurity to form a non-magnetic state. It is possible to show the Fermi liquid nature of the model solution in this low temperature  $T < T_K$  regime. In this respect the Anderson model realizes one paradigmatic example of (local) Fermi liquid system.

The dilute impurity picture, corresponding to the scenario presented above, can explain some properties of heavy fermion compounds like *LaCe* or *CuFe*. Nevertheless, most of the heavy fermion systems require a rather more complicated approach, as the number of localized magnetic moments can be comparable with the number of lattice sites. Systems with more concentrated impurities are described by lattice extension of the Kondo or the Anderson model. The Kondo Lattice Hamiltonian reads:

$$H_{KL} = \sum_{\mathbf{k},\sigma} \epsilon(\mathbf{k}) c_{\mathbf{k},\sigma}^+ c_{\mathbf{k},\sigma} + J \sum_{i,\alpha\beta} \mathbf{S}_i \cdot (c_{i,\alpha}^+ \sigma_{\alpha\beta} c_{i,\beta}) \quad (1.4)$$

The first term of  $H_{KL}$  describes the electrons in the conduction band, while the second one models, via a suitable coupling constant  $J$ , the magnetic interaction between the local moments located at each site of a lattice and the conduction band electrons moments. The Kondo lattice model can be obtained, via a suitable Schrieffer-Wolff transformation, from the Anderson lattice (or periodic Anderson model) in the limit of large correlation. On a general ground one may expect the physics of the concentrated systems to be different in many aspects from that of the dilute models.

One important feature to consider is the role of the inter-moments magnetic interactions and their interplay with the Kondo screening. These interactions are not taken explicitly into account in the Kondo lattice model, but can be derived from the periodic Anderson model.

## 1. Non-Fermi liquid behavior in $d/f$ -electrons metals

---

Their importance is confirmed by the large variety of magnetic orders observed in many heavy fermion systems. To the lowest order intersites magnetic correlations are modeled by the Ruderman-Kittel-Kasuya-Yoshida (RKKY) interaction [79]. The physical mechanism is that of a conduction electron undergoing a two scattering process onto localized  $f$ -moments, mediating an indirect moment-moment magnetic interaction. The temperature scale below which these processes become effective is of order  $T_{RKKY} \simeq J^2 \rho(E_F)$ , where  $\rho(E_F)$  is the conduction band density of states at the Fermi energy and  $J$  the local Kondo coupling. The intermoment magnetic interactions, favoring the formation of magnetic orders, are in competition with the Kondo coupling, favoring the formation of a local Fermi liquid state [21]. In particular the presence RKKY interactions may lead to a reduction of the Kondo temperature. In fact, if the local moments are magnetically ordered, then Kondo screening leading to local moment compensation, may reduce the intersite magnetic energy.

A rather different and important feature to consider when dealing with impurity lattice models, is the so called “exhaustion” phenomenon, first introduced by Nozières [68, 67]. The screening electronic cloud involved in the singlet formation process in the Kondo effect, can be thought to be spatially extended over a distance of the order  $\lambda \simeq v_F / (k_B T_K)$ . In systems with a large concentration of local moments this imply the possibility for the Kondo effect to be non-local. In other words the same screening cloud is required to compensate several local moments, with the consequent reduction of the coherence scale [9]. We shall come back to this problem in the following of this thesis.

Finally it is worth to consider another important aspect of impurity lattice models physics, namely the existence of multiple relevant temperature/energy scales. In dilute impurity problems and in the Kondo limit ( $T < T_K$ ) all the physical quantities scale with  $T_K$ , that defines a single universal energy scale. In contrast, within concentrated systems the Kondo temperature may not be the only relevant scale of the problem [9]. Thus, the existence of other energy scales, driving the behavior and the coherence of the system, have to be taken into account.

### 1.3 Fermi or non-Fermi? Some experimental facts

Beside the unusual low temperatures below which heavy fermion systems acquire normal metallic properties, the interest around these systems is justified by some other intriguing facts too. For example many of the heavy fermion compounds at low enough temperatures either order magnetically, become superconductors, or more surprisingly do not show Fermi liquid properties. In the following we briefly review some experimental observations about heavy fermion compounds. The main goal is to put in evidence the rich variety of low temperature behaviors and the different properties that can be found among the heavy fermion compounds.

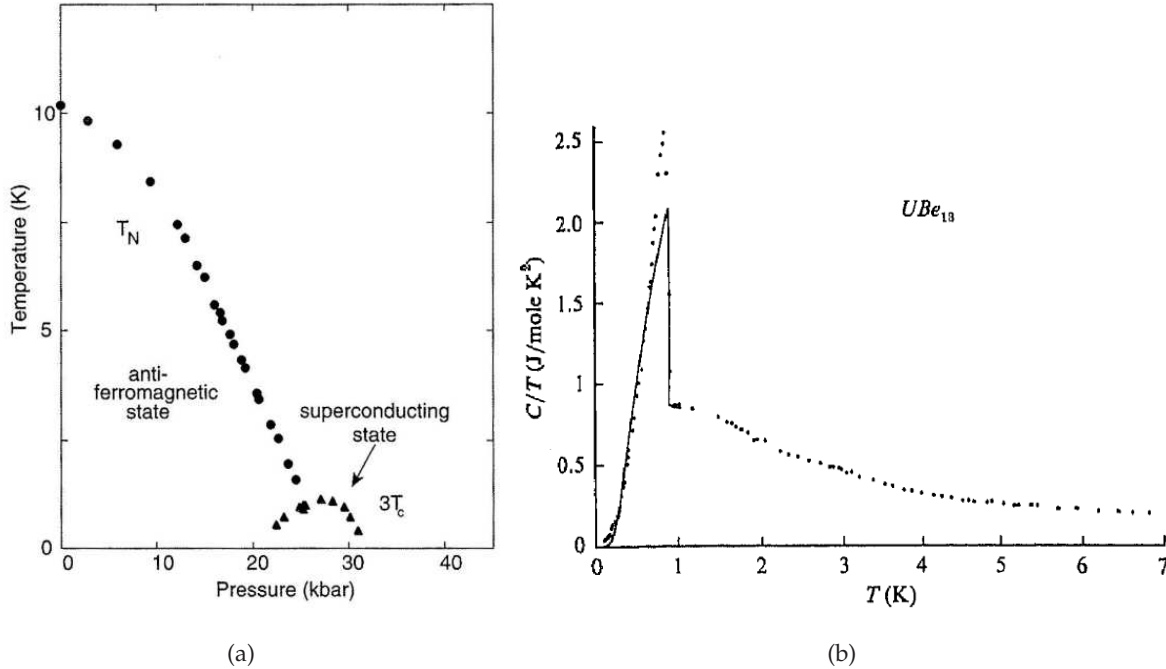


Figure 1.6: (a) Phase diagram of  $CePd_2Si_2$ . At very low temperatures a superconductive dome appears at the end of the Néel temperature line [58]. (b) Specific heat jump at the superconductive transition ( $T_c = 0.9K$ ) of the heavy fermion compound  $UBe_{13}$ . The solid line corresponds to BCS theory fit, [36].

Thus, the term heavy fermions refers to a wide class of systems sharing the characteristic feature of having a large electronic specific heat at very low temperature.

Superconductivity in heavy fermion compounds has been discovered in 1979 in  $CeCu_2Si_2$  at  $T_c = 0.6K$  by Steglich *et al.* [92]. Later on many other compounds have been found to become superconductors, all with critical temperatures around 1K, like  $UBe_{13}$  ( $T_c = 0.9K$ ),  $UPt_3$  ( $T_c = 0.5$ ) or  $CePd_2Si_2$ , see Fig. 1.6(a) [93]. The rather small values of the critical temperatures for the superconductive transition in these systems can be related to the presence of large magnetic moments. While at the beginning the strong magnetism of heavy fermions was considered to be in strong competition with superconductivity, nowadays some interesting ideas have been proposed to explain the pairing mechanism as mediated by magnetic interactions (cf. concluding remarks and perspectives 5.8). Many of the heavy fermions superconductors show a large specific heat anomaly  $\Delta C_v$  at the superconductive process, signalling that the heavy quasiparticles are directly involved in the superconductive process (cf. Fig. 1.7).

In many cases the transition to superconductive phase appears at the boundary of a magnetically (AFM or FM) ordered phase, so that coexistence of magnetic order and superconductivity can be observed. This is the case for example for  $UPd_2Al_3$ ,  $CeCoIn_5$  Fig. 1.7(a) (antiferromag-

## 1. Non-Fermi liquid behavior in *d/f*-electrons metals

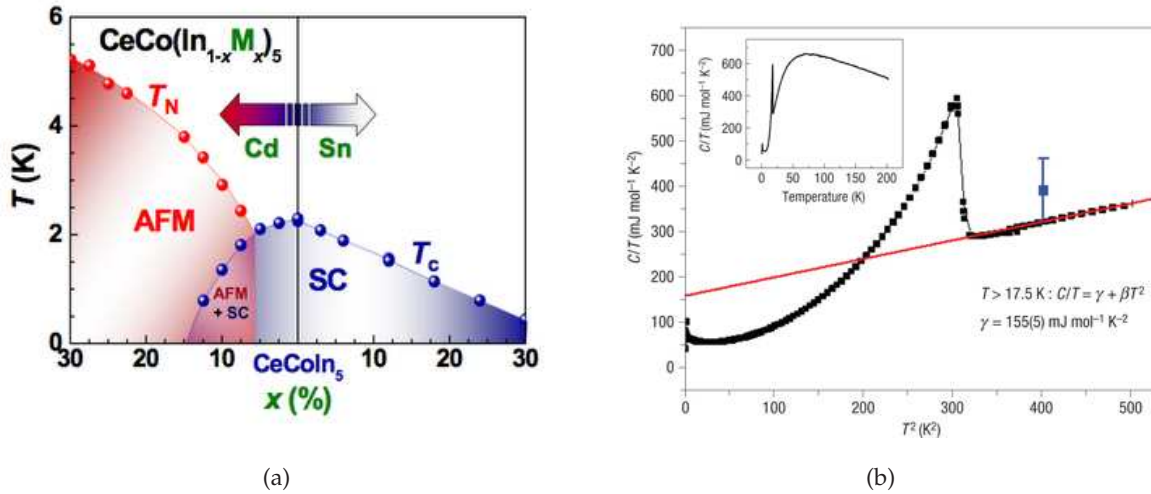


Figure 1.7: (a) Phase diagram for doped  $CeCoIn_5$  with both  $Cd$  and  $Sn$ . The plot illustrates the possible coexistence of antiferromagnetic order in the superconductive phase. (b) Electronic specific heat  $C/T$  as a function of the square of the temperature for the heavy fermion compound  $URu_2Si_2$ . The figure shows the large specific heat anomaly at the “hidden order” transition.

netic order),  $UGe_2$  (ferromagnetic) or for the case of the so-called “hidden order” compound  $URu_2Si_2$  [23]. This latter undergoes a transition at  $T_N = 17K$  to an antiferromagnetic phase characterized by a very small value of the magnetic moment, that is in contrast with the rather large value of the observed specific heat jump, cf. Fig. 1.7(b). The system presents a superconductive transition at  $T_c = 6K$ , with some indications for the coexistence of such a weak magnetic ordering and superconductivity [22].

Heavy fermions are often associated to compounds with a nearly integer valence, *i.e.* Kondo lattices. However, it is worth to observe that anomalous rare-earths like  $Ce$ ,  $Yb$  or  $Sm$  appear with different valencies, giving rise to metallic alloys with a pronounced mixed-valence character, such as  $CeAl_2$ ,  $YbCuAl$ . These systems can have electronic specific heat values much larger than normal metals, *i.e.*  $\gamma \lesssim 400mJ/moleK^2$  [36], but still slightly smaller than the values usually observed in other heavy fermion compounds. Nevertheless, mixed-valence compounds show interesting heavy fermion behaviors at low temperature, with some marked peculiarities. One example is the intermediate valence transition, in which the compound (*e.g.*  $YbInCu_4$ ) undergo a sharp transition associated with a sudden change of its valence as a function of external parameters [15].

One of the most striking and interesting feature of heavy fermions is the deviation at low temperatures from the Fermi liquid predictions, as observed in an increasing number of com-

pounds [94]. Systems showing such a behavior can be roughly grouped under the name of *non-Fermi liquids*. First evidences for breakdown of Fermi liquid properties in heavy fermions have been put in evidence in specific heat and resistivity measurements on the  $Y_{1-x}U_xPd_3$  compound around 1991 [85]. Later on many other compounds have shown a behavior not compatible with the Fermi liquid predictions, such as  $UCu_{5-x}Pd_x$  (cf. Fig. 1.8(a)),  $Ce_7Ni_3$  (cf. Fig. 1.8(b)),  $YbRh_2Si_2$ . The classification of such systems in general categories is a rather complicated task, due to the wide range of physical regimes in which non-Fermi liquid behavior has been observed.

Breakdown of the Fermi liquid properties in many heavy fermions appear in the proximity of a magnetic transition. Experimentally such a transition can be induced by either chemical substitution (doping), applying pressure, or varying external magnetic field. The competition between different magnetic interactions often push to zero the critical temperature associated with such magnetic transition, as well illustrated by the Doniach diagram [21]. Thus, the breakdown of Fermi liquid properties is usually associated to the existence of a quantum phase transition or a quantum critical point in the phase-diagram. However, other reasons (*e.g.* disorder) have also been proposed to explain the non-Fermi liquid behavior in heavy fermions.

The deviations from Fermi liquid paradigm are most of the times characterized measuring the specific heat or the resistivity behavior. As discussed in the first section of this chapter in fact, Landau theory of Fermi liquids predicts precise behavior for the these quantities, (*i.e.* a linear specific heat and a quadratic resistivity). Thus, anomalous behaviors in the resistivity and/or in the specific heat are considered hallmarks of non-Fermi liquid phase.

In particular, many measurements report for the resistivity a behavior, down to very low temperatures, of the form

$$\rho(T) - \rho_0 \simeq AT^\alpha$$

where the constant  $A$  can be either positive or negative and the non-universal exponent  $\alpha$  is such that  $1 \leq \alpha < 2$ . Non-Fermi liquid behavior is generally observed over a temperature range of two or more decades near zero temperature, although in some cases only a smaller temperature range is accessible.

Deviations from the linear specific heat behavior at low temperatures are usually characterized in terms of temperature dependence for the Sommerfeld parameter  $\gamma = C/T$  (constant in the Fermi liquid theory). Many measurements report a characteristic log-divergent behavior for this quantity :

$$C/T \simeq -\log(T)$$

that is protracted over at least two decades of temperature. More severe divergences than the logarithmic one can be observed in some compounds, such as  $UCu_{3.5}Al_{1.5}$  or  $YbRh_2Si_2$ , while

## 1. Non-Fermi liquid behavior in *d/f*-electrons metals

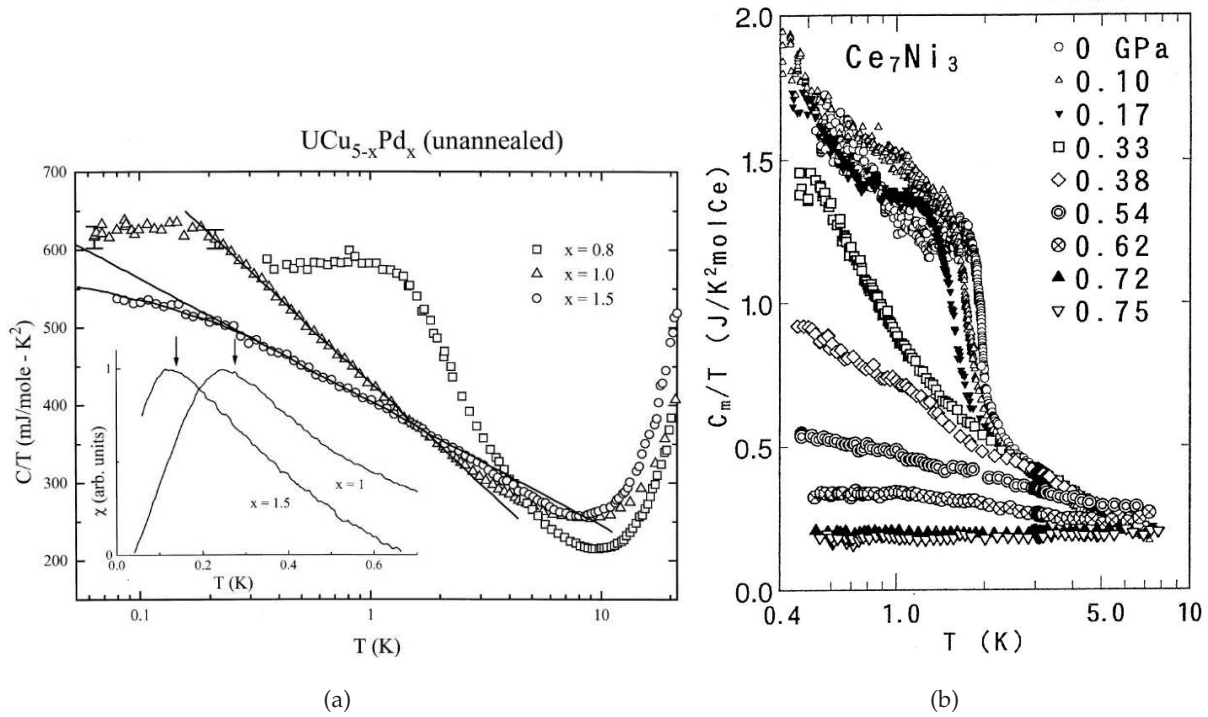


Figure 1.8: (a) electronic specific heat  $C/T$  as a function of  $\log T$  for the heavy fermions  $UCu_{5-x}Pd_x$  [82]. (b) The same quantity for  $Ce_7Ni_3$  [97]. Both the figures present the log-divergent behavior of the specific, corresponding to a significant deviation from the Fermi liquid metallic state.

in some systems a weak temperature dependence of  $\gamma$  is reported, which can be fitted by a square root term:  $C/T = \gamma_0 - A\sqrt{T}$ .

Another quantity that provides some additional insights into the nature of the observed non-Fermi liquid behavior is the entropy. Most of the studied compounds show a small residual entropy at a low fixed temperature, that can be expressed as “renormalized” unquenched spin entropy  $S \simeq B \log(2)$ , with  $B$  going from values below 0.2 to about 0.9. This is a direct indication of the presence of electrons with unscreened magnetic moment actively participating in the non-Fermi liquid behavior.

## 1.4 Schematic overview on NFL phase description

On a theoretical ground the first result relevant for the non-Fermi liquid problem is [35], extending the Ginzburg-Landau-Wilson theory to quantum phase transition. Later, some results about non-Fermi liquid behavior were obtained in [70] considering a suitable generalization of the Kondo problem. After these two early works many other ideas have been put forward to try to explain the origin of the breakdown of the Fermi liquid paradigm in certain classes of materials (including heavy fermion systems). The many ideas elaborated so far can be roughly grouped into three categories [94]: i) overcompensation of the local moments (multi-channel Kondo model), ii) disorder effects (Kondo disorder), and finally iii) neighborhood to some magnetic instability at zero temperature (quantum criticality). We shall now briefly review the main aspects of these three groups. More attention will be dedicated to the quantum criticality approach, motivated by both the increasing interest this is attracting nowadays and its affinity with the central result of this thesis.

### 1.4.1 Multi-channel Kondo model

This approach to the derivation of non-Fermi liquid properties follows the initial work of Nozières and Blandin[70], concerning a generalization of the Kondo model, namely the multi-channel Kondo model. This model describes a single impurity bearing a spin  $S$  coupled via a constant  $J > 0$  to  $N$  degenerate-orbital conduction electrons, *i.e.*  $N$  channel conduction band. Depending on the number of conduction “channels” and the value of the spin of the local impurity one can distinguish three different regimes:

- $N < 2S$  The number of available conduction electron channels is trivially too small to compensate the local spin of the impurity and to form a singlet state.
- $N = 2S$  This case corresponds to the “standard” Kondo model, prototype of the local Fermi liquid state. The number of conduction electrons is just sufficient to screen the local

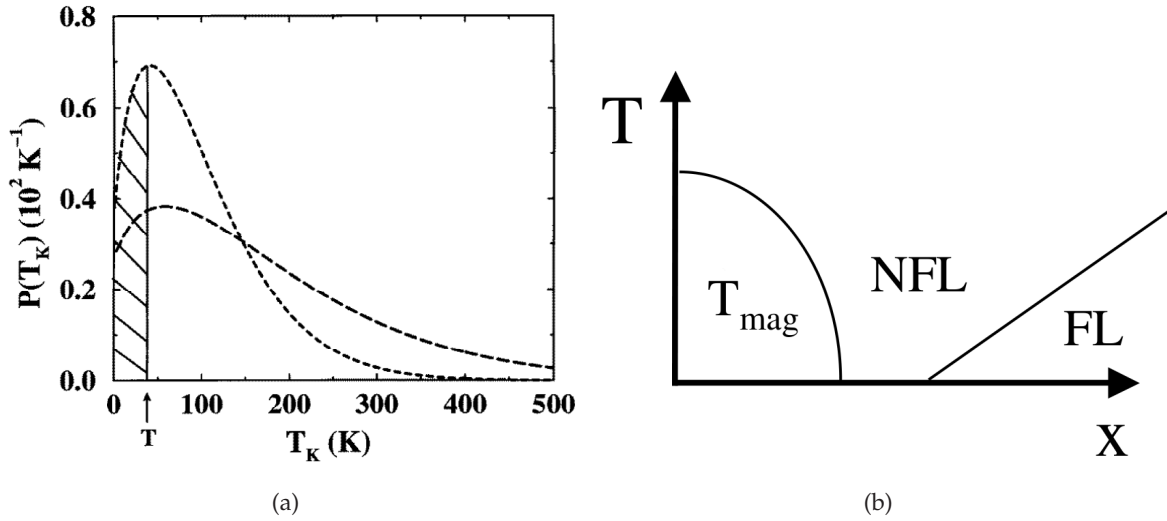


Figure 1.9: (a) Probability distribution of the Kondo temperature [7]. (b) Disorder and competition between magnetic interaction [13]: a schematic phase diagram. It is of interest to compare this with Fig. 5.21

impurity compensating its spin. The main energy scale is fixed by  $T_K$  and the behavior of the macroscopic quantities follow the Fermi liquid prediction at  $T < T_K$ .

- $N > 2S$  The spin of the local impurity is over-screened by the available conduction electrons channel. This lead to a non-Fermi liquid ground state and to a critical power law (or logarithmic) behavior of some measured quantities at zero temperature and zero external field.

The exact solution of the multi-channel Kondo model has been obtained by different author, *e.g.* [4], but the application of this model to heavy fermion systems is not completely clear. The 2-channel Kondo model ( $N = 2$  and  $S = 1/2$ ) describes a non-Fermi liquid state whose critical behavior near  $T = 0$  and zero applied magnetic field ( $H = 0$ ) is characterized by a logarithmic divergent electronic specific heat at low temperature,  $C/T \sim -\log(T/T_K)$ , and a square root behavior of the resistivity  $\rho \sim \rho_0 + AT^{0.5}$  [81].

### 1.4.2 Kondo disorder

In the single impurity Kondo model the Fermi liquid formation requires temperatures smaller than a characteristic energy scale, fixed by the coupling constant and the density of states at the Fermi level by  $T_K \simeq De^{-1/n(0)J}$ . Thus, it is straightforward to realize that if the Kondo temperature is, even locally, driven to zero by some physical mechanism, a breakdown of the Fermi liquid properties should be observed. This is briefly the key concept behind the

Kondo disorder approach to the non-Fermi liquid phase in heavy fermions. Disorder allows for an inhomogeneous “distribution” (with a probabilistic meaning) of the Kondo temperatures throughout the lattice, leading to a breakdown of the expected Kondo screening. Some results for the  $UCu_{5-x}Pd_x$  compounds have been obtained assuming a phenomenological Gaussian distribution for the random variable  $\zeta = n(E_F)J$  [7]. This assumption determines a distribution function  $\mathcal{P}(T_K)$  (cf. Fig. 1.9(a)) for the Kondo temperatures, giving finite probability to the zero Kondo temperature event:  $\mathcal{P}(T_K = 0) \neq 0$ .

Another approach to Kondo disorder has been introduced in [62, 63, 64]. In this work the coupling between strong correlation and disorder is studied using Anderson lattice. Disorder is introduced assuming random distributions for the energy level of the correlated electrons and for their hybridization with the conduction band. This is sufficient to determine a probability distribution of the Kondo temperature. Following this approach it has been possible to derive a linear temperature behavior for the electric resistivity. The solution of this model did not take into account the presence of inter-moments correlations (RKKY). Finally a somewhat different approach along this line has been proposed in [13]. This work stem from the observation that both disorder and neighborhood to magnetic instabilities can be considered as concauses of the breakdown of the Fermi liquid paradigm. It is worth to mention that in both these two approaches the low temperature physics is dominated by the tail around zero temperature of the Kondo temperature distribution, corresponding to the finite probability of having unquenched spins (Griffith phase).

### 1.4.3 Quantum criticality

Many instances of the deviations from Fermi liquid theory in heavy fermion systems are observed in the proximity of a quantum critical point, *i.e.* a magnetic transition with an ordering temperature that is pushed to zero by competing magnetic interactions, [21]. The presence of a quantum critical point in the phase diagram strongly affects the properties of the system at finite temperature. In the context of heavy fermions this corresponds to a failure in the construction of a Fermi liquid state at very low temperatures.

In the classic (as opposed to quantum) phase transition scenario the temperature plays the role of an external parameter driving the approach to the transition. The couplings that appear in the free energy functional implicitly depends on the temperature and their behavior in the neighborhood of the critical temperature  $T = T_c$  fixes the nature of the transition (critical exponents). At the critical point the correlation length diverges and the order parameter  $\phi$  has fluctuations at all scales, making the system scale-independent. It is possible to show that in a number of dimensions  $D = 4$  the fluctuations of the order parameter are Gaussian (upper critical dimension). Time fluctuations of  $\phi$  can be associated with a frequency  $\omega_\phi$ , that

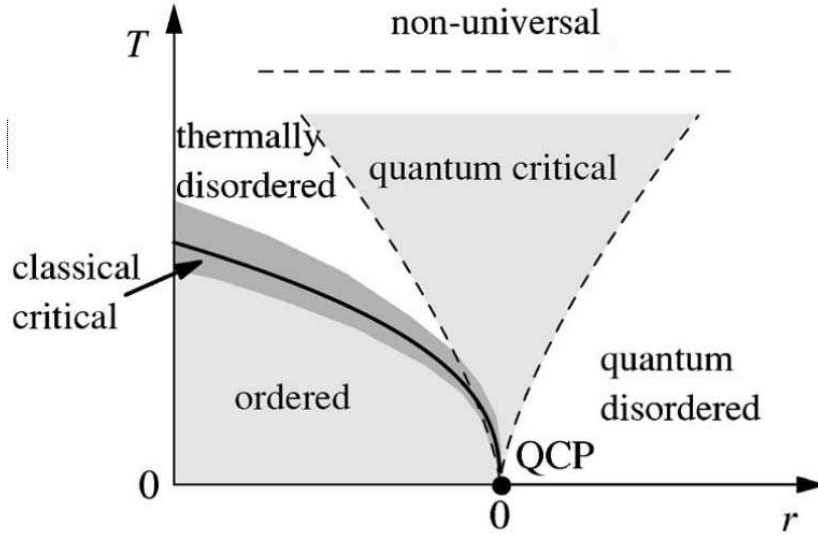


Figure 1.10: Qualitative phase diagram in the neighborhood of a quantum critical point. The tuning parameter is  $r = g - g_c$ . Shaded line above the QCP is the quantum critical region. Solid line indicate the transition towards ordered phase across which classical thermal fluctuations dominate. For low temperature and away from the critical point the systems is dominated by quantum fluctuations by is not ordered (*e.g.* Fermi liquid).

has a vanishing behavior approaching the critical point. A system undergo a classical phase transition if  $k_B T_c \gg \hbar \omega_\phi$ . In the opposite case the transition has a quantum nature.

Quantum phase transitions are driven by some external parameter  $g$ , different from the temperature. This parameter is often identified with the pressure, magnetic field or doping. An useful quantum-classical mapping can be exploited to describe the approach at the quantum critical point  $g = g_c$ . This mapping permits to extend the use of methods already available for the investigation of classical critical phenomena. As already pointed out in [35], in quantum phase transitions static and dynamic degrees of freedom can not be decoupled, as happen in the classical case. Thus, the quantum-classical mapping can only relate a  $d$ -dimensional quantum system to a  $d + z = D$ -dimensional classical system, where  $z$  is a dynamical exponent. This latter describes the scaling of the fluctuation length on the imaginary axis, *i.e.* the correlation time  $\xi_\tau$ , with respect to the correlation length  $\xi$ :

$$\xi_\tau \sim \xi^z \sim |g - g_c|^{-z\nu}$$

where  $|g - g_c|$  define the “distance” from the critical point and  $\nu$  is the correlation-length exponent. The specific value of the dynamical exponent  $z$  depends on the detailed form of the correlation function of the order parameter.

Using scaling arguments only it is possible to derive a schematic phase diagram in the prox-

## 1.4. Schematic overview on NFL phase description

(a)				
	AFM, $z=2$ $d=3$	AFM, $z=2$ $d=2$	FM, $z=3$ $d=3$	FM, $z=3$ $d=2$
$C/T$	$\gamma - a\sqrt{T}$	$c \log(T_0/T)$	$c \log(T_0/T)$	$T^{-1/3}$
$\Delta\chi$	$T^{3/2}$	$\chi_0 - dT$		
$\Delta\rho$	$T^{3/2}$	$T$	$T$	
$T_{NIC}$	$(\delta_c - \delta)^{2/3}$	$(\delta_c - \delta)$	$(\delta_c - \delta)^{3/4}$	$(\delta_c - \delta)$
$T_I$	$(\delta - \delta_c)$	$(\delta - \delta_c)$	$(\delta - \delta_c)^{3/2}$	$(\delta - \delta_c)^{3/2}$
$T_{II}$	$(\delta - \delta_c)^{2/3}$	$(\delta - \delta_c)$	$(\delta - \delta_c)^{3/4}$	$(\delta - \delta_c)$
(b)				
	Ferro, 3-dim	Ferro, 2-dim	AFM, 3-dim	AFM, 2-dim.
$C_m/T$	$-\log T$	$T^{-1/3}$	$\gamma_0 - aT^{1/2}$	$-\log T$
$\chi_Q$	$T^{-4/3}$	$-T^{-1}/\log T$	$T^{-3/2}$	$-(\log T)/T$
$\Delta\rho$	$T^{5/3}$	$T^{4/3}$	$T^{3/2}$	$T$

Figure 1.11:

imity of a quantum critical point, Fig. 1.10 [56]. A continuous finite temperature transition line, ending in a QCP, is the boundary of an ordered phase ( $T < T_c$  and  $g - g_c < 0$ ). Across this line the physics is dominated by thermal fluctuations (“thermally disorder”). At low temperature and for  $g - g_c > 0$  thermal effects are negligible with respect to quantum fluctuations (“quantum disorder”). This regime is characterized by the formation of quasiparticle excitations. At high temperature above the critical point is the quantum critical region. Here both thermal and quantum fluctuations are important. The physical properties of this region are determined by the thermal excitations of the quantum critical ground state, that are not associated to quasiparticle-like excitations. This behavior is reflected in critical power-law dependencies of physical quantities.

The investigation of quantum phase transition in Fermi liquids was started in [35], later retrieved and extended by Millis [61] and other authors. The main model consist in a quantum mechanical generalization of the Landau free energy functional and describes the spin fluctuations physics near a magnetic transition. To the second order the (effective) action is expressed in terms of the inverse dynamical susceptibility  $\chi(\mathbf{k}, \omega_n)$ , the exact expression of which may vary from case to case. Because the dynamic exponent for magnetic transitions is  $z = 2$  (AFM) or  $z = 3$  (FM), the effective dimensionality often exceeds the upper critical dimension:  $d + z > 4$ . Thus the theory can only account for corrections to Gaussian (Fermi liquid) behavior. For example in three-dimensional antiferromagnetic transition this theory predict a non-Fermi liquid specific heat behavior  $C/T = \gamma_0 + A\sqrt{T}$ .

A further improvement of the Hertz-Millis theory has been put forward in [65]. This approach describes weakly interacting spin fluctuations by means of self-consistent renormal-

## 1. Non-Fermi liquid behavior in $d/f$ -electrons metals

---

ization. The key assumption is to replace the quartic interaction term by a phenomenological constraint on the dynamic susceptibility. This approach works also above the upper critical dimension. Because the spin fluctuations mode-mode coupling depends on the temperature, the physical observables show at  $T = 0$  the same non-Fermi liquid behavior as obtained in the Hertz-Millis analysis. Nevertheless, at low temperature the increasing strength of the coupling give rise to a log-divergent electronic specific heat,  $C/T \sim -\log(T)$ , and a linear behavior for the resistivity  $\Delta\rho \sim AT$ .

Lately another approach based on quantum criticality has been proposed to explain non-Fermi liquid behavior [88, 87, 90]. The central idea is that breakdown of the Kondo screening is a spatially local phenomenon (local quantum critical theory). This approach starts from the Kondo lattice model (cf. (1.4)) with an additional term expressing the moment-moment magnetic interaction. The solution of the model is achieved using an extension of Dynamical Mean Field Theory (cf. Chap. 2), termed EDMFT. Within this method the Kondo lattice model is mapped onto an effective Bose-Fermi Kondo model, in which a single impurity is coupled to an electronic reservoir representing the conduction electrons and to a bosonic bath that models the effects of magnetic fluctuations due to the RKKY interaction. A local quantum critical point originates from the competition of the Kondo screening and and the RKKY interactions [21]. In the neighborhood of this QCP fluctuating magnetic field drives the Kondo effect critical, preventing the conduction electrons from screening the local moments. At the critical point this theory predict a critical power-law frequency dependence of the dynamic susceptibility:  $\chi(\mathbf{q}, \omega)^{-1} \simeq f(\mathbf{q}) + A(\omega/\Lambda)^\alpha$ , with a non-universal anomalous exponent  $\alpha$ , that can fit with some experimental data.

The theoretical predictions obtained from the presented different approaches to non-Fermi liquid physics can hardly account for the large variety of behaviors observed in the experiments, cf. [94]. This reveals how far we are from obtaining a general and accurate theoretical description of the breakdown of the Fermi liquid paradigm.

# Theoretical framework: DMFT

## Contents

---

<b>2.1 Insights from mean-field theory: the Ising model</b> . . . . .	<b>30</b>
<b>2.2 Dynamical Mean Field Theory</b> . . . . .	<b>33</b>
2.2.1 Effective action . . . . .	33
2.2.2 Limit of infinite coordination number . . . . .	36
2.2.3 Self-consistency . . . . .	37
<b>2.3 Connection with quantum impurity problem</b> . . . . .	<b>41</b>
<b>2.4 Solution of DMFT equations</b> . . . . .	<b>42</b>
2.4.1 Iterated perturbation theory . . . . .	44
2.4.2 Quantum Monte Carlo . . . . .	45
2.4.3 Exact diagonalization . . . . .	47
2.4.4 Density Matrix Renormalization group . . . . .	52
<b>2.5 Conclusions</b> . . . . .	<b>57</b>

---

In the last two decades a big advance in the understanding of the strongly correlated physics has been possible with the introduction of a powerful theoretical tool, namely Dynamical Mean Field Theory (DMFT) [52]. In this part of the thesis we shall present the main ideas at the heart of this tool and derive the correspondent equations in the simple, but rather illustrative case of the Hubbard model [31]. DMFT is the natural quantum extension of the classical mean field theory, introduced so far to study magnetic properties of spin models, such as Ising. The key idea of this method is that of replacing the quantum many body problem on a lattice with that of a single site coupled to an effective bath, representing the lattice electronic degrees of freedom, supplemented by a self-consistent condition. The mapping becomes exact in the limit of infinite coordination number,  $z \rightarrow \infty$ . This is consequence of the great simplifications, namely

the locality of the theory, this limit brings in the quantum many-body problem. Thus, DMFT provides a controlled approximation scheme that retains the full local quantum nature of the initial problem, in contrast with Hartree-Fock or Slave Bosons mean field [57, 50], and neglects spatial fluctuations.

Even if the infinite coordination number limit could appear somehow “unphysical”, specially when we refer to it as infinite dimensionality limit, this is in reality perfectly justified in many cases. To this end it may be sufficient to consider, for example, the number of nearest neighbor in a 3-dimensional fcc-lattice that is of order  $z \sim O(10)$ . On the other hand approximations making use of the locality of the theory have been introduced even before, the  $z \rightarrow \infty$  limit was studied, specially in the context of heavy fermion physics, where the local nature of the correlated electrons makes this approach particularly suitable.

This chapter is organized as follow: in Sec. 2.1 we review the derivation of the classical mean field theory for the (ferromagnetic) Ising model using the cavity method. This pave the way to the derivation of the dynamical mean field equations for the Hubbard model, presented in Sec. 2.2, and permit us to better understand the conceptual analogies between the two methods. To gain some physical insight about the nature of this approximation scheme we present in Sec. 2.4 its connection with an effective single impurity problem and discuss the related physical interpretation. In Sec. 2.5 we illustrate the general (iterative) method of solution of the DMFT equations and we review some of the numerical methods that can be used to this end.

### 2.1 Insights from mean-field theory: the Ising model

To simplify the introduction of the DMFT, we review in this section the classical mean field theory of spin models. These have been initially introduced to study spontaneous magnetization in metallic materials, like *Fe* or *Ni*, displaying strong ferromagnetism below some critical temperatures. The approach to the problem was to imagine the full system as made of small domains bearing an mean local moment/spin  $S$  pointing in some direction and that could couple to external magnetic field. To model this idea one can write down models describing spins organized on a lattice structure and interacting with some short range potential. The most relevant and studied model is without any doubt the Ising model. On an arbitrary lattice with coordination  $z$ , the (ferromagnetic) Ising Hamiltonian reads:

$$H_{\text{IM}} = - \sum_{ij} J_{ij} S_i S_j - \sum_i h_i S_i \quad (2.1)$$

where  $J_{ij} = J > 0$ . Despite its apparent simplicity the problem posed by the solution of this model, could be highly non-trivial [38, 24]. Many different approximation scheme has been put forward to study the problem posed by paramagnetic-ferromagnetic phase transition, among

which a time-honored place is occupied by mean field theory. After its introduction in the context of spin models, this method has been extended in many directions and in other different areas, thus constituting one of the building block of modern physics.

The key idea is very simple: one focus on a given arbitrary spin of the lattice and assume that the neighboring spins act on the chosen one as an averaged “molecular” magnetic field. The great simplification arise from neglecting the non local fluctuations of the acting field. The accuracy of this method obviously increases when the number of neighbor spins is large enough and the interaction term  $J_{ij}$  is non zero only among nearest neighbor. It can be rigorously proved that the mean field approximation becomes exact in the limit of infinite coordination number (or dimension).

To easily derive the mean field equation one should first observe that the magnetic field acting on the tagged spin (say  $i = 0$ ) as effect of the neighboring sites is (magnetic moment is set equal to 1):

$$h = -\frac{\partial H_{\text{IM}}}{\partial S_0} = h_0 + \sum_j J_{0j} S_j$$

The fluctuations of this magnetic field are obtained by averaging the previous expression. In doing this one can assume the translational invariance of the local magnetization:  $\langle S_j \rangle = \langle S_i \rangle = \langle m \rangle$ :

$$\langle h \rangle = h_0 + \sum_j J_{0j} \langle S_j \rangle = h_0 + zJm$$

In the mean field approximation the fluctuations of  $h$  with respect to its average value are neglected, so:  $h \simeq \langle h \rangle = h_{\text{eff}}$ . This can be rephrased by saying that the actual average value of the effective magnetic field acting on the chosen spin is independent by the instantaneous configuration of one neighboring spin. In the mean field approach we can thus define an effective Hamiltonian:

$$H_{\text{eff}} = -h_{\text{eff}} S_0$$

and easily evaluate the local magnetization:

$$\langle m \rangle = \sum_{S_0=\pm 1} S_0 e^{\beta h_{\text{eff}} S_0} / \sum_{S_0=\pm 1} e^{\beta h_{\text{eff}} S_0} = \tanh(\beta(h_0 + zJm))$$

This transcendental equation for the magnetization is then used to “self-consistently” determine this quantity. Varying the external magnetic field and the temperature the solution of this equation in fact describes the possible phases of the system. Moreover it becomes immediately evident the fact that the coupling constant  $J$  should be rescaled as

$$J \xrightarrow{z \rightarrow \infty} J/z$$

in the limit of infinite coordination number to keep the solution meaningful and the effective field finite.

## 2. Theoretical framework: DMFT

---

We can now turn to a different, slightly more elaborated, derivation of the mean field equation for Ising model, making use of the *cavity method*. This latter is a general method that we will use in the following to derive the DMFT equations. As before, we shall focus on a given (arbitrary) site of the lattice, say  $i = 0$ , but now we proceed to integrate out the degrees of freedom of all sites different from 0, in order to obtain the effective Hamiltonian for the cavity 0. This Hamiltonian is defined by the formula:

$$e^{-\beta H_{\text{eff}}} = \frac{\sum_{S_{i \neq 0}} e^{-\beta H}}{\sum_{S_i} e^{-\beta H}}. \quad (2.2)$$

To perform the sum at numerator we split the Hamiltonian (2.1) into three terms:  $H = H_0 + H^{(o)} + \Delta H$ , where

$$\begin{aligned} H_0 &= -h_0 S_0 \\ H^{(o)} &= - \sum_{ij \neq 0} J_{ij} S_i S_j - \sum_{i \neq 0} h_i S_i \\ \Delta H &= - \sum_i J_{0i} S_0 S_i \end{aligned} \quad (2.3)$$

$H_0$  is the Hamiltonian of the tagged site 0, decoupled from the lattice,  $H^{(o)}$  is the “cavity” Hamiltonian, *i.e.* the Hamiltonian describing the properties of the system with one site removed, and finally  $\Delta H$  is the interaction term between the site 0 to the rest of the system. In particular this last term connect the removed site with its former nearest neighbors. We can rewrite this last term in a more suitable way introducing sources  $\eta_i = J_{0i} S_0$ . With this notation it is easy to recognize that the initial sum is ultimately reduced to the average of the exponential of the interaction respect the cavity Hamiltonian, that is the generating functional of the connected correlations. Thus the effective Hamiltonian reads:

$$H_{\text{eff}} = \text{const.} - h_0 S_0 - \sum_{n=1}^{\infty} \sum_{i_1 \dots i_n} \frac{1}{n!} \eta_{i_1} \dots \eta_{i_n} \langle S_{i_1} \dots S_{i_n} \rangle_{(o)}^c \quad (2.4)$$

As we have noticed in the previous derivation, the limit of infinite dimension should imply a rescaling of  $1/z^{|i-j|}$  of the spin coupling  $J_{ij}$ . With such a rescaling it is straightforward to autoconvince that the only surviving term in (2.4) in the limit  $z \rightarrow \infty$  is that with  $n = 1$ . The effective Hamiltonian reduce to:

$$H_{\text{eff}} = -h_{\text{eff}} S_0 \quad (2.5)$$

where we have introduced the effective field with rescaled coupling:

$$h_{\text{eff}} = h_0 + \sum_i J_{0i} \langle S_i \rangle_{(o)} \quad (2.6)$$

At this point the solution of the problem flow in the very same way as already presented above. That is, one need to relate the effective magnetic field to a local correlation function of the

original lattice. Observing that in the limit of infinite coordination number removing one spin has an effect of order  $1/z$ , one immediately deduce that the local magnetization of the cavity Hamiltonian  $H^{(o)}$  is identical the local magnetization of the original Hamiltonian  $\langle S_i \rangle_{(o)} = \langle S_i \rangle = \langle S_0 \rangle = m$ . Thus the effective Hamiltonian (2.5) becomes:

$$H_{\text{eff}} = -h_{\text{eff}}S_0 = -(h + Jm)S_0 \quad (2.7)$$

While the average local magnetization is given by:

$$m = \langle S_0 \rangle = \tanh(\beta h_{\text{eff}}) \quad (2.8)$$

The last two equations form the mean-field equation for the Ising model. The cavity method permits to formulate the classical mean field theory for Ising spin models exploiting the limit of infinite nearest neighbor and the resulting scaling of correlation functions.

## 2.2 Dynamical Mean Field Theory

This section is entirely devoted to the derivation of the DFMT equations for the one band Hubbard model. Suitable extensions of the method to deal with other, more complicated, models are quite straightforward [31, 32]. In the following section we shall derive the DMFT equation corresponding to the main model studied in this thesis in the next chapter.

DMFT equations could be derived following different approaches, nevertheless the cavity method derivation is particularly simple and illustrative. Moreover it permits an immediate comparison with classical Weiss mean field theory, introduced in the previous section. Similarly to this latter method, the main idea is to obtain an effective local problem averaging out all the degrees of freedom of the lattice problem but those referred to a particular arbitrary site.

As we will see in the following, in the case of a many-fermions problems, this procedure will generate a local Weiss field  $\mathcal{G}_0$  corresponding to the effective magnetic field  $h_{\text{eff}}$  of classical mean field theory.  $\mathcal{G}_0$  defines the main unknown of the theory. A relation that connect the Weiss field to local observables is then constructed to close the equations and self-consistently determine the solution of the problem. This will be done by mean of the large connectivity limit and the simplification it brings into the problem. As well as the classical mean field theory, DMFT becomes exact in the limit of infinite dimension. We illustrate the cavity method construction of the effective model in Fig. 2.1.

### 2.2.1 Effective action

The Hubbard model Hamiltonian on an arbitrary lattice reads:

$$\tilde{H}_{\text{HM}} = H_{\text{HM}} - \mu N = - \sum_{\langle ij \rangle \sigma} t_{ij} (d_{i\sigma}^+ d_{j\sigma} + d_{j\sigma}^+ d_{i\sigma}) - \mu \sum_{i\sigma} d_{i\sigma}^+ d_{i\sigma} + U \sum_i n_{di\uparrow} n_{di\downarrow} \quad (2.9)$$

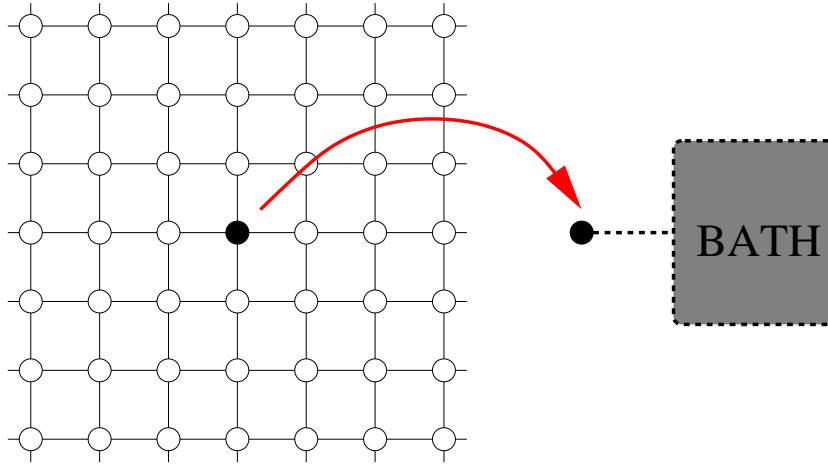


Figure 2.1: Schematic representation of the cavity method construction of the effective impurity problem. One (arbitrary) site is picked out of the lattice and embedded in a self consistent bath obtained by integrating out the remaining degrees of freedom in the lattice. From [28].

where the operators  $d_{i\sigma}$  and  $d_{i\sigma}^+$  destroy and create electrons with spin  $\sigma$  at site  $i$ . The electrons form a band with hopping parameter  $t_{ij} = t\delta_{ij}$ .  $U$  is the energy cost of double occupy any site in the lattice, modeling the strong repulsion originated from electron-electron Coulomb interaction.  $\mu$  is the chemical potential. To fix ideas we will consider throughout the rest of this section the paramagnetic phase of the model. The partition function of the model can be easily written down in a fermionic functional integral formalism introducing a set of Grassmann variables  $d_{i\sigma}(\tau)$ ,  $d_{i\sigma}^+(\tau)$  that for brevity' sake we will indicate with the same symbols as the Hamiltonian operators.

$$Z = \int \mathcal{D}[d^+, d] e^{-S} \quad (2.10)$$

where we have introduced one of the following two functional “measures” (normalized by  $Z$  and  $Z_{eff}$ ):

$$\begin{aligned} \mathcal{D}[d^+, d] &= \prod_i \mathcal{D} d_{i\sigma}^+ \mathcal{D} d_{i\sigma} \\ \mathcal{D}_{(0)}[d^+, d] &= \prod_{i \neq 0} \mathcal{D} d_{i\sigma}^+ \mathcal{D} d_{i\sigma} \end{aligned}$$

and where the action  $S$  is given by

$$\begin{aligned} S &= \int_0^\beta d\tau \left( \sum_{i\sigma} d_{i\sigma}^+(\tau) (\partial_\tau - \mu) d_{i\sigma}(\tau) + H(d_{i\sigma}^+, d_{i\sigma}) \right) \\ &= \int_0^\beta d\tau \left( \sum_{i\sigma} d_{i\sigma}^+(\tau) (\partial_\tau - \mu) d_{i\sigma}(\tau) - \sum_{\langle ij \rangle \sigma} t_{ij} (d_{i\sigma}^+(\tau) d_{j\sigma}(\tau) + d_{j\sigma}^+(\tau) d_{i\sigma}(\tau)) \right. \\ &\quad \left. + U \sum_i n_{di\uparrow}(\tau) n_{di\downarrow}(\tau) \right) \end{aligned} \quad (2.11)$$

The effective action for a particular arbitrary site, say  $i = 0$ , is obtained integrating out the fermionic degrees of freedom at all the lattice sites but the tagged one. This idea can be mathematically formulated as follow:

$$\frac{1}{Z_{\text{eff}}} e^{-S_{\text{eff}}[d_{0\sigma}^+, d_{0\sigma}]} = \frac{1}{Z} \int \mathcal{D}_{(0)}[d^+, d] e^{-S}. \quad (2.12)$$

Here  $Z_{\text{eff}}$  is the partition function corresponding to  $S_{\text{eff}}$ . In order to obtain a formal expression for  $S_{\text{eff}}$  we proceed as done in the case of the Ising model, that is by splitting the action (2.11) into three terms:  $S = S_0 + S^{(o)} + \Delta S$ :

$$\begin{aligned} S_0 &= \int_0^\beta d\tau \left( \sum_{\sigma} d_{0\sigma}^+(\tau) (\partial_{\tau} - \mu) d_{0\sigma}(\tau) + U n_{0\uparrow}(\tau) n_{0\downarrow}(\tau) \right) \\ S^{(o)} &= \int_0^\beta d\tau \left( \sum_{i \neq 0, \sigma} d_{i\sigma}^+(\tau) (\partial_{\tau} - \mu) d_{i\sigma}(\tau) - \sum_{i, j \neq 0, \sigma} t_{ij} \left( d_{i\sigma}^+(\tau) d_{j\sigma}(\tau) + d_{j\sigma}^+(\tau) d_{i\sigma}(\tau) \right) \right. \\ &\quad \left. + U \sum_{i \neq 0} n_{i\uparrow}(\tau) n_{i\downarrow}(\tau) \right) \\ \Delta S &= - \int_0^\beta d\tau \sum_{i\sigma} (t_{i0} d_{i\sigma}^+(\tau) d_{0\sigma}(\tau) + t_{0i} d_{0\sigma}^+(\tau) d_{i\sigma}(\tau)) \\ &= - \int_0^\beta d\tau \sum_{i\sigma} (d_{i\sigma}^+(\tau) \eta_i(\tau) + \eta_i^+(\tau) d_{i\sigma}(\tau)) \end{aligned} \quad (2.13)$$

where  $S_0$  is the action of the site 0 decoupled from the rest of the lattice;  $S^{(o)}$  is the action of the lattice in which the site 0 has been removed together with all the bonds connecting 0 to other sites, *i.e.* it is the ‘‘cavity’’ action;  $\Delta S$  is the ‘‘interaction’’ between the tagged site 0 and the other sites. The formal integration in (2.12) can be performed to obtain:

$$S_{\text{eff}} = \text{const.} + S_0 + \ln \langle e^{-\int_0^\beta d\tau \Delta S} \rangle_{S^{(o)}} \quad (2.14)$$

The last term in this equation is the generating functional of the connected Green’s function of the cavity, as can be recognized by substituting the expression for  $\Delta S$  and using the linked cluster theorem. This general theorem permits to express the average of the exponential in terms of the exponential of the series of the connected Green’s functions of the cavity problem. Therefore we end up with the following formal expression for the effective action

$$\begin{aligned} S_{\text{eff}} &= \text{const.} + S_0 - \sum_{n=1}^{\infty} \sum_{\substack{i_1 \dots i_n \\ j_1 \dots j_n}} \int_0^\beta d\tau_{i_1} \dots d\tau_{i_n} d\tau_{j_1} \dots d\tau_{j_n} \\ &\quad \eta_{i_1}^+(\tau_{i_1}) \dots \eta_{i_n}^+(\tau_{i_n}) \eta_{j_1}(\tau_{j_1}) \dots \eta_{j_n}(\tau_{j_n}) G_{\substack{i_1 \dots i_n \\ j_1 \dots j_n}}^{(o)}(\tau_{i_1} \dots \tau_{i_n}, \tau_{j_1} \dots \tau_{j_n}) \end{aligned} \quad (2.15)$$

While previous expression can appear quite obscure, the cavity Green’s functions have a transparent physical interpretation: it describes the delocalization processes of a  $d$  electron leaving

the site 0, propagating in the lattice, and returning back to the site 0. It is worth to observe that up to now no approximation have been done on the problem. The formulation of the Hubbard model in terms of the effective action we derived is exact. The calculation of the cavity Green's functions is in fact a problem as difficult as the initial one.

### 2.2.2 Limit of infinite coordination number

To make further progress in the solution of the model one should adopt a useful approximation scheme. The large dimensionality limit appears to be a very good candidate, as one can easily argue following the discussion about the exactness of Weiss mean field theory for Ising spin in the same limit. Despite some of the simplifications this limit brings into the problem were already know and used in physics, it is widely accepted that the introduction and the systematic derivation of its consequences in strongly correlated model was by [60]. Metzner and Vollhardt have shown in particular that for this limit to be non trivial, a rescaling of the hopping amplitude  $t_{ij}$  as  $(1/\sqrt{d})^{|i-j|}$  is required, in a similar way of what if required in the context of Ising model case for the coupling  $J$ . A straightforward consequence of this scaling of the hopping parameter is that all the higher orders cavity Green's functions vanish in the infinite connectivity limit, such that only the first term in the sum (2.15) survives [31, 59]. An heuristic justification of this can be given with the following argument. Let's consider the scaling of the first few terms in the sum (2.15).

By the  $t_{ij}$  scaling it follows that the connected 2-point Green's function  $G_{ij}^{(o)}$  scales as  $d^{-|i-j|/2}$  and so the first term is of order 1, provided  $i = j$ . The second term involves a connected 4-point function  $G_{ijkl}^{(o)}$  which falls off as  $(1/d)^{|i-j|/2} (1/d)^{|i-k|/2} (1/d)^{|i-l|/2}$ . When  $i \neq j \neq k \neq l$ , one should deal with four sums contributing with a  $d^4$  term, with four factors of  $t$  contributing with  $1/d^2$  and finally with a factor  $1/d^3$  from  $G^{(o)}$  since  $|i-j|$ ,  $|i-k|$  and  $|i-l|$  are at least 2. Thus the net result has a leading order  $1/d$  and vanish in the infinite dimensional limit. When  $i = j \neq k \neq l$ , there are three sums which give  $d^3$ , but four factors of  $t$  giving  $1/d^2$  and a factor  $1/d^2$  from  $G^{(o)}$  ( $i-l$  and  $k-i$  are at least 2). The leading order result is again  $1/d$ . The same argument can be generalized to higher order. The goal is to show that contributions connecting vertices's  $(i, j)$  with more than 2 lines vanish unless  $i = j$  (local contribution).

Therefore the infinite coordination number limit brings a dramatic simplification in the solution of the problem defined by (2.15). In full analogy with the classical mean field theory, all the contribution with  $n > 1$  will vanish at least as  $1/d$ . The effective action  $S_{eff}$  reduce to

(neglecting unessential constants and explicitly writing  $S_0$ ):

$$S_{eff} = \int_0^\beta d\tau \left( \sum_\sigma d_{o\sigma}^+(\tau) (\partial_\tau - \mu) d_{o\sigma}(\tau) + U n_{o\uparrow}(\tau) n_{o\downarrow}(\tau) \right) + \int_0^\beta d\tau d\tau' d_{o\sigma}^+(\tau) d_{o\sigma}(\tau') \sum_{ij} t_{io} t_{oj} G_{ij}^{(o)}(\tau, \tau') \quad (2.16)$$

We can now introduce the **Weiss field**:

$$\mathcal{G}_0^{-1}(\tau, \tau') = -(\partial_\tau - \mu) \delta_{\tau, \tau'} - \sum_{ij} t_{io} t_{oj} G_{ij}^{(o)}(\tau, \tau') \quad (2.17)$$

that reads in frequency space:

$$\mathcal{G}_0^{-1}(i\omega_n) = i\omega_n + \mu - \sum_{ij} t_{io} t_{oj} G_{ij}^{(o)}(i\omega_n) \quad (2.18)$$

This function is the quantum analogous of the effective magnetic field introduced so far in the context of Ising model. Nevertheless and unlike the classical case, in DMFT the Weiss field is not a number, but a function of the frequency, taking into account the all local quantum fluctuations. DMFT, as any mean-field theory, neglects spatial fluctuations in the system, focusing on the local physics at one (arbitrary) site. But in contrast to other mean field approaches, like Hartree-Fock or slave bosons, it retains all the information about the local quantum dynamics. In other words DMFT describes as a function of the imaginary time the quantum fluctuations this site undergoes between the quantum states  $|0\rangle$ ,  $|\uparrow\rangle$ ,  $|\downarrow\rangle$ ,  $|\uparrow\downarrow\rangle$  by exchanging electrons with the *external* effective bath representing the rest of lattice. In terms of the local Weiss field the effective action  $S_{eff}$  take the simple form:

$$S_{eff} = - \int_0^\beta d\tau d\tau' d_{o\sigma}^+(\tau) \mathcal{G}_0^{-1}(\tau, \tau') d_{o\sigma}(\tau') + \int_0^\beta d\tau U n_{o\uparrow}(\tau) n_{o\downarrow}(\tau) \quad (2.19)$$

The effective action describes the local physics of a site 0 including correlation  $U$  and coupling to an external electronic environment. The connection with this external bath is described by the, *unknown*, Weiss field  $\mathcal{G}_0^{-1}(i\omega_n)$ .

### 2.2.3 Self-consistency

In the effective action (2.19) there is another function to be determined, namely:  $G_{ij}^{(o)}(\tau, \tau')$ , *i.e.* the Green's function that describes the propagation of the electrons in the lattice with cavity. The last step to the construction of the theory is to relate the Weiss field  $\mathcal{G}_0^{-1}(i\omega_n)$  to local quantities one can evaluate from the effective action  $S_{eff}$ . This procedure would be the quantum analog of the magnetization calculation that in Weiss mean field theory produce an implicit relation for the magnetization itself.

## 2. Theoretical framework: DMFT

To obtain such a **self-consistency** relation we start observing that translational invariance of the problem (required by arbitrary choice of tagged site) impose to the correlation functions of the single site to be equal to the *local* correlation functions of the lattice model. Thus, we should relate the cavity Green's function  $G_{ij}^{(o)}(\tau, \tau')$  to the lattice Green's function  $G_{ij}$ . This can always be done by some geometrical relation. In  $d \rightarrow \infty$ , and for a general lattice this can be done by equating the cavity Green's function to the lattice one and subtracting the contribution of the paths visiting the tagged site 0, *i.e.* :

$$G_{ij}^{(o)} = G_{ij} - G_{io}G_{oo}^{-1}G_{oj} \quad (2.20)$$

where  $G_{oo}$  is the local Green's function of the site 0. The contribution of the paths visiting site 0 is proportional to  $G_{io}G_{oj}$ , while site 0 loop should be subtracted. This is achieved dividing by the local Green's function  $G_{oo}$ . This will assure to count only once the contribution of the paths leaving and returning to site 0.

Inserting (2.20) into (3.26) and Fourier transforming to Matsubara frequencies, the Weiss field takes the form:

$$\begin{aligned} \mathcal{G}_0^{-1}(i\omega_n) &= i\omega_n + \mu - \sum_{ij} t_{io}t_{oj} G_{ij}^{(o)}(i\omega_n) \\ &= i\omega_n + \mu - \sum_{ij} t_{io}t_{oj} \left[ G_{ij}(i\omega_n) - G_{io}(i\omega_n)G_{oo}^{-1}(i\omega_n)G_{oj}(i\omega_n) \right] \end{aligned} \quad (2.21)$$

To compute the last two terms in the equation above it is convenient to Fourier transform to  $\mathbf{k}$ -space:

$$G_{ij}(i\omega_n) = \sum_{\mathbf{k}} e^{i\mathbf{k}\cdot\mathbf{R}_{ij}} G(\mathbf{k}, i\omega_n) \quad (2.22)$$

The reciprocal lattice Green's function is

$$G(\mathbf{k}, i\omega_n) = \frac{1}{i\omega_n + \mu - \epsilon(\mathbf{k}) - \Sigma(\mathbf{k}, i\omega_n)} \quad (2.23)$$

where  $\epsilon(\mathbf{k}) = \sum_j t_{ij}e^{i\mathbf{k}\cdot(\mathbf{R}_i - \mathbf{R}_j)}$  is the non-interacting dispersion relation and  $\Sigma$  is the self-energy of the lattice. The key mathematical simplification arising from the  $d \rightarrow \infty$  limit is the locality of the theory. In particular the self-energy lose its  $\mathbf{k}$ -dependence:

$$\Sigma(\mathbf{k}, i\omega_n) \xrightarrow{z \rightarrow \infty} \Sigma(i\omega_n)$$

The sum in the r.h.s of (2.21), converted in sum over the wave vector  $\mathbf{k}$ , can be evaluated as energy integrals introducing the non-interacting density of states:  $\rho_0(\epsilon) = \sum_{\mathbf{k}} \delta(\epsilon - \epsilon(\mathbf{k}))$ . Introducing the abbreviation  $\zeta = i\omega_n + \mu - \Sigma(i\omega_n)$ , (2.21) becomes:

$$\mathcal{G}_0^{-1}(i\omega_n) = i\omega_n + \mu - \int_{-\infty}^{+\infty} d\epsilon \frac{\rho_0(\epsilon)\epsilon^2}{\zeta - \epsilon} - \left( \int_{-\infty}^{+\infty} d\epsilon \frac{\rho_0(\epsilon)\epsilon}{\zeta - \epsilon} \right)^2 / \int_{-\infty}^{+\infty} d\epsilon \frac{\rho_0(\epsilon)}{\zeta - \epsilon} \quad (2.24)$$

Using the following algebraic relations:

$$\int_{-\infty}^{+\infty} d\varepsilon \frac{\rho_0(\varepsilon)\varepsilon^2}{\zeta - \varepsilon} = \zeta \int_{-\infty}^{+\infty} d\varepsilon \frac{\rho_0(\varepsilon)\varepsilon}{\zeta - \varepsilon} \quad (2.25)$$

$$\int_{-\infty}^{+\infty} d\varepsilon \frac{\rho_0(\varepsilon)\varepsilon}{\zeta - \varepsilon} = -1 + \zeta \int_{-\infty}^{+\infty} d\varepsilon \frac{\rho_0(\varepsilon)}{\zeta - \varepsilon} \quad (2.26)$$

we finally obtain:

$$\mathcal{G}_0^{-1}(i\omega_n) = i\omega_n + \mu + G^{-1}(i\omega_n) - R[G(i\omega_n)] \quad (2.27)$$

where  $G(i\omega_n)$  is the interacting local Green's function, *i.e.*  $G(i\omega_n) = G_{00}(i\omega_n)$ , and  $R[G(i\omega_n)]$  is the reciprocal function of the Hilbert transform of the density of states corresponding to the lattice:

$$\tilde{D}(\zeta) = \int_{-\infty}^{+\infty} d\varepsilon \frac{\rho^0(\varepsilon)}{\zeta - \varepsilon}, \quad R[\tilde{D}(\zeta)] = R[G] = \zeta \quad (2.28)$$

Equation 2.27 defines the **self-consistency** condition for the impurity problem. The original lattice structure information is hidden in the reciprocal function of the Hilbert transform, thru the non interacting density of states. Some simplifications can be obtained using lattice structures admitting a closed form for the reciprocal Hilbert transform  $R[G]$ .

Particularly relevant is in this sense the case of the Bethe lattice (or Cayley tree), that is a lattice with sites connected to  $z$  neighbors by only one path. A rather schematic representation of this lattice is shown in Fig. 2.2. In the limit of large connectivity and for nearest-neighbor hopping  $t_{ij} = t/\sqrt{z}$ , its density of states reads

$$\rho^0(\varepsilon) = \frac{1}{2\pi t} \sqrt{4t^2 - \varepsilon} \quad (2.29)$$

and corresponds to a semicircular density of states. The energy unit of the problem is set by the half-bandwidth of this density of states, *i.e.*  $D = 2t = 1$ . On the Bethe lattice, the relation (2.20), connecting the cavity Green's function to the local Green's function of the original lattice, is rather simple. The simplification comes from the fact that the cavity Green's function  $G_{ij}^{(o)}$  is diagonal and, so, identical to the local Green's function of the lattice:

$$G_{ij}^{(o)} = G_{ij}^{(o)} \delta_{ij} = G_{ii} = G_{00}. \quad (2.30)$$

The first equality,  $G_{ij}^{(o)} = G_{ij}^{(o)} \delta_{ij} = G_{ii}^{(o)}$  follows from the special topology of the lattice. Once the site 0 has been removed its neighbors are completely disconnected and the only allowed process is that connecting one site  $i$  with itself, thus  $G_{ij}^{(o)}$  becomes diagonal.

The second equality in (2.30),  $G_{ii}^{(o)} = G_{ii}$ , is only true in  $d \rightarrow \infty$ . Removing the site  $i = 0$  has the effect of locally change the topology: each neighbor  $j$  of  $i = 0$  has now only  $z - 1$  nearest neighbors, instead of not  $z$ . In  $d \rightarrow \infty$ , this is a  $1/z$  effect, and therefore we can identify the local

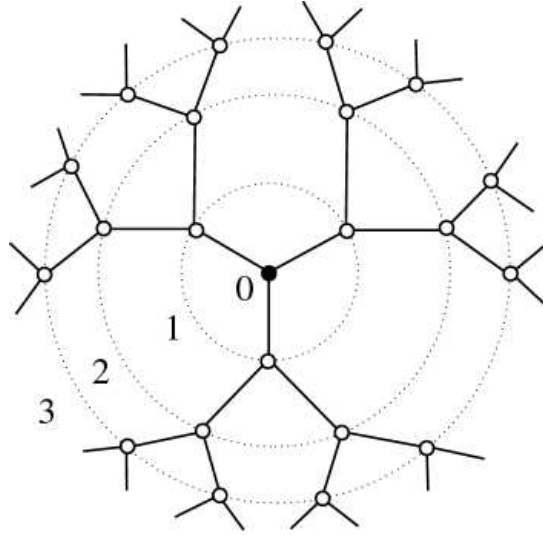


Figure 2.2: Schematic representation of the Bethe lattice with connectivity  $z = 3$  and down to the third order.

Green's function with site  $i = 0$  removed,  $G_{ii}^{(o)}$ , to that of the full lattice  $G_{ii}$ . Finally translational invariance assure that  $G_{ij} = G_{00}$ ,

Then it is straightforward to check that, for any  $\zeta \in \mathbb{C}$ :

$$\tilde{D}(\zeta) = \frac{2 \left( \zeta - s \sqrt{\zeta^2 - D^2} \right)}{D^2} \quad (2.31)$$

with  $s = \text{sign}(\text{Im}(\zeta))$ . Thus:

$$R[G] = \frac{D^2}{2}G - 1/G$$

Substituting this expressions in (2.20) and taking  $t_{oi} = t_{io} = t$  yields the effective quantum impurity action on Bethe lattice:

$$\begin{aligned} S_{\text{eff}} = & \sum_{\sigma} \int_0^{\beta} d\tau \int_0^{\beta} d\tau' d_{o\sigma}^+(\tau) \mathcal{G}_0^{-1}(\tau - \tau') d_{o\sigma}(\tau') \\ & + U \int_0^{\beta} d\tau n_{o\uparrow}(\tau) n_{o\downarrow}(\tau) \end{aligned} \quad (2.32)$$

with

$$\mathcal{G}_0^{-1}(i\omega_n) = i\omega_n + \mu - t^2 G(i\omega_n) \quad (2.33)$$

Eqs. (2.32) and (2.33) are the **dynamical mean-field equations** for the Hubbard model on the Bethe lattice. The former equation corresponds to the so called associated impurity problem of the model. The latter is the self-consistency condition for the impurity problem.

## 2.3 Connection with quantum impurity problem

As we have shown in previous section, the effective action (2.19) describes the local quantum dynamics of a single site of the lattice, coupled to an effective electronic bath. The coupling is encoded in the Weiss field  $\mathcal{G}_0^{-1}(\tau - \tau')$  in terms of a retardation effect. Because of this it is not possible to get an Hamiltonian formulation in terms of local operators only. Nevertheless such a formulation of the problem is made possible by simply reintroducing a description of the effective bath via auxiliary degrees of freedom. The general point of view would then be to associate the tagged site to a local impurity and looking at the effective bath as a “conduction band”, *i.e.* realizing an effective single impurity Anderson model (SIAM) [2, 36].

We shall now show the formal equivalence between the Anderson impurity model action and (2.19), provided an additional self-consistency condition is satisfied [29]. The Hamiltonian formulation of the problem in terms of a SIAM permits us to get some useful physical insight into the problem as well as to perform some practical calculation. It is worth to stress that, being the Hamiltonian representation somehow arbitrary, other Hamiltonians can also be used to represent the problem.

The Hamiltonian of the single Anderson impurity model reads,

$$H_{\text{AIM}} = \sum_{k\sigma} \varepsilon_k p_{k\sigma}^+ p_{k\sigma} + \sum_{k\sigma} V_k (p_{k\sigma}^+ d_\sigma + d_\sigma^+ p_{k\sigma}) + \varepsilon_d \sum_{\sigma} d_\sigma^+ d_\sigma + U n_{d\uparrow} n_{d\downarrow} \quad (2.34)$$

where the operators  $d_\sigma$  and  $d_\sigma^+$  destroys and creates electrons in the impurity with energy  $\varepsilon_d$ , while  $p_{i\sigma}$ ,  $p_{i\sigma}^+$  destroys and creates bath electrons with energies  $\varepsilon_k$ . The impurity orbital is hybridized with each conduction electrons with an amplitude  $V_k$ , and a Coulomb interaction on the impurity site is modeled by the Hubbard term in  $U$ . The action corresponding to this Hamiltonian is given by

$$S = \int_0^\beta d\tau \sum_{k\sigma} p_{k\sigma}^+(\tau) (\partial_\tau + \varepsilon_k - \mu) p_{k\sigma}(\tau) + V_k (p_{k\sigma}^+(\tau) d_\sigma(\tau) + d_\sigma^+(\tau) p_{k\sigma}(\tau)) + \sum_{\sigma} d_\sigma^+(\tau) (\partial_\tau + \varepsilon_d) d_\sigma(\tau) + U n_{d\uparrow}(\tau) n_{d\downarrow}(\tau) \quad (2.35)$$

We can split the action into two parts: a purely local part,  $S_o$ , describing the  $d$  electrons only

$$S_o = \int_0^\beta d\tau \left( \sum_{\sigma} d_\sigma^+(\tau) (\partial_\tau + \varepsilon_d) d_\sigma(\tau) + U n_{d\uparrow}(\tau) n_{d\downarrow}(\tau) \right) \quad (2.36)$$

and a part  $\Delta S$  describing the conduction electrons and their interaction with the impurity site:

$$\Delta S = \int_0^\beta d\tau \sum_{k\sigma} [p_{k\sigma}^+(\tau) (\partial_\tau + \varepsilon_k - \mu) p_{k\sigma}(\tau) + V_k (p_{k\sigma}^+(\tau) d_\sigma(\tau) + d_\sigma^+(\tau) p_{k\sigma}(\tau))] \quad (2.37)$$

## 2. Theoretical framework: DMFT

---

Integrating out the conduction electrons, we obtain an action for the  $d$ -electrons, *i.e.* the impurity, that reads:

$$S_{eff} = \int_0^\beta d\tau d\tau' \sum_\sigma d_\sigma^\dagger(\tau) \mathcal{G}_{0,AND}^{-1}(\tau, \tau') d_\sigma(\tau') + \int_0^\beta d\tau U n_{d\uparrow}(\tau) n_{d\downarrow}(\tau) \quad (2.38)$$

where  $\mathcal{G}_0$  is the non-interacting ( $U = 0$ ) Green's function of the single impurity Anderson model:

$$\mathcal{G}_{0,AND}^{-1}(i\omega_n) = i\omega_n + \mu - \varepsilon_d - \int_{\mathbb{R}} d\omega \frac{\Delta(\omega)}{i\omega_n - \omega} \quad (2.39)$$

and

$$\Delta(\omega) = \sum_k V_k^2 \delta(\omega - \varepsilon_k)$$

is the retarded hybridization function of the impurity with the bath of conduction electrons.

Equation (2.38) supply a representation of the effective action (2.19) only provided the spectral function  $\Delta(\omega)$  is determined as to replicate the local physics of the lattice. This ultimately means that the two set of parameters  $\{V_k, \varepsilon_k\}_{k=1, \dots, N}$ , describing the hybridization of the impurity with the bath levels and their energies, are self-consistently determined. The hybridization function can be approximated, in a very good way, with a finite number of poles, corresponding to a finite representation of the bath:

$$\Delta(i\omega_n) = \sum_k \frac{V_k^2}{i\omega_n - \varepsilon_k} \quad (2.40)$$

It is worth to stress that the hybridization  $V_k$  and the energies of the levels  $\varepsilon_k$  are the (unknown) parameters of the effective SIAM and does not in any case describe analogous quantities of the lattice.

Equating now the Weiss function (2.27) and (2.40), we can reformulate the self-consistency condition in terms of the hybridization function  $\Delta(i\omega_n)$ :

$$\Delta(i\omega_n) = i\omega_n + \mu - \Sigma(i\omega_n) - G^{-1}(i\omega_n) \quad (2.41)$$

In the case of the Bethe lattice, we can obtain a simplified the self-consistency condition, that reads:

$$\Delta(i\omega_n) = t^2 G(i\omega_n) \quad (2.42)$$

In the following this relation will be extensively used to implement the self-consistency condition in exact diagonalization based algorithm.

### 2.4 Solution of DMFT equations

The DMFT equations, despite their formal simplicity, can not (yet?) be solved analytically. Nevertheless the connection with SIAM permits to profit of the several different techniques, that

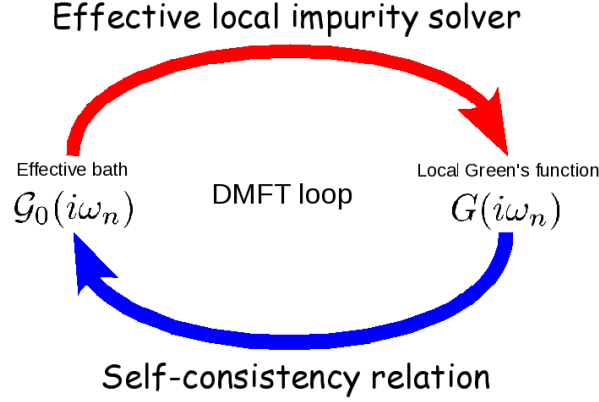


Figure 2.3: Iteration-substitution algorithm used to solve the dynamical mean-field equations. Starting from an initial guess for  $\mathcal{G}_0(i\omega_n)$ , one can solve the associated local impurity problem (top arrow) by using a suitable method. This permits the evaluation of a local Green's function  $G(i\omega_n)$ . The update of the Weiss field  $\mathcal{G}_0^{new}(i\omega_n)$  is then performed by using the self-consistency condition (bottom arrow). This procedure is iterated until the convergence is attained.

have been developed so far to study quantum impurity problem [36]. In practice the solution of DMFT equation can be achieved with a *iteration-substitution* algorithm. This is graphically illustrated in Fig. 2.3 [31].

An initial guess for the Weiss field  $\mathcal{G}_0(i\omega_n)$  fixes the effective impurity problem. This can be treated as an independent problem, described by (2.32), whose “bare” part is known and that can be tackled using any available method, *e.g.* perturbation theory. In particular the local Green's function  $G(i\omega_n)$  can be evaluated. This amount to construct the following correlation function:

$$G(\tau - \tau') = -\langle T d(\tau) d^+(\tau') \rangle_{S_{eff}} \quad (2.43)$$

The connection with quantum impurity model it is often used to obtain the local Green's function from the impurity one. A local self-energy is defined via Dyson equation:

$$\Sigma(i\omega_n) = \mathcal{G}_0^{-1}(i\omega_n) - G^{-1}(i\omega_n) \quad (2.44)$$

In the most general case the local Green's function should be evaluated from the knowledge of the self-energy (obtained from SIAM solution) via the integral over the density of state  $\rho_0(\varepsilon)$  (or summing over wave-vectors):

$$G(i\omega_n) = \int_{\mathbb{R}} d\varepsilon \frac{\rho_0(\varepsilon)}{i\omega_n + \mu - \Sigma(i\omega_n) - \varepsilon} \quad (2.45)$$

As we have seen in previous section in the special case of the Bethe lattice this integral can be analytically performed and yields a closed expression for the local Green's function in terms

of the self-energy.

$$G(i\omega_n) = \frac{2}{i\omega_n + \mu - \Sigma + \text{sign}(i\omega_n) \sqrt{(i\omega_n + \mu - \Sigma)^2 - D^2}} \quad (2.46)$$

Once  $G(i\omega_n)$  and  $\Sigma(i\omega_n)$  have been evaluated, they are used to update the Weiss field  $\mathcal{G}_0^{-1}(i\omega_n)$  using self-consistency condition (2.33). This step produce a new impurity problem to be solved, thus the entire procedure is iterated until convergence is reached, using a suitable convergence criteria.

*At the self consistency point* the impurity Green's function  $G(i\omega_n)$  corresponds to the local Green's function of the original lattice model.

It remains to show how the impurity Green's function can be practically obtained, *i.e.* how to solve (2.43). We shall present in what follow a rather brief overview of some methods that can be used to this end. Some methods are adapted from techniques originally developed to study impurity models, as the SIAM is. Among the many available we largely used the following: iterated perturbation theory (IPT), Hirsch-Fye quantum Monte Carlo (QMC), complete and Lanczos exact diagonalization (ED) and the density matrix renormalization group (DMRG). Using different methods has the advantage to permit a crosscheck of the results and in particular to overcome the problems due to their own range of applicability, that can be somehow complementary.

### 2.4.1 Iterated perturbation theory

The first and perhaps most simple method we shall describe, termed iterated perturbation theory, is based on perturbative expansion of the effective action. Regarding the effective impurity problem as an independent one, the easiest approach one can try is to solve it perturbatively with respect to the local interaction term. Using the Yamada-Yoshida perturbation theory one can readily obtain the second approximation for the impurity self-energy [29, 105, 45, 102]. The contribution is expressed as a two vertex Feynman diagram connected by three "bare" propagators. Thus, for a given Weiss field  $\mathcal{G}_0$ , this second order self-energy reads:

$$\Sigma[\mathcal{G}_0](\tau) = -U^2 \mathcal{G}_0^3(\tau) \quad (2.47)$$

The IPT algorithm is formulated as a self-consistent determination of the couple  $(\mathcal{G}_0, G)$ . The general iteration can be sketched as follow:

$$\mathcal{G}_0(i\omega_n) \rightarrow \Sigma(i\omega_n) = FT[-U^2 \mathcal{G}_0^3(\tau)] \rightarrow G(i\omega_n) \rightarrow \mathcal{G}_0^{new}(i\omega_n) \quad (2.48)$$

where FT indicates the Fourier transformation to Matsubara frequencies. A zero temperature calculation can be done using the real frequency Green's function.

Though this method is actually based on a perturbative expansion, thus it is valid at small  $U$  by construction, it turns out that the second order expression of  $\Sigma$  also capture the large  $U/t$  limit, in the half-filled Hubbard model [105]. In this latter limit, the Weiss field becomes  $\mathcal{G}_0^{-1}(i\omega_n) \approx i\omega_n$  and thus the self-energy reads

$$\Sigma(i\omega_n) = \left(\frac{U}{2}\right)^2 \frac{1}{i\omega_n} \quad (2.49)$$

Now, in the atomic limit, the exact expression of the local Green's function is given by

$$G(i\omega_n) = \frac{1/2}{i\omega_n - U/2} + \frac{1/2}{i\omega_n + U/2} \quad (2.50)$$

for which the self-energy is identical to (2.49). Therefore, the IPT approximation provides an *interpolation scheme* between the weak and the strong coupling limits.

### 2.4.2 Quantum Monte Carlo

Quantum Monte Carlo is a finite temperature calculation, exact in the statistical sense, based on a suitable sampling of the phase space. The associated impurity problem defined by (2.32) is solved using the standard Hirsch-Fye QMC algorithm [37]. Within this method the imaginary time interval  $[0, \beta]$  is discretized in  $L$  time-slices of width  $\Delta\tau = \beta/L$  (where  $\beta$  is the inverse temperature, and  $k_B = 1$ ). The resulting discretized partition function reads

$$Z = \int \mathcal{D}[d^+, d] e^{\sum_{\tau, \tau'} d_{\sigma}^{\dagger}(\tau) \mathcal{G}_0^{-1}(\tau, \tau') d_{\sigma}(\tau') + U \sum_{\tau} n_{\uparrow}(\tau) n_{\downarrow}(\tau)} \quad (2.51)$$

A discrete Hubbard-Stratonovich transformation is performed to decouple the quartic term, at the cost of introducing a set of auxiliary variables, namely the *pseudo-spins*:

$$e^{\Delta\tau U \left( n_{\uparrow} n_{\downarrow} + \frac{1}{2} (n_{\uparrow} + n_{\downarrow}) \right)} = \frac{1}{2} \sum_{s=\pm 1} e^{\lambda s (n_{\uparrow} - n_{\downarrow})} \quad (2.52)$$

the parameter  $\lambda = \text{arccosh}(e^{\Delta\tau/2})$  is fixed by the transformation, while the discrete variable  $s$  is an Ising-like spin variable taking the values  $\pm 1$ . The main advantage of performing this transformation at every imaginary time slice is that the action reduces to a quadratic form:

$$\begin{aligned} Z &= \sum_{s_{\tau}=\pm 1} \int \mathcal{D}[d^+, d] e^{-\sum_{\tau, \tau'} d_{\sigma}^{\dagger}(\tau) \mathcal{G}_0^{-1}(\tau, \tau') d_{\sigma}(\tau') + \lambda \sum_{\tau} s_{\tau} (n_{\uparrow}(\tau) - n_{\downarrow}(\tau))} \\ &= \sum_{s_{\tau}=\pm 1} \int \mathcal{D}[d^+, d] e^{-\sum_{\tau, \tau'} d_{\sigma}^{\dagger}(\tau) \mathcal{G}_{\sigma}^{-1}(\tau, \tau') d_{\sigma}(\tau')} \end{aligned} \quad (2.53)$$

where

$$\mathcal{G}_{\sigma}^{-1}(\tau_l, \tau_l') = \mathcal{G}_0^{-1}(\tau_l, \tau_l') + \sigma \lambda s_l \delta_{l, l'+1} \quad (2.54)$$

is the inverse Green's function for a given fixed pseudo-spins configuration  $(s_1, \dots, s_L)$ . It is worth noting that the introduction of this set of spin variables produce an enlargement of the

## 2. Theoretical framework: DMFT

---

Hilbert space. We will denote throughout this section a spin configuration with the symbol  $\{\underline{s}\} = (s_1, \dots, s_L)$ . Tracing out the Grassmann variables leave us a partition function expressed in terms of the Ising spin variables only:

$$\begin{aligned} Z &= \sum_{\{\underline{s}\}} \det \left[ G_{\uparrow}^{-1}(\{\underline{s}\}) \right] \det \left[ G_{\downarrow}^{-1}(\{\underline{s}\}) \right] \\ &= \sum_{\{\underline{s}\}} \rho(\{\underline{s}\}) \end{aligned} \quad (2.55)$$

where we have introduced the weight for a given pseudo-spin configuration  $\{\underline{s}\}$ ,  $\rho = \det G_{\uparrow}^{-1} \det G_{\downarrow}^{-1}$ .

It is then straightforward to realize that the impurity Green's function can be computed as the weighted average over all possible Ising configurations:

$$G_{\sigma} = \frac{1}{Z} \sum_{\{\underline{s}\}} \rho(\{\underline{s}\}) G_{\sigma}(\{\underline{s}\}) \quad (2.56)$$

This calculation requires a sum over  $2^L$  configurations, and each term of the sum needs the inversion of an  $L \times L$  matrix (cf. (2.54)). If the temperature is small or high precision is required, then the number of time slices could become large and so the dimension of phase space of the Ising spins, making impossible to perform previous sums. In practice one often deal with  $L$  of the order of 10, thus already in the simplest case previous sum can not be exactly evaluated. To overcome this problem one can evaluate the sum using a Monte Carlo method. This basically consist in a Markovian sampling of the phase space. A random spin configuration is generated in the first step, then a random process is built attempting successive spin flips of Ising variables. To generate a Markov process from the spin flip procedure a transition probability should be defined, with the only requirement to satisfy the detailed balance. The most used transition probability used so far are the Metropolis or the heat-bath algorithms:

$$\text{heath - bath : } P(s \rightarrow s') = \frac{\rho'}{\rho + \rho'} \quad (2.57)$$

$$\text{Metropolis : } P(s \rightarrow s') = \begin{cases} 1 & \text{if } \rho' > \rho \\ \frac{\rho'}{\rho} & \text{otherwise} \end{cases} \quad (2.58)$$

in both cases, the transition probability  $P(s \rightarrow s')$  from a configuration  $\{\underline{s}\}$  to  $\{\underline{s}'\}$  is a function of the ratio of the two determinants of  $G(\{\underline{s}\})$  and  $G(\{\underline{s}'\})$ . The ergodicity of the Markov process assure then to visit with equal probability the entire phase space.

The implementation of this algorithm requires now the evaluation of the determinant appearing in the proability weight  $\rho(\{\underline{s}\})$  as well as the inversion of the pseudo-spin Green's function. The key aspect pointed out by Hirsch and Fye [37] is that the non-linearity intrinsic in the expression of the impurity Green's function lead to the existence of a Dyson-like equation,

which relates pseudo-spin Green's function of two different spin configurations  $G = G(\{\underline{s}\})$  and  $G' = G(\{\underline{s}'\})$ :

$$G' = G + (G - 1)(e^{V-V'} - 1)G' \quad (2.59)$$

where  $e^V$  is the diagonal matrix whose elements are  $e^{\sigma\lambda s}$ . If we rewrite this equation as

$$\begin{aligned} \mathcal{A}G' &= G \\ \mathcal{A} &= 1 + (1 - G)(e^{V-V'} - 1) \end{aligned} \quad (2.60)$$

we can recognize that the Green's function  $G'$ , corresponding to a pseudo-spin configuration  $(\{\underline{s}'\})$ , can be obtained from  $G$  by inverting the  $L \times L$  matrix  $\mathcal{A}$ , thus defining a *CLEAN* updating procedure for the Markov process.

A further simplification arises if the Ising configurations  $\{\underline{s}\}$  and  $\{\underline{s}'\}$  differs only for one spin (corresponding the so called *single spin-flip* process). In this case we can obtain  $G'$  from  $G$  *without* computing the inverse of the matrix  $\mathcal{A}$ :

$$G'_{l_1 l_2} = G_{l_1 l_2} + \sum_l \frac{(G_{l_1 l} - \delta_{l_1 l})(e^{V'_l - V} - 1) G_{l l_2}}{1 + (1 - G_{ll})(e^{V'_l - V} - 1)} \quad (2.61)$$

This corresponds to a *DIRTY* updating procedure. The Dyson-like equation (2.59) also allows us to calculate the determinant of  $\mathcal{A}$ , needed to evaluate the transition probability from  $\{\underline{s}\}$  to  $\{\underline{s}'\}$ :

$$\det \mathcal{A} = 1 + (1 - G_{ll})(e^{V'_l - V} - 1) \quad (2.62)$$

Successive dirty updates can lead to a degradation of the solution corresponding to the generation of long range correlations. To avoid numerical instabilities due to the error propagation, we perform a regular inversion of the matrix  $\mathcal{A}$  (clean update) every hundreds fast inversions, *i.e.* dirty updates. To limit systematic errors introduced by the Trotter decomposition we also set  $U\Delta\tau < 1$ . The precision of the calculations then basically depends on two remaining factors, the statistical error and the criterion for the convergence of the solution of the DMFT equations. For the former, we typically perform  $10^5$  sweeps. When required, we may do up to  $10^6$  sweeps, such as near the Mott transition, or to compute the analytic continuation of data to the real axis using the maximum entropy method [33]. The convergence of the solution is indeed controlled by monitoring the behavior with DMFT iteration number of  $G(i\omega_1)$ , the imaginary part of the Green's function at the first Matsubara frequency, which shows the largest variations. We stop the DMFT iterations when the fluctuations of this quantity become of the order of the QMC statistical error and remains stable for a few more iterations.

### 2.4.3 Exact diagonalization

A different approach to the solution of the DMFT equations is based on the exact diagonalization of the finite size representation of the effective problem [31]. The associated single impurity

## 2. Theoretical framework: DMFT

---

Anderson model is composed of infinitely many sites forming the conduction band, and thus the effective bath. In practice nevertheless only a finite number of sites can be handled. Within this method the effective bath is described by a number  $n_s$  of atomic sites and the corresponding problem is diagonalized exactly. It is worth to stress that even if the diagonalization is exact (and in many cases complete) the finite approximation of the effective problem introduce a (in principle big) error in the solution. It turns out that in many cases just a few bunch of sites are sufficient to obtain a good description of the solution. Due to the exponential growth of the Hilbert space dimension, only a number of sites less than 12 can be exactly diagonalized. To this end it is of high importance do adopt a smart strategy to describe the environment. A couple of methods have been developed so far, namely the “chain geometry” [89] and the “star geometry” [11, 77]. In both cases the effective impurity problem consists of a central impurity site, describing the correlated  $d$ -orbital, connected with the bath sites. The topology of this connection distinguish the different approaches. The different atomic arrangements in these two cases are schematically depicted in Fig. 2.4. In this section we shall briefly review ED method, focusing in particular on the star geometry case. The linear chain geometry will be detailed in the next section where the Density Matrix Renormalization Group method will be illustrated.

The star geometry ED provides an adaptive algorithm for the determination of the bath site energies  $\{\varepsilon_k\}$  and the hybridization  $\{V_k\}$ , thus fixing the effective single impurity Anderson model correctly describing the solution of the initial problem. In a rather general way two distinct approach can be distinguished: a) complete diagonalization at finite temperature, b) Lanczos diagonalization at zero temperature. These two methods share as a common feature the determination of the Hamiltonian parameters, *i.e.* the implementation of the self-consistency, performed as a minimization of the impurity Green’s function respect to the Anderson one. The distance to minimize is often chosen to have the following  $\chi^2$  expression:

$$\chi^2 = \sum_{n=0}^{n_{\max}} \left| \mathcal{G}_0^{-1}(i\omega_n) - \mathcal{G}_{0,And}^{-1}(i\omega_n) \right|^2 \quad (2.63)$$

where the Weiss field self-consistently obtained from the evaluated impurity Green’s function is minimized against the single impurity Anderson model non-interacting Green’s function, having the form:

$$\mathcal{G}_{0,And}^{-1}(i\omega_n) = i\omega_n + \mu - \varepsilon_d - \int_{-\infty}^{\infty} d\omega' \frac{\Delta(\omega')}{i\omega_n - \omega'} \quad (2.64)$$

corresponding in the finite size approximation of the impurity problem to:

$$\mathcal{G}_{0,And}^{-1}(i\omega_n) = i\omega_n + \mu - \varepsilon_d - \sum_{l=2}^{n_s} \frac{V_l^2}{i\omega_n - \varepsilon_l} \quad (2.65)$$

The  $\chi^2$  minimization, implemented using some powerful conjugate gradient routines, amount

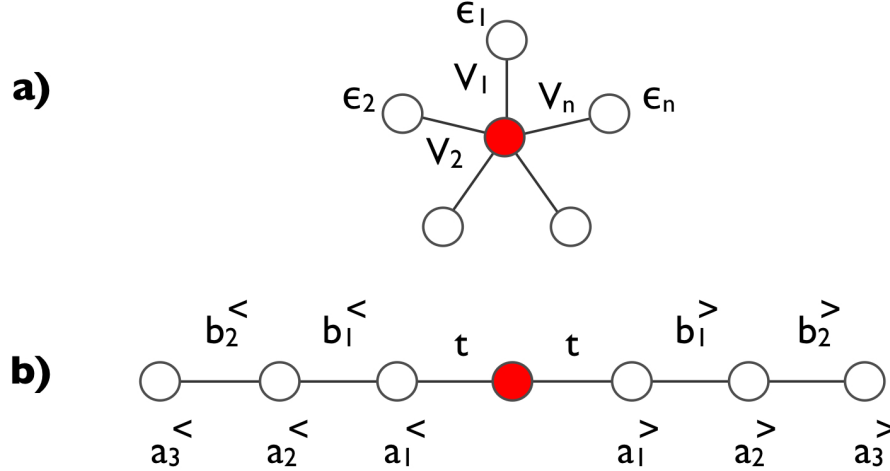


Figure 2.4: Star (a) and linear chain geometry (b) used to represent the effective conduction bath in the exact diagonalization method. Filled circle denotes the impurity site, and open circles are the sites of the bath.

to fit with a finite number of rational functions the Weiss field thus determining the Hamiltonian parameters  $\{V_l, \epsilon_l\}_{l=1, \dots, n_s}$ .

The iterative solution of DMFT equation is implemented as follow: I) The parameters  $\{V_l, \epsilon_l\}$  are guessed, from scratch or reading the solution of a previous calculation. The Hamiltonian matrix is constructed exploiting all the possible symmetries of the problem in order to reduce it to a block form. II) The Hamiltonian matrix is diagonalized in each sector, the target states are obtained (depending on the adopted technique) and impurity Green's function is evaluated. These operations can be performed in two rather general way:

- a) *Lanczos* We are interested in the zero temperature solution of the problem, thus only the ground state has to be determined. Lanczos method is used to accomplish this goal. It amount to a fast and reliable evaluation of the ground state. This method is based on the recursive determination of an orthonormal basis on which the sector Hamiltonian assume a tri-diagonal form. The approximation rely on the fact that this basis is in fact smaller than the full dimension of the sector. The recursion guarantees nevertheless the convergence of the largest eigenvalues of the matrix, thus the ground state [16]. The method starts with the guess of a random state, that it is supposed to have non zero projection onto the ground state, this hypothesis can be tested *a posteriori*. If  $\mathcal{N}$  is the dimension of the Hilbert space of the problem,  $\{|i\rangle\}_{i=1, \dots, \mathcal{N}}$  is the basis, where  $i$  is an index for all the quantum numbers of the operators commuting with  $H$  and  $\{l_i\}_{i=1, \dots, \mathcal{N}}$  is a set of

## 2. Theoretical framework: DMFT

---

random numbers, the initial state is:

$$|f\rangle = \sum_{i=1}^{\mathcal{N}} l_i |i\rangle$$

a Krylov basis  $K_n(H, |f\rangle) = \{|f\rangle, H|f\rangle, \dots, H^n|f\rangle\}$  is then constructed and orthonormalized with Gram-Schmidt procedure, ending in the following recursion relation for the determination of the basis vectors:

$$|f_{n-1}\rangle = H|f_n\rangle - a_n|f_n\rangle - b_n^2|f_{n-1}\rangle \quad (2.66)$$

where

$$\begin{aligned} a_n &= \frac{\langle f_n | H | f_n \rangle}{\langle f_n | f_n \rangle} \\ b_n^2 &= \frac{\langle f_n | f_n \rangle}{\langle f_{n-1} | f_{n-1} \rangle}, \quad b_0 = 0 \end{aligned} \quad (2.67)$$

On this basis the sector Hamiltonian has a tri-diagonal form with parameters  $\{a_n\}$  on the main diagonal and  $\{b_n\}$  on the over- and sub-diagonal.

$$H = \begin{pmatrix} a_0 & b_1 & & & \\ b_1 & a_1 & b_2 & \mathbf{0} & \\ & b_2 & a_3 & \ddots & \\ & \mathbf{0} & \ddots & \ddots & b_n \\ & & & b_n & a_n \end{pmatrix}$$

The diagonalization of the (approximate) Hamiltonian is then straightforward and gives an approximated ground state  $|gs\rangle$ . This can be used as a starting vector for a successive iteration of the full procedure until convergence to the largest eigenvalue of the sector Hamiltonian is reached by construction. Once the ground state  $|gs\rangle$  has been determined correctly, one can proceed to the evaluation of the impurity Green's function. This requires the application of a second Lanczos procedure. The idea is to get the Green's function  $G(z) = G^>(z) + G^<(z)$ , with  $G^>$  and  $G^<$  describing the particles and the holes excitations with respect to the ground state energy  $E_0$ :

$$\begin{aligned} G^>(z) &= \langle gs | d \frac{1}{z - (H - E_0)} d^+ | gs \rangle \\ G^<(z) &= \langle gs | d^+ \frac{1}{z + (H - E_0)} d | gs \rangle \end{aligned} \quad (2.68)$$

using Lanczos technique to reduce the resolvent operator to a tri-diagonal form. This can be done using alternatively as a starting vector the state obtained applying the construction and the destruction operator to the ground state:

$$|f_0^>\rangle = d^+ |gs\rangle$$

$$|f_0^<\rangle = d|gs\rangle$$

Using Lanczos method again lead to the following expression of the Green's functions in the form of continued fraction expansions, with paramaters determined in the previously discussed recursion formula:

$$\begin{aligned} G^>(z) &= \langle f_0^> | \frac{1}{z - (H - E_0)} | f_0^> \rangle = \frac{\langle f_0^> | f_0^> \rangle}{z + E_0 - a_0^> - \frac{b_1^{>2}}{z + E_0 - a_1^> - \frac{b_2^{>2}}{z + E_0 - a_2^> - \dots}}} \\ G^<(z) &= \langle f_0^< | \frac{1}{z + (H - E_0)} | f_0^< \rangle = \frac{\langle f_0^< | f_0^< \rangle}{z - E_0 - a_0^< - \frac{b_1^{<2}}{z - E_0 - a_1^< - \frac{b_2^{<2}}{z - E_0 - a_2^< - \dots}}} \end{aligned} \quad (2.69)$$

- b) Complete diagonalization** We are in this case interested in getting the finite temperature solution of the problem. To this end a complete diagonalization of the Hamiltonian is required [31]. Once a proper vector basis is constructed, typically using the number operator  $N$  and the spin operator  $S_z$  quantum numbers as well as the multiplicity  $g$  to label the states:

$$|i\rangle = |n, s_z, g\rangle$$

the Hamiltonian matrix is constructed in each sector. Its full diagonalization provides all the eigenvalues  $\lambda_i$  and the eigenvectors  $|\lambda_i\rangle$  with  $i = 1, \dots, \dim \mathcal{H}(n, s_z)$ . Iterating the diagonalization over all the sector will then determine the full spectrum of the problem. It is worth to stress that to overcome difficulties due to memory storing of the eigenvectors (that in each sector have dimension  $\dim \mathcal{H}(n, s_z) \times \mathcal{N}$ , with  $\mathcal{N} = 4^{n_s}$ ) high optimization of the calculation is almost mandatory. The ground state can then be easily determined comparing the eigenenergies corresponding to all sectors. The impurity Green's function is readily obtained using its spectral decomposition (or Kallen-Lehman formalism) [57]:

$$G(i\omega_n) = \frac{1}{Z} \sum_{n,m} \frac{\langle m | d^+ | n \rangle (e^{-\beta E_m} + e^{-\beta E_n})}{i\omega_n - (E_m - E_n)} \quad (2.70)$$

where

$$Z = \sum_{n=1}^{\mathcal{N}} \langle n | e^{-\beta H_{And}} | n \rangle = \sum_{n=1}^{\mathcal{N}} e^{-\beta E_n}$$

Despite its simplicity the evaluation of this sum is the bottleneck of the full procedure. It in fact requires the construction, in each sector, of the matrix element of the impurity construction operator, that involve the analysis and sum of a huge amount of states (with their decomposition along the Hilbert space basis). Beside the impurity Green's function basically all the desired functions can be evaluated using the same technique, aka the spectral decomposition. It is worth to underline the for  $\beta \rightarrow \infty$  the exponential terms in

the sum kill the contribution of the high energy states. Thus at very low temperature only few states effectively contribute to the Green's function. Recently an extended Lanczos technique has been developed to construct to solve the impurity problem at very low temperature scales [12].

III) The update of the Weiss field is performed thru self-consistency condition. As pointed out above this step is achieved by  $\chi^2$  fit of the impurity Green's function and lead to the determination of a NEW set of Hamiltonian parameters  $\{V_l, \varepsilon_l\}$ . In full diagonalization case the fit is performed on the Matsubara imaginary axis at a inverse temperature  $\beta$ , while within the Lanczos diagonalization a fictitious inverse temperature  $\tilde{\beta}$  should be introduced to perform the fit. Once the new set of parameters  $\{V_l, \varepsilon_l\}$  is obtained, the full procedure is iterated until convergence is reached.

### 2.4.4 Density Matrix Renormalization group

As we have shown in the previous section, exact diagonalization based algorithms are greatly limited by the exponential growth of the Hilbert space dimension. Thus a substantial improvement can be achieved supplementing these with a renormalization group based algorithm, limiting the growing process. On a very general ground in fact numerical RG can be viewed as a procedure providing a scale by scale cutting scheme for the Hilbert space. This scheme in the Wilson RG is implemented by retaining at each step of the RG flow, the  $m$  lowest eigenstates obtained by exact diagonalization of the effective Hamiltonian on that scale. This procedure thus permits to perform the a multi scale analysis without the plague of the exponential growth of the dimension of the problem. Recently have been realized that the Wilson numerical RG, even being perfect suitable to the analysis of Kondo impurity problems, can gives wrong answers when applied quantum lattice models. On a general ground this can be traced back to the fact that the decimation procedure fails in such cases where the blocks are correlated. This is well illustrated in the case of 1-dimensional particle in the box (or tight-binding) [74]. Let's suppose that we are interested in the ground state of the problem or equivalently in the few low-lying eigenstates. In any given block  $\mathcal{B}_n$  tailing the 1-dimensional interval the ground state is described by the zero internal node wave function  $\psi_0(x)$ . By mean of boundary conditions this function is zero at the borders of the block. This is illustrated in Fig. 2.5. By decimation procedure one can then imagine to construct the ground state for a bigger block  $\mathcal{B}_{n+1}$  using the results obtained from the single blocks  $\mathcal{B}_n$ . Thus the resulting ground state wave function, being the tensor product of the block wave functions, has an internal node in the  $(n + 1)$ -interval (cf. Fig. 2.5). Obviously this lead to a wrong description of the  $\mathcal{B}_{n+1}$  ground state, that is known to have no internal node.

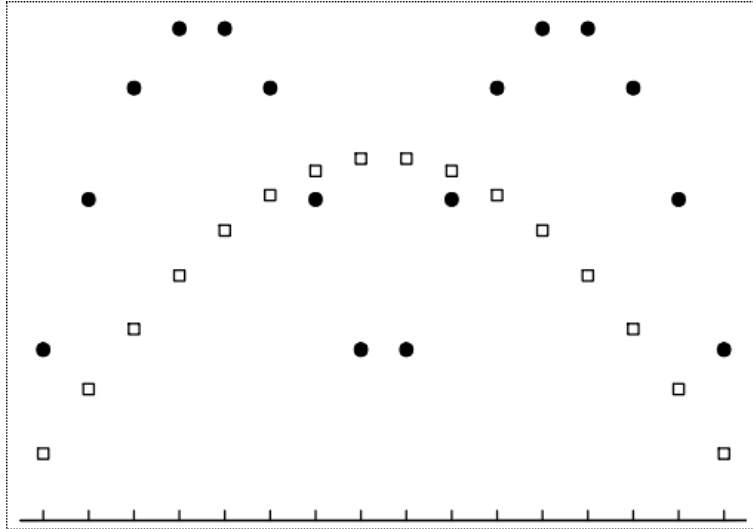


Figure 2.5: Lowest eigenstates for an 8-site blocks (●) and for the 16-sites block (□), for the 1-dimensional tight-binding model. The product of the smaller block eigenstates badly describes the eigenstate of the larger block.

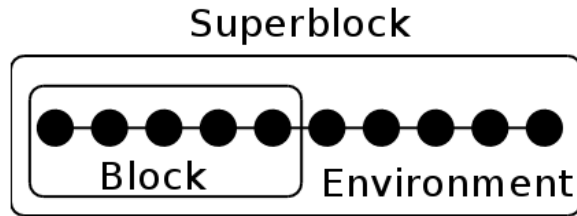


Figure 2.6: DMRG superblock representation. The superblock  $\mathcal{SB}$  is formed by the block  $\mathcal{B}$  and its environment  $\mathcal{E}$ . This overcome the idea of isolated blocks of NRG and lead to the correct solution of quantum lattice models.

Wilson himself proposed that any new RG scheme should be able to obtain the correct solution when applied to the 1-dimensional particle in the box problem. A solution to this failure of the numerical RG has been found by 1992 by White [101]. He proposed a different renormalization scheme, thus a different algorithm to “cut” the Hilbert space size, that is based on the analysis of the reduced density matrix for the  $\mathcal{SB}$ . For this the method is called Density Matrix Renormalization Group. The central idea realized by White is that the building blocks used in the RG procedure have to be considered as related to their environment instead of isolated objects. This lead to the idea of *superblock*  $\mathcal{SB}$  that describes together the block  $\mathcal{B}$  and its environment  $\mathcal{E}$ , as illustrated in Fig. 2.6 [34].

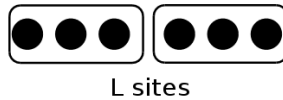
The general DMRG procedure can then be summarized as follow:

## 2. Theoretical framework: DMFT

the superblock  $\mathcal{SB}$  is analyzed and a target state, typically the ground state, is obtained. The “most probable” block  $\mathcal{B}$  states that fit the target state are obtained via the reduced density matrix  $\rho$  by using its first  $m$  eigenstates as a reduced Hilbert space basis (thus defining a cutting procedure).

The general DMRG algorithm, suitable to solve 1-dimensional lattice problems, consists in the following procedure: [83, 74]:

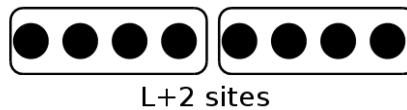
- Form a superblock  $\mathcal{SB}$  with a number of sites sufficiently small such that it can be exactly diagonalized.



- Construct the Hamiltonian for the new larger system starting from the knowledge of  $H_{\mathcal{B},\mathcal{E}}$ .
- obtain (iteratively) the full system Hamiltonian  $H$ . Diagonalize it and get the ground state  $|gs\rangle$ .



- Form the reduced density matrix  $\rho = \text{Tr}_{|\mathcal{E}\rangle} |gs\rangle\langle gs|$  diagonalize it, retain the first  $m$  eigenstates and eigenvalues, form the rotation matrix  $\mathcal{O}$ . Rotate all the operators to the new basis.  $A' = \mathcal{O}^+ A \mathcal{O}$ .
- Rename the  $\mathcal{SB}$  Hamiltonian and restart from point 1



In the recent time several ED-DMRG procedures have been developed for the solution of the DMFT equations [74, 25, 27]. DMRG can in fact be readily adapted to be used as impurity solver in the linear chain geometry scheme. This method permits to grow the linear chain, representing the effective bath, without being plagued by the exponential growth of the Hilbert space dimension of the impurity problem [25]. The key idea of the DMRG method as impurity

solver in DMFT is in fact to start with a small system (*i.e.* a bath with a small number of sites  $n_s$ ) and then systematically increase its size up to an arbitrary length. The effective model Hamiltonian should be first rewritten as a linear chain problem:

$$\begin{aligned}
 H_{\text{eff}} = & \sum_{\substack{i=-n_s, i \neq 0 \\ \sigma}}^{n_s} a_i d_{i\sigma}^+ d_{i\sigma} + \sum_{\substack{i=-(n_s-1), i \neq 0, -1 \\ \sigma}}^{n_s} (b_i d_{i\sigma}^+ d_{i+1\sigma} + h.c.) \\
 & + \sum_{\sigma, i=\pm 1} b_0 (d_{i\sigma}^+ d_{i\sigma} + h.c.) + U n_{\uparrow} n_{\downarrow}
 \end{aligned} \tag{2.71}$$

$H_{\text{eff}}$  describes an impurity connected to two chains (one for describing particle excitations and one hole excitations), each with site energies  $\{a_i^{>/<}\}$  and hopping amplitudes  $\{b_i^{>/<}\}$ . In Fig. 2.4 (b) we have schematically depicted the effective Hamiltonian. DMRG is used to construct iteratively the effective bath. We shall now present the algorithm used to obtain DMFT solution in a rather schematic way, that can be more suitable to organize the several different steps leading to the solution of the effective problem.

1. In the starting situation we have 1 impurity site  $\mathcal{I}$  connected to two left and right blocks  $\mathcal{B}^>, \mathcal{B}^<$  thru two left and right dots sites  $\mathcal{D}^>, \mathcal{D}^<$ . In the DMRG terminology blocks,



superblocks and dots are constituted of sites with 4 states. Each site but the impurity represents the effective bath. The basic *bricks* of the methods, *i.e.* the  $\mathcal{I}$  operators and Hilbert space together with the blocks and dots operators and Hilbert spaces  $\mathcal{H}_{\mathcal{B}^{\gtrless}}, \mathcal{H}_{\mathcal{D}^{\gtrless}}$

2. Construct the left and right superblock  $\mathcal{SB}^>, \mathcal{SB}^<$  Hilbert space as a tensor product of the Hilbert spaces of blocks and dots:

$$\mathcal{H}_{\mathcal{SB}^{\gtrless}} = \mathcal{H}_{\mathcal{B}^{\gtrless}} \otimes \mathcal{H}_{\mathcal{D}^{\gtrless}}$$

This amount to obtain the Hilbert space for each chain (left and right) connected to the impurity site, thus permitting to construct the superblock Hamiltonian operator, in a arbitrary sector (guessing where the ground state is) as well as any other operator needed to get the solution of the problem.

3. Construct the *full* system Hilbert space starting from the result of previous steps:

$$\mathcal{H} = \mathcal{H}_{\mathcal{SB}^>} \otimes \mathcal{H}_{\mathcal{I}} \otimes \mathcal{H}_{\mathcal{SB}^<}$$

as well as the system Hamiltonian and any other operators,

$$H = H_{\mathcal{SB}^>} + H_{\mathcal{I}} + H_{\mathcal{SB}^<} + H_{\mathcal{SB}^>-\mathcal{I}} + H_{\mathcal{I}-\mathcal{SB}^<}$$

## 2. Theoretical framework: DMFT

---

The most general state of the system can then be expressed in terms of the label corresponding to each part of the system. It is worth to recall that these latter are classified in terms of quantum numbers of operators commuting with the Hamiltonian (typically  $N$  and  $S_z$ ).

$$|l\rangle = |i, imp, j\rangle \quad \text{for} \quad |i\rangle \in \mathcal{H}_{SB>}, |imp\rangle \in \mathcal{H}_{\mathcal{I}}, |j\rangle \in \mathcal{H}_{SB<}$$

4. Diagonalize the system Hamiltonian  $H$  and obtain the target states, *e.g.* the ground state  $|gs\rangle$  plus a bunch of few low-lying states. To this end Lanczos or other more refined techniques, such as Block Lanczos, Davidson, etc, should be used.

$$|gs\rangle = \sum_{l=1}^{\dim \mathcal{H}} r_l |l\rangle$$

5. Compute the impurity Green's function  $G(z)$  using a second Lanczos procedure of the very same type as explained in the previous section about ED algorithm. The Green's function is obtained in the following continued fraction form:

$$G(z) = G^>(z) + G^<(z) = \frac{\langle gs|cc^\dagger|gs\rangle}{z - a_0^> - \frac{b_1^{>2}}{z - a_1^> - \dots}} + \frac{\langle gs|c^\dagger c|gs\rangle}{z - a_0^< - \frac{b_1^{<2}}{z - a_1^< - \dots}}$$

6. For each superblock in the system construct the reduced density matrix  $\rho_{i,i'}$  by tracing over the impurity and remaining superblock the density matrix:

$$\rho_{i,i'} = \text{Tr}_{|Env} |gs\rangle \langle gs| = \sum_{imp,j} \langle gs|i, imp, j\rangle \langle i', imp, j|gs\rangle$$

The reduced density matrix is the fully diagonalized to obtain its eigenvectors and eigenvalues. After ordering them the first  $m$  eigenstates are retained such that to fulfill the following relation:

$$\sum_{n>m}^{\dim(\rho)} \lambda_n(\rho) < \varepsilon \sim O(10^{-10})$$

The first  $m$  eigenvectors form a suitable (orthonormal) basis for the corresponding superblock  $\mathcal{SB}^{\cong}$  that best describes the target state. In Fig. 2.7 this concept is illustrated and compared with Wilson RG algorithm.

7. Obtain the transformation matrix  $\mathcal{O}$  having as columns the components of the first  $m$  eigenvectors of  $\rho$ . This matrix is used to rotate all the operators, the Hamiltonian of each superblock in particular, to the new basis:

$$A' = \mathcal{O}^\dagger A \mathcal{O}$$

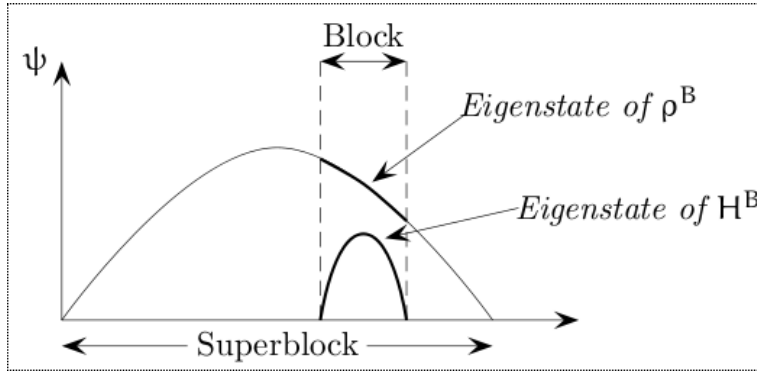


Figure 2.7: The target state description obtained projecting via the density matrix, *i.e.* using the reduced density matrix eigenstates as a basis, is a better approximation with respect to the RG lowest eigenstates construction.

8. Add 1 site, namely the dot  $\mathcal{D}$ , per side such that  $L' = L + 2$ . Rename the superblocks in blocks and restart from point 3 with a larger chain and using the information collected at each step.
9. When  $L = L_{max}$ , fixed *a priori* get the ground state in the adjacent sectors with one more and one less particle in the chain  $N = n \pm 1$  and with spin up and down. If the ground state energy in one of these sectors is smaller, move to that changing the initial particle number and restart the full calculation. Else exit the iteration of the chain length.

The DMFT self-consistency is then achieved cutting the impurity Green's function, obtained with an arbitrary number of continued fraction parameters, to the actual number of sites in the chain, such that the following relation between continued fractions is fulfilled:

$$t^2 G(z) = \Delta(z)$$

It is worth to observe that DMRG algorithm is in reality embedded in two outer loops, namely the DMFT loop and a loop on the adiabatic increasing of the maximum length of the chain  $L_{max}$  (finite size algorithm). We shall also point out that the ED-DMRG method makes no *a priori* approximations and is only limited by the number of sites in the effective bath that can be handled, for calculation time reasons. In practice, we use up to 50 sites to represent the bath.

## 2.5 Conclusions

In this chapter we have introduced the main theoretical tool used throughout this thesis, namely the Dynamical Mean Field Theory (DMFT). This method was developed in the last 20 years to

## 2. Theoretical framework: DMFT

---

deal with strongly correlated electron models.

Before entering in the details of this theory, we reviewed classical Weiss mean field theory for spin models, focusing on the ferromagnetic Ising model. We derived the main equations for this theory using first standard heuristic arguments and, later, using the so-called cavity method construction.

In the next part of the chapter we introduced the main concepts of DMFT. Using the cavity method we derived the expression of the effective action describing the local physics of a tagged single site interacting with an effective electronic bath replacing the initial many-body problem. To close the DMFT equation, *i.e.* to determine the local Weiss field describing the single site quantum fluctuations, we have derived the self-consistency condition, connecting the Weiss field to the local lattice Green's functions. The derivation of this relation was made possible by the use of the infinite dimensionality limit, that is necessary to reduce the full many-body problem to a local one.

We have illustrated then the intimate connection of the obtained local problem with quantum impurity models. This was used to obtain a simple physical interpretation of the theory, in terms of an effective quantum impurity interacting with conduction electrons. Finally we explained the iterative algorithm that should be used to obtain the solution of the DMFT equations and reviewed several techniques implementing this algorithm.

# Periodic Anderson Model

## Contents

---

<b>3.1 PAM and solvable limits</b> . . . . .	<b>60</b>
3.1.1 Non-interacting limit . . . . .	63
3.1.2 Atomic limit . . . . .	63
<b>3.2 DMFT solution of PAM</b> . . . . .	<b>69</b>
<b>3.3 Internal energy</b> . . . . .	<b>72</b>
<b>3.4 Long range order DMFT equations</b> . . . . .	<b>74</b>
3.4.1 Antiferromagnetic order . . . . .	74
3.4.2 AFM order and homogeneous magnetic field . . . . .	76
<b>3.5 Conclusions</b> . . . . .	<b>78</b>

---

Heavy fermion compounds are metallic alloys formed by rare-earths or actinides, *e.g.* *Ce*, *U* or *Yb*. One of the characteristic features of these compounds is the presence of large local magnetic moments from the *f*-orbitals and wide conduction bands formed by the *s/p*-orbital electrons. Being the number of local moments often of the same order of the lattice sites, the microscopic derivation of the heavy fermion description should be based on suitable extensions of the single impurity models, *e.g.* the Kondo lattice model (KL). This latter represents the most natural generalization of the Kondo impurity model to concentrate systems [36]. In its simplest form the KL model describes electrons in a conduction band locally coupled to the magnetic moments of a lattice of impurities. Within this model a first description of the competition between magnetic orders and local Kondo effect has been achieved and summarized in the well known “Doniach” diagram [21]. The Kondo lattice picture is nevertheless more appropriate for nearly integer valence systems, in which the *f*-orbital electron are extremely localized. Relaxing this hypothesis would lead us to consider a more general model, namely the *periodic Anderson*

### 3. Periodic Anderson Model

---

*model.* The Kondo lattice model can be thought as the large  $U$  effective model of the PAM. More formally it is possible to deduce the KL model from the PAM using a suitable extension of the Schrieffer-Wolff transformation, holding for the single impurity Anderson model [84]. With respect to the KL, periodic Anderson model is able to capture the essential physics of heavy fermions compounds having also more mixed-valence character. Its great generality is accompanied by a wide class of behavior and regimes, that up to now have not been completely cleared out.

In Sec. 3.1 we shall introduce and discuss the periodic Anderson model, namely the main model used in this thesis. After having derived the general equations of the model, we will discuss two non-trivial solvable limits. In Sec. 3.2 we will present the derivation of the Dynamical Mean Field equations for the paramagnetic periodic Anderson model. In Sec. 3.3 we shall obtain an expression for the internal energy of the model, in the framework of DMFT. This will be used in the following chapters to get some thermodynamical quantities such specific heat. The extension of the mean field equations to the case of long range magnetic ordering or in presence of external magnetic field are briefly discussed in Sec. 3.3. Finally an overview of the main concepts introduced in this chapter is given in section Sec. 3.4

#### 3.1 Periodic Anderson Model and some solvable limits

Periodic Anderson model is one among the simplest strongly correlated electrons model. In its minimal form PAM describes one conduction band formed by independent electrons with dispersion  $\epsilon(\mathbf{k})$ , hybridizing thru an amplitude  $V_{pd}$  with a lattice of non-dispersive electrons experiencing a strong on-site repulsion due to Coulomb interaction  $U$ . The periodic Anderson model Hamiltonian can be written as:

$$\begin{aligned} \tilde{H} = H - \mu N = & - \sum_{\langle ij \rangle \sigma} t_{ij} (p_{i\sigma}^+ p_{j\sigma} + h.c.) + (\epsilon_p - \mu) \sum_{i\sigma} n_{pi\sigma} \\ & + (\epsilon_d - \mu) \sum_{i\sigma} n_{di\sigma} + V_{pd} \sum_{i\sigma} (d_{i\sigma}^+ p_{i\sigma} + p_{i\sigma}^+ d_{i\sigma}) \\ & + U \sum_i (n_{di\uparrow} - \frac{1}{2}) (n_{di\downarrow} - \frac{1}{2}) \end{aligned} \quad (3.1)$$

Note that, despite the fact we shall deal with heavy fermion systems (usually involving  $p$ - and  $f$ -orbital electrons), we are using here a transition metal oxides notation. So that  $p_{i\sigma}$  and  $p_{i\sigma}^+$  are the destruction and creation operators corresponding to the conduction band electrons. These electrons have an energy  $\epsilon_p$  and an hopping amplitude  $t_{ij}$ . For sake of simplicity we will assume that the hopping is isotropic and homogeneous,  $t_{ij} = t\delta_{ij}$ . The operators  $d_{i\sigma}$  and  $d_{i\sigma}^+$  destructs and creates electrons in the  $d$ -orbital with an energy  $\epsilon_d$ . Without any loss of generality we will assume throughout this work that  $\epsilon_d = 0$ . The strong local Coulomb interaction

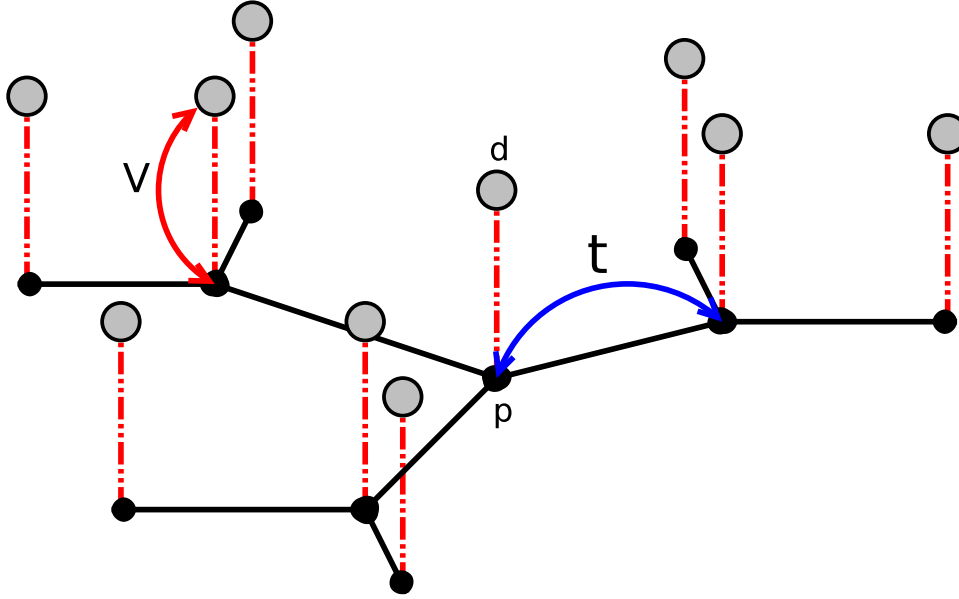


Figure 3.1: Schematic representation of the periodic Anderson model on a Bethe lattice with  $z = 3$ . Each lattice site (full black circles) hybridizes locally with the on-site  $d$ -orbital (gray circle). The hybridization is indicated with the double dotted-dashed red line while the amplitude is indicated with  $V$ . Two electrons on the  $d$ -orbital experience a Coulomb repulsion  $U$ , while the hopping amplitude between the  $p$ -orbitals at neighboring sites (black lines)  $i$  and  $j$  is  $t_{ij} = t\delta_{ij}$ .

experienced by the more localized electrons is modeled by the Hubbard term in  $U$ , expressing the cost of double occupy  $d$ -sites.  $V_{pd}$  is the hybridization amplitude between the  $p$ - and  $d$ -orbitals, namely it express' the probability for a conduction band electron to hop in to the localized  $d$ -orbital and vice-versa. It is worth to note that the interaction term used here has the so-called "magnetic" form. This is particularly suitable to study the physics at or near the Mott transition. In such a regime in fact this term approximately vanish at the Hartree-Fock level. In Fig. 3.1 we show a schematic 3-dimensional representation of the PAM on the Bethe lattice.

An important parameter used to characterize the various regimes of the PAM is the energy separation between the conduction band and the  $d$ -orbital energy level. This quantity defines the bare charge-transfer energy  $\Delta_0 = |\epsilon_p - \epsilon_d|$  of the model. We shall see in the following, that this value is modified as effect of finite hybridization, so that even in the non interacting limit  $\Delta_0$ , does not provide a good estimate for the charge-transfer energy and should be substituted with a more appropriate expression.

In order to obtain the general expression of the PAM Green's function let us introduce the self-energy matrix  $\hat{\Sigma}(\mathbf{k}, i\omega_n)$ . In the normal phase and in presence of only one interaction term,

### 3. Periodic Anderson Model

this matrix reads:

$$\hat{\Sigma}(\mathbf{k}, i\omega_n) = \begin{pmatrix} \Sigma_{dd}(\mathbf{k}, i\omega_n) & 0 \\ 0 & 0 \end{pmatrix} . \quad (3.2)$$

Then, we observe that in the operator basis corresponding to the pure (*i.e.* non-mixed) electronic state described by the operators  $p_{i\sigma}, p_{i\sigma}^+$  and  $d_{i\sigma}, d_{i\sigma}^+$  the non-interacting matrix propagator is non diagonal and reads:

$$\hat{G}_0^{-1}(\mathbf{k}, i\omega_n) = \begin{pmatrix} i\omega_n + \mu - \epsilon_d & V_{pd} \\ V_{pd} & i\omega_n + \mu - \epsilon_p - \epsilon(\mathbf{k}) \end{pmatrix} \quad (3.3)$$

where  $\epsilon(\mathbf{k})$  is the band dispersion, defined as the Fourier transform of the hopping term  $t_{ij}$ :

$$\epsilon(\mathbf{k}) = \sum_{|i-j|} e^{-i\mathbf{k}\cdot|i-j|} t_{ij} .$$

Lattice Green's functions are obtained making use of the Dyson equation:

$$\hat{G}(\mathbf{k}, i\omega_n)^{-1} = \hat{G}_0^{-1}(\mathbf{k}, i\omega_n) - \hat{\Sigma}(\mathbf{k}, i\omega_n) \quad (3.4)$$

that component by component reads:

$$\begin{aligned} G_{pp}^{-1}(\mathbf{k}, i\omega_n) &= i\omega_n + \mu - \epsilon_p - \epsilon(\mathbf{k}) - \frac{V_{pd}^2}{i\omega_n + \mu - \epsilon_d - \Sigma(\mathbf{k}, i\omega_n)} \\ G_{dd}^{-1}(\mathbf{k}, i\omega_n) &= i\omega_n + \mu - \epsilon_d - \Sigma(\mathbf{k}, i\omega_n) - \frac{V_{pd}^2}{i\omega_n + \mu - \epsilon_p - \epsilon(\mathbf{k})} \\ G_{pd}^{-1}(\mathbf{k}, i\omega_n) &= G_{dp}^{-1}(\mathbf{k}, i\omega_n) = \frac{(i\omega_n + \mu - \epsilon_d - \Sigma(\mathbf{k}, i\omega_n))}{V_{pd}} G_{pp}^{-1}(\mathbf{k}, i\omega_n) \end{aligned}$$

Note that, being interested here in the paramagnetic phase of the model, all the spin indices have been dropped.

Beside these quantities it is worth to define an "effective" self-energy for the conduction band electrons  $\Sigma_{pp}(\mathbf{k}, i\omega_n)$ . This function describes the interaction processes that the  $p$ -electrons undergo through the hybridization with the correlated  $d$ -electrons:

$$\Sigma_{pp}(\mathbf{k}, i\omega_n) = \frac{V_{pd}^2}{i\omega_n + \mu - \epsilon_d - \Sigma(\mathbf{k}, i\omega_n)} \quad (3.5)$$

It is important to stress that this quantity does not define an independent self-energy, even if it formally satisfies a Dyson equation. Fixed the self-energy corresponding to the interaction term in the Hamiltonian, this function is uniquely determined.

The local lattice Green's functions are obtained performing the summation over momenta  $\mathbf{k}$ . This sum can be transformed into an energy integral introducing the non-interacting density of states  $\rho_0(\epsilon) = \sum_{\mathbf{k}} \delta(\epsilon - \epsilon(\mathbf{k}))$ :

$$G_{\alpha\alpha}(i\omega_n) = \frac{1}{N} \sum_{\mathbf{k}} G_{\alpha\alpha}(\mathbf{k}, i\omega_n) = \int \rho_0(\epsilon) G_{\alpha\alpha}(\epsilon, i\omega_n) d\epsilon \quad (3.6)$$

with  $\alpha\alpha = pp, dd$ .

### 3.1.1 Non-interacting limit

We start this brief analysis of the solvable limits of the model with the simple case of no interaction, *i.e.*  $U = 0$ . The solution of the model in this limit is rather simple, consisting in the diagonalization of Hamiltonian (3.1). This can be done in any dimension and for any lattice structure. The non-interacting model describes a system of two hybridized one-particle bands, determined by the eigenenergies of the model Hamiltonian:

$$E_{\pm}(\mathbf{k}) = \frac{1}{2} \left( \epsilon_d + \epsilon_p + \epsilon(\mathbf{k}) - 2\mu \pm \sqrt{(\epsilon(\mathbf{k}) - \Delta_0)^2 + 4V_{pd}^2} \right)$$

In Fig. 3.2 we present a summary of the solution of the model in the 1-dimensional case with cosine dispersion, while in Fig. 3.3 we report the  $\mathbf{k}$ -dispersion of the spectral density. It is interesting to observe that the spectral weight is redistributed among the two hybridized bands in such a way that near the indirect gap the solution has more  $d$ -character, cf. Fig. 3.3.

As effect of the hybridization the “bare” charge-transfer energy  $\Delta_0$  is renormalized to a greater value, that can be estimated as the difference between the centers of mass of the two hybridized bands:  $\Delta \sim E_+ - E_- > \Delta_0$ . This should be kept in mind at the time of studying the effects of the correlation.

The Green’s functions of both the electronic species can be obtained from the expressions already derived in the previous section and read ( $z \in \mathbb{C}$  and  $\alpha\alpha = pp, dd$ ):

$$G_{\alpha\alpha}(\mathbf{k}, z) = \frac{Z_{\alpha\alpha,+}(\mathbf{k})}{z + \mu - E_-(\mathbf{k})} + \frac{Z_{\alpha\alpha,-}(\mathbf{k})}{z + \mu - E_+(\mathbf{k})}$$

where the “residues” at the poles  $Z_{\alpha\alpha,\sigma}$  have the form:

$$Z_{dd,\pm}(\mathbf{k}) = Z_{pp,\mp}(\mathbf{k}) = \frac{1}{2} \left[ 1 \mp \frac{\epsilon(\mathbf{k}) - \Delta_0}{\sqrt{(\epsilon(\mathbf{k}) - \Delta_0)^2 + 4V_{pd}^2}} \right]$$

The non-interacting limit of the periodic Anderson model can be used as a basic model to describe the renormalization of the effective mass due to the hybridization. The analytic solution (in the infinite dimension limit) will be of much important in the following of this thesis.

### 3.1.2 Atomic limit

The second solvable limit consist in the solution of the periodic Anderson model with a vanishing hopping of the conduction electrons (atomic limit):  $t_{ij} = 0$ , or in the limit  $t/U \rightarrow 0$ . In this limit the model reduce to a set of disconnected “dimers” (two sites model) formed by one  $p$ -orbital hybridizing with a  $d$ -orbital thru an amplitude  $V_{pd}$ . A correlation term  $U$  is also present on sites  $d$ .

### 3. Periodic Anderson Model

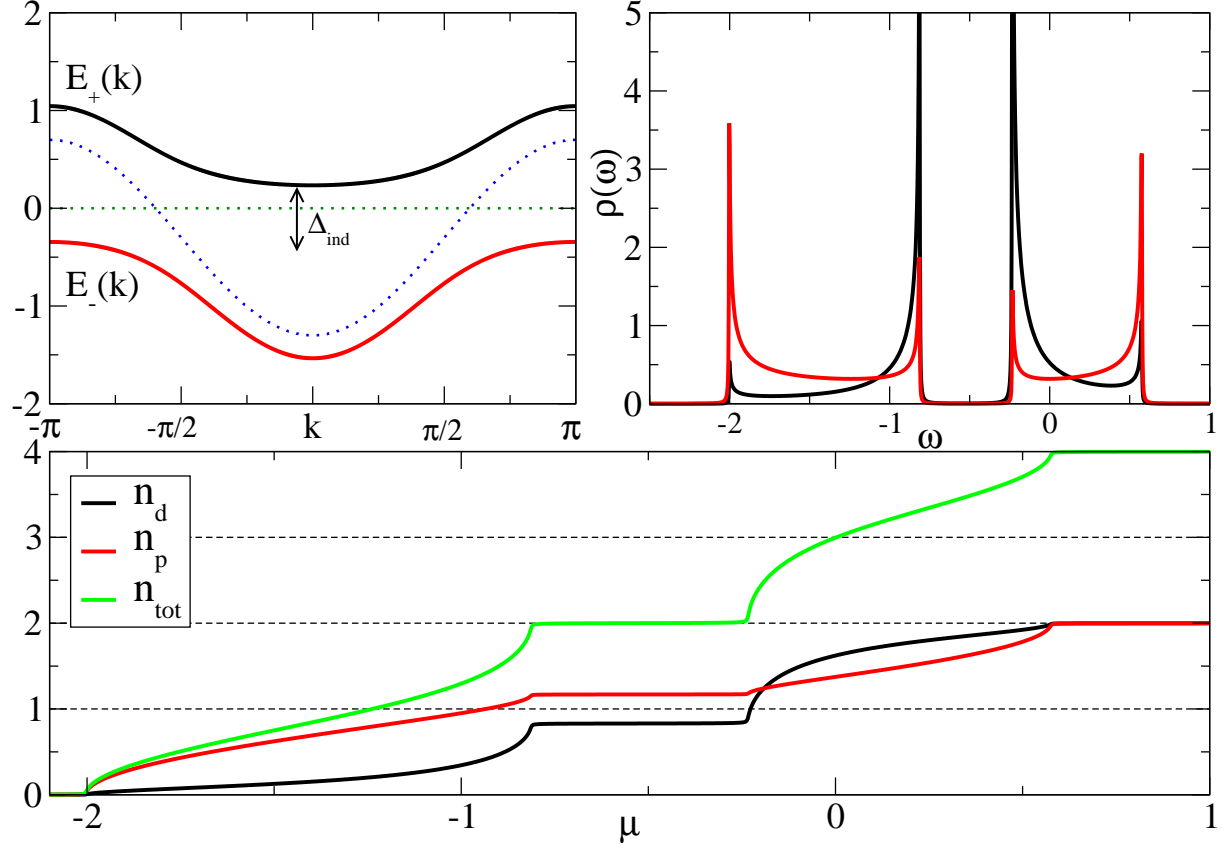


Figure 3.2: The figure illustrates the non-interacting solution of the PAM in 1-dimension and with a dispersion  $\epsilon(\mathbf{k}) = -2 \cos(\mathbf{k})$ . Top left panel: solid lines are the two eigenenergies  $E_{\pm}(\mathbf{k})$  for  $U = 0$ ,  $\Delta_0 = 0.25$ ,  $t_{pd} = 0.5$ . Dashed lines correspond to the bare dispersion of the conduction band and the correlated electrons level for  $t_{pd} = 0$ . Top right panel: density of states for the  $p$  and  $d$  electrons, red and black line resp. for the same model parameters as in the left panel and a value of the chemical potential such that  $n_p + n_d = 3$ . At the boundary of the DOS van-Hove singularities are well evident. Note that the hybridized bands are now separated by a large gap  $\Delta > \Delta_0 = |\epsilon_p - \epsilon_d|$ . Bottom panel: particle occupation  $n_d$  (black line),  $n_p$  (red) and  $n_{\text{tot}}$  (green) as a function of the chemical potential for  $U = 0$ ,  $\Delta_0 = 0.25$ ,  $t_{pd} = 0.5$ .

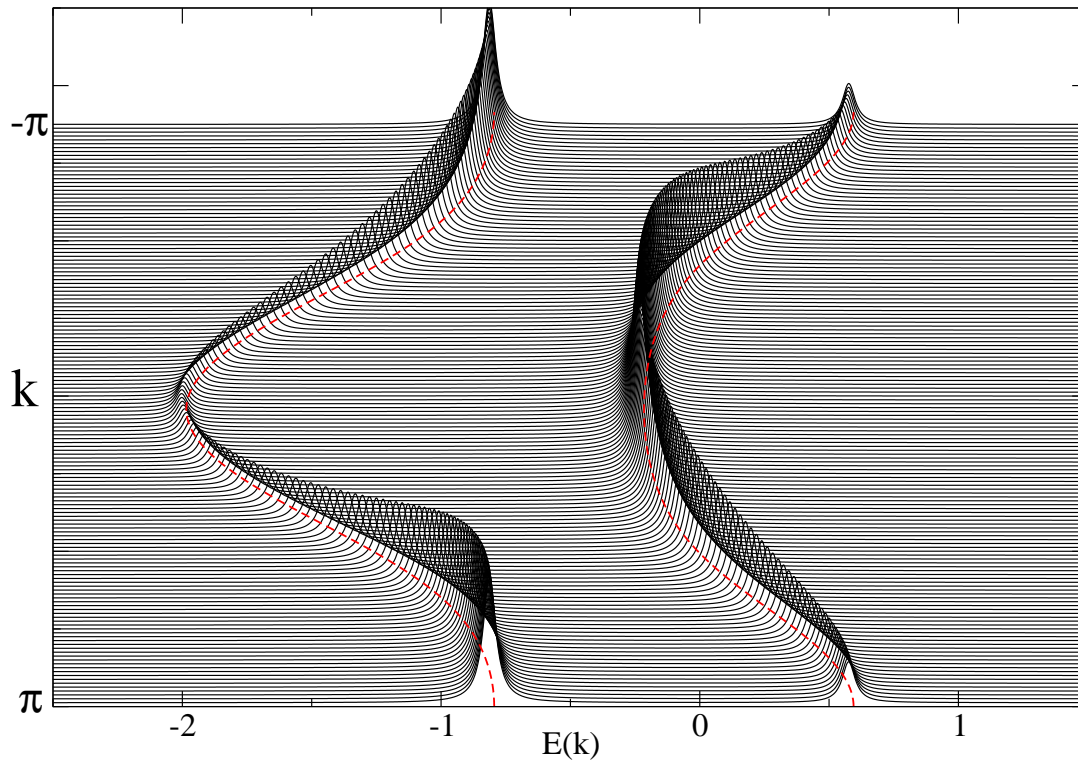


Figure 3.3: Evolution of the spectral density of the non-interacting model in 1-dimension with cosine dispersion as a function of  $\mathbf{k}$ . The figure shows in a direct way how the correlated character is redistributed among the two hybridized bands  $E_{\pm}(\mathbf{k})$ . The larger renormalization of the mass, as effect of the hybridization only, corresponds to more the pronounced peak appearing where the bands are more flat.

### 3. Periodic Anderson Model

In this limit, a four dimensional Hilbert space is associated to each site of the dimer. Thus, the total Hilbert space has dimension  $\mathcal{N} = 16$ . The model Hamiltonian is represented by a sparse  $16 \times 16$  matrix, that can be solved with no effort by any mathematical software.

Nevertheless, as the model Hamiltonian commutes with the total number of particle operator  $\hat{N}$ , with the total spin operator  $\hat{S}$  and with the spin projection operator  $\hat{S}_z$  it can be represented in a blocks form, each of which corresponds to a sector of the Hilbert space with a given set of quantum numbers, [66].

We shall adopt the following shorthand notation to indicate the state vectors:

$$|d_\uparrow d_\downarrow; p_\uparrow p_\downarrow\rangle = d_\uparrow^\dagger p_\uparrow^\dagger d_\downarrow^\dagger p_\downarrow^\dagger |0\rangle$$

thus, for example the state with two electrons in the  $d$ -orbital and one electrons with spin  $\uparrow$  in the  $p$ -orbital reads:

$$|\uparrow\downarrow; \uparrow\rangle = d_\uparrow^\dagger p_\uparrow^\dagger d_\downarrow^\dagger |0\rangle$$

- **N=0, N=4**

The model reduce in both cases to a one-dimensional problem. The empty case has zero energy  $E = 0$  and the eigenstate is  $|0\rangle$ . The completely filled case has  $E = 2\epsilon_p + 2\epsilon_d + U$  while the eigenstate is  $|\uparrow\downarrow; \uparrow\downarrow\rangle$ .

- **N=1**

The one-particle sector has dimension 2, states are classified in a doublet with  $S_z = \pm 1/2$ . The matrix Hamiltonian is represented in this sector as:

$$H = \begin{pmatrix} \epsilon_d & V_{pd} \\ V_{pd} & \epsilon_p \end{pmatrix} \quad (3.7)$$

The eigenenergies are obtained solving the secular equation:  $H|d; p\rangle = E_\pm^{(1)}|d; p\rangle$

$$E_\pm^{(1)} = \frac{1}{2} \left[ \epsilon_p + \epsilon_d \pm \sqrt{\Delta_0^2 + 4V_{pd}^2} \right]$$

The corresponding eigenstates are expressed as suitable linear combination of the one  $p$ - or one  $d$ -electron states with suitable spin value:

$$|E_+^{(1)}, \sigma\rangle = \frac{1}{\mathcal{N}^{(1)}} \left[ -\gamma^{(1)}|\sigma; 0\rangle + |0; \sigma\rangle \right] \quad (3.8)$$

$$|E_-^{(1)}, \sigma\rangle = \frac{1}{\mathcal{N}^{(1)}} \left[ |\sigma; 0\rangle + \gamma^{(1)}|0; \sigma\rangle \right] \quad (3.9)$$

with

$$\gamma^{(1)} = \frac{2V_{pd}}{\Delta_0 + \sqrt{\Delta_0^2 + 4V_{pd}^2}}, \quad \mathcal{N}^{(1)} = \sqrt{1 + \gamma^{(1)2}}$$

- **N=3**

The solution of the model in this sector proceeds in the very same way as the previous case with  $N = 1$ . The three-particles (one-hole) sector has dimension 2 and the states can be classified in a doublet. The matrix is reduced to a  $2 \times 2$  matrix of the form:

$$H = \begin{pmatrix} \epsilon_p + 2\epsilon_d + U & V_{pd} \\ V_{pd} & 2\epsilon_p + \epsilon_d \end{pmatrix} \quad (3.10)$$

The eigenenergies are:

$$E_{\pm}^{(3)} = \frac{1}{2} \left[ 3\epsilon_p + 3\epsilon_d + U \pm \sqrt{(\Delta_0 + U)^2 + 4V_{pd}^2} \right]$$

while the eigenstates are obtained as linear combination of the three electron states:

$$|E_+^{(3)}, \sigma\rangle = \frac{1}{\mathcal{N}^{(3)}} \left[ -\gamma^{(3)} |\uparrow\downarrow; \sigma\rangle + |\sigma; \uparrow\downarrow\rangle \right] \quad (3.11)$$

$$|E_-^{(3)}, \sigma\rangle = \frac{1}{\mathcal{N}^{(3)}} \left[ |\uparrow\downarrow; \sigma\rangle + \gamma^{(3)} |\sigma; \uparrow\downarrow\rangle \right] \quad (3.12)$$

where the coefficients are expressed as:

$$\gamma^{(3)} = \frac{2V_{pd}}{\Delta_0 - U + \sqrt{\Delta_0^2 + 4V_{pd}^2}}, \quad \mathcal{N}^{(3)} = \sqrt{1 + \gamma^{(3)2}}$$

- **N=2**

The spin symmetry can be used to classify the states within this sector. Total spin operator has eigenvalues  $s = 0, 1$  thus the states can either be triplets or singlets. In the former case the spin part of the wave-function is symmetric, thus the interaction  $U$  play no role in the system, *i.e.* double occupancy of  $d$ -orbital is forbidden by Pauli principle. The  $S = 1$  Hamiltonian reads:

$$H = \begin{pmatrix} \epsilon_p + \epsilon_d & 0 & 0 \\ 0 & \epsilon_p + \epsilon_d & 0 \\ 0 & 0 & \epsilon_p + \epsilon_d \end{pmatrix} \quad (3.13)$$

The eigenstates are all degenerate with an energy  $E = \epsilon_p + \epsilon_d$ , but they can be labelled by the spin projection quantum number:

$$|n = 2, s_z = -1\rangle = |\downarrow; \downarrow\rangle \quad (3.14)$$

$$|n = 2, s_z = 0\rangle = \frac{1}{\sqrt{2}} [|\uparrow; \downarrow\rangle - |\downarrow; \uparrow\rangle] \quad (3.15)$$

$$|n = 2, s_z = 1\rangle = |\uparrow; \uparrow\rangle \quad (3.16)$$

### 3. Periodic Anderson Model

On the other hand the case  $S = 0$  is more interesting. The representation of the Hamiltonian is a  $3 \times 3$  matrix of the form:

$$H = \begin{pmatrix} 2\epsilon_d + U & \sqrt{2}V_{pd} & 0 \\ \sqrt{2}V_{pd} & \epsilon_p + \epsilon_d & \sqrt{2}V_{pd} \\ 0 & \sqrt{2}V_{pd} & 2\epsilon_p \end{pmatrix} \quad (3.17)$$

Eigenenergies are obtained solving a third order secular equation. of the form:

$$E^3 + aE^2 + bE + c = 0$$

that after some length but straightforward algebra can be re-expressed in the form:

$$z^3 + pz = q$$

with  $z = x + a/3$ ,  $p = b - a^2/3$  and  $q = 2a^3/27 - ab/3 + c$ . Now imposing that  $p/3 = uv$  and that  $z - u - v$  the equation assume the, more natural, form:  $u^3 - v^3 = q$  or:

$$\begin{cases} u^6 - qu^3 - \left(\frac{p}{3}\right)^3 = 0 \\ v = \frac{p}{3u} \end{cases} \quad (3.18)$$

having the following, formal, solutions:

$$u = \left( \frac{q}{2} \pm \sqrt{\left(\frac{q}{2}\right)^2 + \left(\frac{p}{3}\right)^3} \right)^{1/3} \quad (3.19)$$

The eigenenergies  $E_1^{(2)}, E_2^{(2)}, E_3^{(2)}$  are the 3 solutions from (3.19) and one can suppose to order them such that  $E_1^{(3)} \leq E_2^{(2)} \leq E_3^{(2)}$ . The eigenstates can then be written as a linear combination of basis vector of the singlet subspace:

$$|E_k^{(2)}\rangle = \alpha_k^{(2)} |\uparrow\downarrow; 0\rangle - \beta_k^{(2)} (|\uparrow; \downarrow\rangle - |\downarrow; \uparrow\rangle) + \gamma_k^{(2)} |0; \uparrow\downarrow\rangle$$

where  $k = 1, 2, 3$  and the coefficients are, [66]:

$$\begin{cases} \alpha_k^{(2)} = \frac{2V_{pd}\beta_k^{(2)}}{E_k^{(2)} - 2\epsilon_d - U} \\ \beta_k^{(2)} = \left[ \left( \frac{2V_{pd}}{E_k^{(2)} - 2\epsilon_d - U} \right)^2 + \left( \frac{2V_{pd}}{E_k^{(2)} - 2\epsilon_p} \right)^2 + 2 \right]^{-1/2} \\ \gamma_k^{(2)} = \frac{2V_{pd}\beta_k^{(2)}}{E_k^{(2)} - 2\epsilon_p} \end{cases} \quad (3.20)$$

### 3.2 DMFT solution of PAM

There are several different approach one can use to tackle the problem of the solution of the periodic Anderson model, such as perturbative expansions in terms of the hybridization, or mean-field approaches like slave-bosons or furthermore variational based calculations. All these approaches have different drawbacks that make sometime the solution available only under particular regimes. In recent years a powerful technique has been developed to solve strongly correlated electron model, based on the expansion around the infinite coordination number limit,  $z \rightarrow \infty$ , of  $1/z$ . In particular it can be demonstrated the locality, *i.e.* momentum independence, of the irreducible self-energy [60]:

$$\Sigma(k, i\omega_n) \xrightarrow{z \rightarrow \infty} \Sigma(i\omega_n) \quad (3.21)$$

It is worth to note that, despite the advantages one can obtain from using the infinite connectivity limit, local interactions like Hubbard  $U$  term remain non trivial and thus interesting. Based on (3.21), Dynamical Mean Field Theory provides a set of closed equation to solve the interacting problem in a well defined approximation scheme.

The main idea of DMFT is to map the quantum many-body problem posed by (3.1) onto an effective quantum impurity problem for the correlated  $d$ -electrons, supplemented by a self-consistency condition fixed by requiring to the effective model to replicate the physics of the original lattice model. The effective problem describes the local quantum fluctuations at an arbitrary  $d$ -orbital of the original lattice problem, but neglects all spatial fluctuations. The DMFT equations for the periodic Anderson model can be derived using the same technique presented in Chap. 2 for the Hubbard model [43, 44, 31]. To simplify the notation let us introduce the following set of Grassman variables:  $\psi_{i\sigma}^+ = \{p_{i\sigma}^+, d_{i\sigma}^+\}$  and  $\psi_{i\sigma} = \{p_{i\sigma}, d_{i\sigma}\}$ . The action corresponding to the model Hamiltonian (3.1) reads:

$$S = \int_0^\beta d\tau \left( \sum_{i\sigma} \psi_{i\sigma}^+(\tau) (\partial_\tau - \mu) \psi_{i\sigma}(\tau) + H(\psi_{i\sigma}^+, \psi_{i\sigma}) \right) \quad (3.22)$$

We shall now derive the effective action for the PAM using the cavity method. We pick out one single site/dimer of the lattice, say  $i = 0$ , and integrate out all the remaining electronic degrees of freedom. To take advantage of the matrix notation introduced above, we perform this integration in two steps. First we integrate out all the lattice degrees of freedom with the exception of single tagged “dimer”. Later we shall integrate out the non-correlated orbital degrees of freedom to obtain a single site effective theory. The first integration reads:

$$\frac{1}{Z_{\text{eff}}} e^{-S'_{\text{eff}}[\psi_{0\sigma}^+, \psi_{0\sigma}]} = \frac{1}{Z} \int \prod_{i \neq 0, \sigma} \mathcal{D}\psi_{i\sigma}^+ \mathcal{D}\psi_{i\sigma} e^{-S} \quad (3.23)$$

### 3. Periodic Anderson Model

Proceeding as done for the Hubbard model we separate the action (3.22) in three terms:  $S = S_o + S^{(o)} + \Delta S$ , respectively the action of the local site (dimer), the action of the lattice without the tagged site and the terms connecting the site with the rest of the lattice.

$$\begin{aligned}
S_o &= \int_0^\beta d\tau \sum_\sigma \psi_{o\sigma}^+(\tau) \begin{pmatrix} \partial_\tau + \epsilon_p - \mu & V_{pd} \\ V_{pd} & \partial_\tau + \epsilon_d - \mu \end{pmatrix} \psi_{o\sigma}(\tau) + \int_0^\beta d\tau U \tilde{n}_{do\uparrow}(\tau) \tilde{n}_{do\downarrow}(\tau) \\
S^{(o)} &= \int_0^\beta d\tau \sum_{i \neq o, \sigma} \psi_{i\sigma}^+(\tau) \begin{pmatrix} \partial_\tau + \epsilon_p - \mu & V_{pd} \\ V_{pd} & \partial_\tau + \epsilon_d - \mu \end{pmatrix} \psi_{i\sigma}(\tau) \\
&\quad - \int_0^\beta d\tau \sum_{i, j \neq o, \sigma} \psi_{i\sigma}^+(\tau) \begin{pmatrix} t_{ij} & 0 \\ 0 & 0 \end{pmatrix} \psi_{j\sigma}(\tau) + \text{h.c.} + \int_0^\beta d\tau U \sum_{i \neq o} \tilde{n}_{di\uparrow}(\tau) \tilde{n}_{di\downarrow}(\tau) \\
\Delta S &= - \int_0^\beta d\tau \sum_{i\sigma} \psi_{i\sigma}^+(\tau) \begin{pmatrix} t_{io} & 0 \\ 0 & 0 \end{pmatrix} \psi_{o\sigma}(\tau) + \text{h.c.} \\
&= - \int_0^\beta d\tau \sum_{i\sigma} (c_{i\sigma}^+(\tau) \eta_i(\tau) + \eta_i^+(\tau) c_{i\sigma}(\tau))
\end{aligned} \tag{3.24}$$

where  $\tilde{n}_{di\sigma} = n_{di\sigma} - 1/2$ . Using this decomposition, the equation (3.23) becomes formally identical to the corresponding expression obtained in Chap. 2 for the Hubbard model. Thus, the same considerations apply taking the infinite coordination number limit. We obtain the following expression for the effective action  $S'_{\text{eff}}$ :

$$S'_{\text{eff}} = - \int_0^\beta d\tau \int_0^\beta d\tau' \sum_\sigma \psi_{o\sigma}^+(\tau) G_0^{-1}(\tau, \tau') \psi_{o\sigma}(\tau') + U \int_0^\beta d\tau \tilde{n}_{do\uparrow}(\tau) \tilde{n}_{do\downarrow}(\tau) \tag{3.25}$$

On the Bethe lattice the matrix  $G_0^{-1}$  reads:

$$G_0^{-1}(i\omega_n) = \begin{pmatrix} i\omega_n + \mu - \epsilon_p - t^2 G_{pp}(i\omega_n) & V_{pd} \\ V_{pd} & i\omega_n + \mu - \epsilon_d \end{pmatrix} \tag{3.26}$$

Where  $G_{pp}(i\omega_n)$  is the local Green's function of the conduction band electrons, describing the quantum fluctuations of the  $p$ -electrons at a given lattice site.

Finally we can obtain the single orbital effective action integrating out the contribution of the non-correlated  $p$ -orbital. This integration is straightforward and gives:

$$S_{\text{eff}} = - \int_0^\beta d\tau \int_0^\beta d\tau' \sum_\sigma d_\sigma^+(\tau) \mathcal{G}_0^{-1}(\tau - \tau') d_\sigma(\tau') + U \int_0^\beta d\tau [n_{d\uparrow}(\tau) - \frac{1}{2}] [n_{d\downarrow}(\tau) - \frac{1}{2}] \tag{3.27}$$

The action (3.27) is written in terms of the operators corresponding to the  $d$ -orbital of an arbitrary site of the lattice. The bare propagator  $\mathcal{G}_0^{-1}(i\omega_n)$  in (3.27) represents the local *Weiss* field, describing the quantum fluctuations at the correlated orbital of an arbitrary site of the lattice.

This function is the main unknown of the DMFT scheme and its functional expression depends on the initial lattice structure. In the case of the Bethe lattice this function reads:

$$\mathcal{G}_{0,dd}^{-1}(i\omega_n) = i\omega_n + \mu + \epsilon_d - \frac{V_{pd}^2}{i\omega_n + \mu + \epsilon_p - t^2 G_{pp}(i\omega_n)} \quad (3.28)$$

The previous expression of the Weiss field put in evidence the relation between the  $d$ -orbital and the conduction band electrons at the  $p$ -orbitals. The electrons at the correlated orbitals can delocalize thru the lattice only hybridizing with the conduction band electrons. It is worth to recognize in the denominator in the r.h.s of (3.28) the “Weiss field of the  $p$ -electrons”. Thus, in terms of the effective single impurity Anderson model, the following relation holds:

$$\Delta(i\omega_n) = \frac{V_{pd}^2}{i\omega_n + \mu + \epsilon_p - t^2 G_{pp}(i\omega_n)}$$

It remains to obtain an expression for the conduction band electron local Green’s function. This can be readily done using relations (3.4), (3.5) and the non-interacting Bethe lattice DOS  $\rho_0(\epsilon) = \frac{1}{2\pi t^2} \sqrt{4t^2 - \epsilon^2}$ :

$$\begin{aligned} G_{pp}(i\omega_n) &= \int_{\mathbb{R}} \frac{\rho_0(\epsilon) d\epsilon}{i\omega_n + \mu - \epsilon_p - \Sigma_{pp}(i\omega_n) - \epsilon} \\ &= \tilde{D}(i\omega_n + \mu - \epsilon_p - \Sigma_{pp}(i\omega_n)) \end{aligned} \quad (3.29)$$

The  $p$ -electron local Green’s function  $G_{pp}(i\omega_n)$  indirectly depends on the local self-energy  $\Sigma(i\omega_n)$ . Thus, to close the DMFT equation it is necessary to obtain the solution of the effective impurity problem defined by (3.27) and to determine the local self-energy:

$$\begin{aligned} G_{dd}(i\omega_n) &= -\langle d(i\omega_n) d^\dagger(i\omega_n) \rangle_{\text{S}_{\text{eff}}} \\ \Sigma(i\omega_n) &= \mathcal{G}_0^{-1}(i\omega_n) - G_{dd}^{-1} \end{aligned}$$

The iterative solution of the DMFT equations starts with a guess on the Weiss field  $\mathcal{G}_0^{-1}(i\omega_n)$ , this fixes the effective quantum impurity problem to solve. The solution of this problem, achieved using an appropriate solver (cf. Chap. 2), permits to get the local Green’s function of  $d$ -orbital electrons  $G_{dd}$  and the local self-energy  $\Sigma(i\omega_n)$  using the Dyson equation. The knowledge of this latter function is sufficient to determine the  $p$ -electron local Green’s function and finally to update the Weiss field (3.28). The process should be iterated until convergence to a self-consistent solution is achieved. Convergence is in fact a highly non trivial problem to analyze. The iteration-substitution scheme used to obtain DMFT solution defines a discrete non-linear dynamical system, whose convergence should in principle be checked each time by small changing the initial conditions (*i.e.* the guess). In practice the method is sufficiently stable and reliable to require this analysis only near critical regimes, *i.e.* where locating the local minima of

### 3. Periodic Anderson Model

the free energy can be numerically hard to accomplish. At the self-consistent point the Green's functions of the effective impurity model should correspond to the local Green's functions of the original lattice problem. In a more schematic fashion the DMFT iterative solution scheme is resumed in Fig. 3.4.

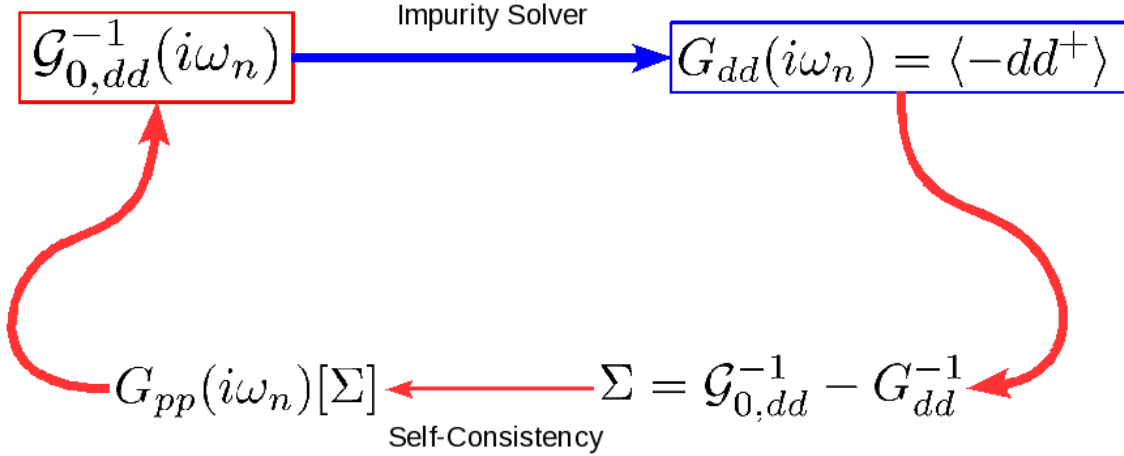


Figure 3.4: DMFT iterative scheme for periodic Anderson model: starting from a guess for the Weiss field  $\mathcal{G}_0^{-1}(i\omega_n)$  it is possible to solve the (effective) impurity problem. This will produce an impurity Green's function  $G_{dd}(i\omega_n)$  and the local self-energy  $\Sigma(i\omega_n)$ . This will uniquely determine the local conduction electrons Green's functions  $G_{pp}(i\omega_n)$ . This latter is needed to update the Weiss field using the self-consistency relation and restart the full procedure.

### 3.3 Internal energy

Beside the calculation of local spectral properties, the DMFT approach can also be used to evaluate, in the  $z \rightarrow \infty$  limit, interesting thermodynamical quantities. Thermodynamical observables can be deduced as derivatives of the internal energy  $\Omega$ , that can be expressed in terms of local Green's functions only. In this respect, the evaluation of the internal energy does not pose any serious theoretical problem within DMFT framework, being the local Green's function the direct output of the DMFT equations.

We shall now derive a suitable expression for the internal energy of the periodic Anderson model in the infinite dimensions limit [98]. From the definition of internal energy [57, 38] and the expression of the model Hamiltonian (3.1), one has:

$$\Omega = T \lim_{\eta \rightarrow 0^+} \sum_n e^{i\omega_n \eta} \mathcal{E}(i\omega_n) \quad (3.30)$$

where the functional  $\mathcal{E}(i\omega_n)$  is a shorthand notation for all the lattice sums of the thermal

averages of the different terms appearing in (3.1). Recalling that

$$G(\mathbf{k}, i\omega_n) = \int_0^\beta d\tau e^{i\omega_n \tau} \langle T_\tau (c_{\mathbf{k}}^+(\tau) c_{\mathbf{k}}(0)) \rangle,$$

it becomes possible to express  $\mathcal{E}(i\omega_n)$  as a sum of different contributions, modulo unessential constants:

$$\mathcal{E}(i\omega_n) = \mathcal{E}_{kin} + \mathcal{E}_{pot} + \mathcal{E}_{pot} + \mathcal{E}_\varepsilon + \mathcal{E}_\mu$$

where, using equation of motions arguments, one has respectively:

$$\begin{aligned} \mathcal{E}_{kin} &= \sum_{\mathbf{k}, \sigma} \varepsilon(\mathbf{k}) G_{pp}(\mathbf{k}, i\omega_n) \\ \mathcal{E}_{pot} &= \sum_{\mathbf{k}, \sigma} \Sigma(i\omega_n) G_{dd}(\mathbf{k}, i\omega_n) \equiv U \langle n_{d,\uparrow} n_{d,\downarrow} \rangle - U \langle n_d \rangle / 2 \\ \mathcal{E}_{hyb} &= \sum_{\mathbf{k}, \sigma} t_{pd} (G_{pd}(\mathbf{k}, i\omega_n) + G_{dp}(\mathbf{k}, i\omega_n)) \\ \mathcal{E}_\varepsilon &= \sum_{\mathbf{k}, \sigma} \varepsilon_p G_{pp}(\mathbf{k}, i\omega_n) + \varepsilon_d G_{dd}(\mathbf{k}, i\omega_n) \\ \mathcal{E}_\mu &= - \sum_{\mathbf{k}, \sigma} \mu (G_{pp}(\mathbf{k}, i\omega_n) + G_{dd}(\mathbf{k}, i\omega_n)) \end{aligned} \quad (3.31)$$

The off-diagonal Green's function  $G_{pd}(\mathbf{k}, i\omega_n)$  can be expressed in terms of the  $p$ -electron Green's function.

$$G_{pd}(i\omega_n) = \frac{V_{pd}}{i\omega_n + \mu - \varepsilon_d - \Sigma(i\omega_n)} G_{pp}(\mathbf{k}, i\omega_n) \quad (3.32)$$

We shall now proceed to the evaluation of all the  $\mathbf{k}$ -sums appearing in (3.31). This will permit to deal with local quantities only. We start from the hybridization term. Summing the previous equation (3.32) over the wave-vector  $\mathbf{k}$  one obtains:

$$E_{hyb} = 2\Sigma_{pp}(i\omega) G_{pp}(i\omega_n).$$

where the factor 2 comes from the equality  $G_{pd}(i\omega_n) = G_{dp}(i\omega_n)$  and  $G_{pp}(i\omega_n)$  is given by equation (3.29).

On the other hand the  $\mathbf{k}$ -sum appearing in the kinetic energy contribution, involving the dispersion relation, can be evaluated by expressing it in terms of energy integral and the use of simple algebraic relations to improve convergence of the Matsubara sums (cf. (3.30)):

$$\begin{aligned} E_{kin} &= \int_{\mathbb{R}} d\varepsilon \frac{\varepsilon \rho_0(\varepsilon)}{i\omega_n + \mu - \varepsilon_p - \Sigma_{pp}(i\omega_n) - \varepsilon} \\ &= i\omega_n (G_{pp}(i\omega_n) - \tilde{D}(i\omega_n)) + (\mu - \varepsilon_p) G_{pp}(i\omega_n) + \int_{\mathbb{R}} d\varepsilon \frac{\rho_0(\varepsilon) \varepsilon}{i\omega_n - \varepsilon} \end{aligned} \quad (3.33)$$

Finally, noting that:

$$T \lim_{\eta \rightarrow 0^+} \sum_n e^{i\omega_n \eta} G(i\omega_n) = n(T)$$

### 3. Periodic Anderson Model

---

and that

$$\sum_n \int_{\mathbb{R}} d\varepsilon F(\varepsilon) \frac{1}{i\omega_n - \varepsilon} = \int_{\mathbb{R}} d\varepsilon F(\varepsilon) \sum_n \frac{1}{i\omega_n - \varepsilon} = \int_{\mathbb{R}} d\varepsilon F(\varepsilon) n_F(\varepsilon; T),$$

where  $n_F$  is the Fermi momentum distribution function, we are able to perform the Matsubara sums in equation (3.30), term by term obtaining:

$$\begin{aligned} E_{free} &= \int_{\mathbb{R}} d\varepsilon \rho_0(\varepsilon) \varepsilon n_F(\varepsilon; T) \\ E_{kin} &= E_{free} + (\mu - \epsilon_p) n_p(T) + T \lim_{\eta \rightarrow 0^+} \sum_n e^{i\omega_n \eta} i\omega_n (G_{pp}(i\omega_n) - \tilde{D}(i\omega_n)) \\ E_{hyb} &= 4T \lim_{\eta \rightarrow 0^+} \sum_n e^{i\omega_n \eta} \Sigma_{pp}(i\omega_n) G_{pp}(i\omega_n) \\ E_{pot} &= TU \langle n_{d,\uparrow} n_{d,\downarrow} \rangle(T) - \frac{1}{2} TU n_d(T) \\ E_\varepsilon &= \epsilon_p n_p(T) + \epsilon_d n_d(T) \\ E_\mu &= -\mu (n_p(T) + n_d(T)) \end{aligned} \tag{3.34}$$

The internal energy of the periodic Anderson model in the DMFT framework is given by the sum of all the terms appearing in (3.34):

$$\Omega = E_{kin} + E_{hyb} + E_{pot} + E_\varepsilon + E_\mu$$

Operatively the evaluation of the previous Matsubara sums in (3.34) may result quite complicated, due to the very slow decay of some functions. Thus it becomes mandatory to use the largest possible number of Matsubara frequencies to perform the sums, in relation with the given value of the temperature. Beside this also some other expedients have to be taken into account to improve the calculation, such as integration of the tails (*i.e.* mean field subtraction).

## 3.4 Long range order DMFT equations

### 3.4.1 Antiferromagnetic order

The DMFT equations are easily extended to cover phases with long range magnetic orders, such as the antiferromagnetic or the ferromagnetic one. As this latter requires only to include the linear coupling to the homogeneous magnetic field into the self-consistency condition [31], we will discuss with more details the case of the antiferromagnetic order.

Let us consider the response of the lattice problem to a staggered magnetic field inducing an antiferromagnetic order. In the Nèel phase one can consider two nested sublattices  $A$  and  $B$  such that conduction electrons on sublattice  $A$  hop to sites in sublattice  $B$ , vice-versa. In this

situation the Hamiltonian 3.1 takes the form:

$$\begin{aligned}
 \tilde{H} = H - \mu N = & - \sum_{\langle ij \rangle \sigma} t_{ij} (p_{A i \sigma}^+ p_{B j \sigma} + h.c.) + \sum_{i \sigma \alpha = A, B} (\epsilon_p - \mu_{\alpha \sigma}) n_{p i \sigma \alpha} \\
 & + \sum_{i \sigma \alpha = A, B} (\epsilon_d - \mu_{\alpha \sigma}) n_{d i \sigma \alpha} + V_{pd} \sum_{i \sigma \alpha = A, B} (d_{i \sigma \alpha}^+ p_{i \sigma \alpha} + p_{i \sigma \alpha}^+ d_{i \sigma \alpha}) \\
 & + U \sum_{i \alpha = A, B} (n_{d i \uparrow \alpha} - \frac{1}{2}) (n_{d i \downarrow \alpha} - \frac{1}{2})
 \end{aligned} \tag{3.35}$$

where the coupling to the staggered magnetic field  $B_i = \pm B$  (everywhere will be clear its distinction from the sublattice label), for  $i \in A, B$  respectively, has been absorbed into the chemical potential,  $\mu_{\sigma \alpha} = \mu + \sigma h$  with  $h = g \mu_B B / 2$  and  $\mu_B$  the Bohr magneton. Then to simplify the notation one can introduce suitable Grassman variables  $\psi_{\mathbf{k} \sigma} = (p_{\mathbf{k} \sigma A}, p_{\mathbf{k} \sigma B}, d_{\mathbf{k} \sigma A}, p_{\mathbf{k} \sigma B})$ . The action of the model will reads in terms of these variables as:

$$S_{AF} = \int_0^\beta d\tau d\tau' \sum_{\mathbf{k} \sigma} \psi_{\mathbf{k}, \sigma}^+ \hat{G}_{0, \mathbf{k}, \sigma}^{-1} \psi_{\mathbf{k}, \sigma} + U \int_0^\beta d\tau \sum_{i, \alpha = A, B} (n_{d i \uparrow \alpha} - \frac{1}{2}) (n_{d i \downarrow \alpha} - \frac{1}{2})$$

Where the bare propagator is represented in matrix form as:

$$\hat{G}_{0, \mathbf{k}, \sigma}^{-1} = \begin{pmatrix} i\omega_n - \epsilon_p + \mu_{A\sigma} & -\epsilon(\mathbf{k}) & -V_{pd} & 0 \\ -\epsilon(\mathbf{k}) & i\omega_n - \epsilon_p + \mu_{B\sigma} & 0 & -V_{pd} \\ -V_{pd} & 0 & i\omega_n - \epsilon_d + \mu_{A\sigma} & 0 \\ 0 & -V_{pd} & 0 & i\omega_n - \epsilon_d + \mu_{B\sigma} \end{pmatrix} \tag{3.36}$$

We can proceed in the same way we did for the paramagnetic case to obtain the general form of the Green's functions of the model in the antiferromagnetic phase. Let us consider the self-energy matrix  $\hat{\Sigma}_\sigma(\mathbf{k}, i\omega_n)$ . In the limit of infinite dimension this function lose its dependence on the momentum  $\mathbf{k}$ . Then, the lattice Green's function are obtained by means of the Dyson equation:

$$\hat{G}_\sigma^{-1}(\mathbf{k}, i\omega_n) = \hat{G}_{0, \sigma}^{-1}(\mathbf{k}, i\omega_n) - \hat{\Sigma}_\sigma(i\omega_n) \tag{3.37}$$

The element by element expressions corresponding to this equation are greatly simplified with the introduction of the following compact notations:

$$\begin{aligned}
 \alpha_{A, B} &= i\omega_n - \epsilon_p + \mu_{A, B\sigma} \\
 \gamma_{A, B} &= i\omega_n - \epsilon_d + \mu_{A, B\sigma} - \Sigma_{A, B, \sigma}(i\omega_n) \\
 \zeta_{A, B\sigma} &= \alpha_{A, B} - \frac{V_{pd}^2}{\gamma_{A, B}} = i\omega_n - \epsilon_p + \mu_{A, B\sigma} - \frac{V_{pd}^2}{i\omega_n - \epsilon_d + \mu_{A, B\sigma} - \Sigma_{A, B, \sigma}(i\omega_n)}
 \end{aligned} \tag{3.38}$$

The inverting of the matrix defined in (3.37) is straightforward and lead to the following expression for the lattice Green's function of the conduction band electrons in a given sublattice,

### 3. Periodic Anderson Model

---

say A:

$$\begin{aligned}
G_{pp,A,\sigma}(\mathbf{k}, i\omega_n) &= \frac{\gamma_A(\alpha_B\gamma_B - V_{pd}^2)}{V_{pd}^4 - V_{pd}^2(\alpha_A\gamma_A + \alpha_B\gamma_B) + \gamma_A\gamma_B(\alpha_A\alpha_B - \epsilon(\mathbf{k})^2)} \\
&= \frac{\alpha_B - V_{pd}^2/\gamma_B}{\frac{V_{pd}^4}{\gamma_A\gamma_B} - V_{pd}^2\left(\frac{\alpha_A}{\gamma_B} + \frac{\alpha_B}{\gamma_A}\right) + \alpha_A\alpha_B - \epsilon(\mathbf{k})^2} \\
&= \frac{\zeta_{B,\sigma}}{\zeta_{A,\sigma}\zeta_{B,\sigma} - \epsilon(\mathbf{k})^2}
\end{aligned} \tag{3.39}$$

At this point it is necessary to observe that in the operators base used for the bipartite lattice structure, a special symmetry for the lattice functions holds. In particular:

$$\Sigma_{A,-\sigma}(i\omega_n) = \Sigma_{B,\sigma}(i\omega_n) = \Sigma_{\sigma}(i\omega_n) \tag{3.40}$$

and thus:

$$\zeta_{A,-\sigma} = \zeta_{B,\sigma} = \zeta_{\sigma} \quad .$$

This symmetry may be used to restore the ‘‘locality’’ of the equations and permits to deal with a given sublattice at time (*e.g.* A), greatly simplifying solution of the problem and the evaluation of the local Green’s functions.

The conduction band electrons local Green’s function  $G_{pp,\sigma}(i\omega_n)$  is thus obtained by integrating over all the momenta in the reduced Brillouin zone the expression in (3.39):

$$\begin{aligned}
G_{pp,\sigma}(i\omega_n) &= \zeta_{-\sigma} \int_{\mathbb{R}} d\varepsilon \frac{\rho_0(\varepsilon)}{\zeta_{\sigma}\zeta_{-\sigma} - \varepsilon} \\
&= \sqrt{\frac{\zeta_{-\sigma}}{\zeta_{\sigma}}} \check{D}(\sqrt{\zeta_{\sigma}\zeta_{-\sigma}})
\end{aligned} \tag{3.41}$$

The self-consistency condition finally takes the following expression:

$$\mathcal{G}_{0\sigma}^{-1}(i\omega_n) = i\omega_n + \mu_{\sigma} + \epsilon_d - \frac{V_{pd}^2}{i\omega_n + \mu_{\sigma} + \epsilon_p - t^2 G_{pp-\sigma}(i\omega_n)}$$

#### 3.4.2 AFM order and homogeneous magnetic field

The key aspect used in the previous section to derive DMFT equations for the antiferromagnetic order is the existence of a lattice symmetry related to the bipartite lattice structure, (cf. (3.40)). By the way, we are eventually interested in studying the effects of an homogeneous magnetic field on the antiferromagnetically ordered phase. This requires a slightly different implementation of the self-consistency, that makes no use of the previous symmetry. In this case the self-consistency condition will retain the full dependence of the local Green’s functions on the sublattices.

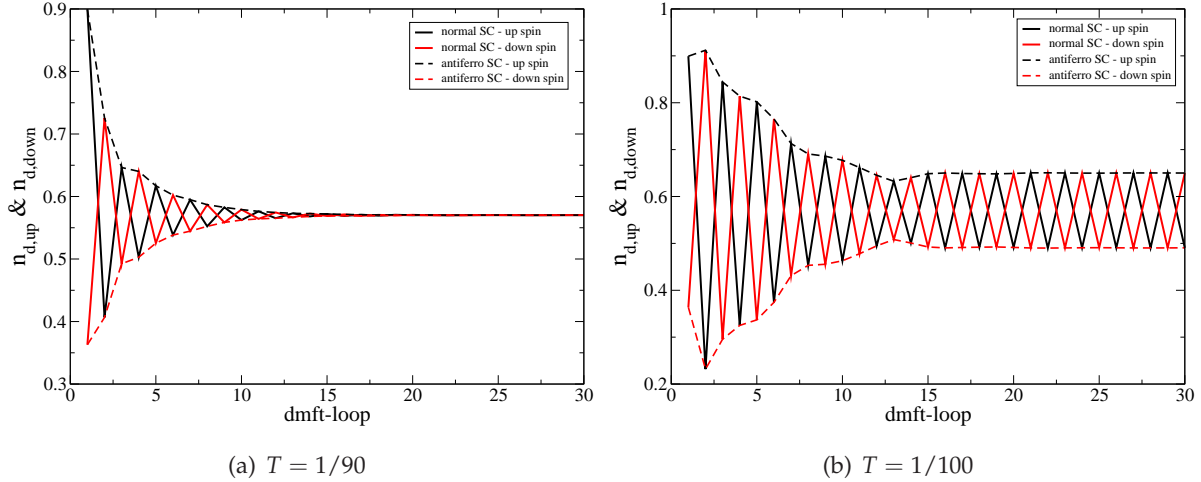


Figure 3.5:  $d$ -electron particle numbers per spin as a function of the DMFT loop. The two plots compare the behavior of this quantity as obtained with the two methods discussed in the text.

Let us consider an external homogeneous magnetic field  $B_{ext}$ , different from the staggered one introduced before. Then following the calculations illustrated in the previous section, it should become immediately clear that antiferromagnetic self-consistency condition in the presence of such an homogeneous magnetic field will consist in a set of two coupled equations for the Weiss fields (on each sublattice), namely:

$$\begin{aligned} \mathcal{G}_{0A\sigma}^{-1} &= i\omega_n + \bar{\mu}_{A\sigma} + \epsilon_d - \frac{V_{pd}^2}{i\omega_n + \bar{\mu}_{A\sigma} + \epsilon_p - t^2 G_{ppB\sigma}(i\omega_n)} \\ \mathcal{G}_{0B\sigma}^{-1} &= i\omega_n + \bar{\mu}_{B\sigma} + \epsilon_d - \frac{V_{pd}^2}{i\omega_n + \bar{\mu}_{B\sigma} + \epsilon_p - t^2 G_{ppA\sigma}(i\omega_n)} \end{aligned} \quad (3.42)$$

where the modified chemical potential now includes the coupling with the external magnetic field:  $\bar{\mu}_{A,B\sigma} = \mu_{A,B\sigma} + \sigma\mu_B B_{ext}/2$ .

At zero applied field the solutions corresponding to the different self-consistencies should agree. This is illustrated in Fig. 3.5, where the behavior of the  $d$ -orbital particle number per spin is reported as a function of the DMFT loop. Data are obtained with complete ED calculations at 1% doping respect the a Mott insulating state (cf. next chapter 3), at zero applied field. The figures compare, for two values of the temperature, the solution as obtained with the “antiferromagnetic self-consistency” derived in the previous section, with that obtained using the coupled “normal self-consistencies” in (3.42). In this latter case the solution oscillates due to exchanging roles of the  $A$  and  $B$  sublattices.

Upon increasing the strength of the external homogeneous magnetic field the solution is expected to fully polarize. For moderate values of it the competition of the antiferromagnetic and ferromagnetic orders may drive the system critical (cf. Sec. 5.7).

## 3.5 Conclusions

In this chapter we have introduced the main model used throughout the rest of this thesis, namely the periodic Anderson model. This is particularly suited for its application to the description of heavy fermion systems. The model describes orbital electrons forming a conduction band and hybridizing with a set of non-dispersive electrons also experiencing a local strong interaction. After having introduced the main model and discussed its physical meaning, we studied its solvable limits, namely the non-interacting limit  $U = 0$  and the atomic one, *i.e.* with  $t/U \rightarrow 0$ . The former limit permits us to gain physical insight about the formation of hybridized bands and the mass renormalization due this effect. The latter gave us useful insight on the model in the limit of strong correlation (*e.g.* physically corresponding to the Mott insulating phase) and about the structure of the Hilbert space of the model. In order to solve the model in some controlled approximation scheme we have derived the DMFT equations for the model using the cavity method and discussed the iterative scheme used to solve them. As an immediate application of the DMFT framework for the PAM we have illustrated the derivation of the internal energy expression. This will be used in the following to study some thermodynamic properties of the model. As a further step we extended the DMFT equation for the PAM to magnetically ordered phases. Beside the simple case of ferromagnetic order that does not require particular modification with respect to the paramagnetic case, we have presented with some details the derivation of the DMFT equation for the antiferromagnetic ordered phase. Later we have shown how to re-obtain the equations for the antiferromagnetic phase by making no a priori assumption on the symmetry of the phase. This lead us to a rather different formulation of the self-consistency condition, allowing us to handle the effect of an homogeneous external magnetic field on antiferromagnetic order.

# Mott insulators and metal-insulator transitions in the periodic Anderson model

## Contents

---

<b>4.1 PAM description of Mott insulators</b> . . . . .	<b>81</b>
4.1.1 Zaanen-Sawatzky-Allen diagram . . . . .	81
4.1.2 Mott insulator within PAM . . . . .	84
<b>4.2 Doping driven MIT</b> . . . . .	<b>94</b>
4.2.1 Type I metal insulator transition: $\delta < 0$ . . . . .	95
4.2.2 Type II metal insulator transition: $\delta > 0$ . . . . .	98
<b>4.3 Conclusions</b> . . . . .	<b>103</b>

---

Normal metals are usually very well described by a standard tight-binding picture. This is based on the independent particle approximation, for which electrons are treated as single particles (with renormalized parameters) moving in the periodic potential of the lattice ions. In this framework the electron-electron interactions are partially screened and the electrons can be described as travelling waves. The large overlap of the orbital wave functions give rise to the formation of broad energy bands, associated with a large value of the kinetic energy. In this picture metals are described as systems with partially filled valence bands, whereas insulators corresponds to completely filled (or empty) valence bands.

However, there are some materials for which the independent particle picture of itinerant electrons does not apply. These systems show rather narrow valence bands, due to the small overlap of *d*- or *f*-orbital wave functions. In this situation the electrons can spend most of

## 4. Mott insulators and metal-insulator transitions in the PAM

---

the time around a given lattice ions, feeling a strong electron-electron Coulomb interaction. In extreme cases the interaction can be so strong to lead to the localization of the electrons.

Thus, tuning the strength of the Coulomb interaction (respect to the kinetic energy) can transform a metallic system with an half-filled valence band into an insulator, *i.e.* a Mott metal-insulator transition.

The metal-insulator transition in strongly correlated systems remains one of the central problems of modern condensed matter physics. In the last 20 years the development of Dynamical Mean Field Theory (cf. Chap. 2) made possible to greatly increase the general knowledge about this phenomenon.

The minimal model generally used to tackle this problem is the Hubbard model [39, 40, 41]. This describes the competition between kinetic energy gain of conduction band electrons and local repulsion due to the strong Coulomb interaction. Despite its simplicity the solution of this model is not known, with the notable exception of the 1-dimensional case and few other exact results in two dimensions [55].

The DMFT solution of the Hubbard model has made possible the construction of a scenario for the Mott transition, today considered as a standard reference. At low temperatures and moderate interaction, the half-filled Mott insulator may be driven to a correlated metallic state through a first order transition [78, 76, 31]. This can occur as a function of the correlation strength, temperature or doping. The first order line ends at finite temperature in a critical point and the critical region can be described by a Ginzburg-Landau theory [48, 47].

Motivated by the applicability of the periodic Anderson model as a schematic model for both heavy fermion systems and transition metal oxides, we want here to investigate the PAM description of Mott insulating states and of the metal-insulator transitions. We shall see that DMFT solution of the PAM can capture the Mott insulating states in the different regimes where this may occur, in agreement with the Zaanen-Sawatzky-Allen (ZSA) diagram [103].

In this diagram the Mott insulating states are classified as either Mott-Hubbard or Charge-Transfer. The former regime applies to the early transition metal oxides, such as titanates and vanadates, but we shall demonstrate in the next chapter that it may also be relevant for heavy fermions. Instead, the CT regime applies to the cuprates, such as the high  $T_c$  superconductors, or manganites [42].

After having established the existence of the Mott insulating state, we shall focus on the analysis of the (paramagnetic) metal-insulator transitions occurring upon doping the insulator in the Mott-Hubbard regime. We will find that the nature of the transition driven by either positive or negative doping can have a different qualitative scenario with respect to the rather standard one of the Hubbard model. In particular we shall see that in negative doping case, dubbed **type I** transition, the scenario is indeed similar to the one realized in the Hubbard

model. In the other case, dubbed **type II**, the correlated metal can not be associated to the formation of a narrow Kondo-like resonance at the Fermi level and its mass does not diverge at the transition. Moreover our results indicate that this metal-insulator transition is of second order as no signs of coexistent solutions were observed. We shall argue that the correlated metallic state obtained in this latter case can be interpreted as a liquid of “Zhang-Rice” singlets [104]. The (anomalous) properties of this metallic state will be studied in the next chapter.

In the Sec. 4.1 of this chapter we present and discuss the Mott insulating state obtained from DMFT solution of PAM, in relation with the ZSA diagram. In Sec. 4.2 we discuss the general features of the metal insulator transition induced by doping the Mott-Hubbard “parent insulator”, with more details for the type II transition. Finally a summary of the results obtained in this chapter is given in Sec. 4.3

## 4.1 PAM description of Mott insulators

### 4.1.1 Zaanen-Sawatzky-Allen diagram

Systems formed by correlated  $d/f$ -orbital electrons and uncorrelated conduction band electrons, such as transition metal oxides or heavy fermions, can describe two different types of Mott (*i.e.* correlation induced) insulators. The classification of these insulators is based on the nature of the lowest energy excitation of the system. In the context of transition metal oxides this classification posed a long standing problem, that was tackled mainly using effective one-band model, such as Hubbard, obtaining wrong results about both the nature of the phases and the size of the gap. Taking into account a more sophisticated model, including a charge-transfer energy scale  $\Delta$ , Zaanen, Sawatzky and Allen [103] have derived a phase diagram  $U$ - $\Delta$  for the classification of the Mott insulating states and/or of the transition metal oxides. The ZSA diagram is shown in Fig. 4.1. It describes the different phases of the transition metal oxides, classifying the correlated insulators (unshaded regions) and the weakly correlated metallic states (colored regions). The nature of the different regions appearing in this diagram can be understood in terms of the relative values of the interaction  $U$  with respect to the charge-transfer energy  $\Delta$ . We shall now discuss briefly the nature of the Mott insulating regimes appearing in the ZSA diagram.

According to this diagram (cf. Fig. 4.1), and assuming the Fermi level lies above both the conduction band and the lower Hubbard band, a *Charge-Transfer* insulator is obtained in the regime  $U > \Delta$ . In this case the smallest excitation corresponds to the transfer of a charge from the conduction band to the upper Hubbard band. It is worth underlining that the insulating character of the solution is independent of the position of the lower Hubbard band, that can or can not be overlapped with the conduction band. This in fact would not change the nature

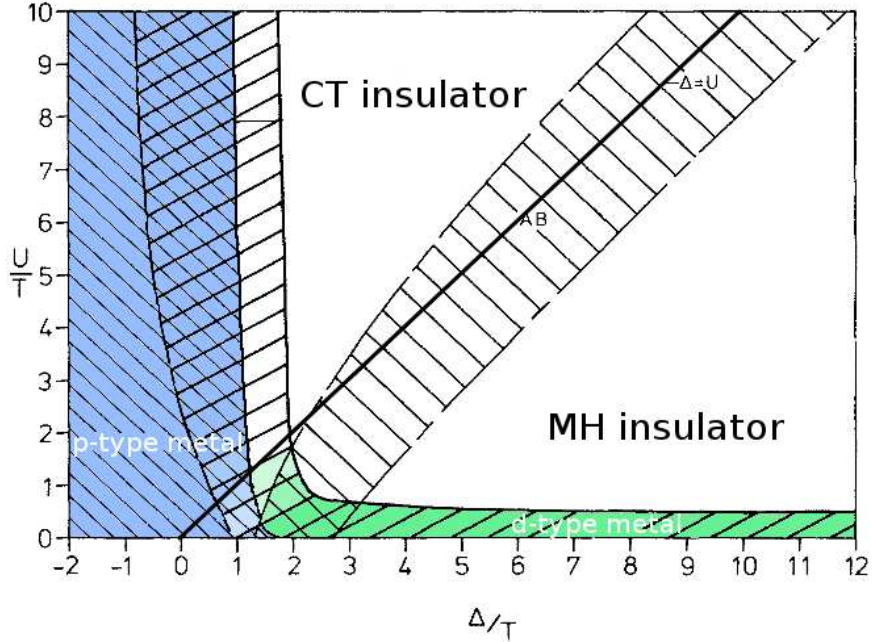


Figure 4.1: ZSA diagram. The Mott-Hubbard and Charge-Transfer insulating phases are explicitly indicated in the plot. The  $d$ -type metallic state (green) is indicated for small  $U$  and the  $p$ -type metal (blue) is indicated for small  $\Delta$

of the smallest energy gap, see Fig. 4.2. An estimate of this gap is obtained considering the excitation process of an electron from the conduction band to the  $d$ -band. This will correspond to the creation of a  $d$ -type quasi-particle and a  $p$ -type quasi-hole. Their delocalization will lead to a broadening of the corresponding levels. We indicate with  $W_d$  and  $W_p$  respectively the bandwidth of  $d$ -type and  $p$ -type excitation. The energy cost to pay to transfer a charge from conduction band to the upper Hubbard band, *i.e.* the activation energy, is thus:

$$A_e \sim \Delta - \frac{W_p + W_d}{2}$$

where  $\Delta > \Delta_0$  is the energy distance between the center of the conduction band and the upper Hubbard band. Late transition metal oxides and in particular the parent insulators of the high  $T_c$  superconductors (cuprates), are classified as charge-transfer insulators.

On the other hand the case  $U \lesssim \Delta$  describes a system where the Mott gap between the two Hubbard subbands is the smallest energy gap and thus the insulating state is dubbed *Mott-Hubbard*. In such systems the correlated Hubbard bands lie near the Fermi level and are flanked by wider bands. The energy cost of transferring a charge from the lower to the upper Hubbard bands is roughly:

$$A_e \sim U - W_d$$

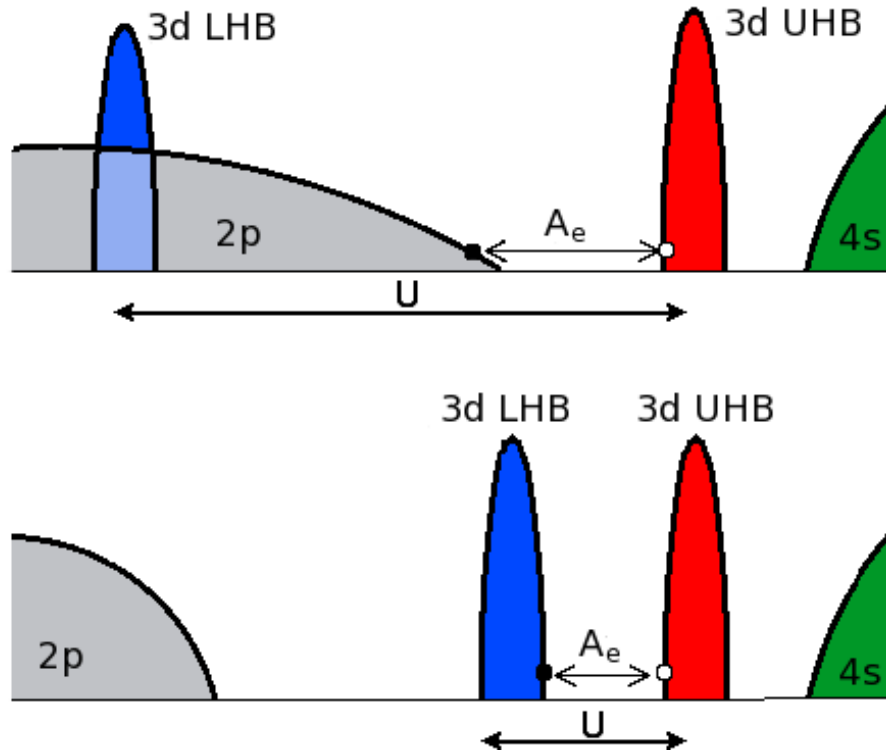


Figure 4.2: Schematic electronic structure for charge-transfer insulator (top) and Mott-Hubbard (bottom).  $A_e$  indicate the activation energy.

The MH insulating state is often associated with the oxides of the early transition metals, such as vanadates or titanates, but it is also adequate to describe certain heavy fermion compounds, as will be demonstrated in this thesis. A cartoon of the two different regimes is shown in Fig. 4.2.

It is important to stress that both MH and CT insulating states result from the strong correlation, *i.e.* Mott insulators. Analyzing the ZSA diagram in Fig. 4.1 it is possible to note the existence of two distinct metallic phases. One is the weakly correlated  $d$ -type metal, appearing for  $U < W_d$ . In this region the correlations are too small to open a Mott gap, independently of the position of the conduction band ( $\Delta$ ). The other is the  $p$ -type metallic state, appearing for  $\Delta < (W_p + W_d)/2$ . In this regime the overlap of the conduction band with upper Hubbard band prevents the formation of an insulating state for any value of the correlation. The qualitative analysis that led to the ZSA diagram is confirmed by experiments. In Fig. 4.3 we present some results obtained with X-ray photoemission technique on transition metal oxides all across the  $d$ -series, from  $Ti$  to  $Cu$ . Based on the correlation and charge-transfer values experimentally observed, the compounds have been placed in a  $U$ - $\Delta$  phase diagram very similar to the ZSA one. It is interesting to observe that many compounds believed to be of Mott-Hubbard

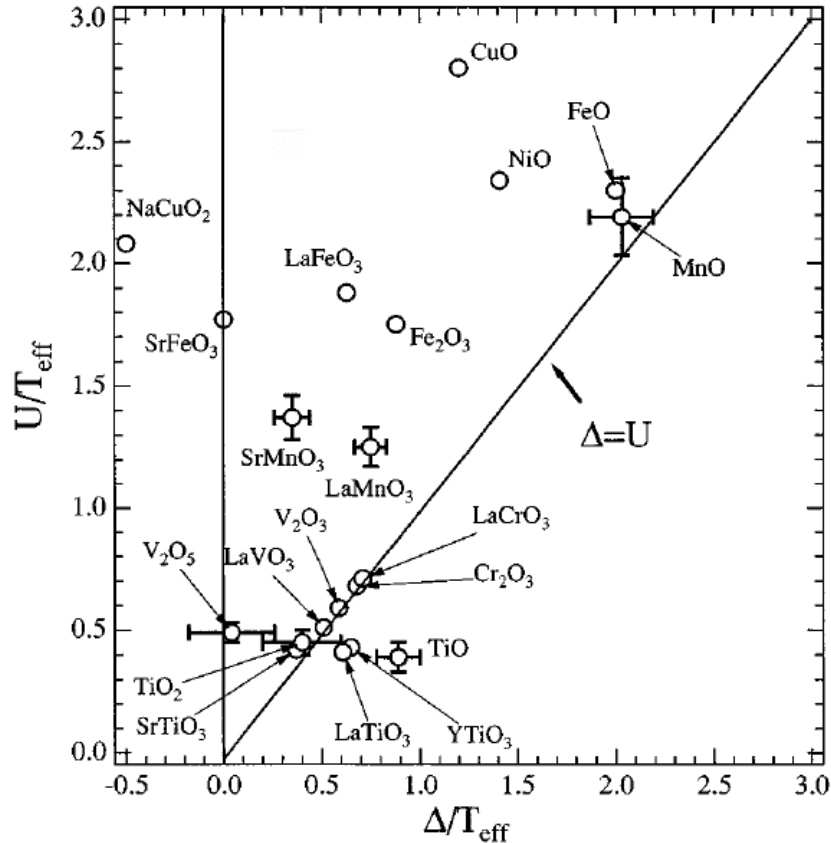


Figure 4.3:  $U$ - $\Delta$  diagram of oxides of transition metals in the  $d$ -orbital series from X-ray photoemission measurements, from [8]

type, appears more near to the separation line  $U = \Delta$ .

#### 4.1.2 Mott insulator within PAM

In this section we will show how the DMFT solution of the periodic Anderson model can describe the opening of a Mott gap at the Fermi level, *i.e.* the formation of a Mott insulator, for sufficiently large values of the correlation  $U$  and for different choices of the other model parameters. The results are roughly divided in two parts. The first is dedicated to the Mott-Hubbard (MH) regime while the second is dedicated to the Charge-Transfer (CT). We shall underline the existence, in the MH regime, of a symmetry of the model with respect to the sign of the charge-transfer energy  $\Delta = \epsilon_p - \epsilon_d$ . Fixed the position of the  $d$ -orbitals level  $\epsilon_d = 0$ , this symmetry will corresponds simply to a reflection of the position of the conduction band:

$$\epsilon_p \rightarrow -\epsilon_p$$

provided the value of the chemical potential  $\mu$  is adjusted to have particle-hole symmetry. We also recall that, due to the non-magnetic form of the interacting term, one expects for sufficiently large  $U$  the spectral densities to split into two Hubbard bands around the Fermi level.

#### 4.1.2.1 Mott-Hubbard regime

To begin with we present the formation of the Mott insulating state in the Mott-Hubbard regime. We first discuss the scenario obtained placing the conduction band below the Fermi level, with  $\Delta_0 = 1$ . With this choice the conditions for the MH regime are fulfilled already for an intermediate value of the correlation  $U$ . On the other hand, we do not get a vanishing effective hopping of the correlated electrons  $t_{eff} \sim V_{pd}^2/\Delta$ , cf. Chap. 3. The charge-transfer energy appearing in the previous expression for  $t_{eff}$  is  $\Delta \geq \Delta_0$ , where the equality holds only for vanishing hybridization and correlation. Thus a too large initial value for  $\Delta_0$  will lead to a too small (fixed the hybridization amplitude  $V_{pd}$ )  $t_{eff}$  that can be hard to handle numerically. The non-interacting model describes a system of two hybridized bands, one retaining most of the  $d$ -orbital character that we term *correlated* band and the other with almost only  $p$ -character that we term *uncorrelated* band. The chemical potential has been adjusted to keep the total filling of the narrow correlated band equal to one.

Now, we shall show how the expected scenario for the formation of the Mott gap borne out from the DMFT solution of the periodic Anderson model. In Fig. 4.4 we present the evolution of the spectral densities of both orbital electrons for an increasing value of the correlation and half-filling of the correlated band. This provide us direct insight on the nature of the solution. In the top panel of the figure we report the non interacting (analytic) solution for  $V_{pd} = 0.9$  and  $\mu = 0.529$ , corresponding to  $n_{tot} = 3$ . As can be appreciated from the figure, because of the strong hybridization the spectral weight is redistributed among the two orbitals, such that the correlated band lies near the Fermi level and bear most of the  $d$ -character, whereas the non correlated band lies at higher energy and retain most of the  $p$ -electrons character. Note that the center of mass of the uncorrelated band is no more placed at  $\omega = -1$ , as would for  $V_{pd} = 0$ , but is placed at  $\omega \gtrsim -2$ , such that  $\Delta \gtrsim 2 > \Delta_0$ .

The central panel of Fig. 4.4 report the weakly correlated solution obtained for  $U = 0.8$ . The correlated band shows the development of a three peak structure, formed by a large central resonance at the Fermi level, flanked by the two precursors of the Hubbard subbands. This is a clear DMFT hallmark of the correlated metallic nature of this state [31]. The DOS has been obtained by QMC calculation at  $T = 1/64$  and the analytic continuation has been performed with Maximum Entropy Method. Surprisingly the resonance and the Hubbard subbands are well visible also in the  $p$ -electron weight of the correlated band (red dashed line). This not expected result for the non-interacting conduction band electrons should be entirely attributed

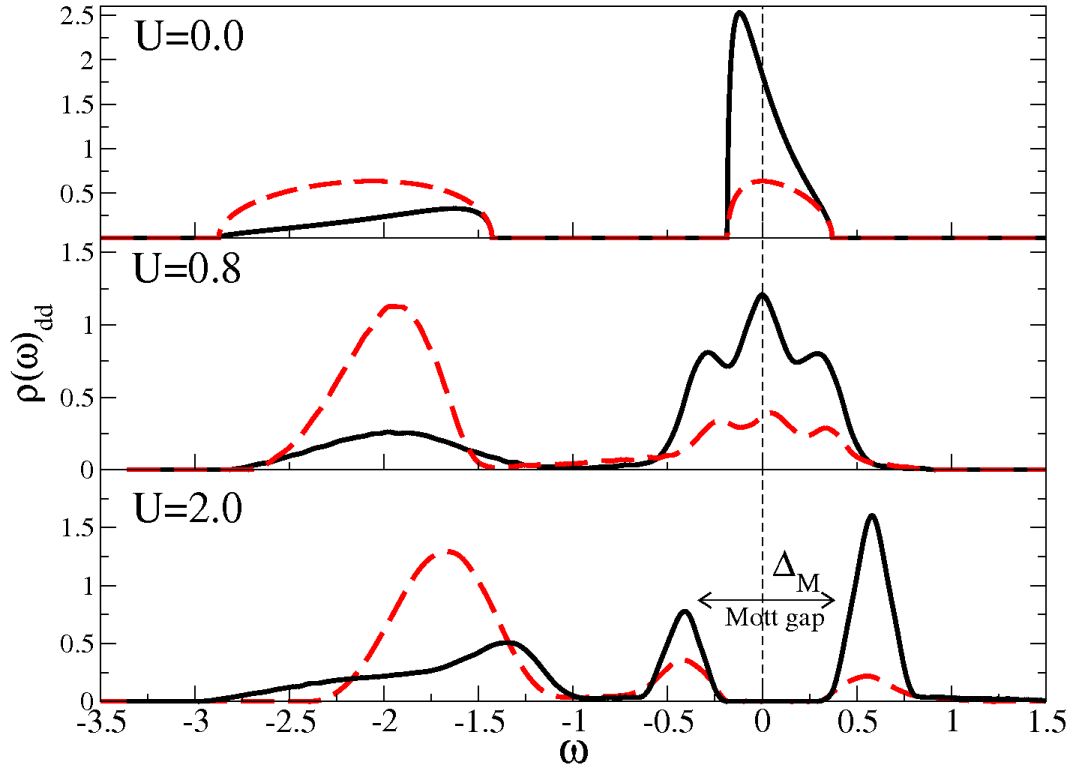


Figure 4.4: Evolution of the  $p$ - (dashed red line) and  $d$ -electron (solid black line) density of states as a function of increasing correlation. Data are from QMC at  $T = 1/64$ ,  $n_{tot} = 3$ ,  $V_{pd} = 0.9$ ,  $\Delta = 1$ ,  $\epsilon_p = -1$ . Top panel: non interacting DOS. Central panel: DOS for intermediate value of  $U$ . The correlated bands at the Fermi level develop the typical three peaks structure. Bottom panel: Opening of the Mott gap at the Fermi energy indicating the formation of Mott insulating state. The mismatch on the position and shape of the non-correlated band at large (negative) energy should be attributed to failure of MEM to describe high energy features.

to the strong hybridization with the correlated electrons at the  $d$ -sites. Thus, the  $p$ -electrons experience an indirect interaction, leading to the formation of structures that are in principle expected only for correlated electrons.

Finally in the bottom panel we show how the DMFT model solution capture the formation of a Mott gap at the Fermi energy when the interaction becomes larger than the effective hopping of the  $d$ -electron:  $U \gtrsim t_{eff}$ . In particular the figure reports the DOS for a value of the interaction  $U = 2$ . Note that as effect of hybridization,  $\Delta > \Delta_0$  but  $U \lesssim \Delta$ . As in the central panel of this figure, the results have been obtained with a QMC calculation at  $T = 1/64$ , supplemented by MEM to get real axis data.

In this Mott insulating state the DOS consists of three features. At low energy the plot shows the splitting of the correlated band around the Fermi level into two Hubbard bands, separated by a Mott gap of the order  $U$ . At higher (negative) energy the contribution of the non correlated band is still visible. On the same line of what has been found for the weak correlated solution we observe that, despite the  $p$ -electrons are non-interacting, the strong hybridization with the correlated  $d$ -electrons induce a splitting in the  $p$ -character of the correlated band DOS. Thus, the systems shows a *Mott insulating state in both orbitals* (no Orbital Selective Mott transition).

We would now comment shortly on the validity of the Maximum Entropy Method. This method is widely used to perform analytic continuation from imaginary axis data to real axis, that is where the observables have a physical meaning. MEM being based on probabilistic inference is not able to reproduce “quantitatively” all the details of the solution, but has a great qualitative validity [33]. Moreover the MEM gives a quite poor description of the high energy features, so the position of the non correlated band is not always efficiently described, as it is evident by comparing the solutions in the central and bottom panel of Fig. 4.4 with the analytic solution at  $U = 0$ . Nevertheless, this method is able to capture the large difference in the spectral weight distribution as well as the formation of substructures induced by correlation, that are both of physical importance.

For completeness and to further stress the generality of this scenario about the formation of Mott insulating state within the PAM, we show the results for the evolution of the DOS in the (specular) symmetric regime. This latter has been obtained by inverting the position of the conduction band and by adjusting the value of the chemical potential  $\mu$  such as to have an half-filled correlated band, necessary condition for the Mott insulator to form. In the top panel of Fig. 4.5 we present the DOS for the non interacting solution of the model. As can be appreciated by comparing with the solution in the top panel of Fig. 4.4, the inversion of the position of the uncorrelated band does not affects the spectral weight distribution among the two orbitals. In the weakly correlated regime (central panel) the characteristic three peaks structure appears, similar to that observed in the symmetric case already discussed. A narrow resonance shows

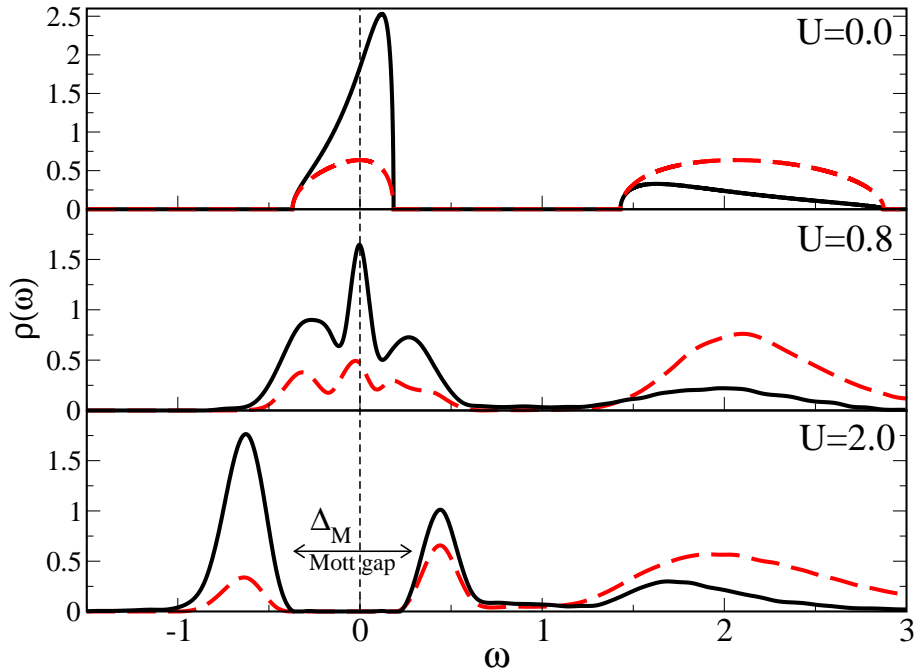


Figure 4.5: Evolution of the  $p$ - (dashed red line) and  $d$ -electron (solid black line) density of states as a function of increasing correlation. Data are from QMC at  $T = 1/64$ ,  $n_{tot} = 1$ ,  $V_{pd} = 0.9$ ,  $\Delta = 1$ ,  $\epsilon_p = 1$ . Top panel: non interacting DOS. Central panel: DOS for intermediate value of  $U$ . The correlated bands at the Fermi level develop the typical three peaks structure. Bottom panel: opening of the Mott gap at the Fermi energy for large value of the correlation, indicating the formation of Mott insulating state.

up at the Fermi level, flanked by two substructures that will develop into the Hubbard bands. The eventual mismatches between the figures shown here and those obtained in the symmetric regime for  $\epsilon_p < 0$  (Fig. 4.4), should be related to the use of Maximum Entropy Method. Finally in the bottom panel of Fig. 4.5 we observe how further increasing the correlation produce the opening of a Mott gap at the Fermi level. As before the DOS in this plot has been obtained for  $U = 2$ . Again the figure shows the existence of three main features to be associated to the lower Hubbard band, for  $\omega \simeq -0.5$ , to the upper Hubbard band for  $\omega \simeq 0.5$  and to the uncorrelated band for  $1 \lesssim \omega \lesssim 3$ .

To overcome the limitations of the MEM and to better clarify the insulating nature of the model solution obtained for large values of the correlation (cf Fig. 4.4 and Fig. 4.5), we shall now characterize the insulating state from the behavior of the imaginary part of the one particle Green's functions for both  $d$ - and  $p$ -orbital electrons. In Fig. 4.6(a) we present data from the exact solution at  $U = 0$  and  $T = 0$  of the model, illustrating the metallic nature of the non-interacting solution. This is signalled by the finite intercepts of both  $\text{Im}G_{pp}(i\omega_n)$  and

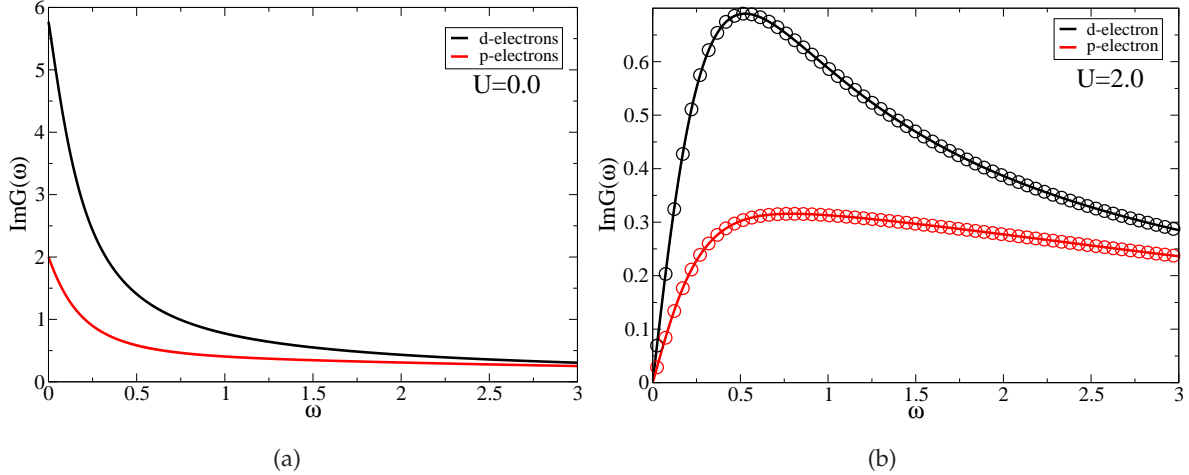


Figure 4.6: Behavior of the imaginary part of the Green's function on Matsubara axis for both electronic species. Red and black lines correspond to  $p$ - and  $d$ -electrons respectively. (a) illustrate the metallic character of the solution at  $U = 0$ ,  $T = 0$ , (b) shows that the existence of an insulating solution for large correlation. Data are obtained with QMC at  $T = 1/128$  ( $\circ$  and  $\circ$  for  $d$ - and  $p$ -electrons resp.) and DMRG at  $T = 0$  for the same model parameters as in Fig. 4.4

$\text{Im}G_{dd}(i\omega_n)$  at zero frequency, corresponding to the density of states at the Fermi level. On the other hand, Fig. 4.6(b) shows the vanishing behavior of the same functions for large value of the correlation. In this plot a correlation  $U = 2$  has been used, corresponding to the solution in the bottom panel of Fig. 4.4. Data are obtained from both QMC at  $T = 1/128$  (circles) and DMRG at  $T = 0$ . These latter are plotted on a continuous set of frequencies (solid lines). The excellent agreement between the two methods, at finite and zero temperatures, underline the correctness of our solutions.

Finally to remark the insulating character of the model solutions illustrated in the previous paragraph, we present the behavior of the total filling  $n_{tot} = n_p + n_d$  as a function of the chemical potential. The goal is to show that in correspondence with the discussed Mott insulating states, a plateau appears in the  $n_{tot}(\mu)$  curves at an odd integer value. Mott-Hubbard insulating state has been obtained adjusting the chemical potential to keep fixed the total filling at  $n_{tot} = 3$  (or  $n_{tot} = 1$ ), that is the half-filling of the correlated band. Varying the chemical potential inside the spectral gap does not produce any change in the occupation number. The presence of such a region of incompressible states, *i.e.* with  $\kappa = \partial n / \partial \mu = 0$ , is illustrated in Fig. 4.7. This plot report the behavior of the total filling in the non interacting limit (black lines) and for a large value of the correlation  $U = 2$  (red open symbols). The region of variation of the chemical potential does not cover the full support of the DOS, but it is restricted to an sufficiently large interval around the Mott gap. The two plots show how the correlation induces the formation

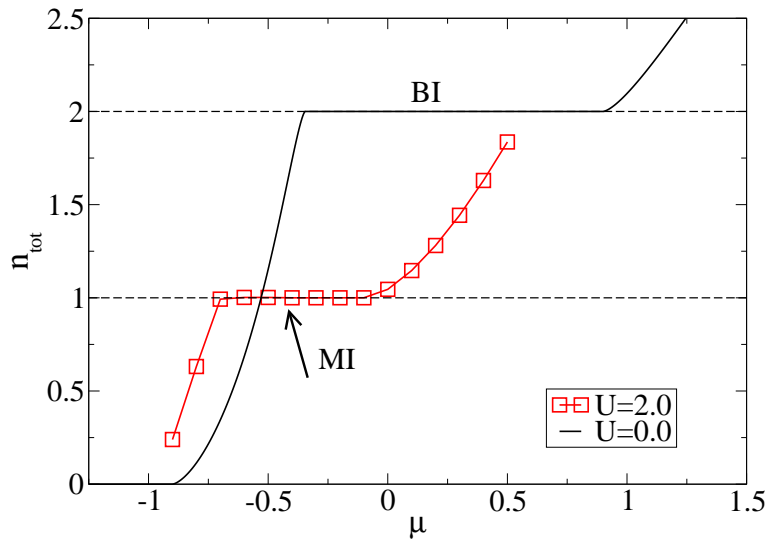
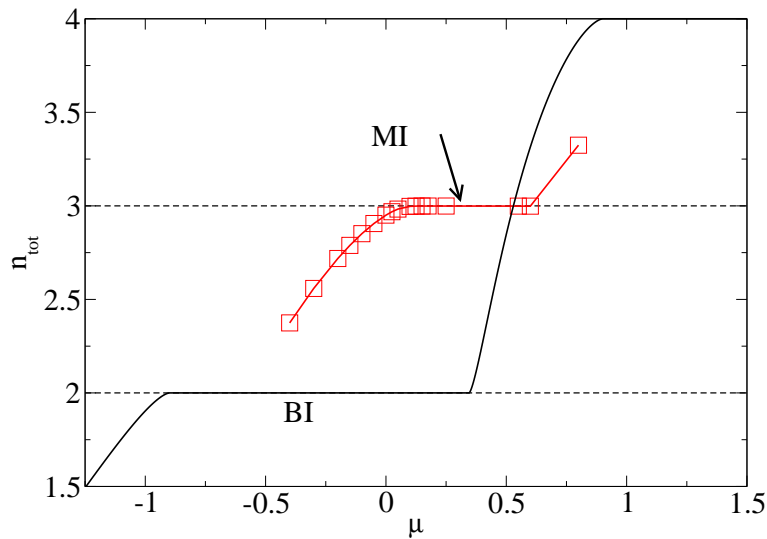

 (a)  $\epsilon_p = 1$ 

 (b)  $\epsilon_p = -1$ 

Figure 4.7: Formation of the Mott insulating state from the behavior of the total number of particles as a function of the chemical potential, in a small regime around the Mott gap. The two panels compare the solution for two values of the correlation  $U = 0$  (black line),  $U = 2$  ( $\square$ ). (a) Non-interacting solution goes from the completely empty band  $n_{tot} = 0$  up to the band insulator (BI) at  $n_{tot} = 2$ , corresponding to filling up the correlated band. For large  $U$  this band opens a gap as illustrated by the red line and symbols (MI). (b) Non-interacting solution goes from band insulator  $n_{tot} = 2$  to the completely filled regime  $n_{tot} = 4$ . The large value of  $U$  leads to the formation of a plateau at  $n_{tot} = 3$  (MI).

of a region of incompressible states at an integer odd value of the total filling, corresponding to the half-filling of the correlated band, *i.e.*  $n_{tot} = 1$  or  $n_{tot} = 3$  respectively for  $\epsilon_p > 0$  or  $\epsilon_p < 0$ . At the boundaries of the two plots the band insulating states, corresponding to completely filled or empty bands ( $n_{tot} = 0, 2, 4$ ), are visible.

#### 4.1.2.2 Charge-Transfer regime

In this work we shall focus mainly on the MH regime, motivated by its application to the description of heavy fermion systems. Nevertheless, we will show in this section how the DMFT model solution of the PAM capture the formation of a Charge-Transfer insulator. This could further underline the goodness and the generality of the model solution. Accordingly to the previous discussion about the classification of the Mott insulating states in the TMO, we should set  $\Delta < U$  in order to place the model in the CT regime (cf Sec. 4.1). To this end we fixed  $\Delta_0 = 0.25$  and  $V_{pd} = 0.5$ . This value of the bare charge-transfer energy reveals to be sufficiently large to place the system out-side the  $p$ -type metallic phase, cf. Fig. 4.1. On the other hand, in this regime  $U$  should overcome the value of the charge-transfer energy  $\Delta$ , so to exclude numerical difficulties deriving from a too large value of  $U$ , we have chosen  $\Delta_0$  small enough.

In Fig. 4.8 we demonstrate the formation of a charge-transfer insulating state by means of the evolution of the DOS as a function of increasing correlation. In the top panel we reported the spectral densities of both  $p$ - and  $d$ -electrons, corresponding to the parameters discussed above and in the non interacting limit. The solution has been obtained at  $T = 0$  and for a total filling  $n_{tot} = 3$ , corresponding to the half-filling of the correlated band (with the same meaning discussed in the previous section). The hybridization between the two electron orbitals lead to the formation of two bands, separated by the indirect gap  $\Delta \simeq 1 > \Delta_0$ . In the bottom panel we present the DOS for a large value of the correlation, namely  $U = 3$ , large enough to exceed the charge-transfer gap. The solution has been obtained using ED technique at zero temperature. Its validity has been benchmarked against similar calculation performed with ED/DMRG, complete ED and QMC. ED and ED/DMRG methods have been used to overcome difficulties arising from using MEM in regimes with important features appearing at high energy. The solution shows the existence of a spectral gap at the Fermi level, similar to that already observed in the Mott-Hubbard case. Here, nevertheless, the gap is no more placed between the two high features corresponding to the Hubbard bands, but rather between the upper Hubbard band and the wide feature corresponding to the non correlated band. This distance corresponds to the charge-transfer gap. Both  $p$ - and  $d$ -orbital electrons density of states present three main structures: at large negative energy the contribution of the lower Hubbard band is visible with prevalently  $d$ -electron character. This feature has been pushed away by

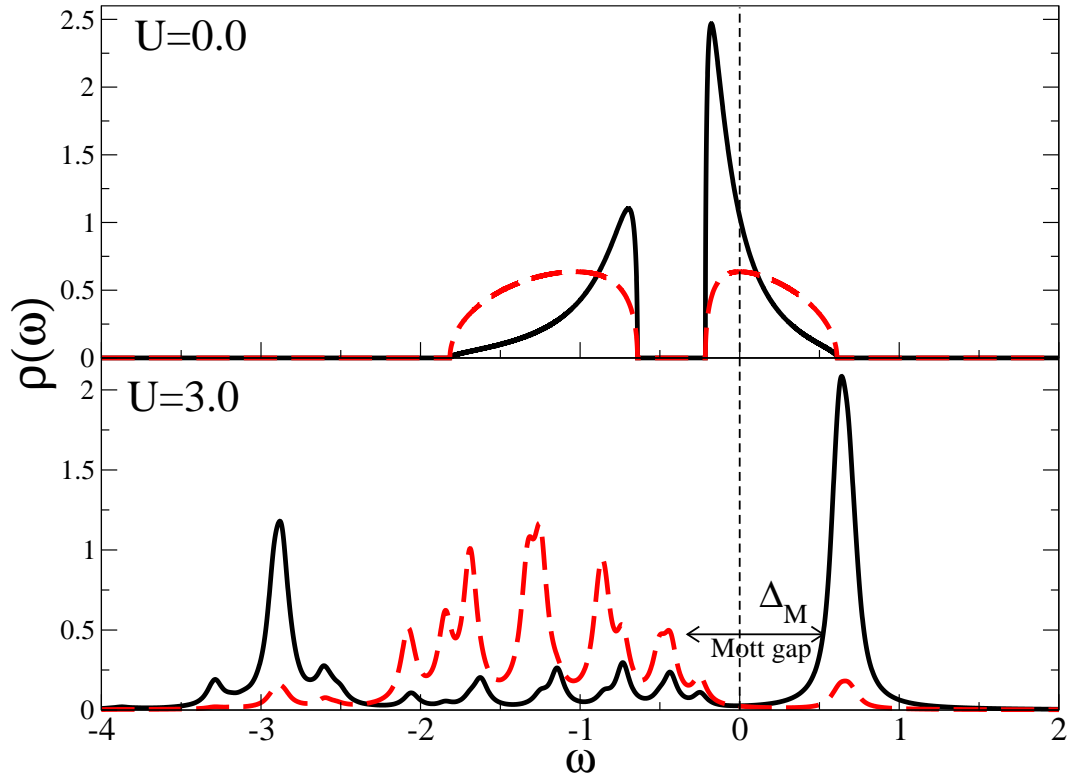


Figure 4.8: Opening of the Mott gap in the charge transfer regime of the PAM, from the evolution of the DOS. Top panel: non interacting DOS of the two orbitals  $p$  (red dashed line) and  $d$  (solid black line), obtained from analytic solution for  $\Delta = 0.25$ ,  $V_{pd} = 0.5$ ,  $n_{tot} = 3$ . Bottom panel:  $p$ - and  $d$ -electron DOS for  $U = 3$  and all other parameters as in top panel. Data are obtained from ED-DMRG calculations at  $T = 0$  and thus the curves show the typical structure with poles due to finite size effect. Poles are broaden with Lorentzian function and indicate qualitatively the positions of the bands.

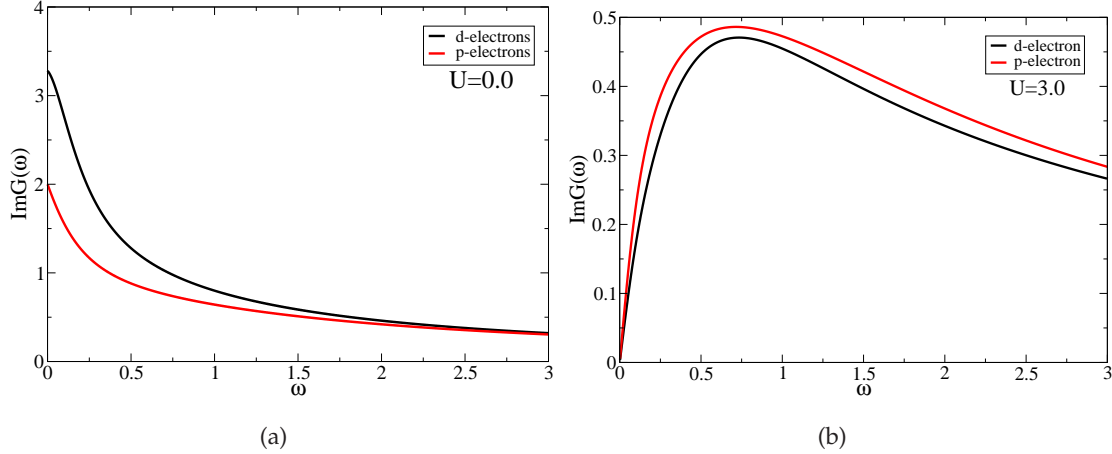


Figure 4.9: Correlation driven metal-insulator transition illustrated with the imaginary part of the Green's function of  $p$ - (red line) and  $d$ -electrons (black line). Model parameters are fixed as in the previous figure. (a)  $\text{Im}G_{pp}(i\omega_n)$  and  $\text{Im}G_{dd}(i\omega_n)$  in the non interacting case. (b) Same functions for a large value of the correlation  $U = 3$ . Data are from DMRG calculation at  $T = 0$  and show the onset of a Mott insulating state in the charge-transfer regime.

the large value of the correlation. At intermediate energies ( $-2 \lesssim \omega \lesssim 0$ ) it is possible to distinguish the contribution of the uncorrelated band, the spectral weight of which is remarkably large in the  $p$ -projection as compared to the  $d$ -electron one. Finally above the Fermi level it is possible to see the contribution of the upper Hubbard band with mainly  $d$ -character. We should also mention that the apparent multiple peaks structures of the main three features appearing in the DOS are merely due to the discreteness of the finite number of sites used to describe the environment in the ED technique. Nevertheless, the splitting of the narrow band at the Fermi energy with the consequent opening of a large Mott gap  $\Delta_M$  is clearly observed.

On the same line of what has been done before for the MH regime, we shall underline the insulating nature of the CT regime by means of the imaginary part of the Green's functions  $G_{pp}(i\omega_n)$  and  $G_{dd}(i\omega_n)$ . In Fig. 4.9(a) we present the behavior of these two functions for the non interacting solution of the model at  $T = 0$ . The metallic character is evident from the finite intercept of the functions, equal to  $\rho_{pp}(0)$  and  $\rho_{dd}(0)$ . On the other hand, in Fig. 4.9(b) we show the behavior of the same functions for  $U = 3$  and zero temperature, from DMRG calculations. The insulating character of the solution is evident by the vanishing behavior of the two imaginary parts of the Green's functions  $\text{Im}G_{pp}(i\omega_n)$ ,  $\text{Im}G_{dd}(i\omega_n)$ .

#### 4.1.2.3 Mott gap size

The size of the Mott gap in the Mott-Hubbard regime is naively expected of be of order  $U$ , since it should mostly reflect the energetic cost to doubly occupy the  $d$  orbitals. However, our results

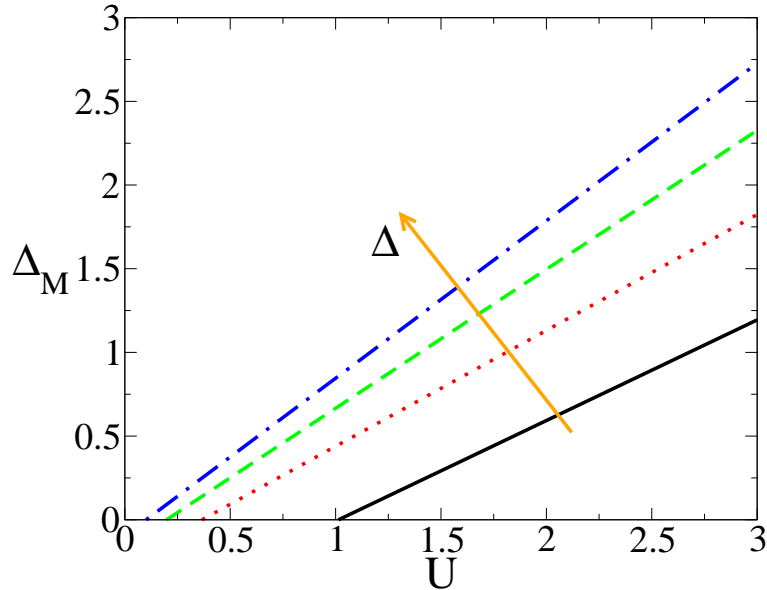


Figure 4.10: Size of the Mott gap  $\Delta_M$  as a function of correlation  $U$ , for several different position of the conduction band:  $\epsilon_p = -1$  (black line),  $-2$  (red dotted line),  $-3$  (green dashed line),  $-6$  (blue dot-dashed line), from bottom to top as indicated by the orange arrow.

show that the Mott gap  $\Delta_M$  may be substantially smaller than the bare value  $U$ . In Fig. 4.10 we plot  $\Delta_M$  as a function of  $U$ , for several values of the bare position of the  $p$ -band  $\epsilon_p$ , which amount to increase the charge transfer energy  $\Delta_0$ . As the energy of the  $p$ -orbitals is shifted down to larger (negative) energies, the effective bandwidth of the narrow band at the Fermi energy decreases. In addition, the  $p$ -electron band becomes essentially full with  $n_p \rightarrow 2$  as  $\epsilon_p \rightarrow -\infty$  (and keeping  $t_{pd}$  fixed). This implies a decreasing mixed-valence character of the electrons at the Fermi energy. In this limit the size of the Mott gap approaches the “bare” value  $\Delta_M \approx U$ . However, it is interesting to observe that the smaller values of  $\epsilon_p$  lead to a substantial renormalization of the size of the expected Mott gap. This effect can be thought as due to an effective screening the  $p$ -electrons provide, or, in more naive terms, because the electrons only “feel” the repulsive term  $U$  during the time they spend on the  $d$ -orbital, but not when they visit the  $p$  site. So as the mixed  $p$ - $d$  character is increased, the effect of the  $U$  is renormalized downwards.

## 4.2 Doping driven MIT

So far we have discussed the PAM description of different Mott insulating state. In particular we have seen in the MH regime that the model solution is characterized, similarly to the Hubbard model, by the presence of two incoherent Hubbard bands above and below the Fermi

energy. However, unlike Hubbard model, the size of the gap, *i.e.* the separation between the Hubbard bands, may be substantially smaller than  $U$  if the hybridization is large. In this section we shall study the metal-insulator transition obtained by doping the “parent” Mott insulator, with the introduction of a given finite amount of either hole- or electron-type charges. Upon doping, the insulating state will be destroyed in favor of a correlated metallic state. To remain on a general ground and to be independent from the symmetry discussed above in section 4.1, we shall adopt the following definition of the doping parameter:

$$\delta = \begin{cases} n_{tot} - 1 & \text{if } \epsilon_p > 0 \\ 3 - n_{tot} & \text{if } \epsilon_p < 0 \end{cases}$$

As was already reported in [91], we will show that the Mott transition of type I ( $\delta < 0$ ) has a qualitatively different scenario with respect to the type II transition ( $\delta > 0$ ). The former will essentially reproduce the known scenario for the Mott MIT that is realized in the DMFT solution of one band Hubbard model [31, 49, 26, 100]. This was somehow not surprising, since we have tuned the parameters of the model to be in a regime where the identification of the low energy physics of the PAM and the one band Hubbard model was expected to hold. However we shall see that the type II metal insulator transition shows a qualitatively different scenario. In particular we shall demonstrate that this transition has a second order character and that it is nearly temperature independent, at least down to values of the temperatures of the order  $T \lesssim 10^{-3}D$ , where  $D = 2t$  is the bare half-bandwidth of the conduction band fixing the energy unit of the problem. The origin of this quite unexpected result is associated to the tendency of the system, in the  $\delta > 0$  regime, to form local singlets, reminiscent of the celebrated Zhang-Rice singlets introduced in the context of the high- $T_c$  superconductors [104]. In the following we will briefly review the results for the type I transition and will describe with more details the scenario for type II metal insulator transition. This latter in fact provide the framework for the development of a new approach to heavy fermion non-Fermi liquid phase, that will be the subject of the next part of this thesis.

#### 4.2.1 Type I metal insulator transition: $\delta < 0$

We will describe in this section the metal insulator transition induced by negative doping the Mott insulating state. We shall demonstrate that the scenario offered by this transition is qualitatively identical as that of the single band Hubbard model. To gain some direct insights in the physics of this transition, we first study the change in the density of states upon tiny negative doping the Mott insulating state. In Fig. 4.12 we report the DOS of the two orbital electrons for  $\mu = 1.234$ , corresponding to a doping of about  $\delta < 5\%$ . The data were obtained from a high precision QMC calculation at  $T = 1/80$  and are analytically continued on the real axis

#### 4. Mott insulators and metal-insulator transitions in the PAM

---

with MEM. Furthermore the results have been benchmarked with finite temperature ED calculations and with zero temperature ED/DMRG, finding in both cases a remarkable agreement. The figure illustrates the presence of a narrow resonance at the Fermi level associated with the formation of quasi-particles. The peak appears at the edge of the upper Hubbard band and it is well separated from the lower. Indeed, we have observed that the formation of this quasiparticle peak requires a rather small temperature, that can be interpreted in the DMFT framework as the temperature scale for the onset of the local Kondo screening. The spectral weight fraction carried by the coherent quasi-particle peak is about  $|\delta|$  and it is proportional to the renormalization constant  $Z$ . This latter can be obtained from the imaginary part of the self-energy and indicates an enhancement of the effective mass with respect to its bare value. The strong renormalization of this quasi-particles is confirmed by both the width of the resonance at the Fermi level and by the behavior of the renormalization constant  $Z$  (not shown). In the same figure it is possible to appreciate the huge difference in the spectral distribution of the quasi-particle weight among the two electron species. The  $d$ -electron DOS bears most of the spectral intensity while the other electron orbital has a reduced weight. This is interpreted as a first hint of the fact that the correlated  $d$ -electrons “drive” the transitions, as we will explain in the following.

The nature of the transition has been characterized by studying the behavior of the particle number as a function of the chemical potential,  $n(\mu)$ . We have shown the existence of a region of coexistence of the insulating and metallic solutions. At finite temperature the model shows a discontinuity in the occupation and in other quantities such as double occupancy or moment formation. This is interpreted as a clear signal of the first order character of the Mott transition. In the inset of Fig. 4.12 we illustrate this point through the analysis of the  $d$ -orbital occupation  $n_d = G_{dd}(\tau \rightarrow 0^+)$ . The figure shows that the insulating solution (open black circles) can be continued till a critical value of the chemical potential is reached. Here a sudden breakdown of the solution appears, with a jump to the same metallic solution one could get for this value of  $\mu$ . On the other hand we have observed that the metallic solution can be continued till a different critical value of chemical potential. Here the solution becomes unstable, in favor of the insulating state, with a rather small jump in the particle occupation.

This scenario for the metal insulator transition is qualitatively similar to that of the Hubbard model. To understand the physical origin of this behavior one should consider that the  $p$ -orbitals are, in this negative doped regime, almost completely occupied (with either particles or holes), while the correlated orbitals are nearly half-filled  $n_d \sim 1$ . This situation however does not prevent the  $d$ -electrons to delocalize by higher order process of superexchange type, permitted by hybridization with the conduction band. This leads to the formation of a strong antiferromagnetic correlation between neighboring correlated electrons and to the onset of Kondo

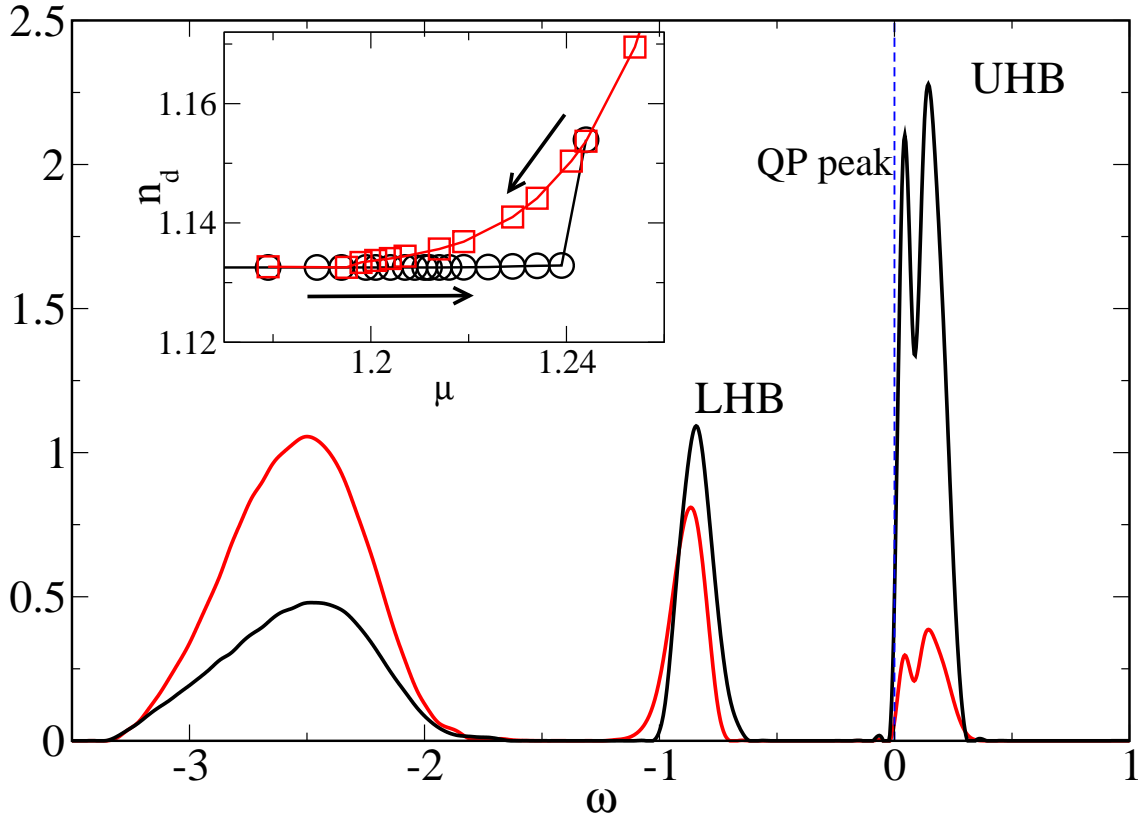


Figure 4.11: Density of states of  $p$ - and  $d$ -electrons (red and black solid line resp.) for  $U = 2$ ,  $\Delta = 1$ ,  $t_{pd} = 0.9$  and  $T = 1/64$ , as obtained from QMC calculations. The value of chemical potential is  $\mu = 1.234$  and corresponds to tiny negative doping, *i.e.* particle doping. Inset: number of  $d$ -electrons as a function of the chemical potential. The hysteresis loop indicated by the arrows corresponds to the coexistence of the metallic ( $\square$ ) and insulating ( $\circ$ ) solutions.

screening process involving  $d$ -orbital electrons only. Thus the physical mechanism driving the Mott transition is almost identical to what can be observed in the DMFT solution of the one band Hubbard model. Namely a one correlated band of electron with strong antiferromagnetic correlations between local moments ( $J \simeq t_{eff}^2/U$ ), undergoing a scattering process that can lead, in suitable conditions, to the local moment compensation (Kondo effect), giving rise to a metallic state.

### 4.2.2 Type II metal insulator transition: $\delta > 0$

This section is devoted to the study of the type II metal insulator transition. Previously we have shown the existence of a Mott transition, driven by negative doping and having the same characteristics as the Hubbard model scenario. Thus, based on the often implicit assumption that the Hubbard model describes the low energy physics of the periodic Anderson model, one can naively expect a particle-hole symmetry to hold. We shall demonstrate in this section that in fact this is not generally the case [91], and we will discuss the physical reasons behind this rather surprising result.

Making a parallel with the previous section, we shall start by illustrating the metal insulator transition from the point of view of density of states in the tiny positive doping regime. In Fig. 4.12 we present our results from high quality QMC calculations, supplemented by MEM based analytic continuation, at a temperature  $T = 1/64$ , keeping fixed all the other model parameters except the chemical potential. The figure shows the  $d$ - and  $p$ -electrons DOS for a doping of the order  $\delta \simeq 5\%$ , corresponding to  $\mu \simeq 0.53$ . The DOS is characterized by the formation of a strong and narrow resonance at the Fermi level, flanking the lower Hubbard band. The first striking difference with respect to the negative doping scenario is the relevance of the  $p$ -electron spectral weight compared to the  $d$ -electron one. The non correlated orbital shows the formation of a rather strong resonance, with roughly half the weight of the corresponding peak in the  $d$ -electron DOS. This directly suggest that the solution have an important mixed valence character, as will be further stressed in the following of this thesis. A second remark concerns the width of this resonance that is much more important than what has been observed in the negative doped case. This hints a completely different origin of the resonance and the fact that the underlying electronic excitations are not strongly renormalized. A further comment can be made about the temperature dependence of this resonance. Contrary to what happen in the negative doped case, where the quasiparticle peak appears at temperatures smaller than a coherence scale associated with the local Kondo screening, the present resonance appears already for large temperatures of the order  $T \lesssim V_{pd}^2/\Delta$ , and remain basically unchanged throughout the studied temperature range.

Useful insights about the nature of the transition are obtained by studying the behavior of

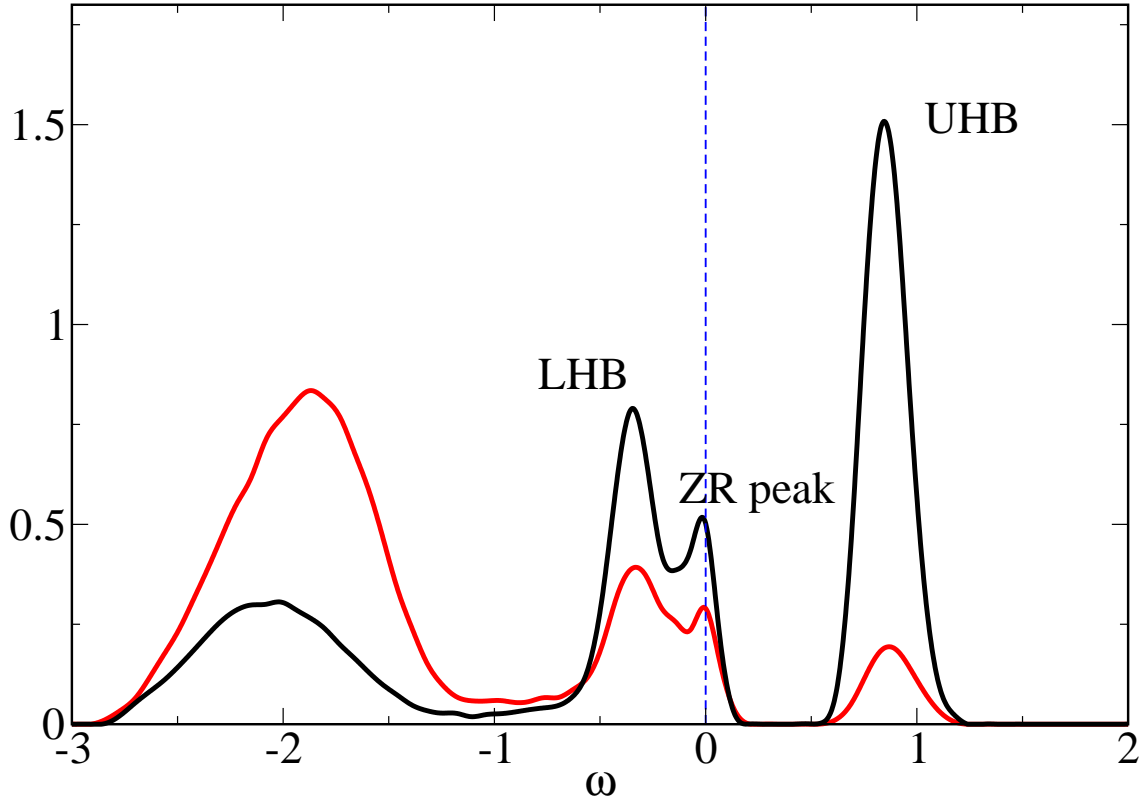


Figure 4.12: Density of states of  $p$ - and  $d$ -electrons (red and black solid line resp.) for  $U = 2$ ,  $\Delta = 1$ ,  $t_{pd} = 0.9$ . Data are obtained from QMC calculations at  $T = 1/64$  and analytically continued on the real axis with Maximum Entropy Method. Chemical potential is fixed to  $\mu = 0.529$ , corresponding to tiny positive doping, *i.e.* doping with holes, of about  $\delta \simeq 0.05$ . The central peak (at the Fermi level) corresponds to the formation of Zhang-Rice like singlets. This is flanked by Hubbard bands and at high (negative) energy the uncorrelated band is visible.

the number of particles as a function of both temperature and chemical potential. Motivated by the presence of an hysteresis loop in the negative doping case, we have first performed a systematic analysis of the variation of the particle occupation, as a function of chemical potential at a step by step decreasing temperature. Starting from the insulating phase and continuing the solution well deep the metallic phase and viceversa, we did not find any trace of coexistent solution neither with QMC nor with ED, down to temperatures of the order  $\beta = 1/128$ , and with ED/DMRG, thus formally at  $T = 0$ . Instead the number of particle has shown to be nearly temperature independent as a function of chemical potential in this regime. This is illustrated in Fig. 4.13. In the main plot we present a set of different data, all obtained from high quality QMC calculations and successively benchmarked with complete ED calculations. The data were obtained for several decreasing temperatures, in a range of positive doping covering three order of magnitudes. The results show the independence of the value of the particle number from the temperature. Data obtained at different temperatures all lie on a single curve (black dashed line) and accumulate, at vanishing doping, at the insulating value indicated by the dashed-dotted red line. It is worth to note the high stability of the data, of high importance considered the statistical nature of QMC based calculations. In order to better compare the results for the particle number in this regime with what has been found for the negative doping regime, we present in the inset of Fig. 4.13 the  $d$ -orbital occupation as a function of the chemical potential in a wide range of variation across the Mott insulator and for three different temperatures. The curve  $n(\mu)$  has a rather strong temperature dependence of the negative doping side (right) compared to the weak or null dependence in the positive doping side (left).

Up to our current numerical capacity we are led to the conclusion that the metal-insulator transition driven by positive doping in the Mott-Hubbard regime is a quantum phase transition, *i.e.* occurring through a  $T = 0$  and zero doping Mott point. Therefore the  $\delta > 0$  metal insulator transition has a qualitatively different scenario with respect to the  $\delta < 0$  case, and, consequently, also qualitatively different from the Hubbard model scenario.

The physical origin underlying the existence of such a new and different scenario for the Mott transition can be understood analyzing the moment-moment correlation function between the two orbital electrons, namely:

$$\langle m_{z,d} \cdot m_{z,p} \rangle = \langle (n_{d,\uparrow} - n_{d,\downarrow}) \cdot (n_{p,\uparrow} - n_{p,\downarrow}) \rangle$$

Considering that the correlated  $d$ -orbitals are almost half-filled, *i.e.*  $n_d \simeq 1$ , one can relate the main source of difference between the two discussed regimes to the large effect on the transition of the conduction band electrons. The  $p$ -orbitals are almost completely filled (either by particles or holes) in the Mott insulating state. Upon negative doping (in our notation) an increasing of their occupancy is observed. The saturation of the occupancy of these orbitals favors the formation of superexchange-like correlations between  $d$ -orbital electrons. In this case the conduction

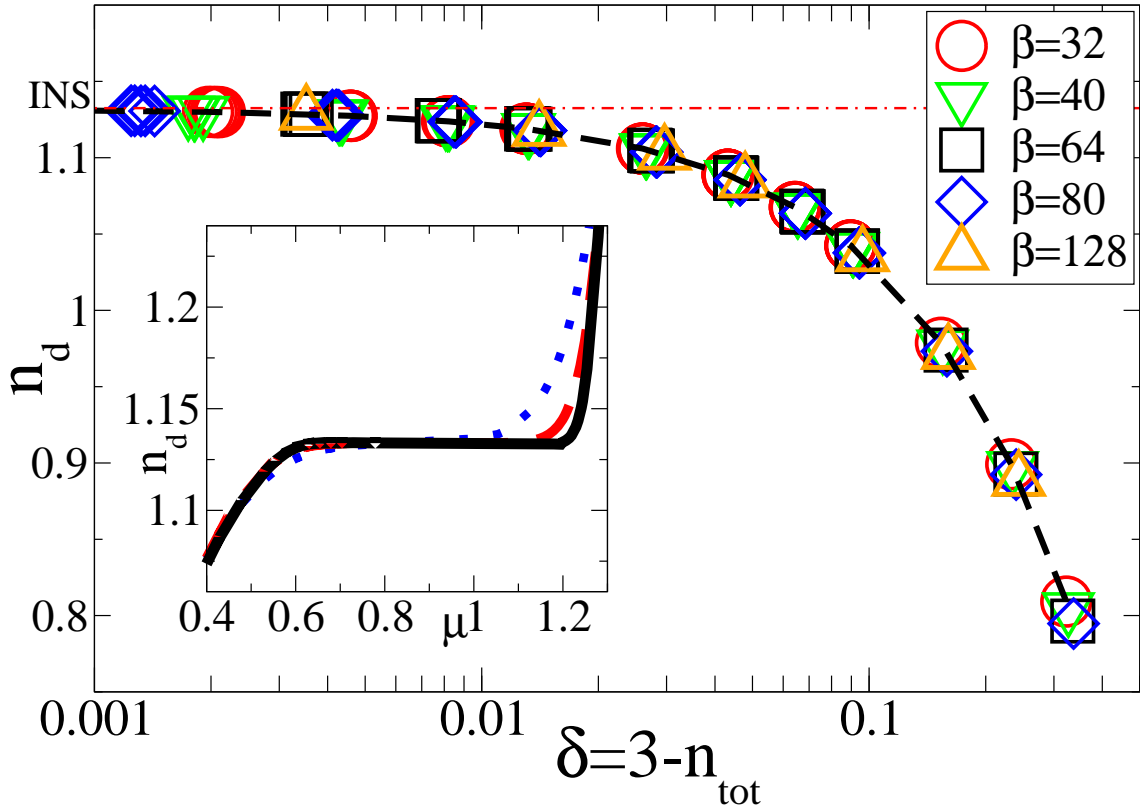


Figure 4.13: Main panel:  $d$ -electron number of particle as a function of doping in a log-linear scale and for several decreasing temperatures,  $T = 1/32$  ( $\circ$ ),  $T = 1/40$  ( $\nabla$ ),  $T = 1/64$  ( $\square$ ),  $T = 1/80$  ( $\diamond$ ),  $T = 1/128$  ( $\triangle$ ). Data are from QMC calculation. The points all lie almost on the same curve (black dashed line) and converge towards the value attained in the insulator (different from the unity). Inset: comparison of the temperature dependence of the  $d$ -electron particle number in the two boundaries of the Mott gap. Data are from QMC at  $T = 1/16$  (blue dotted line),  $T = 1/32$  (red dashed line) and  $T = 1/64$  (black solid line).

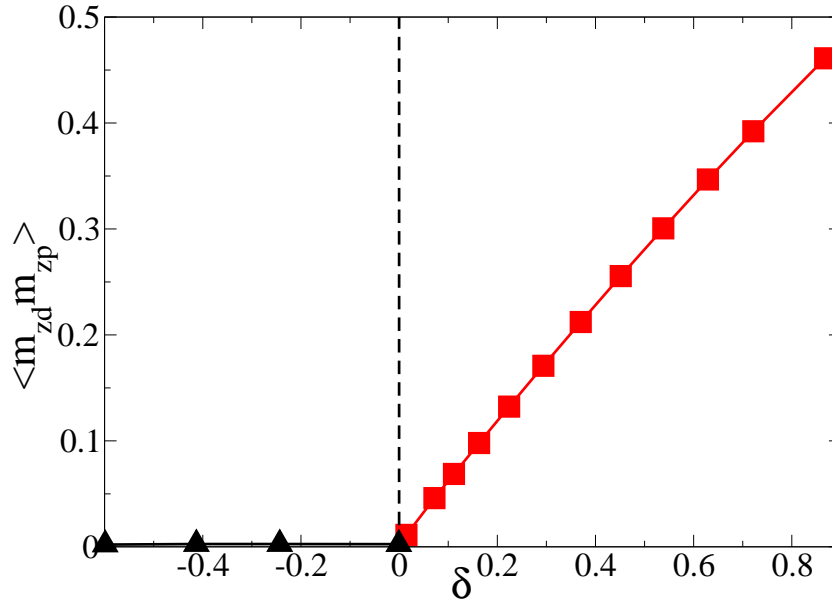


Figure 4.14: Moment-moment correlation between two orbital electron  $p$  and  $d$ , as a function of doping in the positive and negative regions. Data are obtained with ED at  $T = 1/128$  and have been benchmarked with zero temperature ED and ED-DMRG calculations, finding an almost perfect agreement. Other model parameter are  $U = 2$ ,  $V_{pd} = 0.9$ ,  $\Delta = 1$ .

band electrons do not participate actively to the screening process that lead to the formation of the metallic state, having as a unique role that of permitting the indirect delocalization of the correlated  $d$ -electrons. On the other hand, in the positive doped regime, a substantial reduction of the  $p$ -orbitals occupation can be observed. This effect is explained observing that the  $d$ -orbitals are quasi half-filled (the difference respect to perfect half-filling being attributed to the presence of few double occupancies), thus upon positive doping the system will free with more probability sites in the conduction band. In this way the system can gain a significant amount of energy by forming local  $p$ - $d$  singlet states.

This picture is substantiated by the behavior of the moment-moment correlation as a function of doping, reported in Fig. 4.14. The figure shows that while on the negative doping side this correlation is negligible and vanish with increasing doping, on the positive doping side it has a linear increasing behavior. Thus doped charge carriers into the conduction band antiferromagnetically bind to the (almost) singly occupied  $d$ -orbital electrons. The formed singlets remind the celebrated Zhang-Rice singlet, introduce so far to derive Hubbard model from a multi band model for copper oxides [104]. The breakdown of the Hubbard scenario in the positive doping regime is directly related to the formation of these singlets. The  $d$ -electrons, in fact, binding to the doped carriers lose their spin phase information, preventing the formation of strong antiferromagnetic correlation between neighboring  $d$ -moments, that is an essential

ingredient in the Hubbard scenario recipe.

### 4.3 Conclusions

We have introduced and discussed the Zaanen-Sawatzky-Allen diagram for the classification of the Mott insulating states. Then we have shown how these states can be obtained within the DMFT solution of the periodic Anderson model. In particular this model is able to describe the onset of an insulating state driven by correlation in both the Mott-Hubbard case, when the distance between the Hubbard bands defines the smallest gap, and the Charge-Transfer case, where the smallest energy gap is defined by the distance between a conduction band and upper Hubbard band. Motivated by the application of this model to the context of the heavy fermions we concentrated our attention to the Mott-Hubbard regime. This can in fact account for the configuration often observed in the framework of the heavy fermion systems, where a highly localized orbital electrons coexist with a wide conduction band. Once the existence of such insulating states have been demonstrated we have proceeded studying the different types of metal insulator transitions that can be induced upon doping the “parent” Mott insulating state.

In particular we have shown that type I transition ( $\delta < 0$ ) reproduce the same qualitative scenario of the well known DMFT solution of the Hubbard model. Whereas the type II transition obtained upon positive doping the Mott insulator produce a different scenario. In this latter case in fact the transition has been shown to be of the second order and temperature independent, *i.e.* it is a quantum phase transition at zero doping. The former instead show a first order character, underlined by an hysteresis loop in some physical quantities. We gave a physical interpretation of the mechanisms leading to the formation of these two different scenarios for the doping driven Mott transitions. In particular we have shown that the metallic state realized in the positive doping case can be interpreted as a liquid of Zhang-Rice singlets, formed between the doped conduction band particles and the local moment of the correlated  $d$ -orbitals.



# Non-Fermi liquid phase and Mottness scenario for Heavy Fermions

## Contents

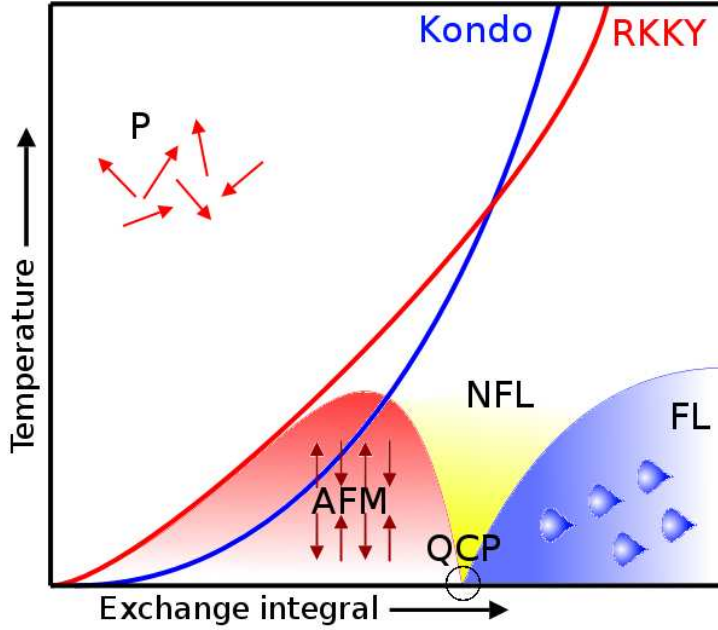
---

<b>5.1 Correlated metallic state: a liquid of singlets</b> . . . . .	109
<b>5.2 Non-Fermi liquid state</b> . . . . .	116
<b>5.3 Temperature crossover to Fermi liquid</b> . . . . .	120
<b>5.4 Spin susceptibility</b> . . . . .	124
5.4.1 Enhanced spin susceptibility . . . . .	124
5.4.2 Exhaustion and coherence scale . . . . .	126
<b>5.5 Magnetic properties</b> . . . . .	129
5.5.1 External magnetic field . . . . .	129
5.5.2 Antiferromagnetic ordering . . . . .	132
<b>5.6 Thermodynamics</b> . . . . .	134
5.6.1 Specific heat and effective mass . . . . .	134
5.6.2 Entropy . . . . .	138
<b>5.7 Mottness scenario</b> . . . . .	141
5.7.1 T - $\delta$ phase diagram . . . . .	141
5.7.2 Competing magnetic interactions: T - $B_{ext}$ phase diagram . . . . .	144
<b>5.8 Conclusions</b> . . . . .	147

---

Since the discovery, in 1975, of the heavy fermion behavior in  $CeAl_3$ , the inter-metallic compounds containing rare-earths or actinides elements have posed a number of serious challenges to the condensed matter physics community.

## 5. Non-Fermi liquid phase and Mottness scenario for Heavy Fermions



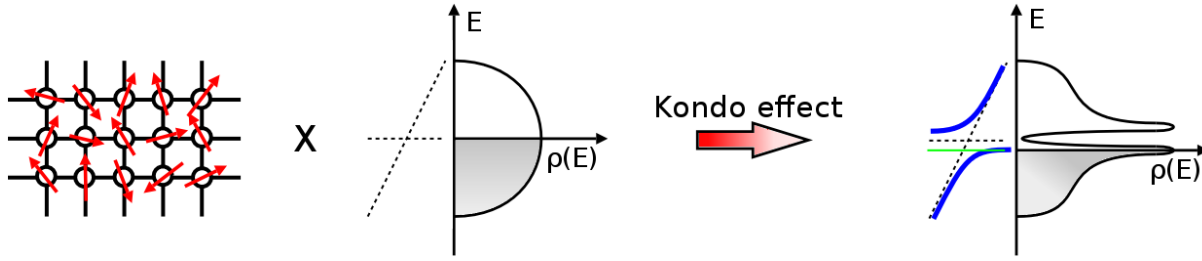
(a) Schematic Doniach diagram

These materials are characterized by an extraordinarily large value of the electronic specific heat constant  $\gamma = \lim_{T \rightarrow 0} C/T \simeq O(1)J/\text{moleK}^2$ , reaching values up to three orders of magnitude larger than normal metals. Because of this feature these compounds are termed “heavy fermions”.

As first proposed by Doniach [21], heavy fermions compounds can be regarded as dense Kondo lattice systems. The  $f$ -orbitals brought from the rare-earths/actinides form a lattice of highly localized magnetic moments “immersed” in a conduction band of itinerant electrons.

In this scenario the formation of heavy electrons is related to the antiferromagnetic interaction between the delocalized electrons and the concentrated local magnetic moments, *i.e.* Kondo effect. The Kondo interaction can lead to the formation of two different behavior. At low temperature it should be expected that every local moment get screened by the spin of the conduction electrons, with the consequent construction of an overall non magnetic singlet state. On the other the polarization of the conduction band caused by local singlet formation can cause the formation of indirect moment-moment correlation favoring magnetic ordering, *i.e.* RKKY interaction.

The competition between these two tendencies has been qualitatively summarized in the Doniach diagram (see figure (a)). For low value of the Kondo exchange integral  $J$ , the RKKY energy scale  $T_{RKKY} \simeq J^2\rho(E_F)$  exceeds the Kondo scale  $T_K \simeq Ce^{-1/J\rho(E_F)}$ , thus the systems find it more convenient to magnetically order (*e.g.* AFM). On the other side, for large value of  $J$ ,  $T_K > T_{RKKY}$  so that the system gain energy compensating the localized moments and forming



(b) Formation of the Kondo resonance and of the hybridized bands

a Fermi liquid with strongly renormalized effective mass (heavy fermion).

A renewal of the interest around the heavy fermions physics came in 1991 with the discovery of possible deviations from the Fermi liquid theory predictions in some compounds. Later on many other heavy fermions systems have been found to show “non-Fermi” liquid properties [94]. However, the theoretical understanding of the breakdown of the Fermi liquid paradigm in heavy fermion systems remains one of the open problems of strongly correlated physics. Among the many ideas put forward to explain this phenomenon, a predominant role is played by the so-called quantum criticality [35, 61, 88] (cf. Chap. 1). From the point of view of this approach the breakdown of the Fermi liquid properties in heavy fermion systems is related to the proximity to a magnetic instability at  $T = 0$ , *i.e.* the existence of a quantum phase transition or a quantum critical point in the phase diagram.

The existence of a quantum critical point in the heavy fermions phase diagram can be naively understood from the analysis of the Doniach diagram. The critical temperature associated with magnetic ordering, say  $T_N$ , follows at small  $J$  the RKKY temperature. Nevertheless, upon increasing the strength of the exchange integral the ordering temperature can be driven to zero by the competition with local moment compensation. The point at which  $T_N \rightarrow 0$  is a quantum critical point separating the magnetically ordered phase from a non-magnetic Fermi liquid metal. In the region above this QCP the strong coupling of the order parameter fluctuations with the itinerant electrons degrees of freedom can prevent the formation of coherent electronic excitations (Fermi liquid state).

The usual approach to the microscopic derivation of the heavy fermions behavior is based on the analysis of the periodic Anderson model (cf. Chap. 3). Because of its generality this model can capture many of the different regimes in which heavy fermion behavior has been observed, including the Kondo lattice regime. The presence of localized magnetic moments is usually taken into account fixing  $n_f = 1$ . In this regime and for an half-filled conduction band ( $n_p = 1$ ) the model solution describe the formation of two hybridized bands separated by an indirect gap  $\Delta_{ind}$ . The Kondo peak at the Fermi level, consequence of the resonant scattering of the conduction electrons on the localized moment, get splitted in two by the onset of such

## 5. Non-Fermi liquid phase and Mottness scenario for Heavy Fermions

---

indirect gap, see figure (b). A Kondo insulator (*i.e.* a band insulator with  $n_f + n_p = 2$ ) appears placing the chemical potential inside the indirect gap. However, an heavy fermions state is readily available upon slightly doping this insulating regime,  $n_p < 1$ . The Kondo resonance get pinned at the chemical potential once this has been placed inside the hybridized band, cf. figure (b). In this regime the renormalization of the effective mass due solely to the hybridization (cf. Chap. 3) sums up with the effects of the correlation, leading to the formation at low temperatures of a Fermi liquid heavy fermion metal. This concept can be well illustrated using a qualitative quasiparticle picture (renormalized bands) [36]. This yields for the effective mass:

$$\frac{m^*}{m} = 1 + \frac{V_{pd}^2}{Z[\epsilon_d + \Sigma(\mathbf{k}_F, 0)]^2}$$

where  $\Sigma(\mathbf{k}, \omega)$  is the self-energy,  $Z = [1 - \partial\Sigma/\partial\omega]^{-1}$  is the renormalization constant and  $\mathbf{k}_F$  is the Fermi wave-vector.

Changing point of view on the problem, one can recognize that the localization of the  $f$ -orbital electrons is an effect of the strong correlation. Therefore, it may appear more natural to found the microscopic derivation of the heavy fermion behavior on the proximity to a Mott insulating state, induced by correlation effect on the half-filled correlated band.

In the last part of this thesis we shall demonstrate that the metallic state obtained by slightly positive (cf. Chap. 4 for the notation) doping the Mott-Hubbard insulator has an heavy fermion character. Thus, our approach provide a new point of view on the description of the heavy fermion physics. Furthermore and quite surprisingly, this metallic state shows a breakdown of the Fermi liquid properties, down to vanishing temperatures. The presence of such small temperature scales can be traced back to the well known exhaustion problem, [68, 67, 95].

Similarly to the canonical quantum criticality approach to non-Fermi liquids (cf. Chap. 1), this novel NFL state is located in the neighborhood of a quantum phase transition. Nevertheless, unlike the standard quantum criticality scenario, the relevant transition here is a Mott metal-insulator transition.

The origin of this novel non-Fermi liquid phase has been associated with the strong fluctuating nature of the local magnetization of the correlated electrons, consequence of competing magnetic interactions. The local fluctuating magnetization coupling to the electronic degrees of freedom of the doped charges, prevent the formation of well defined quasiparticles, *i.e.* of a Fermi liquid state. Thus, we demonstrate that local temporal fluctuations alone can provide a sufficient source of scattering to produce an inchoerent metallic state.

We find that the non-Fermi liquid state can be tuned by either doping or magnetic field, in qualitative agreement with some non-Fermi liquid phenomenology observed in heavy fermions.

The chapter is structured as follow: Sec. 5.1 is dedicated to the study of the correlated metallic phase obtained upon tiny positive doping the Mott insulator. We will show that this metallic

state is formed by a liquid of Zhang-Rice singlets and we will review its properties. Moreover we shall demonstrate that the system is placed in a mixed-valence regime. In Sec. 5.2 we will report evidences for the breakdown of Fermi liquid properties in the tiny positive doped metal. We will show that the resonance at the Fermi level characterizing this metallic state is associated to short-lived electronic states. Section 5.3 is devoted to the study of the temperature crossover to a normal Fermi liquid phase. To obtain useful insights about the nature and the origin of this novel NFL state we shall study in Sec. 5.4 the local spin susceptibility and in Sec. 5.5.1 the magnetic properties of the NFL phase. In particular we will show that Fermi liquid is restored by either application of a sufficiently strong external magnetic field or by the onset of order phase like antiferromagnetic one. Thermodynamic properties of the NFL phase are reported in Sec. 5.6, where we study the specific heat behavior, and in Sec. 5.7 where we present results about entropy behavior. Finally in Sec. 5.8 we summarize the results in two phase diagrams and we discuss the Mottness scenario.

## 5.1 Correlated metallic state: a liquid of singlets

In this section we present results to illustrate the nature of the correlated metallic state obtained upon tiny positive doping the Mott-Hubbard insulator, whose existence has been the subject of the previous chapter 4. To deal with a specific case, we fix the position of the conduction band to be below the Fermi level, that is below the correlated electron level fixed at  $\epsilon_d = 0$ . In the non interacting and non hybridized limit  $U = V_{pd} = 0$ , the conduction band is completely filled:  $n_p = 2$ . Nevertheless, finite values of the hybridization  $V_{pd}$  will produce a reduction of the  $p$ -electron filling  $n_p < 2$ , pushing a substantial amount of the  $p$ -electron spectral density to the Fermi level.

**Remark 1:** In this regime the Mott insulating state occurs at  $n_{tot} = 3$ . The non-correlated band, *i.e.* the hybridized band whose support contains  $\epsilon_p < 0$  is completely filled, while the correlated band, *i.e.* the hybridized band near the Fermi level is half-filled.

**Remark 2:** All the results reported in this chapter can be extended to the symmetric regime obtained by placing the conduction band above the Fermi level, *i.e.* with  $\epsilon_p > 0$ .

**Remark 3:** The initial position of conduction band  $\epsilon_p$  respect to the Fermi level is almost irrelevant with respect to the results obtained in this thesis, provided the conditions discussed in chapter 4 for the formation of a Mott-Hubbard insulating state are verified.

To start with we analyze the correlated metallic state, from the point of view of the density of states. In figure Fig. 5.1 we present the result of a very high quality QMC calculation at  $T = 1/128$ , analytically continued on the real axis using the Maximum Entropy Method. The figure shows the spectral density of both electronic species, in a small energy region around the

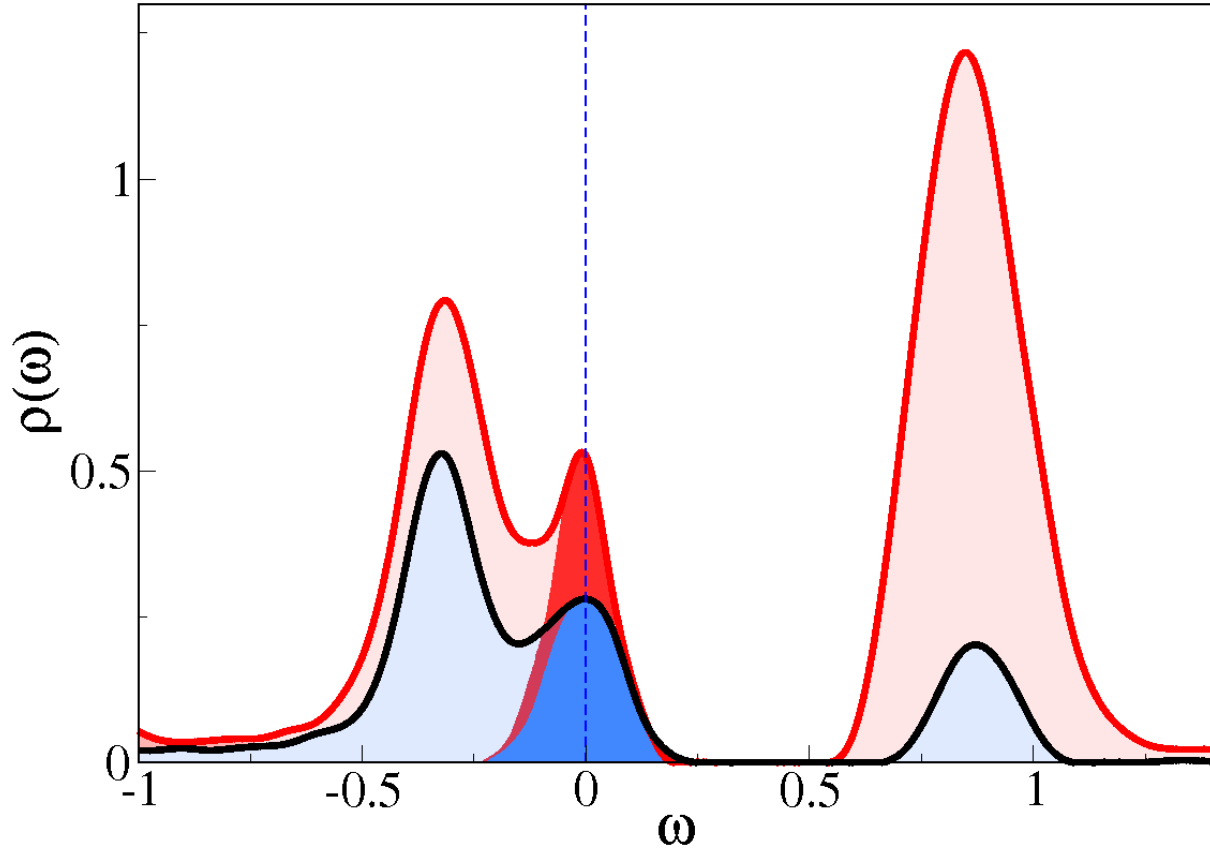


Figure 5.1: Main panel: density of states for the  $p$ - (black line and blue filling) and  $d$ -electron (red line and red filling) from QMC calculation at  $T = 1/128$  supplemented by Maximum Entropy Method analytic continuation. The model parameters are:  $U = 2$ ,  $V_{pd} = 0.9$ ,  $\Delta = 1$ ,  $\mu = 0.55$  and  $\delta \simeq 0.01$ . The weight of the two resonances is underlined with color more intense color filling.

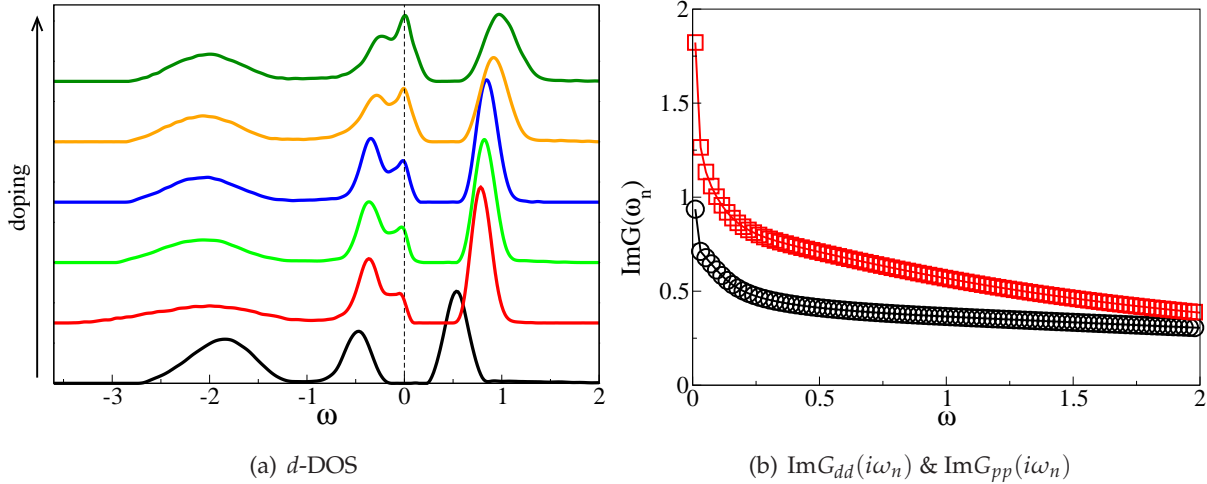


Figure 5.2: (a) Evolution of the  $d$ -orbital electron DOS as a function of increasing doping from Mott insulator to metallic state (bottom to top). Data are from QMC + MEM at  $T = 1/64$ ,  $V_{pd} = 0.9$ ,  $\Delta = 1$  and for different values of chemical potential (from bottom to top):  $\mu = 0.83, 0.58, 0.55, 0.53, 0.48, 0.43$  corresponding respectively to  $\delta = 0.0, 0.001, 0.01, 0.05, 0.1, 0.15$ . (b): imaginary part of the  $p$ - ( $\circ$ ) and  $d$ -electrons ( $\square$ ) Green's function as obtained from ED solution of the model at  $T = 1/300$  and  $\mu = 0.53$  ( $\delta = 0.05$ ), with the same model parameters as before.

Fermi level. The main feature is the presence of a broad resonance at the Fermi level for both the orbital electrons. These resonances flank the lower Hubbard band (placed just below the Fermi energy) and are well separated from the upper Hubbard band visible at small positive energies. Thus, the density of states has the typical three peak structure emerging from the DMFT description of a correlated metal. It is worth to point out that the  $p$ -electrons spectral weight at the resonance is, at least qualitatively, comparable with that of the correlated  $d$ -electrons. This is a first evidence of the mixed-valence character of the solution of the model in this tiny doped regime. In contrast the  $p$ -orbital spectral weight of the quasi-particle peak obtained in the tiny negative doped regime was drastically reduced with respect to the  $d$ -electrons weight (cf. Chap. 4). The spectral weight of the two resonances has been evidenced by intense color filling in the figure. Interestingly the resonances show the typical peak-dip-hump structure well known in the framework of photoemission experiments.

To better illustrate the generality of this scenario as a function of the doping, we show in Fig. 5.2(a) results about the evolution of the  $d$ -electrons projection of the density of states for several increasing values of the (hole) doping. The figure illustrates the formation and the evolution of the resonance at the Fermi level. Data are collected from QMC plus MEM calculations at  $T = 1/64$ ,  $U = 2$ ,  $V_{pd} = 0.9$ ,  $\Delta_0 = 1$  and  $\delta = 0.0, 0.001, 0.01, 0.05, 0.1, 0.15$ . In the bottom part of the plot we show the DOS corresponding to the Mott insulating solution, with

## 5. Non-Fermi liquid phase and Mottness scenario for Heavy Fermions

---

the two Hubbard bands well separated in energy by a spectral gap at the Fermi level. Placing the chemical potential slightly inside the lower Hubbard band corresponds to the introduction into the system of a small number of charge carriers of hole type. The direct result is the metallization of the solution, with the formation of an electronic resonance at the Fermi level. This is well illustrated by the second curve from the bottom, corresponding to a doping of the order  $10^{-3}$ . Upon further increasing the doping the system shows a progressive increasing of the resonance weight, coming with a transfer of spectral weight from the lower Hubbard band to the peak at the Fermi level. This is directly related to the fact that this metallic state is associated with the formation of local singlets, that on its hand is directly proportional to the number of  $p$ -holes freed in the system (doping).

The three peaks structure at low energy is well preserved along all the presented range of doping as well as the peak-dip-hump feature, indicating that the obtained results are genuine features and not artifacts of the qualitative method used to perform the analytic continuation.

The metallic character of the solution in the hole doped regime is illustrated also by the behavior of the imaginary part of the one particle Green's function. In Fig. 5.2(b) we report the results of an ED calculation at  $T = 1/300$  for  $\mu = 0.53$ ,  $\delta = 0.05$  and both the  $p$ - and  $d$ -electron Green's function. The increasing behavior at low energy of both  $\text{Im}G_{pp}(i\omega_n)$  and  $\text{Im}G_{dd}(i\omega_n)$ , showing a finite intercept at zero frequency, further demonstrate the metallic nature of the solution, beyond the qualitative results already presented.

An interesting aspect of this correlated metallic state is its mixed-valence character. The Mott insulating state occurs for a sufficiently large value of the correlation and half-filling of the correlated band. In the present regime this is achieved by fixing  $n_{tot} = 3$ . By the way, this will not imply, as naively one could expect, that  $n_d = 1$  and  $n_p = 2$ . The strong hybridization, mixing the two electronic species, has the effect of pushing the orbitals filling towards non integer values. This behavior implies that the Mott localization does not occurs for the correlated orbital electrons but rather for a "composite" correlated object retaining part of both the  $d$ - and the  $p$ -character. To underline the mixed-valence character of the solution we present in Fig. 5.3 the behavior of the particle numbers as a function of the chemical potential in a very large range of variation. Data are collected from QMC calculations at fixed temperature  $T = 1/64$  and have been benchmarked against similar calculations performed with complete ED and ED/DMRG at finite and zero temperature respectively.

Starting from the extreme left (far negative value of chemical potential), the figure shows an increasing behavior of the different fillings for increasing  $\mu$ , corresponding to the occupation of the non correlated band. Once this band has been completely filled a band insulating state shows up at  $n_{tot} = 2$  and for  $-1 \lesssim \mu \lesssim 0$ . Further increasing the value of the chemical potential corresponds to filling up the lower Hubbard band. Thus, we observe an increasing behavior

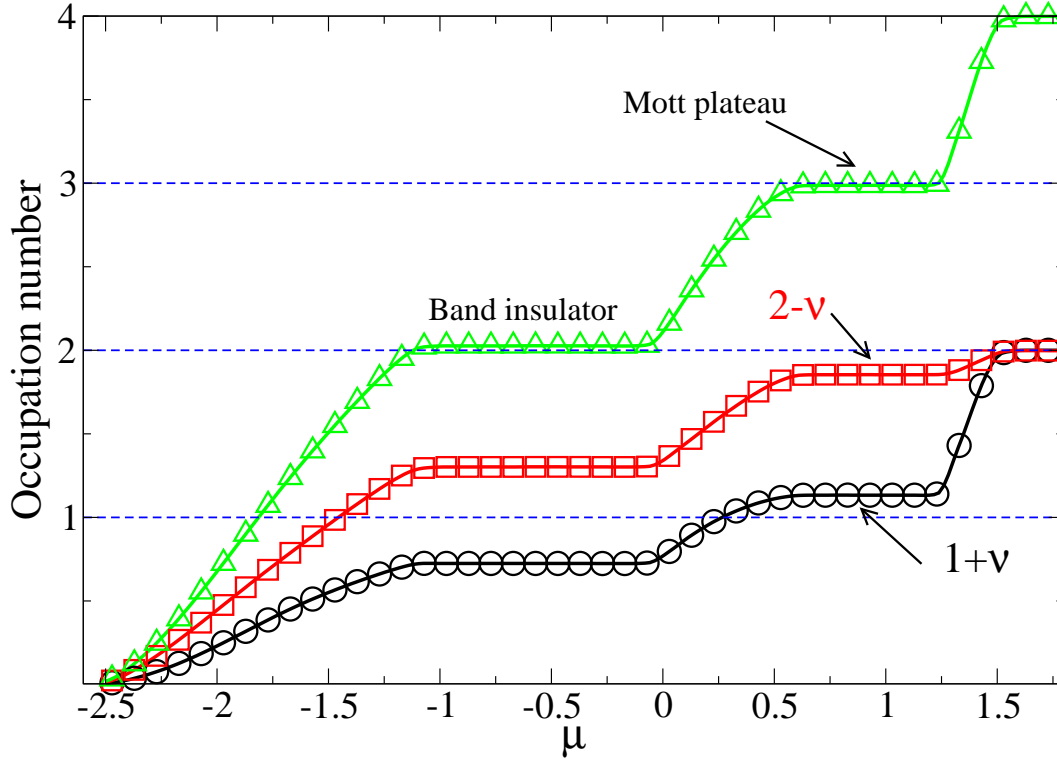


Figure 5.3: Total ( $\triangle$ ) and partial  $n_d$  ( $\circ$ ) and  $n_p$  ( $\square$ ) particle numbers, as a function of the chemical potential. The data are obtained from QMC at  $T = 1/64$  and for  $U = 2$ ,  $V_{pd} = 0.9$  and  $\Delta = 1$ . The figure shows the behavior of particle numbers in the full range of  $\mu$  from the completely empty system regime ( $\mu \lesssim -2.5$ ) to the completely filled one ( $\mu > 1.5$ ). A band insulator appears at  $n_{tot} = 2$  for  $-1 \lesssim \mu \lesssim 0$ , corresponding to the completely filled non correlated band regime. Instead a Mott plateau appears for  $0.5 \lesssim \mu \lesssim 1.2$  at  $n_{tot} = 3$ , thus having half-filled the correlated band. Partial fillings in the Mott insulating regime clearly illustrate the mixed-valence character of the solution.

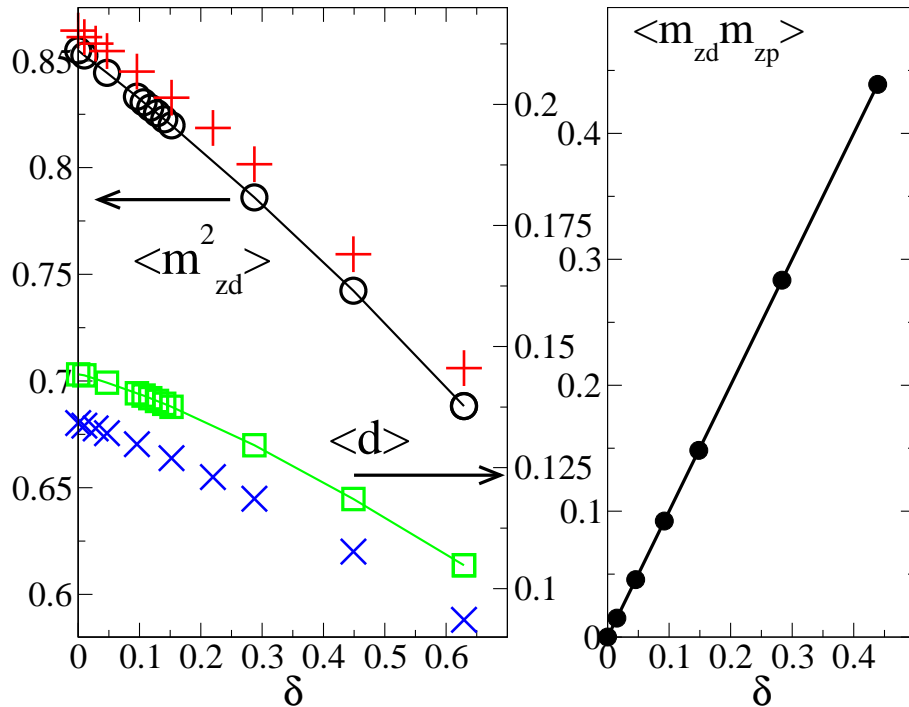


Figure 5.4: Left panel:  $d$ -electrons local moment  $\langle m_{z,d}^2 \rangle$  from ED ( $\circ$ ) and QMC ( $+$ ), double occupation  $\langle d \rangle$  from ED ( $\square$ ) and QMC ( $\times$ ) as a function of doping. The former refers to the left  $y$ -axis while the latter to the right  $y$ -axis as indicated by the black arrows. Both data are from calculations performed at  $T = 1/64$  and  $U = 2.0$ ,  $V_{pd} = 0.9$ ,  $\Delta = 1$ . The small mismatch between the two methods is due to the finite discretization error in QMC. Right panel: momentum-moment correlation  $\langle m_{z,d} \cdot m_{z,p} \rangle$  ( $\bullet$ ) between the two electron species as a function of doping  $\delta = 3 - n_{tot}$ , data from ED at  $T = 1/128$ .

of the particle numbers. When the total filling reaches the value  $n_{tot} = 3$ , corresponding to the half-filling of the correlated hybridized band, a Mott gap opens and a plateau of incompressible states appears. Identical plateaux are observed for the orbital fillings, but interestingly these occur at non-integer values  $n_d = 1 + \nu$  and  $n_p = 2 - \nu$ , with  $\nu \approx 0.13$  for the chosen values of the model parameter  $U = 2$ ,  $V_{pd} = 0.9$ ,  $\Delta = 1$ . This clearly illustrates the mixed-valence character of the model. The specific value of  $\nu$ , roughly measuring the strength of the mixed-valence character, is a general function of the both hybridization, correlation and temperature.

The mixed-valence character of this model solution is more natural than what could be naively expected. This feature is related to the strong hybridization between the two electronic species. In this respect removing mixed-valency, without falling into the symmetric regime of the PAM characterized by the Kondo insulating state, requires suitable limits to be exploited such as  $\Delta \rightarrow \infty$ ,  $U \rightarrow \infty$  or finally  $V_{pd} \rightarrow 0$ .

Before entering into the details of the nature of the correlated metallic state, we shall emphasize some properties of the model solution that can be immediately understood from the analysis of the  $d$ -electron local moment  $\langle m_{z,d}^2 \rangle = \langle (n_{d,\uparrow} - n_{d,\downarrow})^2 \rangle$  and the double occupancy  $\langle d \rangle = \langle (n_{d,\uparrow} \cdot n_{d,\downarrow}) \rangle$ . The rather large value of the correlation  $U$ , with respect to the effective bandwidth of the correlated band, push the system into a regime in which the occupation of the  $d$ -electrons is nearly close to one (cf. Fig. 5.3). Thus, despite the strong mixed-valency, the  $d$ -electrons magnetic moment is expected to be large. This is well illustrated in the left panel of Fig. 5.4 where the local magnetic moment of the  $d$ -orbital electrons is shown as a function of doping. The results are obtained from finite temperature ED calculation and are compared with same temperature QMC calculations. The two sets of data show the same behavior as a function of carriers concentration, even if a small mismatch between the two calculations is visible. This systematic error has to be addressed to the discretization of the imaginary time axis at the heart of the Hirsch and Fye QMC technique. Upon positive doping the local moment slowly decreases, losing about 20% of its value in the reported doping variation ( $\Delta\delta \gtrsim 60\%$ ), remaining sizeable throughout this range.

The screening effect of the doped  $p$ -type carriers on the correlated electrons local moment is at the origin of the decreasing behavior of the  $d$ -moment as a function of doping. This effect is proportional to the value of the doping. On the other hand, doping has a small but finite probability of removing electrons from the doubly occupied  $d$ -orbitals, slightly increasing the average value of the correlated electrons local moment. This second effect is illustrated in the bottom part of the left panel of Fig. 5.4, where the double occupancy of the  $d$ -orbitals is reported as a function of the doping. The scale is reported on the right  $y$ -axis. The average double occupation of the correlated orbitals is rather small, due to of the large value of  $U$ , but it is still finite as effect of strong hybridization and finite temperature. Upon increasing the doping this quantity shows a reduction of about 30% throughout the reported doping range. The competition between the screening effect and the reduction of the value of the double occupancy explains the slower decay of the  $d$ -electrons local moment. This behavior has a strong impact in the nature of the correlated metal.

Finally we gain some insights about the nature of this correlated metallic state studying the moment-moment correlation  $\langle m_{z,d} \cdot m_{z,p} \rangle$  between the two orbital electrons. The behavior of this quantity as a function of the doping is reported in the right panel of Fig. 5.4. Data have been obtained from an ED calculation at  $T = 1/128$ . This calculation has been also compared with similar calculations at  $T = 0$  from both ED and ED/DMRG finding a very good agreement. The presence of such robust local moments in the system favor the formation of local singlets by antiferromagnetic binding between the doped  $p$ -carriers (holes) and the local  $d$ -moments

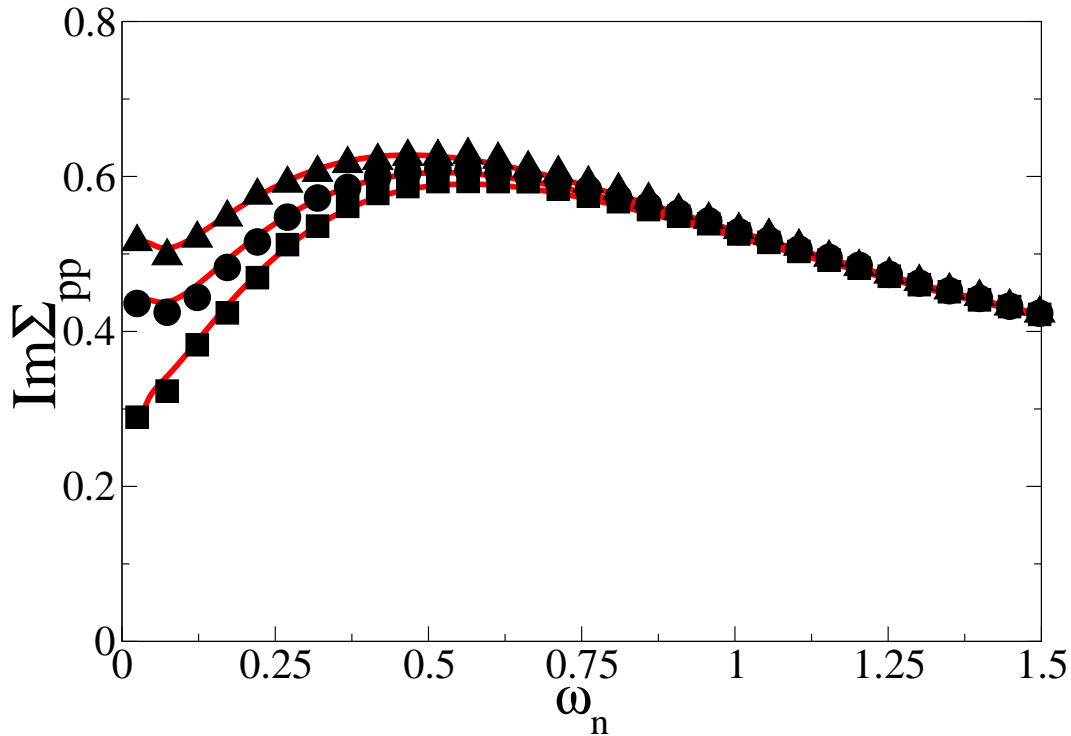


Figure 5.5: Imaginary part of the conduction electron self-energy  $\text{Im}\Sigma_{pp}(i\omega_n)$  in the tiny hole doped regime, from QMC calculations at  $T = 1/128$ ,  $U = 2$ ,  $V_{pd} = 0.9$ ,  $\Delta = 1$  and for  $\delta = 0.015$  (■),  $\delta = 0.05$  (●),  $\delta = 0.1$  (▲), and  $\mu = 0.58, 0.53$  and  $0.48$  respectively. Solid line show the same quantity from ED-DMRG calculation for the same model parameters. DMRG data are obtained for large finite cluster of 40 sites and are plotted down to the smallest energy pole (IR cut-off).

(Kondo effect). The doped  $p$ -holes gain an energy roughly of the order:

$$J_{ZR} \simeq v \frac{V_{pd}^2}{\Delta - \Delta_M}$$

where the small number of doped  $p$ -holes  $v$  is approximately cancelled by the energy cost in the denominator. The linear increasing behavior of the moment correlation substantiate this picture. Thus, the correlated metallic state can be described as a liquid of local singlets.

## 5.2 Non-Fermi liquid state

As pointed out in the first part of this thesis, in the framework of Fermi liquid theory metallic states are described in terms of electronic excitations having particle-like character. This is consequence of the particular nature of the fermionic degrees of freedom, imposing severe limitations to the scattering processes that the electrons near the Fermi surface can undergo. These are expressed in terms of phase-space constraints for the evaluation of the inverse life-time of

the quasiparticle excitations (cf. Sec. 1.1). Landau’s intuition has been to realize that a 1 to 1 correspondence between the non-interacting and the interacting system was possible, adiabatically turning on the interaction. The coherent superposition of the interacting states forms electronic excitations near the Fermi surface that are sufficiently long lived with respect to the rate of change of the interaction. This justify the interpretation of the Fermi liquid in terms of “quasi-particles”, *i.e.* excitations retaining many physical properties of the bare electrons, but whose effective mass is renormalized by the presence of the interaction.

In the more sophisticated language of Green’s functions, Fermi liquid theory assumption can be reformulated requiring that the imaginary part of the self-energy *vanish* near the Fermi surface as the square of the energy. To make contact with the discussion in Sec. 1.1 it is worth to recall that the scattering rate of the process discussed there defines the lowest contribution to the self-energy. Then, by Fermi liquid theory it should be possible to approximate the self-energy with the following expression:

$$\Sigma(\omega, \mathbf{k}_F) \simeq A + B\omega + i\Gamma\omega^2 \quad \text{for } \omega \rightarrow 0 \quad \text{and} \quad A, B, \Gamma \in \mathbb{R}.$$

This means that the decay rate of the excitations near the Fermi surface is much smaller than their energy. In the finite temperature formalism the Green’s functions and the self-energies are expressed in terms of Matsubara imaginary frequencies  $\omega \rightarrow i\omega_n = i\pi T(2n + 1)$ , so that a rotation to the imaginary axis is required. In the DMFT framework, where the self-energy becomes local losing its dependence on the wave-vector  $\mathbf{k}$ , one expects the imaginary part of self-energy to linearly vanish as  $i\omega_n \rightarrow 0$ :

$$\Sigma(i\omega_n \rightarrow 0) \simeq i\omega_n\alpha + \beta \quad \text{with} \quad \alpha, \beta \in \mathbb{R}$$

Surprisingly the self-energy corresponding to the correlated metallic state introduced in the previous section does not share this property. The imaginary part of the conduction electron self-energy shows, in a finite region of doping, a non vanishing behavior at low frequency and down to exponentially small temperatures. This imply that the correlated metallic state obtained upon positive doping the Mott insulator is not associated to long-lived quasiparticles but rather to incoherent, *i.e.* short-lived, electronic excitations.

In Fig. 5.5 we present some evidences for this breakdown of the Fermi liquid phase. In this figure we report the low energy behavior of the imaginary part of the conduction electron self-energy,  $\text{Im}\Sigma_{pp}(i\omega_n)$ , for three different values of the chemical potential, corresponding to three values of the doping, such that  $\delta \lesssim 10\%$ . The imaginary part of the reported self-energies has a large finite intercept at zero energy. Interestingly, while for very small doping  $\text{Im}\Sigma_{pp}(i\omega_n)$  has a linearly decreasing behavior extrapolating at a finite value at zero energy, for slightly larger values of the doping the self-energy reaches a minimum and acquires a linearly increasing behavior. Thus, the result shown in Fig. 5.5 reveals the non-Fermi liquid character of the

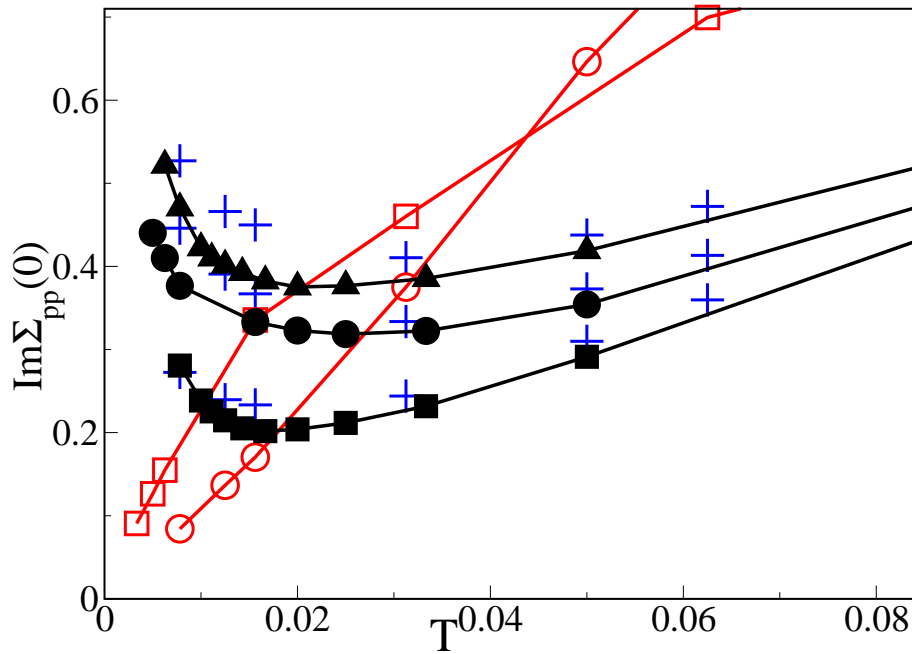


Figure 5.6: Scattering rate or inverse scattering time  $\text{Im}\Sigma_{pp}(i\omega_n \rightarrow 0)$  as a function of temperature for  $\delta = 0.015$  (■),  $\delta = 0.05$  (●),  $\delta = 0.1$  (▲) from ED calculations. Data from QMC are reported as a reference for the very same values of the doping (+). Data for higher doping  $\delta = 0.44$  (○) and  $\delta = 0.29$  (□) are reported to show the crossover to Fermi liquid regime.

correlated metallic state obtained upon tiny hole doping the Mott insulating state. The DMFT solution of the model in this tiny hole doped regime was obtained with both accurate QMC and ED/DMRG calculations. QMC data have been obtained for temperatures down to  $T = 1/128$  and with a number of sweeps of the order  $10^6$  such that to minimize the systematic (statistical) error, while the  $T = 0$  DMRG results have been obtained describing the effective electronic bath with up to 30 sites. Due to the existence of an infrared cut-off in the DMRG solution, connected with the finite size of the bath, the corresponding results are plotted down to the smallest energy pole. This roughly corresponds to a temperature of the same order of those accessible within QMC. Further calculations performed at lower temperatures using complete ED confirm the results shown in this figure. As evident by looking at Fig. 5.5 the accordance between the two numerical solutions is very satisfactory.

Furthermore, we have studied the stability of this novel NFL regime with respect to changes in the model parameters, such as the correlation  $U$ , the hybridization  $V_{pd}$  or the charge transfer energy  $\Delta$ . In particular, the results show that NFL state persist upon decreasing the correlation  $U$  till the disappearing of the Mott insulating state ( $U \lesssim t_{eff}$ ).

A more systematic analysis of  $\text{Im}\Sigma_{pp}(i\omega_n)$  as a function of temperature permits to obtain useful insights about the scattering rate of the charge carriers as a function of temperature. This quantity has been obtained as extrapolation of the imaginary part of the self-energy corresponding to the DMFT solution for many different temperatures. By definition the finite intercept of the self-energy describes, for any fixed temperature, the inverse life-time of the electronic excitations, and thus is directly proportional to the resistivity  $\rho(T)$  (cf. Sec. 1.1). In Fig. 5.6 we report our results about the scattering rate for the same values of the doping as those used in the previous Fig. 5.5 (filled symbols). The results illustrate the anomalous behavior of the resistivity down to small temperature in the region of doping corresponding to the observed NFL phase. In the same plot we report the scattering rate behavior corresponding to larger value of doping (open symbols). For small values of the doping the resistivities show a minimum as a function of the temperature, after which they acquire a *linearly* increasing behavior with negative slope. This behavior of the resistivity has been observed in some heavy fermion compounds showing non-Fermi liquid properties. Increasing resistivity behavior as a function of decreasing temperature is usually associated to systems with a certain degree of (structural) disorder. The slope of the resistivity behavior as a function of temperature is in fact believed to mirror the order in the underlying lattice [94].

For larger values of doping the resistivity acquires again the expected behavior of normal metallic state.  $\rho(T)$  has a nearly linear vanishing behavior as a function of decreasing temperature that eventually turns into a  $T^2$  at very low temperature/energy scales as required by Fermi liquid theory (cf. Chap. 1).

### 5.3 Temperature crossover to Fermi liquid

The DMFT solution of a strongly correlated electron model, such as the periodic Anderson model, entirely rely on the (numerical) solution of the associated effective single impurity Anderson model (SIAM). Quantum impurity models have received in the past a great deal of attention and a lot of results are now available by means of powerful non-perturbative methods. The scenario that borne out from the solution of the SIAM describes the crossover from the unscreened impurity regime for  $T > T_K \simeq De^{-1/J\rho(E_F)}$ , in which the coupling constant  $J$  is small and permits perturbative treatment, to a completely screened regime for  $T < T_K$ , in which the impurity local moment has been completely compensated and the coupling constant  $J$  becomes non-perturbatively large. Thus, at low temperature the solution of the Anderson impurity model describes the formation of a local Fermi liquid state.

Motivated by these remarks one expects the Fermi liquid properties of the DMFT model solution, in the regime we are looking at, to be restored in the limit of small temperature. Nevertheless, the crossover to a Fermi liquid state may appear at vanishing temperature scales, in qualitative agreement with the observed behavior in heavy fermion systems. In the following we shall demonstrate that the non-Fermi liquid state can be driven to a Fermi liquid thru a crossover at temperatures exponentially small in the doping. Later on we will derive an estimate of the temperature connected with the Fermi liquid formation and we will show how this can be integrated in a scenario explaining some phenomenology of the heavy fermions.

Numerically speaking the description of the temperature crossover can be, and in fact is, an extraordinarily difficult task to achieve because of the presence of small energy scales. In this respect QMC method should be excluded, being strongly limited to solution of DMFT equations in the large-to-mid ( $T > 1/160$ ) temperature range, as a consequence of the imaginary time axis discretization. Instead, complete ED method can accomplish this goal, but this requires in practice an high optimization of the algorithm and the use of rather large number of sites to describe the effective bath. The agreement between the two methods has been checked down to the lowest accessible temperature. The issue of the temperature crossover, even if partially clarified by our calculations, remains open to a systematic analysis with other suitable numerical methods or improvements.

We present in figure 5.7 our results about the temperature crossover to Fermi liquid state. The figure report the evolution of the imaginary part of the conduction electron self-energy  $\text{Im}\Sigma_{pp}(i\omega_n)$  for several decreasing temperatures. Based on the idea that the crossover temperature may be exponentially small, the doping has been chosen sufficiently large ( $\delta \simeq 0.15$ ) to permit the numerical observation of the crossover at temperatures accessible by our methods. The figure is divided in panels each of which reports the low energy behavior of  $\text{Im}\Sigma_{pp}(i\omega_n)$

### 5.3. Temperature crossover to Fermi liquid

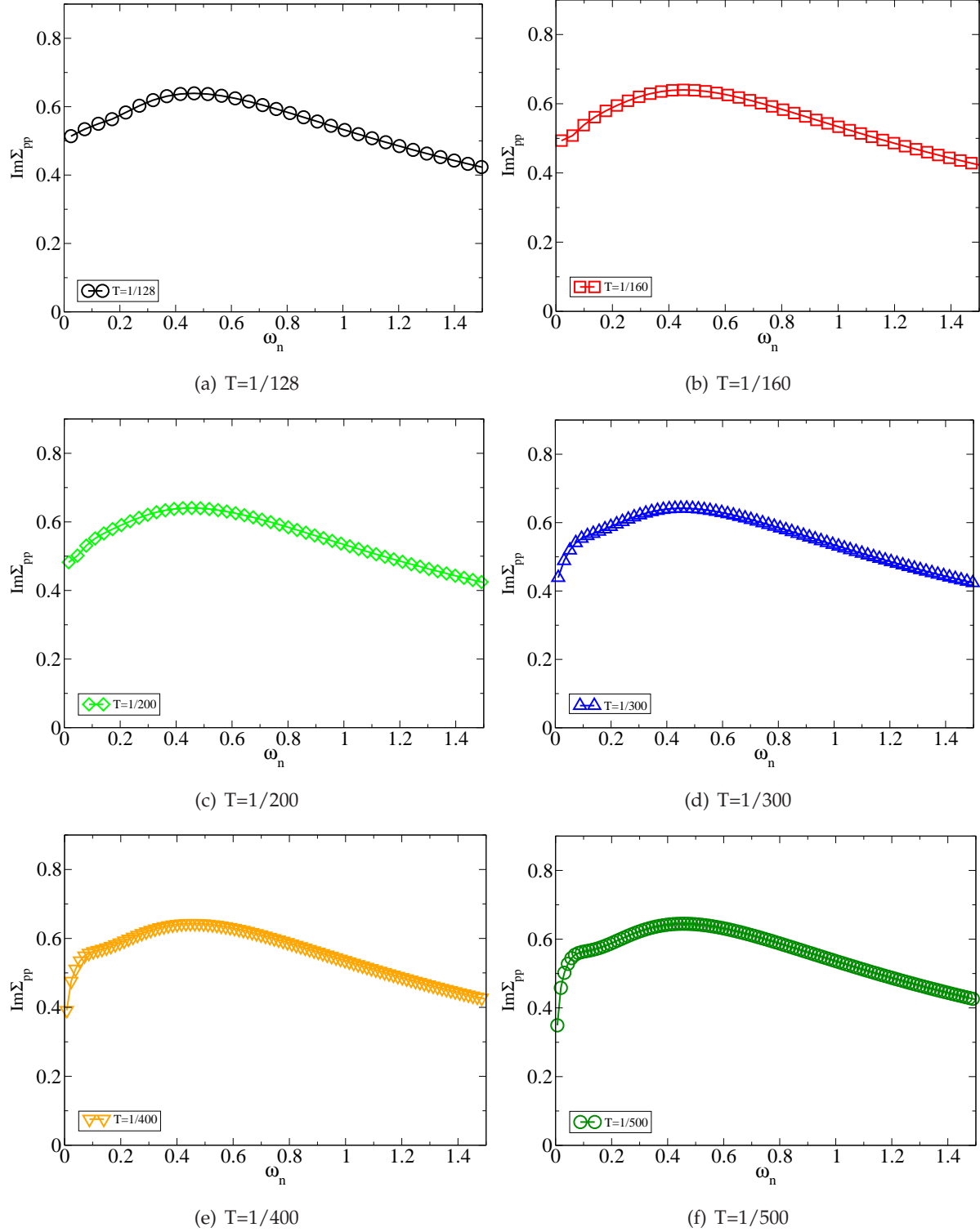


Figure 5.7: Crossover to Fermi liquid metal from the evolution of the low energy behavior of  $\text{Im}\Sigma_{pp}(i\omega_n)$ . Data are from complete ED and  $\delta \simeq 0.15$ . For smaller doping crossover could be observed at a much smaller temperature scale.

## 5. Non-Fermi liquid phase and Mottness scenario for Heavy Fermions

---

corresponding to a specific temperature (indicated below). The top left panel corresponds to the highest temperature ( $T = 1/128$ , cf. Fig. 5.5). The temperature decreases upon moving to the right on each row and to the bottom, till lowest value is reached in the bottom right panel ( $T = 1/500$ ).

As can be appreciated, the imaginary part of the  $p$ -electron self-energy has a finite intercept at the highest temperatures, cf. Fig. 5.7(a). This behavior persists for slightly smaller temperatures, Fig. 5.7(b), 5.7(c). At lower temperatures the  $\text{Im}\Sigma_{pp}(i\omega_n)$  starts developing a vanishing behavior of the scattering rate, Fig. 5.7(d). Nevertheless, the finite intercept is driven to zero only upon further decreasing the temperature, cf. Fig. 5.7(d) and 5.7(f). Thus the construction of a local Fermi liquid state, with vanishing imaginary part of the self-energy, takes place over a long range of temperatures (crossover) and is achieved only at very small temperature scales.

The systematic analysis of the evolution of the low temperature conduction electron self-energy as a function of doping (where possible) permits to obtain the behavior of the resistivity in the region of crossover between the non-Fermi and the the Fermi liquid phase.

As follows from the discussion preceding Fig. 5.7, the anomalous linear increasing resistivity observed in the non-Fermi liquid region, is expected to undergo an inversion of its behavior when a characteristic crossover temperature is reached. The existence of such a inversion region in the resistivity behavior is observed in heavy fermion compounds.

In Fig. 5.8 we present some results confirming this expectation. The behavior of the scattering rate in a region corresponding to very low temperatures is plotted for some values of the doping in the NFL phase. In the most doped case ( $\delta \simeq 0.15$  black diamonds and line)  $\rho(T)$  has a quasi-constant or slowly increasing behavior till a crossover temperature about  $T \simeq 1/200$  is reached. Below this temperature the scattering rate starts decreasing, signalling the incipient formation of a Fermi liquid state. For a slightly smaller value of the doping ( $\delta \simeq 0.1$  green circles and line) the resistivity shows a more marked increasing behavior that it is arrested and converted into a vanishing one only upon lowering the temperature below a scale much smaller than the previous case, namely  $T = 1/500$ . Smaller values of doping are, with respect to the evaluation of low temperature behavior of the resistivity, almost inaccessible with our methods. So far, we did not find any trace of Fermi liquid crossover for very small values of the doping and down to the smallest analyzed temperature. Nevertheless one can reasonably guess that tiny hole doping region may share the same behavior observed for larger values of doping.

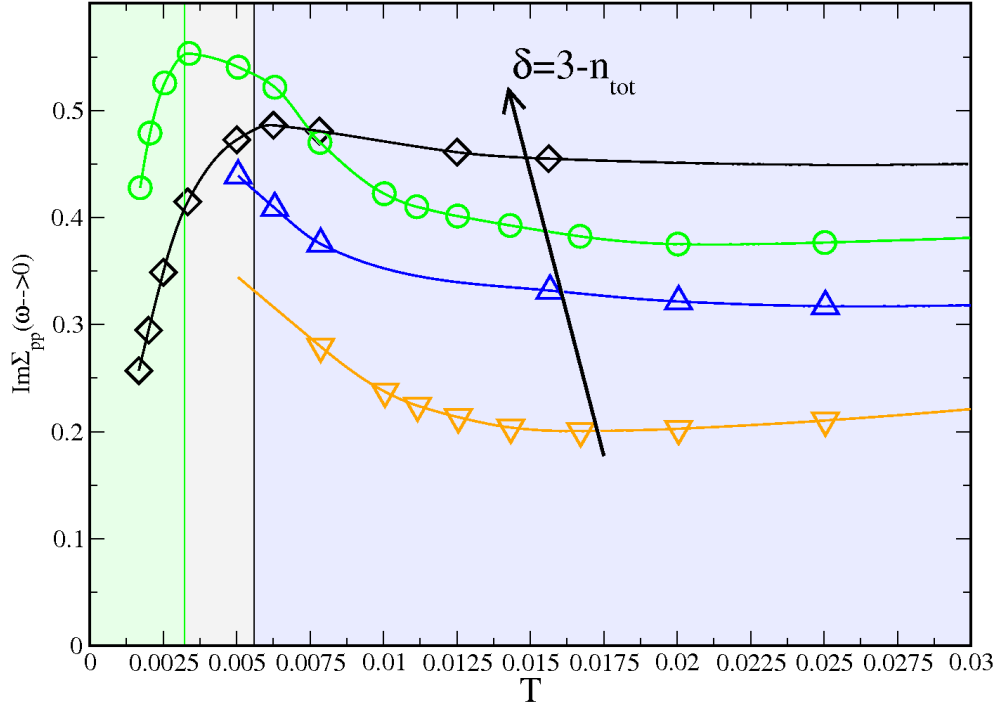


Figure 5.8: Inverse scattering rate at very low temperatures in the non-Fermi liquid regime. Data are from finite temperature ED for  $U = 2$ ,  $V_{pd} = 0.9$ ,  $\Delta = 1$  and for  $\mu = 0.43$  ( $\diamond$ ),  $\mu = 0.48$  ( $\circ$ ),  $\mu = 0.53$  ( $\triangle$ ),  $\mu = 0.58$  ( $\nabla$ ), of doping respectively  $\delta = 0.15, 0.10, 0.05, 0.01$ . The crossover point is shifted towards zero with decreasing doping. The arrow indicate the direction of increasing doping. Shaded regions underline the changing behavior in the resistivity.

## 5.4 Spin susceptibility

### 5.4.1 Enhanced spin susceptibility

In order to get some insights about the origin of this novel non-Fermi liquid state we shall study the magnetic properties of the system. The first quantity we are interested in is the local spin susceptibility, describing the response of the system to a *local* magnetic field. Local spin susceptibility is defined as:

$$\chi_{loc}(T) = \int_0^\beta \langle S_{z,d}(\tau) \cdot S_{z,d}(0) \rangle d\tau$$

where the expected value under the integral sign is the imaginary time spin-spin correlation function.  $\chi_{loc}$  can be easily calculated in QMC by means of the pseudo-spins  $\{\sigma\}$  representation, introduced via the Hubbard-Stratonovich transformation (cf Chap. 2):

$$\langle S_{z,d}(\tau) \cdot S_{z,d}(0) \rangle = \langle (n_{d,\uparrow}(\tau) - n_{d,\downarrow}(\tau)) \cdot (n_{d,\uparrow}(0) - n_{d,\downarrow}(0)) \rangle = \frac{1}{1 - e^{-\Delta\tau U}} \langle \sigma(\tau)\sigma(0) \rangle$$

where all the thermal averages have to be evaluated in the QMC sense, *i.e.* they are represented as Markov sampling in the pseudo-spins configuration space. The local spin susceptibility can also be evaluated within complete ED method using spectral decomposition of the correlation function  $\chi(\tau - \tau') = \langle S_{z,d}(\tau) \cdot S_{z,d}(\tau') \rangle$ , *i.e.*

$$\chi(\tau - \tau') = \frac{1}{Z} \sum_{n,m} e^{-\beta E_n} |\langle m | S_{z,d} | n \rangle|^2 e^{-(E_n - E_m)(\tau - \tau')}$$

In a metallic environment and at high temperature the local spin susceptibility has a typical Curie-Weiss  $T^{-1}$  behavior. The thermal energy per electron is so large that the electrons become magnetically decoupled and act as free spins. Instead, at low temperature the spin susceptibility is expected to saturate, showing a weak or constant temperature dependence (Pauli behavior), in agreement with Fermi liquid theory predictions. In the context of quantum impurity models this low temperature behavior can be interpreted as the onset of a compensation of the local magnetic moments, carried out by the conduction band electrons. Thus, the zero temperature limit of the inverse of the local spin susceptibility provides a reliable way to estimate the Kondo temperature scale, below which a local Fermi liquid state is expected to form.

In this section we want to demonstrate that throughout the non-Fermi liquid regime (tiny hole doping) the system remains highly magnetic, having electrons behaving as nearly free magnetic moments. In correspondence to this the system shows an enhanced low temperature local spin susceptibility. Normal Pauli behavior is recovered only upon further increasing the doping.

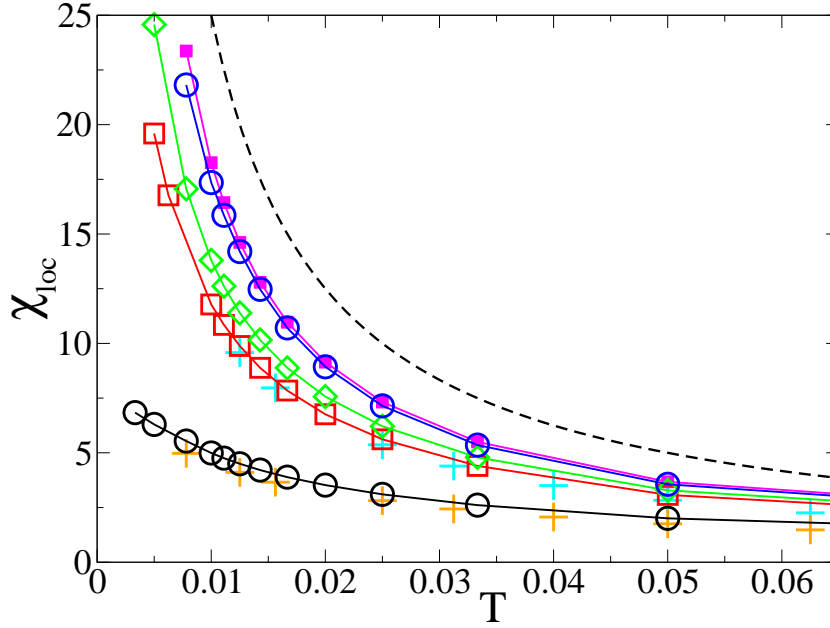


Figure 5.9: Local spin susceptibility  $\chi_{loc}(T)$  as a function of temperature for different values of doping. Data are from both QMC and finite temperature ED, for  $U = 2$ ,  $V_{pd} = 0.9$ ,  $\Delta = 1$  and for:  $\delta = 0.0$  (■),  $\delta = 0.01$  (○),  $\delta = 0.1$  (◇),  $\delta = 0.15$  (□ from ED and + from QMC),  $\delta = 0.45$  (○ from ED and + from QMC). The spin susceptibility is strongly enhanced in the tiny doped regime.

In Fig. 5.9 we present some results about the temperature behavior of the local spin susceptibility from both QMC and finite temperature ED calculations. As can be appreciated the two methods have a remarkable accord in the full available temperature range. In particular this figure shows the behavior of  $\chi_{loc}(T)$  for an increasing value of the doping, from the Mott insulator to the highly doped metallic state, this latter having Fermi liquid properties. As already pointed out (cf. Fig. 5.4) in the Mott insulating state the  $d$ -orbital electrons bear large magnetic moments, that are protracted throughout a long range of doping. Correspondingly the spin susceptibility is expected to have Curie behavior  $\chi_{loc}(T) \propto T^{-1}$ . Our results actually confirm this expectation, see Fig. 5.9. The local spin susceptibility of the undoped solution (magenta line and symbols) has a strictly diverging behavior, that can be directly compared with the  $1/4T$  behavior of free spins shown in the same figure (dashed black line).

On the other hand to the large doping solution of the model corresponds a Pauli-like spin susceptibility, with a weak temperature dependent behavior (open black circles and orange crosses). This is associated to the existence of a Fermi liquid metallic state, characterized by well formed local singlets.

In contrast to the expected Fermi liquid behavior, the local spin susceptibility of the systems

## 5. Non-Fermi liquid phase and Mottness scenario for Heavy Fermions

---

in the tiny (hole) doped regime has a strong Curie-Weiss  $\chi_{loc} \propto 1/(T + T_0)$  behavior. This quantity is greatly enhanced at low temperature throughout the non-Fermi liquid region and does not show any trace of saturation down the smallest analyzed temperature. Thus, the non-Fermi liquid regime corresponds, in terms of spin susceptibility, to a long crossover region between Curie-Weiss and Pauli behavior. It is worth to observe that the non-Fermi liquid local susceptibility  $\chi_{loc}(T)$  has a rather small change in its behavior in correspondence of a large variation of the (hole) doping  $\Delta\delta \simeq 20\%$ . The enhancement of the local spin susceptibility in the low doping region may be associated to a protracted screening effect of the doped  $p$ -holes to the more localized  $d$ -electrons, as already noticed in [95].

### 5.4.2 Exhaustion and coherence scale

The enhanced local spin susceptibility in the non-Fermi liquid phase should imply the non “effectiveness” of the Kondo screening of the  $d$ -local moments, down to vanishingly small temperatures. Lack of efficiency of the screening process within impurity lattice problems is generically associated to the *exhaustion* phenomenon [67, 9].

Exhaustion is a physical mechanism taking place in situations where the number of active conduction electrons near the Fermi surface, carrying out the screening of the local magnetic moments is strongly reduced, *i.e. exhausted*. This phenomenon has been originally proposed by Nozières to explain the suppression of the Kondo temperature scale in Kondo lattice systems [68]. The argument proposed by Nozières was roughly the following. In an exhausted system and for temperatures smaller than  $T_K$  (*i.e.* the Kondo temperature scale) the system is made of singlets and non screened local moments. The screening electron can visit different local spins by breaking the formed local singlet state and forming another one at a different lattice site. Thus the system behaves as an effective Hubbard model for unscreened local moments with a given hopping constant. One can think at this effective model as describing the dynamics of the screening clouds. Nevertheless the important point to realize is that the coherence scale associated to this model is strongly reduced. In fact, in the exhaustion limit the number of effective available conduction electrons  $N_c$  is much smaller than the number of concentrated impurities  $N_{imp}$ :  $N_c \ll N_{imp}$ . Thus the coherence scale, estimated by  $T_{coh} \sim tN_c/N_{imp}$ , may be much smaller than the expected Kondo temperature scale.

Recently [95, 96, 99] exhaustion has been invoked in the context of the DMFT solution of the periodic Anderson model, to explain the protracted screening in a metallic phase realized upon emptying the conduction band and by fixing the occupation of the correlated orbitals to one,  $n_d = 1$ . In this “Kondo lattice regime” a straightforward comparison with the original argument proposed by Nozières holds.

A natural question to pose, concerning the problem we are studying, is about the relevance

of the exhaustion in the observed breakdown of Fermi liquid phase. To answer this question it should be observed that the regime of the PAM in which this novel non-Fermi liquid state appears is substantially different from the Kondo lattice regime, in which the exhaustion regime has been originally associated and studied.

The DMFT solution of the periodic Anderson model in the regime we are focusing on shows a strong mixed-valence character, cf. Fig. 5.3. In consequence of this the number of available conduction band electrons is always finite being  $n_p = 2 - \nu$ , e.g.  $\nu \simeq 0.14$  in the Mott insulating state and with the model parameters previously specified. Nevertheless, because of the proximity to the Mott metal-insulator transition point, the real number of available carriers is strongly reduced. This number does not correspond to the nominal filling of the non correlated band, but rather to the number of doped charge carriers in the system,  $p$ -holes in the present case.

From this point of view the nearness of the system to a Mott transition point naturally (as opposite to the fine tuning of the conduction band filling in [95]) generates an exhaustion of the charge carriers. This lead to a lack of effectiveness of the screening process of the doped charge carriers ( $p$ -holes) on the large local  $d$ -moments, as a function of both doping and temperature.

A second, a perhaps more substantial, difference with respect to standard exhaustion regime is the magnetic stability of our regime. In the classical picture of exhausted systems magnetism plays in fact a major role. The ratio of the RKKY to Kondo temperature scale is greatly enhanced, thus the onset of magnetically ordered phases is generally favored. Instead the non-Fermi liquid phase observed in the proximity of the Mott transition does not appear to be screened out by the onset of any magnetic order, as will be proved in the next section.

Having cleared out, with the previous considerations, the role of exhaustion in the non-Fermi liquid regime, we can now derive an estimate for the coherence temperature of the model. An universal relation between the local Kondo temperature  $T_K$  and the temperature scale below which the screening process becomes effective, say  $T_{coh}$ , is still lacking. In this respect some results have been obtained numerically in [95, 96] and analytically in [9], invalidating the estimated relation originally proposed by Nozières. Nevertheless, following the discussion about the physical interpretation of the local spin susceptibility, it appears natural to use this latter quantity to extrapolate the coherence scale. In particular  $T_{coh}$  can be computed by the  $x$ -axis intercept of the following fit on the local spin susceptibility

$$1/\chi_{loc}(T) \propto T + T_{coh}$$

The coherence temperature describes the crossover from the non-Fermi liquid to a normal Fermi liquid phase, being the temperature below which the screening of the local  $d$ -moments by the doped  $p$ -type charge carriers becomes effective. We show in Fig. 5.10 the results of the previous extrapolation of the coherence temperature. Data have been obtained by fitting local spin

## 5. Non-Fermi liquid phase and Mottness scenario for Heavy Fermions

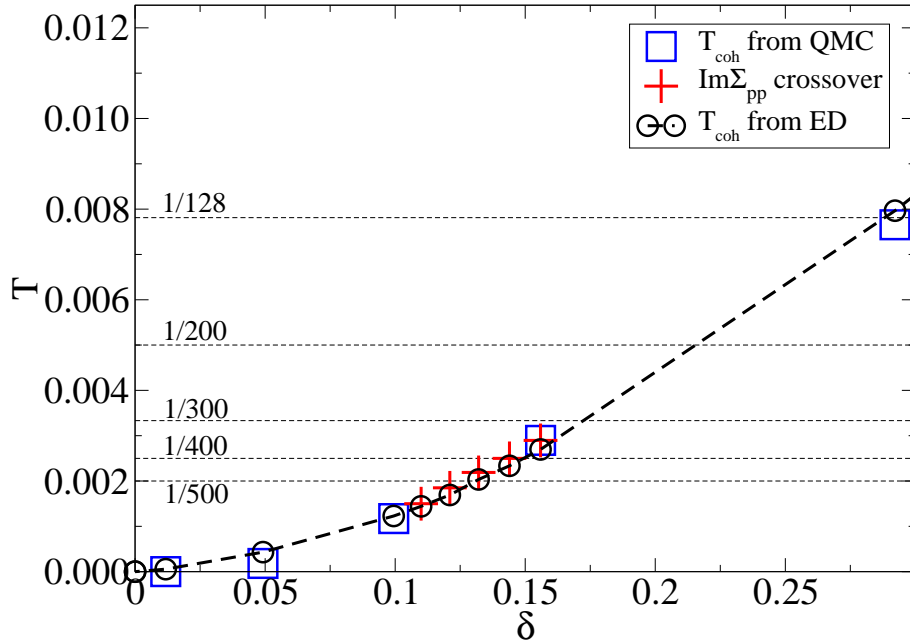


Figure 5.10: Coherence temperature scale as extrapolated from zero temperature limit of the local spin susceptibility in Fig. 5.8. Data are obtained by both ED ( $\circ$ ) and QMC ( $\square$ ) calculations finding a rather good agreement. Crossover point estimated from the behavior of the imaginary part of the conduction electron self-energy  $Im\Sigma_{pp}(i\omega_n)$  are plotted in the figure. This illustrate the physical meaning of this energy scale as that of being the temperature below which Fermi liquid regime is restored in the system. Some temperatures used in the actual calculations are reported for reference.

susceptibility (cf. Fig. 5.9) from complete ED (dashed black line and circles) and QMC (open blue squares), finding a remarkable good agreement. The same agreement is found comparing this quantity with the crossover point estimated from the low temperature evolution of the imaginary part of the conduction electron self-energy (red crosses). This provides a crosscheck of the estimated coherence temperature against an independent description of the crossover, validating our physical interpretation of the results.

As shown in Fig. 5.10,  $T_{coh}$  has an exponential behavior as a function of the doping of the form  $T_{coh} \simeq e^{-1/\delta}$ . In particular this result imply that the non-Fermi liquid phase may exist down to vanishingly small temperatures. It is worth to underline that the exponentially small behavior of the coherence temperature arise despite the model parameters have been initially chosen order one (in unit of the  $D = 2t$ ). Thus ruling out the possibility that this could be related to a “special” choice of the parameter regime. In fact the smallness of the coherence scale and the consequent breakdown of Fermi liquid phase down to vanishingly small temperatures, is entirely due to the proximity to the Mott transition point, *i.e.* thus the term *Mottness* proposed

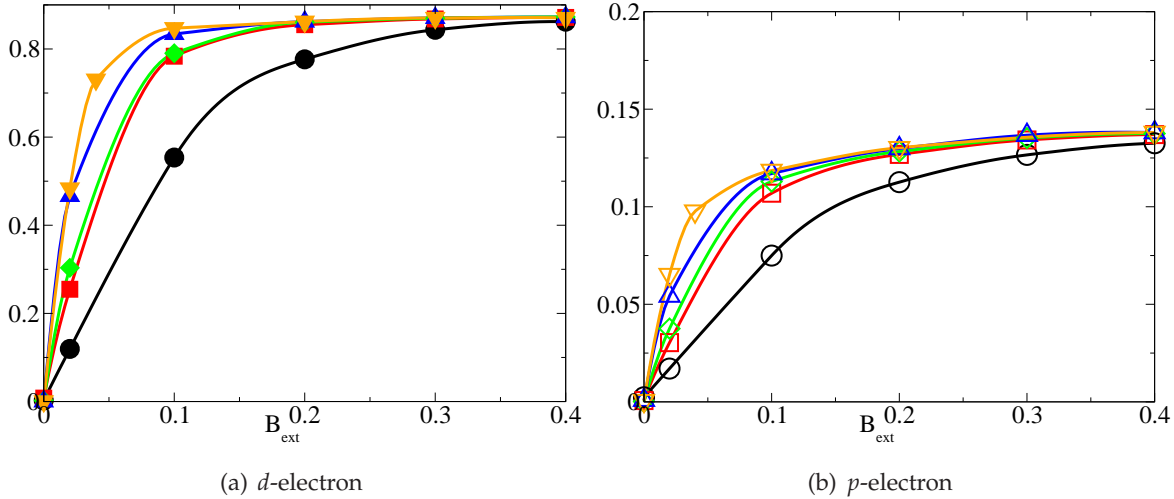


Figure 5.11: Magnetization as a function of external magnetic field for both orbital electrons  $d$  (a) and  $p$  (b). Data are from QMC at temperatures:  $T = 1/16$  (●),  $T = 1/32$  (■),  $T = 1/40$  (◆),  $T = 1/64$  (▲),  $T = 1/80$  (▼). Note that  $p$ -magnetization is much reduced with respect to the  $d$ -orbital one.

for this scenario.

## 5.5 Magnetic properties

### 5.5.1 External magnetic field

Useful information about the nature of the non-Fermi liquid phase are obtained studying the effects of magnetic ordering. In this section we shall study the response of the system to the application of an external homogeneous magnetic field  $B_{ext}$ . In a conventional Fermi liquid magnetic fields normally do not have significant impact, they merely produce a small magnetic polarization of the carriers. However in the regime we are focusing on, with a strong magnetic coupling between the light and heavy electrons combined with an enhanced local spin susceptibility, one may expect the effect of an external magnetic field to be important.

In the parameter regime we are focusing on, the main source of magnetism are the highly localized  $d$ -electrons. This can be easily deduced from the analysis of results shown in Fig. 5.4. The correlated orbitals are nearly half-filled ( $n_d \simeq 1$ ), thus their local moment is large. Moreover, the decreasing behavior of the  $d$ -orbital double occupancy as a function of doping and the lack of efficiency in the screening process both enhance their active role in the magnetism of the system. On the other hand  $p$ -orbitals are almost completely filled, so we expect them to be almost magnetically inert and to not contribute significantly to the response of the system, see

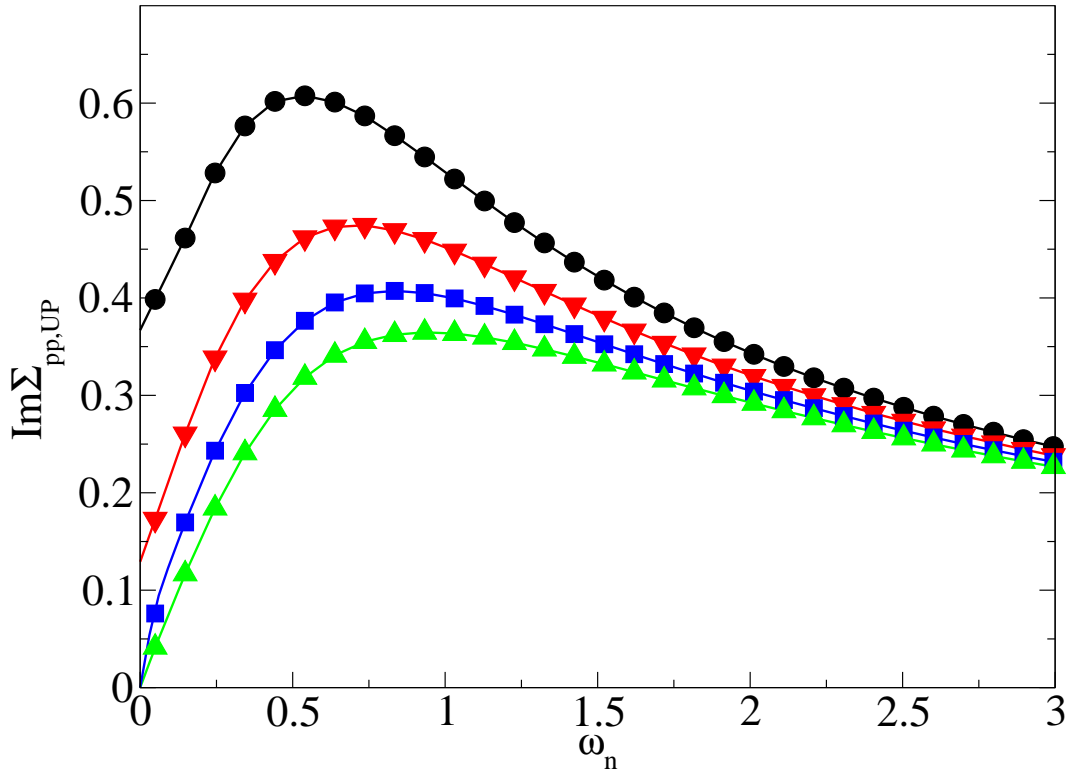


Figure 5.12: Main panel: imaginary part of the majority-spin  $p$ -electron self-energy under an external magnetic field  $h$  as a function of Matsubara frequency. Data from QMC solution at  $T = 1/64$  and  $\delta = 0.05$  ( $\mu = 0.53$ ). The  $B_{ext} = 0$  paramagnetic NFL state is shown with circles. The rapid crossover to the Fermi liquid phase is observed as a function of increasing field strength  $B_{ext} = 0.0$  ( $\bullet$ ),  $0.02$  ( $\blacktriangledown$ ),  $0.04$  ( $\blacksquare$ ),  $0.1$  ( $\blacktriangle$ )

Fig. 5.11. Nevertheless, the conduction band electrons can be indirectly affected by the orientation of the  $d$ -electrons local moment, by virtue of the antiferromagnetic binding between the doped  $p$ -holes and local  $d$ -moment. In other words we expect the Kondo screening process to greatly benefit by polarization of the  $d$ -moments induced by the action of an external magnetic field.

In Fig. 5.12 we show results from QMC calculations at  $T = 1/64$  about the low energy behavior of  $\text{Im}\Sigma_{pp}(i\omega_n)$  for an increasing strength of the external magnetic field  $B_{ext}$ . The other model parameters are:  $U = 2$ ,  $V_{pd} = 0.9$ ,  $\Delta = 1$  and  $\mu = 0.53$  corresponding to a doping of  $\delta = 0.05$ . As the figure shows the finite intercept of the imaginary part of the conduction electron self-energy is driven to zero as a small magnetic field is turned on. Thus the non-Fermi liquid state is driven towards a normal (Fermi liquid) metallic state, by the action of an external magnetic field. It is worth noting that the strength of the magnetic field producing this recovery of the Fermi liquid is about  $0.05D$ , thus of the same order of magnitude compared to

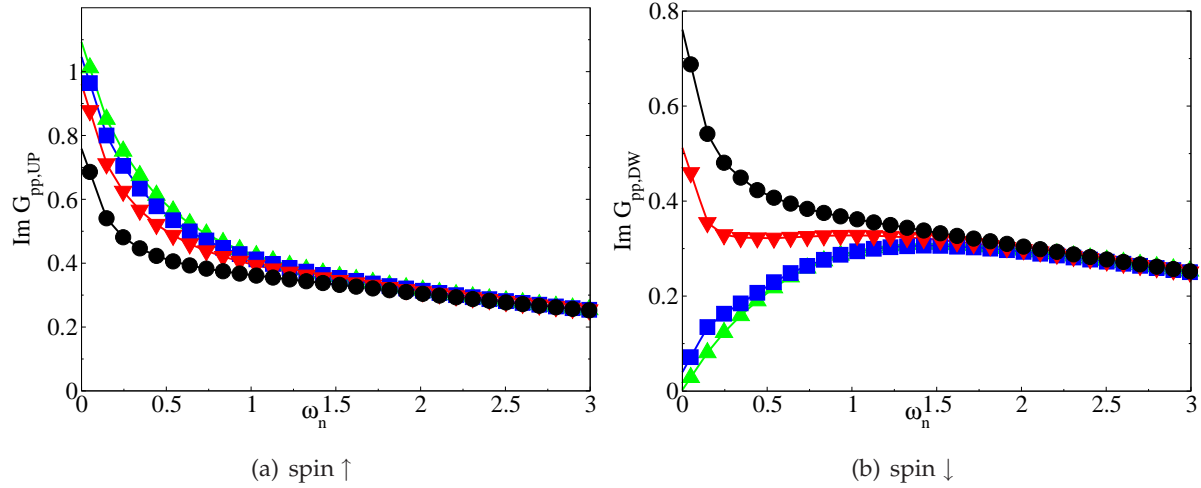


Figure 5.13: Imaginary part of conduction band electron Green's function  $\text{Im}G_{pp,\sigma}(i\omega_n)$  for increasing strength of external magnetic field:  $B_{ext} = 0.0$  ( $\bullet$ ),  $0.02$  ( $\blacktriangledown$ ),  $0.04$  ( $\blacksquare$ ),  $0.1$  ( $\blacktriangle$ ). The majority spins (a) increase their metallic character upon polarization of the system. Minority spins are driven to insulating state (b).

the temperature we are focusing on and two order of magnitude smaller than the bare model parameters.

The physical interpretation of this crossover to a Fermi liquid state driven by external magnetic field it is quite straightforward. Upon increasing the magnetic field, at constant doping, a larger and larger number of local  $d$ -moments get polarized. The few charge carriers, namely  $p$ -holes, are then greatly simplified in the work of screening out the local moments themselves, leading to a restore of a Fermi liquid metallic phase with coherent motion of the charge carriers. In other words the polarization of  $d$ -orbital local moments permits the screening cloud to dynamically screen the  $d$ -electrons local moments, dramatically increasing the coherence scale of the system. The coherent motion of the doped carriers with majority spins is then balanced by the insulating nature of the minority spins charge carriers. This phenomena is illustrated in the Fig. 5.13. There we present the behavior of both spin up and spin down Green's functions for the same strengths of the external magnetic field used in previous Fig. 5.12. In particular Fig. 5.13(a) shows the increasing metallization of the majority spin charge carriers, consequence of the Fermi liquid crossover already discussed. On the other hand the minority spins are driven towards an insulating state, characterized by the vanishing behavior of the imaginary part of their Green's function as illustrated in Fig. 5.13(b).

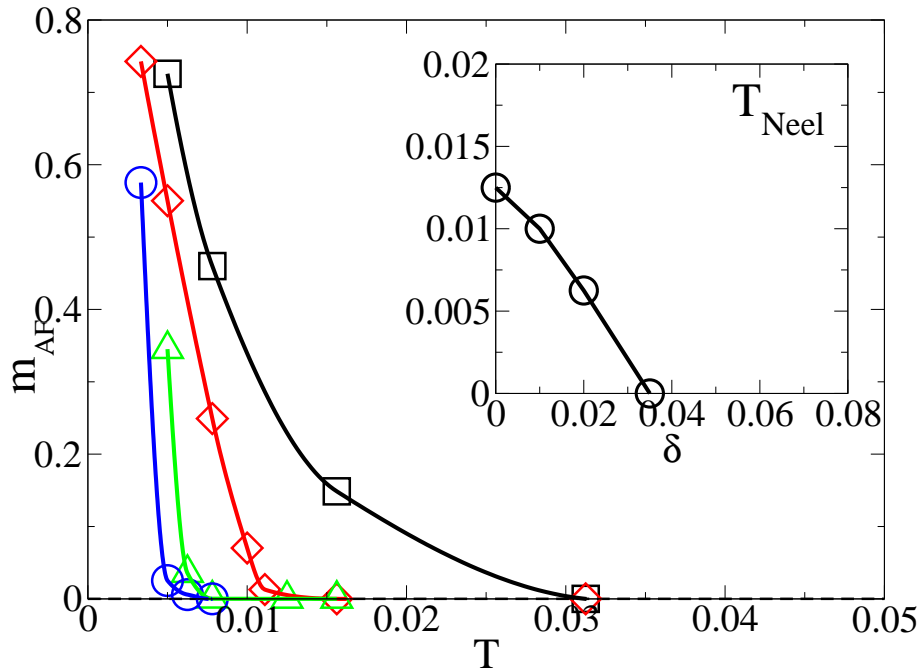


Figure 5.14: Main panel: evolution of the staggered magnetization  $m_{AF}$  as a function of temperature, for different values of doping  $\delta = 0$  ( $\square$ ),  $0.01$  ( $\diamond$ ),  $0.02$  ( $\triangle$ ),  $0.03$  ( $\circ$ ). Data are from finite temperature ED. Inset: Néel temperature as a function of doping.

### 5.5.2 Antiferromagnetic ordering

The local spin susceptibility behavior shows that the correlated electrons at the  $d$ -orbitals behaves as nearly independent spins in the paramagnetic phase. Nevertheless, they can develop weak antiferromagnetic correlations, resulting from super-exchange mechanism, *i.e.* magnetic exchange of neighboring  $d$ -electrons thru hybridization with the non correlated  $p$ -orbitals. The presence of such correlations may lead to the formation of antiferromagnetically ordered phase.

In this section we shall present results concerning the onset of an antiferromagnetic order in the periodic Anderson model and we will discuss the related properties. Most of the presented calculations have been realized with complete Exact Diagonalization, better designed to handle the small energy/temperature scales at which the weak antiferromagnetic correlations may become important. The obtained results have been compared, where possible, to QMC calculations in order to crosscheck their validity. The symmetry breaking in favor of an antiferromagnetic phase has been studied using the extension of DMFT technique detailed in Sec. 3.4.

To start with, we report in Fig. 5.14 results about the behavior of the staggered magnetization as a function of temperature for several values of the doping. We expect the Néel temperature to be maximum in the undoped regime, *i.e.* the Mott insulator. This is because the energy

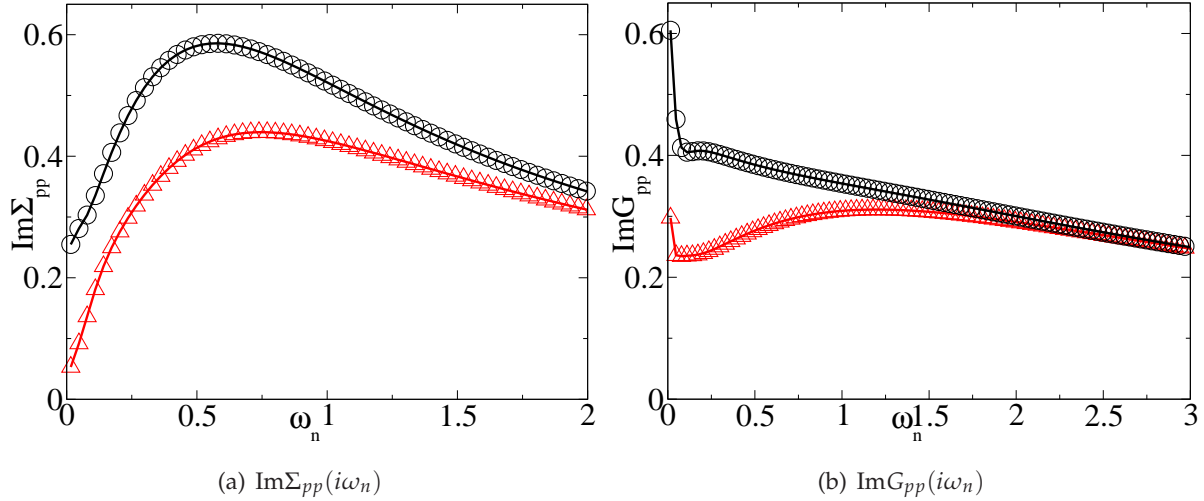


Figure 5.15: (a) Comparison between paramagnetic phase ( $\circ$ ) and antiferromagnetic phase ( $\triangle$ )  $\text{Im}\Sigma_{pp,\sigma}(i\omega_n)$  for  $U = 2.0$ ,  $V_{pd} = 0.9$ ,  $\Delta = 1$  and  $\delta = 0.01$ . (b) Comparison between the same magnetic phases and model parameters for  $\text{Im}G_{pp,\sigma}(i\omega_n)$ . The finite doping antiferromagnetic solution is a metallic state with Fermi liquid properties.

gain in developing antiferromagnetic correlations between neighboring correlated orbitals is not diminished by local Kondo screening effects. This expectation is confirmed by our calculations, as it is shown in the main panel of the figure. In the Mott insulating state staggered magnetization start to deviate from zero at temperatures of the order  $T_{Neel} \simeq 2 \cdot 10^{-2}$ . The transition from paramagnetic to antiferromagnetic phase is rather smooth and take place over a finite range of temperatures. Slightly increasing the value of the doping produce a shift of the ordering temperature to lower values. For  $\delta = 0.01$  we the transition onset at  $T_{Neel} \simeq 10^{-2}$ . This tendency is confirmed upon further increasing the doping, as demonstrated by the behavior of the staggered magnetization corresponding to larger values of the doping  $\delta = 0.02$ ,  $0.03$ . The decreasing behavior of the ordering temperature comes with an increasing sharpness of the transition, hint of an increasing criticality. At the largest analyzed value of the doping we observe an increase of the staggered magnetization of about 60% in a temperature range  $\Delta T \sim 5 \cdot 10^{-3}$ . Nevertheless, no trace of discontinuity has been observed in the order parameter. The Néel temperature continue decreasing as a function of increasing doping till it vanishes for a value of the doping  $\delta \simeq 0.04$ . This last value has been obtained by extrapolating the finite temperature curve and crosschecked with zero temperature results obtained from Lanczos ED. The behavior of  $T_{Neel}$  as a function of doping is reported in the inset of Fig. 5.14.

The transition from paramagnetic non-Fermi liquid metallic phase to the antiferromagnetic metallic phase comes with a restoring of the Fermi liquid properties. This is well illustrated in Fig. 5.15(a), where the imaginary parts of  $\Sigma_{pp}(i\omega_n)$  in the paramagnetic NFL phase (circles)

and for a value of the doping  $\delta = 0.01$ , is compared with the corresponding solution in the antiferromagnetic phase (triangles up). Data in the figure corresponds to a complete ED calculation at  $T = 1/200$ . The large finite intercept appearing in the NFL phase is driven to zero with the onset of ordered phase. The metallic character of the AFM solution is illustrated in Fig. 5.15(b), where we show the behavior of the imaginary part of the conduction electrons Green's functions in both the PM (circles) and AFM phase (triangles up).

The physical interpretation of the metallic character of the AFM phase is straightforward. In fact as soon as the local moments get ordered in a Néel state the doped charge carriers have no problem to form coherent electronic waves (with doubled wave-vector) and to get delocalized. This is in perfect agreement with what has been found in previous section where (ferro)magnetic ordering induced by external magnetic field was seen to restore Fermi liquid properties in the metallic phase.

In the last part of this thesis we shall show that the competition between magnetic interactions, namely the antiferromagnetic exchange introduced above and the ferromagnetic ordering indirectly induced by the delocalization of the doped charges, can drive the system critical and lead to a breakdown of Fermi liquid properties.

## 5.6 Thermodynamics

### 5.6.1 Specific heat and effective mass

To better compare our results to experiments and to underline the heavy fermion non-Fermi liquid character of the solution we shall now study some thermodynamic properties of the model. In particular we shall devote this and the following section to the analysis of the specific heat  $C_v$  and the entropy  $S$  as a function of the temperature. Both these two quantities are directly related to the effective mass of the charge carriers of system and are commonly used to determine the nature of the metallic state of the analyzed heavy fermion compound (cf. Chap. 1).

In order to evaluate the specific heat of the system, one needs to compute the internal energy  $\Omega$  of the model. This operation can be achieved using the expression derived in Sec. 3.3 starting from the knowledge of local Green's functions only. Once the internal energy has been obtained, specific heat  $C_v$  can be derived with (numerical) differentiation with respect to the temperature:

$$C_v(T) = \frac{\partial \Omega(T)}{\partial T} \quad .$$

Operatively the evaluation of the internal energy requires some care. The algorithm introduced in Sec. 3.3 has been in fact obtained using finite temperature formalism, thus conver-

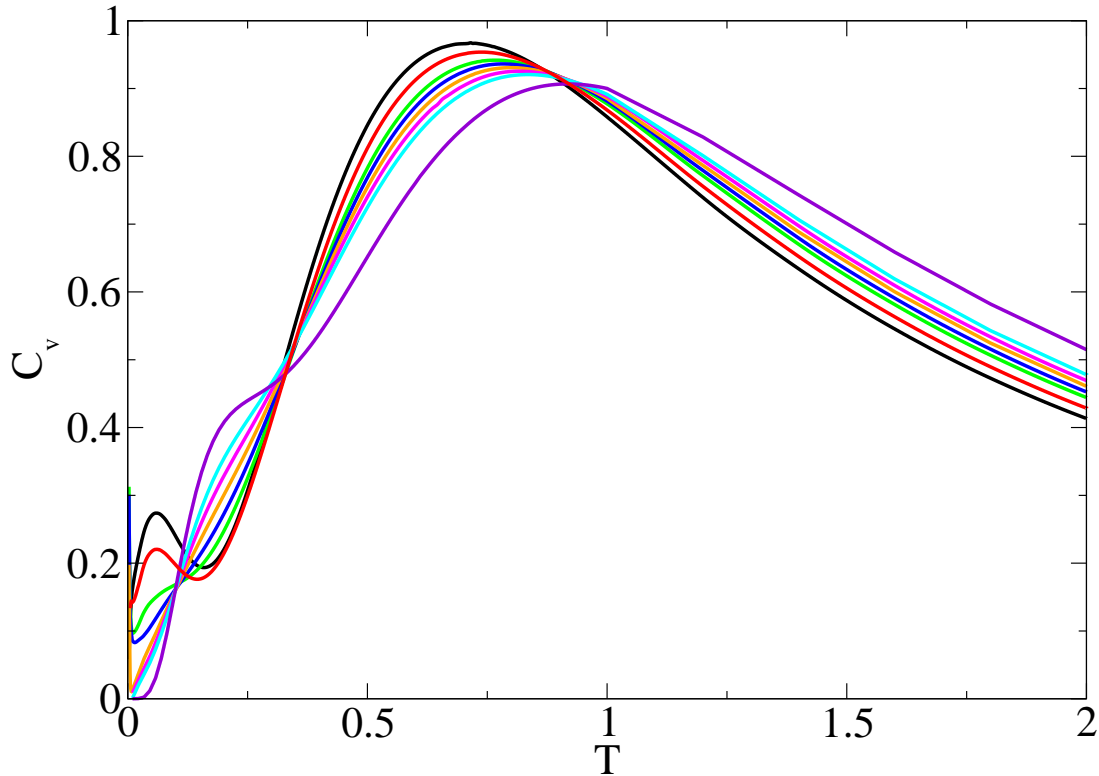


Figure 5.16: Specific heat behavior in the full temperature range and for several different values of doping,  $\delta = 0.45$  (black),  $0.29$  (red),  $0.16$  (green),  $0.10$  (blue),  $0.05$  (orange),  $0.01$  (magenta),  $0.001$  (cyan),  $0.0$  (purple), corresponding to the following values for the chemical potential  $\mu = 0.23, 0.33, 0.43, 0.48, 0.53, 0.58, 0.63, 0.83$ . Data are obtained from numerical differentiation of finite temperature ED calculations. Several benchmarks have been performed to crosscheck the validity of the algorithm.

gence of the Matsubara sums should be checked, being the Green's function slowly decaying (non-summable) in imaginary frequency. So, in order to get reliable results, some optimization strategies have to be taken into account. Beside this a huge number  $N_\omega$  of Matsubara frequency has to be evaluated at the every temperature  $N_\omega \simeq 10^6$ , causing a serious slowing down of the calculation for any fixed set of model parameters. Results for internal energy  $\Omega$  and specific heat  $C_v$  have been obtained using rather long calculations based on the exact diagonalization algorithm, with a slowly varying temperature, such that to insure a good numerical differentiation of the energy. The results obtained for several different values of the chemical potential  $\mu$ , from the Mott insulating state to the Fermi liquid metallic state at large doping, are shown in the following Fig. 5.16.

The first striking feature, shared by all the curves obtained for different values of the doping, is the large contribution at high temperature ( $T \simeq 0.75D$ ) that corresponds to the thermal

## 5. Non-Fermi liquid phase and Mottness scenario for Heavy Fermions

---

activation of the non-correlated band contribution at high energy (cf. Fig. 4.12). The long tails, sizeable till temperature of the order  $T \simeq 4D$  (not shown) are reached, have the same origin.

The specific heat at large doping (black and red lines) is characterized by the presence at low temperatures ( $T \lesssim 0.125$ ) of broad peak contribution. This corresponds to the activation of the incoherent features at the Fermi level, containing a large number of electronic states, that characterize the DMFT solution in this metallic regime. This rather large contribution is well separated, by a dip at about  $T \simeq 0.2$ , from the huge contribution at high temperature already discussed. Upon decreasing the value of the doping, the dip gets slowly filled by transfer of specific heat contribution from low to high temperature. This corresponds to a reduction of the number of available low energy states and to the formation of an electronic resonance at the Fermi level flanking the lower Hubbard band. Thus, we expect an increasing in the very low temperature contribution to the specific heat, related to the activation of such electronic excitations at the Fermi level characterizing the correlated metallic state (cf. Fig. 5.1).

Interestingly the specific heat behavior in the non-Fermi liquid phase, corresponding to small values of the doping, shows a long feature-less behavior from high to low temperature (blue, orange, magenta and cyan line). This behavior is protracted till a characteristic temperature scale weakly dependent on the doping. This long quasi-linear behavior comes with the almost complete disappearing of the broad feature at low temperature observed in the Fermi liquid regime. This behavior of the NFL specific heat is related to two circumstances: i) the weight of the electronic resonances at the Fermi level is proportional to the value of the doping (cf. Fig. 5.2(a)), ii) the lack of coherence of these resonances, that characterizes the non-Fermi liquid state at this range of temperatures and that is recovered only at much lower temperature.

Finally, the specific heat in the Mott insulating state (purple line in Fig. 5.16) shows the characteristic exponential behavior, corresponding to the presence of a spectral gap at the Fermi level and to the thermal activation of the Hubbard bands features. This behavior has been crosschecked with the solution obtained in the atomic limit of the model, finding a remarkable good agreement.

After having discussed the general behavior of the specific heat on a large temperature scale, we shall now concentrate on the low temperature regime. The results of our calculations are shown in Fig. 5.17. This figure shows the evolution of the specific heat for a decreasing value of doping, from large doping Fermi liquid phase (black line) to the Mott insulating state (purple line).

The large specific heat contribution characterizing the high doping Fermi liquid metallic phase (black and red line) acquires a linear behavior  $C \simeq \gamma T$  at low temperature, as predicted by Fermi liquid theory. The electronic specific heat constant  $\gamma$  is directly related to the size of the effective mass  $m^*/m$ . Thus, the large value attained by this constant in the high doping

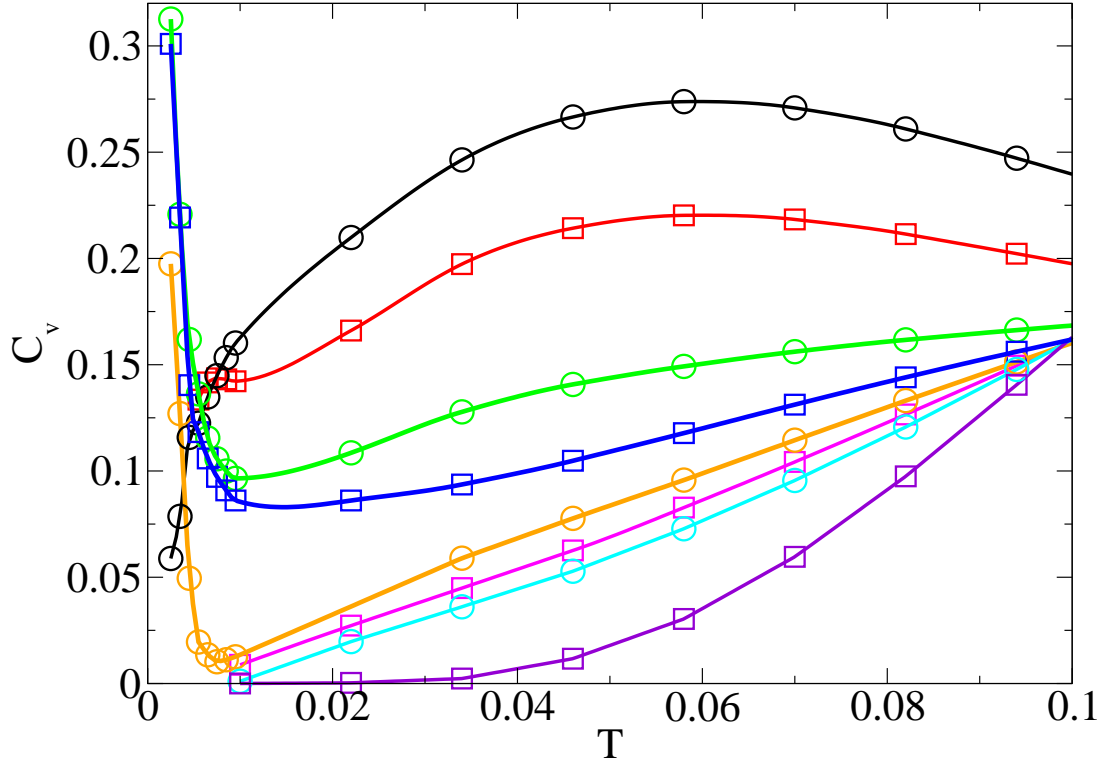


Figure 5.17: Specific heat  $C_v$  in the low temperature regime and for doping values from metallic high doping Fermi liquid region to Mott insulating state. From top to bottom:  $\delta = 0.45$  ( $\circ$ ),  $0.29$  ( $\square$ ),  $0.16$  ( $\circ$ ),  $0.10$  ( $\square$ ),  $0.05$  ( $\circ$ ),  $0.01$  ( $\square$ ),  $0.001$  ( $\circ$ ),  $0.0$  ( $\square$ ), corresponding to the following values for the chemical potential  $\mu = 0.23, 0.33, 0.43, 0.48, 0.53, 0.58, 0.63, 0.83$ . Data are from numerical differentiation of finite temperature ED calculations.

metallic phase corresponds to the formation of a Fermi liquid metal with strongly renormalized masses, *i.e.* an heavy fermion Fermi liquid state.

The specific heat behavior in the non-Fermi liquid phase is characterized by a large log-divergent behavior  $C/T \simeq -\log(T)$ . Logarithmic divergences in the specific heat are commonly considered as an hallmark of the breakdown of the Fermi liquid properties of the metallic state (cf. Chap. 1). The existence of a crossover to a Fermi liquid phase at very low temperatures (cf. Sec. 5.3), coming with the formation of coherent quasiparticle excitations, hints that at sufficiently low temperature the specific heat may crossover to the expected linear Fermi liquid behavior. Thus, the log-divergent behavior may be interpreted as the precursor of the formation, at low enough temperature of a coherent quasiparticle with a dramatically enhanced effective mass. Nevertheless, at sufficiently low doping the exponential vanishing of the crossover temperature can make the linear Fermi liquid behavior unobservable to all purposes.

It is then worth to observe how exhaustion of the charge carriers is reflected on the specific

## 5. Non-Fermi liquid phase and Mottness scenario for Heavy Fermions

---

heat behavior. The rather smooth formation of the large log-divergence at low temperature and intermediate doping (green and blue line) assumes a more sudden character upon lowering the value of the doping. The formation of logarithmic divergence becomes unobservable with our algorithm at doping smaller than 1%, *i.e.* very near to the Mott metal-insulator transition point.

### 5.6.2 Entropy

Other useful insights about the microscopic nature of this novel non-Fermi liquid phase and the formation of an heavy fermion state at very low temperatures can be deduced by examining the entropy. This quantity may reveals the temperature evolution of the quenching of the local moments, indicating in particular to what extent they may participate in the breakdown of the Fermi liquid properties.

Entropy  $S$  can be directly evaluated from the knowledge of the specific heat, using the following thermodynamic relation:

$$S(T) = \int_0^T dT' \frac{C_v(T')}{T'} .$$

In the very high temperature limit  $S(T)$  is expected to saturate to  $S_\infty = \log(16)$ . This value corresponding to the activation of the  $4 \times 4$  degrees of freedom of the two orbitals per site forming the periodic Anderson model (cf. atomic limit of the model Sec. 3.1). We checked the existence of this limit both by calculating the entropy from the long tail of the specific heat shown in Fig. 5.16 and by evaluating the entropy within the atomic limit solution of the model. This latter has found to be in a remarkable good agreement with the entropy behavior of the Mott insulating solution.

Exploiting the existence of such an high temperature limit we may rewrite the previous formula for the entropy as follow:

$$S(T) = \log(16) - \int_T^\infty dT' \frac{C_v(T')}{T'}$$

Despite its apparent simplicity this second expression has the main advantage of being independent of the details of the specific heat behavior at temperatures smaller to those at which the entropy is evaluated. Thus the entropy function is obtained by solving the model at very high temperature and then slowly decreasing it, till breakdown at low temperatures of the algorithm used to get the specific heat . In practice a suitable interpolating scheme has been used to increase the number of points of the specific heat function and to obtain smoother curves.

In the inset of the next Fig. 5.19 we illustrate the saturation of the entropy to  $\log(16)$  by showing the behavior of the entropy for different values of the doping, from the Mott insulator

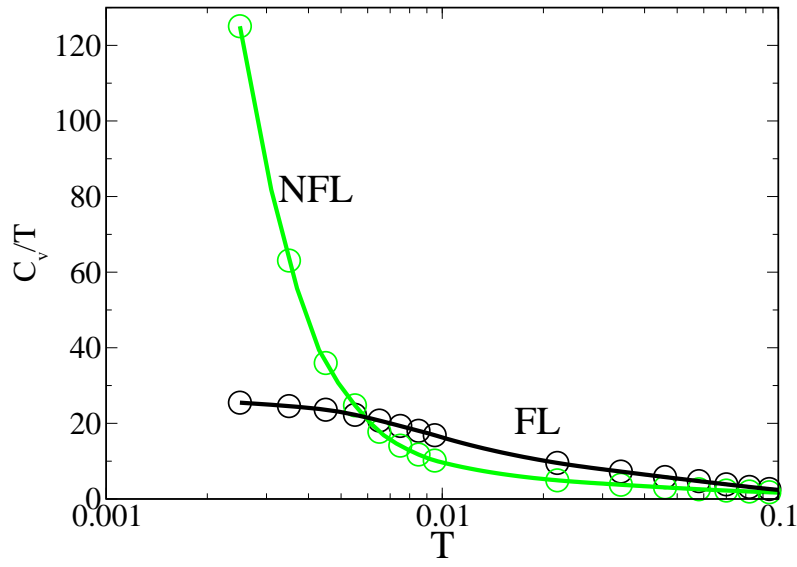
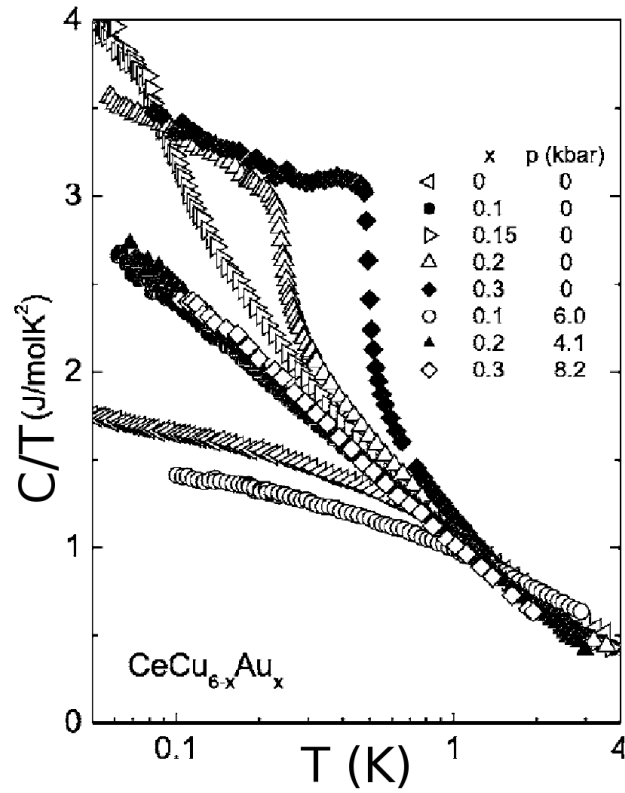
(a)  $C_v/T$  Vs.  $\log(T)$ . DMFT calculation(b)  $C_v/T$  Vs.  $\log(T)$ . Experimental results for  $CeCu_{6-x}Au_x$ 

Figure 5.18: *Qualitative* comparison between the electronic specific heat obtained within our theory and experimental results for an heavy fermion compound.

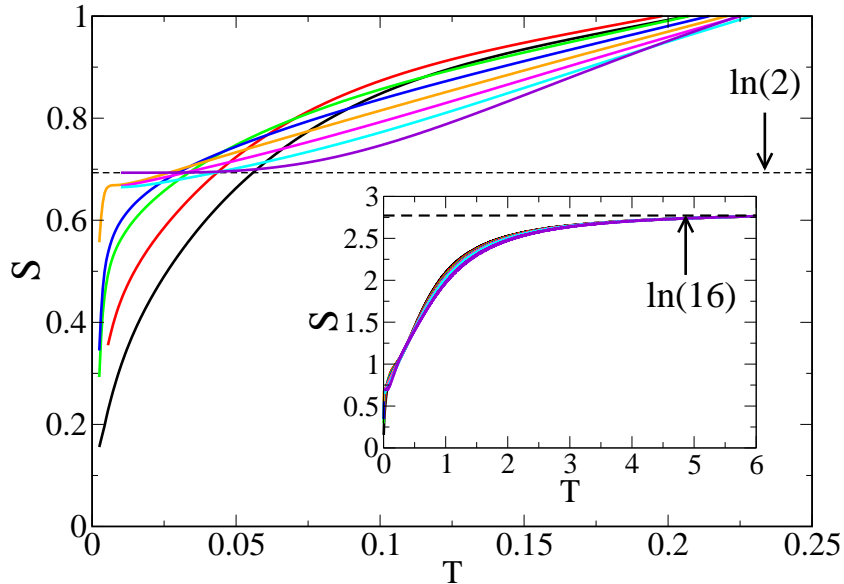


Figure 5.19: Entropy  $S(T)$  as a function of low temperature and for several different values of doping across the NFL region. The doping and the colors of the curves are the same as in Fig. 5.16. Data are obtained by numerical numerical integration of fitting curves of the specific heat  $C_v$ . Inset: high temperature limit of the entropy. The curves show a saturation to  $\log(16)$  corresponding to the activation of all degrees of freedom at a single site of the PAM.

to the large doped Fermi liquid, in a wide temperature range. Due the presence of very long tails in the specific heat behavior, the saturation appears to be effective only for temperatures of the order  $T \simeq 5D$ .

In the main panel of same figure 5.19, we present the results of our calculations, namely the low temperature behavior of the entropy for the same values of the doping discussed in the previous section.

The entropy behavior of the Mott insulating state (purple line) shows a residual entropic contribution of  $S(T = 0) = \log(2)$ . This value is attained at finite temperature and corresponds to the existence of unquenched spins in the insulating phase. It is interesting to observe that, despite this Mott insulating state is obtained by localization of a composite object, the behavior of the residual entropy is in perfect agreement with the results of the one band Hubbard model [31].

On the opposite side, the Fermi liquid metallic state obtained at large values of the doping shows a linearly vanishing behavior of the entropy at low temperature (black line). This behavior corresponds to the formation of heavy effective masses for the charge carriers. The value of the linear slope becomes larger and larger upon decreasing the doping, signalling the increasing renormalization effect of the effective masses (red line).

In correspondence of the logarithmic divergences observed for the specific heat, the entropy acquire a steeper behavior at low temperature (green and blue lines). Approaching the Mott insulator this critical behavior of the entropy is enhanced. For doping of about  $\delta \sim 5\%$  the entropy  $S(T)$  shows the existence of a “plateau” at a value  $S \simeq C \log(2)$ , with  $C < 1$ . This can be associated with the exhausted screening of the unquenched local moments.

The lack of precision of the algorithm used in this work does not permit us to observe the evolution of such a feature for smaller value of the doping, even if a clear tendency of the entropy curves to form plateaux below  $\log(2)$  can be clearly appreciated [10].

From the knowledge of the entropy as a function of temperature other interesting insights can be obtained, about the formation of the Zhang-Rice singlets. As we have discussed above, the formation of such states is the result of the Kondo screening process that takes place between the doped carriers (namely  $p$ -holes) and the more localized  $d$ -orbital electrons. We have estimated the coherence temperature below which the liquid of singlets characterizing this metallic state acquires Fermi liquid properties. Nevertheless no information about the temperature at which the screening process start have been derived. We are now in the position of filling this hole. The temperature below which the screening process starts taking place can in fact be estimated as the value of the temperature at which the entropy of the metallic solution attains a value  $S(T_{unq}) = \log(2)$ . This value corresponds to the presence in the system of unquenched spin, Thus, the onset of a screening process at temperatures  $T_q < T_{unq}$  should lead to a smaller value of the entropy  $S(T_q) < \log(2)$ . As one can easily understand from the analysis of Fig. 5.19 this quantity, estimating from below the  $T_{Kondo}$  scale for the formation of local singlets, is a slowly decreasing function of the doping and results to be much larger than the coherence scale reported in Fig. 5.10.

## 5.7 Mottness scenario

We shall now summarize the results obtained about this novel heavy fermions non-Fermi liquid state in two phase diagrams. We discuss both the physical origin of the breakdown of the Fermi liquid properties and how the non-Fermi liquid state can be tuned by either doping or external magnetic field. The obtained phase diagrams account for some properties of the non-Fermi liquid phase in heavy fermion systems and are in qualitatively agreement with some of the NFL phenomenology observed in experiments [94].

### 5.7.1 $T - \delta$ phase diagram

In the previous sections we have shown the existence of a non-Fermi liquid state in the DMFT solution of the periodic Anderson model. Moreover we have observed the crossover to a nor-

## 5. Non-Fermi liquid phase and Mottness scenario for Heavy Fermions

---

mal Fermi liquid metallic phase at very low temperature, as well as the formation of an antiferromagnetic order for low enough temperature and doping. All these results can be summarized in a phase diagram temperature versus doping, presented in the following Fig. 5.20. This phase diagram has been obtained by extrapolating to zero energy of the imaginary part of the conduction electron self-energy  $\text{Im}\Sigma_{pp}(\omega \rightarrow 0)$ , *i.e.* the scattering rate, for many different values of doping and temperature. The results so obtained have been normalized to the maximum value attained by each self-energy function:  $\max\{\text{Im}\Sigma_{pp}(i\omega_n)\}$ .

The figure describes the character of the DMFT solution of the model thru the behavior of the normalized scattering rate as a function of both doping and temperature. Comparison with real temperature has been obtained by fixing the energy unit  $D = 2t$ , corresponding to the half bandwidth of the conduction electrons density of states. In the present case we have chosen it such that  $D = 1eV \simeq 10^4K$  (with  $k_B = 1$ ). This parameter can of course be adjusted in order to obtain a better comparison with experimental results.

In the phase diagram of Fig. 5.20 we show how cooling down the system may lead to increasing critical character of the DMFT model solution, eventually ending in a breakdown of the Fermi liquid properties at very low temperatures and small values of doping.

For a large value of the doping and low enough temperatures the solution has Fermi liquid metallic character. This is illustrated by the wide dark-blue region on the right bottom part of phase diagram (FL). The triangular shape of this Fermi liquid region underline the fact that exponentially small temperatures are required at low doping to construct coherent electronic excitations and to form the Fermi liquid metallic state. This behavior is also underlined by the coherence temperature  $T_{coh}$ , indicated in the phase diagram by the dashed blue line and circles. This line roughly separates the more blueish area corresponding to the Fermi liquid metallic phase from the critical area in light orange and white where the system shows non-Fermi liquid properties. The coherence temperature has been obtained by extrapolation to zero temperature of the local spin susceptibility  $\chi_{loc}(T)$  (cf. Sec. 5.4). The low temperature Fermi liquid region below the dashed blue line is characterized by an enhanced effective mass, hinted by the steep linear behavior of the electronic specific heat  $\gamma = C/T$ . Thus, this region corresponds to an heavy fermion metallic phase.

On the other side of the plot, for low doping ( $\delta < 0.04$ ), it is well visible a second deep-blue region, corresponding to the antiferromagnetic *metallic* phase. This region is delimited by the solid green line indicating the evolution of the Néel temperature as a function of doping. The normal metallic behavior in the AFM phase is due to the Néel ordering of the local moments permitting to the doped charges to easily delocalize.

In between these two well defined metallic phases the system shows a large region where Fermi liquid properties breakdown. The large finite value of the normalized scattering rate, in

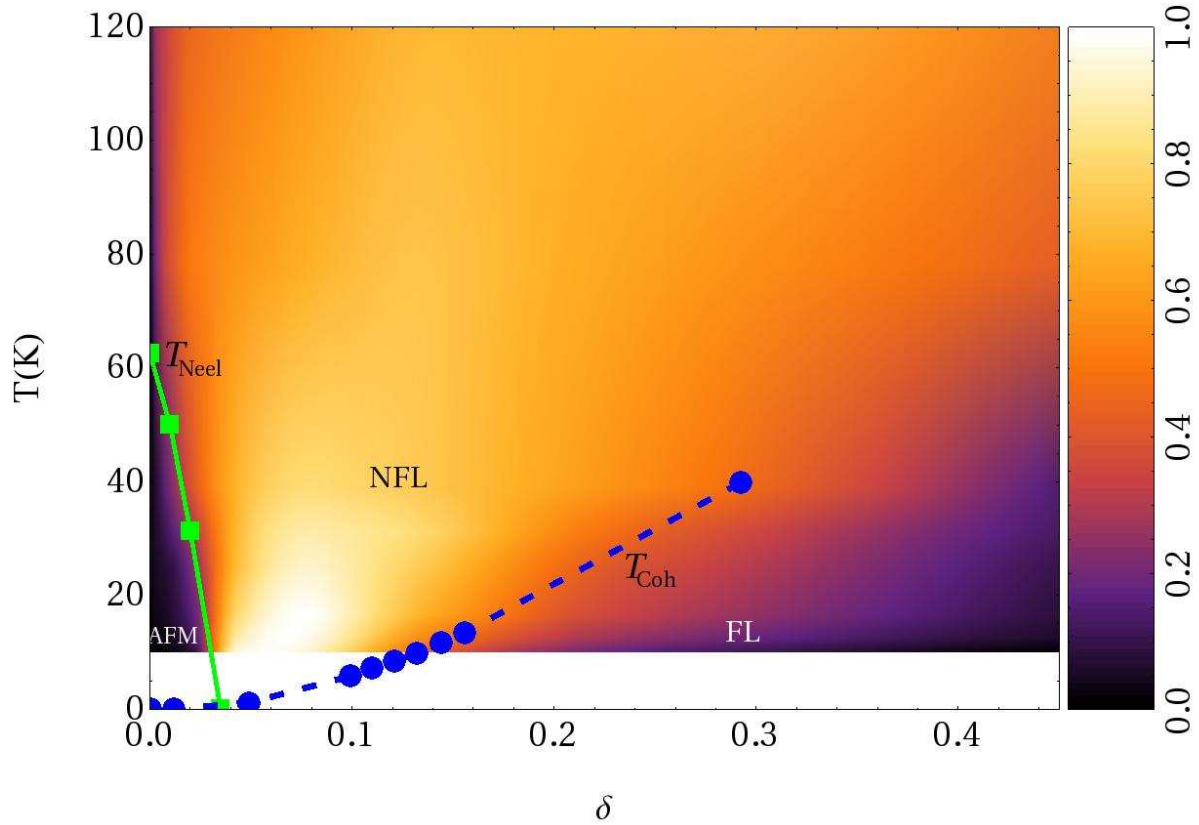


Figure 5.20: Intensity plot of the scattering rate  $\text{Im}\Sigma_{pp}(\omega \rightarrow 0)$  as a function of doping  $\delta$  and  $T$ . For visualization, the scattering rates are normalized to  $\max\{\text{Im}\Sigma_{pp}(\omega_n)\}$  at each  $(\delta, T)$ . The green solid line with square dots at low  $\delta$  is  $T_{\text{Neel}}$  and gives the AFM phase boundary (The  $T=0$  data-point is obtained from ED). The blue dashed line with circle dots denotes the numerical estimate for the crossover scale  $T_{\text{coh}}$ . It is obtained from the extrapolation of the low  $T$  behavior of  $1/\chi_{\text{loc}}(T)$  (cf Sec. 5.4).

## 5. Non-Fermi liquid phase and Mottness scenario for Heavy Fermions

---

the figure corresponding to the orange-to-white critical region (NFL), indicates the increasing critical character of the model solution. The fluctuating nature of the local moments of the correlated electrons prevents the formation of coherent electronic waves, *i.e.* long-lived quasiparticles. The non-Fermi liquid character of the solution is underlined, besides the finite scattering rate, by the log-divergent behavior of the electronic specific heat  $\gamma = C/T \simeq -\log(T)$ . This result is in qualitative agreement with many experimental observation of breakdown of the Fermi liquid properties in heavy fermion systems, cf. Fig. 5.18. At low dopings conventional Kondo screening becomes effective only at extremely low (*i.e.* vanishing) temperature. This behavior is related to the exhaustion problem, induced by the proximity to the Mott transition point ( $T = 0, \delta = 0$ ).

Interestingly the non-Fermi liquid phase is not screened out from the onset of the AFM metallic phase. This demonstrates that the non-Fermi liquid state is stabilized by magnetism. Magnetic stability is a property that is not shared with standard exhaustion scenario. Because of the presence of large unscreened magnetic moments, exhausted systems are usually found to be unstable towards magnetic ordering.

Thus, the scenario we propose and that is illustrated by the phase diagram in Fig. 5.20 describes the transition from a paramagnetic non-Fermi liquid state to an antiferromagnetic metallic one, qualitatively similar to what is often observed in heavy fermion compounds with non-Fermi liquid properties [94]. Preventing the system to antiferromagnetically order, *e.g.* introducing lattice frustration in order to suppress the ordering temperature scale, would permit to the paramagnetic non-Fermi liquid phase to persist till the boundary with the Mott insulator at zero doping. In this case we would obtain a scenario for the non-Fermi liquid to paramagnetic insulator, or spin glass, transition. These type of transitions, far from magnetically ordered phases, are observed in some heavy fermion compounds.

### 5.7.2 Competing magnetic interactions: $T - B_{ext}$ phase diagram

The stability with respect to magnetic ordering is a strong property of the non-Fermi liquid phase, which can be traced back to its physical origin. In our scenario the breakdown of the Fermi liquid properties down to exponentially small temperature is due to the strong magnetic frustration of the  $d$ -electrons local moment. The incoherent nature of these local moments is consequence of the competition between two different magnetic interactions.

Neighboring localized  $d$ -orbital electrons in the Mott insulating state develop sizeable *antiferromagnetic* correlations, as a results of super-exchange processes induced by the finite hybridization with the conduction band. These can be understood in terms of the mapping of the correlated band (near the Fermi level) to the Hubbard model. This antiferromagnetic interaction persist in the low doping limit and is responsible for the AFM metallic state observed in

the phase diagram of Fig. 5.20.

On the other hand it should be realized that at larger values of the doping and low temperatures, in a regime dominated by Fermi liquid properties, a competing *ferromagnetic* interaction appears. This interaction is indirectly induced by delocalization of the doped charges involved in the Kondo screening process, with a mechanism reminding the Nagaoka ferromagnetism.

To understand how delocalization of the doped  $p$ -type carriers (holes) and the Kondo screening can indirectly lead to the formation of ferromagnetic exchange let's considering the following. The doped carriers, say  $p$ -holes, are subject to a strong on-site antiferromagnetic interaction with the local  $d$ -moments, in terms of impurity model this interaction corresponds to the local Kondo screening. Nevertheless, the doped carriers also need to delocalize in order to gain kinetic energy. But each time a  $p$ -hole hops from one site to its nearest neighbor it may break the magnetic bound with the correlated electrons, losing a substantial amount of energy. Moreover it left a local moment unscreened thus increasing the fluctuating nature of the local magnetization. Therefore in order to hop, the doped holes need the neighboring local moments to have the same magnetic orientation as the one on the current site. Thus the system can gain energy from ordering the local  $d$ -moments ferromagnetically. The gain is double: beside the kinetic energy gained by delocalization, this process prevent the doped charges to lose the local Kondo binding energy.

This discussion is substantiated by our study of the response of the system to the application increasing external magnetic field strength  $B$  on the antiferromagnetic metallic phase. The results of this calculation are reported in the following Fig. 5.21. We mapped out the phase diagram as a function of temperature and external field  $B$ , by analyzing the behavior of the scattering rate of the system  $\text{Im}\Sigma_{pp}(\omega \rightarrow 0)$ , normalized to the maximum value of the same function, in a wide range of temperature and forcing field.

At  $B \rightarrow 0$  the solution corresponds to the antiferromagnetic metallic state at  $\delta = 0.01$  already discussed in the previous sections. The Fermi liquid character of the solution corresponds in the phase diagram to the small dark region in the bottom left part of the plot, enclosed by the light green dashed curve.

Upon increasing the external magnetic field the system is driven to a critical/non-Fermi liquid phase, corresponding to the light orange-to-white region. This calculation demonstrate that the breakdown of the Fermi liquid properties can be understood as resulting from the competition between antiferromagnetic correlations driving the AFM phase and the ferromagnetic interaction, favored by the application of the external magnetic field. Upon increasing the strength of the external magnetic field the large local magnetic  $d$ -moments become strongly frustrated and act as scattering centers for the motion of the doped charge carriers ( $p$ -holes). From the point of view of the underlying effective impurity model the AFM/FM competition

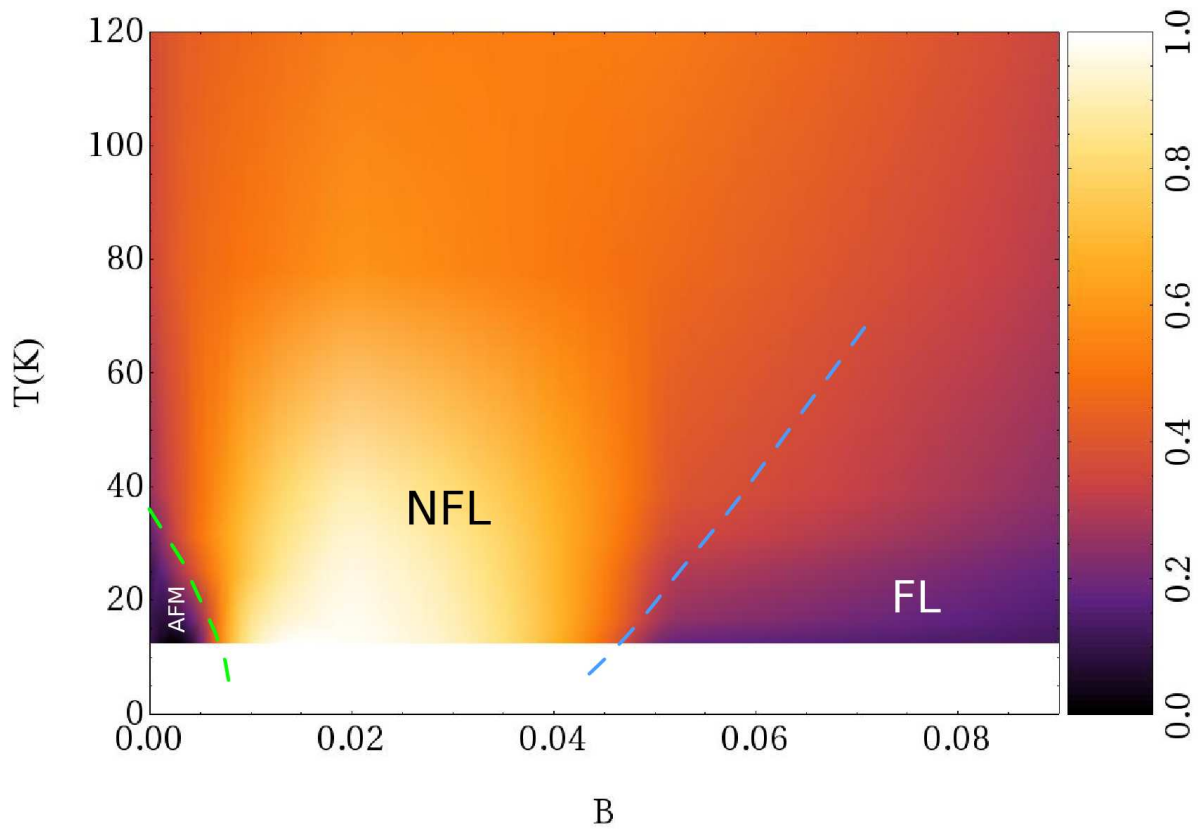


Figure 5.21: Intensity plot of the scattering rate  $\text{Im}\Sigma_{pp}(\omega \rightarrow 0)$  as a function of external magnetic field  $B_{ext}$  and  $T$ , at fixed doping  $\delta = 0.01$ . For visualization, the scattering rates are normalized to  $\max\{\text{Im}\Sigma_{pp}(\omega_n)\}$  at each  $(B, T)$ .

lead to an highly fluctuating local magnetization. The local fluctuating magnetic field couples to the itinerant degrees of freedom of the doped charges, preventing the formation of a coherent electronic waves.

For large enough  $B$  the magnetic field induces ferromagnetic order to the local  $d$ -moments, thus leading to the formation of a normal polarized metallic state, corresponding in the phase diagram in Fig. 5.21 to the large blueish region on the bottom right part of the plot and separated by the light blue dashed line.

Our results demonstrate that a *local* fluctuating magnetization, produced by unquenched moments, acts a sufficient source of scattering for the doped charges in order to prevent the formation of a Fermi liquid metallic state. The resulting NFL phase can be tuned by both doping or magnetic field resulting in different phase diagrams. These can account for some of the many aspects of the non-Fermi liquid phenomenology in heavy fermions systems. Indeed several scenario for the breakdown of the Fermi liquid phase and its transition to a metallic phase, such as towards an AFM or a FM or moreover to a Spin Glass state, are readily available with the DMFT solution of the model.

## 5.8 Conclusions

In conclusion we have illustrated with the Mottness scenario for non-Fermi liquid in heavy fermion systems. We have first discussed the properties of the correlated metal, obtained upon positive doping the Mott insulating state (cf. Chap. 4). This metallic state is formed by a liquid of local singlets, resulting from Kondo binding between the large magnetic moments of the correlated electrons and the doped charge carriers (*e.g.*  $p$ -holes).

Surprisingly this correlated metal does not follow, down to vanishing temperature, the usual Fermi liquid predictions, *i.e.* can not be described in terms of long-lived electronic excitations. The formation of Fermi liquid state is recovered only cooling down the system to temperature exponentially small in the doping (coherence temperature  $T_{coh}$ ). The existence of such a reduced coherence scale, with respect to the rather large Kondo temperature, is an hallmark of exhaustion phenomena. The presence of exhaustion in our model solution is related to the proximity to the Mott insulating state. We underlined the main differences with the standard exhaustion mechanism, introduced in the context of Kondo lattice problem.

The system in the non-Fermi liquid state recovers the usual Fermi liquid properties by the application of an external homogeneous magnetic field. On the other hand near the Mott insulating state correlated  $d$ -orbitals, bearing large magnetic moments, can develop antiferromagnetic correlations. These lead to formation of antiferromagnetic order in the limit of low doping and low enough temperatures. The physical origin of the observed breakdown of the

## 5. Non-Fermi liquid phase and Mott scenario for Heavy Fermions

---

Fermi liquid properties has been traced back to the existence of two competing magnetic interaction, namely the antiferromagnetic super-exchange and a ferromagnetic correlation induced by carriers delocalization. This competition lead to the formation of strongly fluctuating local magnetization, that prevent the formation of long-live electronic waves, *i.e.* quasiparticles.

# Concluding remarks and perspectives

The main goal achieved in the work presented in this thesis has been the derivation of the “Mottness” scenario, *i.e.* a scenario based on the proximity to a Mott transition, for the non-Fermi liquid phase of heavy fermion systems. The presented results and phase diagrams are in qualitative agreement with the observed non-Fermi liquid heavy fermion phenomenology. We have also shown that the non-Fermi liquid state can be tuned by either doping or magnetic field, similarly to what can be observed in the experiments.

The results of this thesis have been obtained in the framework of DMFT solution of a canonical strongly correlated model commonly used to study heavy fermion systems, namely the periodic Anderson model. We demonstrated that, contrary to conventional expectations, a non-Fermi liquid state can be readily obtained within DMFT. Moreover, our approach shares an important ingredient with other common approaches to non-Fermi liquid behavior [94, 14], namely the proximity to a quantum phase transition. But unlike the other approaches, within the scenario we proposed the relevant quantum transition is a Mott metal-insulator transition.

This approach presents a slightly different point of view on the breakdown of the Fermi liquid properties in strongly correlated models, showing that coupling to long wavelength magnetic fluctuations (totally absent in DMFT) is not a prerequisite for the realization of a non-Fermi liquid scenario. *Local* temporal magnetic fluctuations alone, in our case originated by strong competition of magnetic interactions, can provide a sufficient source of scattering in order to prevent the formation of coherent electronic excitations.

Our results, offering a rather new approach to the challenge posed by non-Fermi liquid behavior in correlated systems, is open to further researches in several directions. The first and probably most interesting direction to follow is to study the possible existence of a superconductive phase at very low temperature. In fact, at temperatures of the order of the coherence scale, the ferromagnetic correlations induced by delocalization of the doped charges may promote the formation of superconductive pairs between doped charges. Thus, the pairing mechanism could be induced by magnetic interactions rather than phonons coupling. Interestingly

the temperature scale below which superconductivity may be effective will be of the same order of magnitude of that generally observed in heavy fermion compounds (*i.e.* about 1K, cf. Chap .1).

On the other hand, the connection of our scenario with the recently proposed Kondo breakdown near selective Mott transition it is worth to be clarified, looking for possible contact points [72, 73]. Despite no orbital selective Mott transition is possible in our model, the inclusions of other terms in the initial Hamiltonian (cf. (3.1)) such as local correlation on the conduction band, may break this property and lead to an OSMT [18], in the neighborhood of which non-Fermi liquid state can be observed. Recently some results concerning the existence at zero temperature of an OSMT in the PAM has been obtained by [17], studying the competition of the Kondo and RKKY interaction (Doniach diagram) by means of a suitable cluster extension of DMFT. On this line it would be of some interest to explore the affinity of the Mottness scenario obtained within DMFT solution of the PAM and the Doniach diagram.

Going back to the ZSA diagram discussed in Sec. 4.1, it is worth to mention that many of the results presented in this thesis for the Mott-Hubbard regime have been extended to the Charge-Transfer case. Nevertheless the relevance of a Mottness scenario for non-Fermi liquid formation in high  $T_c$  superconductors, or other charge-transfer compounds, remains a questionable problem requiring further study. In this respect, it may be interesting to study the evolution of our scenario with the introduction of a non-local hybridization. Simple model containing this term, *e.g.* [30], have been studied to investigate the DMFT description of strongly correlated superconductivity.

# Bibliography

- [1] A. A. Abrikosov. *Fundamentals of the theory of metals*. New York, NY ;Elsevier Science Pub. Co. Inc., 1988. [13](#)
- [2] P. W. Anderson. Localized Magnetic States in Metals. *Phys. Rev.*, 124(1):41–53, Oct 1961. [41](#)
- [3] P. W. Anderson. *Basic notions of condensed matter physics*. Addison Wesley Publishing Company, 1984. [10](#)
- [4] N. Andrei and C. Destri. Solution of the multichannel kondo problem. *Phys. Rev. Lett.*, 52(5):364–367, Jan 1984. [24](#)
- [5] R. Arita, K. Held, A. Lukoyanov, and V. Anisimov. Doped mott insulator as the origin of heavy-fermion behavior in  $LiV_2O_4$ . *Physical Review Letters*, 98(16):166402, 2007. [14](#)
- [6] N. Ashcroft and N. Mermin. *Solid State Physics*. Saunders College, Philadelphia, 1976. [3](#), [14](#)
- [7] O. O. Bernal, D. E. MacLaughlin, H. G. Lukefahr, and B. Andraka. Copper nmr and thermodynamics of  $UCu_{5-x}Pd_x$ : Evidence for kondo disorder. *Phys. Rev. Lett.*, 75(10):2023–2026, Sep 1995. [24](#), [25](#)
- [8] A. E. Bocquet, T. Mizokawa, K. Morikawa, A. Fujimori, S. R. Barman, K. Maiti, D. D. Sarma, Y. Tokura, and M. Onoda. Electronic structure of early 3d-transition-metal oxides by analysis of the 2p core-level photoemission spectra. *Phys. Rev. B*, 53(3):1161–1170, Jan 1996. [84](#)
- [9] S. Burdin, A. Georges, and D. R. Grempel. Coherence Scale of the Kondo Lattice. *Phys. Rev. Lett.*, 85(5):1048–1051, Jul 2000. [18](#), [126](#), [127](#)

## BIBLIOGRAPHY

---

- [10] S. Burdin and V. Zlatic. Multiple temperature scales of the periodic anderson model: the slave bosons approach. 2008. [141](#)
- [11] M. Caffarel and W. Krauth. Exact diagonalization approach to correlated fermions in infinite dimensions: Mott transition and superconductivity. *Phys. Rev. Lett.*, 72(10):1545–1548, Mar 1994. [48](#)
- [12] M. Capone, L. de’ Medici, and A. Georges. Solving the dynamical mean-field theory at very low temperatures using the Lanczos exact diagonalization. *Phys. Rev. B*, 76(24):245116, 2007. [52](#)
- [13] A. H. Castro Neto, G. Castilla, and B. A. Jones. Non-fermi liquid behavior and griffiths phase in  $f$ -electron compounds. *Phys. Rev. Lett.*, 81(16):3531–3534, Oct 1998. [24](#), [25](#)
- [14] P. Coleman. Theories of non-fermi liquid behavior in heavy fermions. *Physica B: Condensed Matter*, 259-261:353–358, 1999. [4](#), [8](#), [149](#)
- [15] B. Coqblin. Strongly Correlated Electron Behaviors and Heavy Fermions in Anomalous Rare-earth and actinide Systems. volume 846, pages 3–93. AIP, 2006. [14](#), [15](#), [20](#)
- [16] E. Dagotto. Correlated electrons in high-temperature superconductors. *Rev. Mod. Phys.*, 66(3):763–840, Jul 1994. [49](#)
- [17] L. De Leo, M. Civelli, and G. Kotliar. Cellular dynamical mean-field theory of the periodic Anderson model. *Phys. Rev. B*, 77:075107, 2008. [150](#)
- [18] L. de’ Medici, A. Georges, and S. Biermann. Orbital-selective mott transition in multi-band systems: Slave-spin representation and dynamical mean-field theory. *Phys. Rev. B*, 72(20):205124, Nov 2005. [150](#)
- [19] L. Degiorgi. The electrodynamic response of heavy-electron compounds. *Rev. Mod. Phys.*, 71(3):687–734, Apr 1999. [16](#)
- [20] L. Degiorgi, S. Thieme, H. R. Ott, M. Dressel, G. Grüner, Y. Dalichaouch, M. B. Maple, Z. Fisk, C. Geibel, and F. Steglich. The electrodynamic response of heavy-electron materials with magnetic phase transitions. *Zeitschrift fur Physik B Condensed Matter*, 102:367–380, Feb. 1997. [16](#)
- [21] S. Doniach. The kondo lattice and weak antiferromagnetism. *Physica B: Condensed Matter*, 91:231–234, 1977. [18](#), [21](#), [25](#), [28](#), [59](#), [106](#)
- [22] J. Flouquet. On the heavy fermion road, 2005. [20](#)

- [23] J. Flouquet, G. Knebel, D. Braithwaite, D. Aoki, J. P. Brison, F. Hardy, A. Huxley, S. Raymond, B. Salce, and I. Sheikin. Magnetism and superconductivity of heavy fermion matter, 2005. [20](#)
- [24] G. Gallavotti. *Statistical Mechanics: a short treatise*. Springer-Verlag, 1999. [30](#)
- [25] D. J. García, K. Hallberg, and M. J. Rozenberg. Dynamical Mean Field Theory with the Density Matrix Renormalization Group. *Phys. Rev. Lett.*, 93(24):246403, Dec 2004. [54](#)
- [26] D. J. García, E. Miranda, K. Hallberg, and M. J. Rozenberg. Mott transition in the Hubbard model away from particle-hole symmetry. *Phys. Rev. B*, 75(12):121102, 2007. [95](#)
- [27] F. Gebhard, E. Jeckelmann, S. Mahler, S. Nishimoto, and R. Noack. Fourth-order perturbation theory for the half-filled Hubbard model in infinite dimensions. *Eur. Phys. J. B*, 36(4):491–509, 2003. [54](#)
- [28] A. Georges. Strongly Correlated Electron Materials: Dynamical Mean-Field Theory and Electronic Structure. volume 715, pages 3–74. AIP, 2004. [34](#)
- [29] A. Georges and G. Kotliar. Hubbard model in infinite dimensions. *Phys. Rev. B*, 45(12):6479–6483, Mar 1992. [41](#), [44](#)
- [30] A. Georges, G. Kotliar, and W. Krauth. Superconductivity in the two band Hubbard model in infinite dimensions. LPTENS-93-10. [150](#)
- [31] A. Georges, G. Kotliar, W. Krauth, and M. J. Rozenberg. Dynamical mean-field theory of strongly correlated fermion systems and the limit of infinite dimensions. *Rev. Mod. Phys.*, 68(1):13, Jan 1996. [4](#), [29](#), [33](#), [36](#), [43](#), [47](#), [51](#), [69](#), [74](#), [80](#), [85](#), [95](#), [140](#)
- [32] A. Georges, G. Kotliar, and Q. Si. Strongly Correlated Systems in Infinite Dimensions and Their Zero Dimensional Counterparts. *Int. J. Mod. Phys. B*, 6(5):705–730, 1992. [33](#)
- [33] J. E. Gubernatis, M. Jarrell, R. N. Silver, and D. S. Sivia. Quantum Monte Carlo simulations and maximum entropy: Dynamics from imaginary-time data. *Phys. Rev. B*, 44(12):6011–6029, Sep 1991. [47](#), [87](#)
- [34] K. A. Hallberg. Density-matrix algorithm for the calculation of dynamical properties of low-dimensional systems. *Phys. Rev. B*, 52(14):R9827–R9830, Oct 1995. [53](#)
- [35] J. A. Hertz. Quantum critical phenomena. *Phys. Rev. B*, 14(3):1165–1184, Aug 1976. [4](#), [7](#), [23](#), [26](#), [27](#), [107](#)

## BIBLIOGRAPHY

---

- [36] A. C. Hewson. *The Kondo Problem to Heavy Fermions*. Cambridge University Press, New York, N.Y., 1993. [14](#), [17](#), [19](#), [20](#), [41](#), [43](#), [59](#), [108](#)
- [37] J. E. Hirsch and R. M. Fye. Monte Carlo Method for Magnetic Impurities in Metals. *Phys. Rev. Lett.*, 56(23):2521–2524, Jun 1986. [45](#), [46](#)
- [38] K. Huang. *Statistical Mechanics*. Wiley, April 1987. [13](#), [30](#), [72](#)
- [39] J. Hubbard. Electron correlations in narrow energy bands. *Proc. Roy. Soc. (London)*, A:238, 1963. [80](#)
- [40] J. Hubbard. Electron correlations in narrow energy bands II. The degenerate band case. *Proc. Roy. Soc. (London)*, A277:237, 1964. [80](#)
- [41] J. Hubbard. Electron correlations in narrow energy bands III. An improved solution. *Proc. Roy. Soc. (London)*, A:401, 1964. [80](#)
- [42] M. Imada, A. Fujimori, and Y. Tokura. Metal-insulator transitions. *Rev. Mod. Phys.*, 70(4):1039–1263, Oct 1998. [80](#)
- [43] M. Jarrell. Symmetric periodic anderson model in infinite dimensions. *Phys. Rev. B*, 51(12):7429–7440, Mar 1995. [69](#)
- [44] M. Jarrell, H. Akhlaghpour, and T. Pruschke. Periodic anderson model in infinite dimensions. *Phys. Rev. Lett.*, 70(11):1670–1673, Mar 1993. [69](#)
- [45] H. Kajueter and G. Kotliar. New Iterative Perturbation Scheme for Lattice Models with Arbitrary Filling. *Phys. Rev. Lett.*, 77(1):131–134, Jul 1996. [44](#)
- [46] S. Kondo, D. Johnston, C. Swenson, F. Borsa, A. Mahajan, L. Miller, T. Gu, A. Goldman, M. Maple, D. Gajewski, et al.  $\text{LiV}_2\text{O}_4$ : A heavy fermion transition metal oxide. *Physical Review Letters*, 78(19):3729–3732, 1997. [14](#)
- [47] G. Kotliar. Landau theory of the Mott transition in the fully frustrated Hubbard model in infinite dimensions. *Eur. Phys. J. B*, 11(1):27–39, Sep 1999. [80](#)
- [48] G. Kotliar, E. Lange, and M. J. Rozenberg. Landau Theory of the Finite Temperature Mott Transition. *Phys. Rev. Lett.*, 84(22):5180–5183, May 2000. [80](#)
- [49] G. Kotliar, S. Murthy, and M. J. Rozenberg. Compressibility Divergence and the Finite Temperature Mott Transition. *Phys. Rev. Lett.*, 89(4):046401, Jul 2002. [95](#)

- [50] G. Kotliar and A. E. Ruckenstein. New functional integral approach to strongly correlated fermi systems: The gutzwiller approximation as a saddle point. *Phys. Rev. Lett.*, 57(11):1362–1365, Sep 1986. [30](#)
- [51] G. Kotliar, S. Y. Savrasov, K. Haule, V. S. Oudovenko, O. Parcollet, and C. A. Marianetti. Electronic structure calculations with dynamical mean-field theory. *Rev. Mod. Phys.*, 78(3):865, 2006. [4](#)
- [52] G. Kotliar and D. Vollardt. Strongly Correlated Materials: Insights from dynamical mean-field theory. *Phys. Today*, 57(3):53–59, 2004. [4](#), [29](#)
- [53] L. Landau. The theory of a Fermi liquid. *Soviet Physics JETP*, 3:920–925, 1957. [8](#)
- [54] L. Landau. On the theory of a Fermi liquid. *Soviet Physics JETP*, 8:70–74, 1959. [8](#)
- [55] E. H. Lieb and F. Y. Wu. Absence of mott transition in an exact solution of the short-range, one-band model in one dimension. *Phys. Rev. Lett.*, 20(25):1445–1448, Jun 1968. [80](#)
- [56] H. Löhneysen, A. Rosch, M. Vojta, and P. Wölfle. Fermi-liquid instabilities at magnetic quantum phase transitions. *Reviews of Modern Physics*, 79(3):1015–1075, 2007. [27](#)
- [57] G. D. Mahan. *Many-Particle Physics*. Plenum, New York, N.Y., 2nd edition, 1993. [30](#), [51](#), [72](#)
- [58] N. Mathur, F. Grosche, S. Julian, I. Walker, D. Freye, R. Haselwimmer, and G. Lonzarich. Magnetically mediated superconductivity in heavy fermion compounds. *Nature*, 394(6688):39–43, 1998. [19](#)
- [59] W. Metzner. Linked-cluster expansion around the atomic limit of the hubbard model. *Phys. Rev. B*, 43(10):8549–8563, Apr 1991. [4](#), [36](#)
- [60] W. Metzner and D. Vollhardt. Correlated Lattice Fermions in  $d = \infty$  Dimensions. *Phys. Rev. Lett.*, 62(3):324–327, Jan 1989. [4](#), [36](#), [69](#)
- [61] A. J. Millis. Effect of a nonzero temperature on quantum critical points in itinerant fermion systems. *Phys. Rev. B*, 48(10):7183–7196, Sep 1993. [4](#), [27](#), [107](#)
- [62] E. Miranda, V. Dobrosavljević, and G. Kotliar. Kondo disorder: a possible route towards non-Fermi-liquid behaviour. *Journal of Physics Condensed Matter*, 8:9871–9900, Nov. 1996. [3](#), [25](#)
- [63] E. Miranda, V. Dobrosavljević, and G. Kotliar. Disorder-Driven Non-Fermi-Liquid Behavior in Kondo Alloys. *Physical Review Letters*, 78:290–293, Jan. 1997. [25](#)

## BIBLIOGRAPHY

---

- [64] E. Miranda, V. Dobrosavljević, and G. Kotliar. Non-Fermi liquid behavior as a consequence of Kondo disorder. *Physica B Condensed Matter*, 230:569–571, Feb. 1997. [25](#)
- [65] T. Moriya and T. Takimoto. Anomalous properties around magnetic instability in heavy electron systems. *Journal of the Physical Society of Japan*, 64(3):960–969, 1995. [27](#)
- [66] C. Noce. The periodic Anderson model: Symmetry-based results and some exact solutions. *Phys. Rep.*, 431:173–230, Aug. 2006. [66](#), [68](#)
- [67] Nozières. Some comments on Kondo lattices and the Mott transition. *Eur. Phys. J. B*, 6(4):447–457, 1998. [6](#), [18](#), [108](#), [126](#)
- [68] P. Nozières. Impuretés magnétiques et effet Kondo. *Ann. Phys. Fr.*, 10(1):19–35, 1985. [6](#), [18](#), [108](#), [126](#)
- [69] P. Nozières. *Theory of Interacting Fermi systems*. Westview Press, 1997. [3](#), [10](#), [11](#)
- [70] P. Nozières and A. Blandin. Kondo effect in real metals. *J. Physique*, 41:193–211, 1980. [3](#), [7](#), [23](#)
- [71] R. H. Ott. *Progress in Low Temperature Physics*, 6(21):5, 1987. [16](#)
- [72] C. Pépin. Kondo Breakdown as a Selective Mott Transition in the Anderson Lattice. *Phys. Rev. Lett.*, 98(20):206401, 2007. [150](#)
- [73] C. Pépin. Selective Mott transition and heavy fermions. *Phys. Rev. B*, 77(24):245129, 2008. [150](#)
- [74] I. Peschel, X. Wang, M. Kaulke, and K. Hallberg. *Density Matrix Renormalization*. Springer-Verlag, Berlin, 1999. [52](#), [54](#)
- [75] M. J. Rozenberg, R. Chitra, and G. Kotliar. Finite Temperature Mott Transition in the Hubbard Model in Infinite Dimensions. *Phys. Rev. Lett.*, 83(17):3498–3501, Oct 1999. [4](#)
- [76] M. J. Rozenberg, G. Kotliar, and X. Y. Zhang. Mott-Hubbard transition in infinite dimensions. II. *Phys. Rev. B*, 49(15):10181–10193, Apr 1994. [4](#), [80](#)
- [77] M. J. Rozenberg, G. Moeller, and G. Kotliar. The metal-insulator transition in the Hubbard model at zero temperature. *Mod. Phys. Lett. B*, 8(8):535–543, 1994. [48](#)
- [78] M. J. Rozenberg, X. Y. Zhang, and G. Kotliar. Mott-Hubbard transition in infinite dimensions. *Phys. Rev. Lett.*, 69(8):1236–1239, Aug 1992. [4](#), [80](#)

- [79] M. A. Ruderman and C. Kittel. Indirect exchange coupling of nuclear magnetic moments by conduction electrons. *Phys. Rev.*, 96(1):99, Oct 1954. [18](#)
- [80] S. Sachdev. *Quantum Phase Transitions*. Cambridge, 1999. [8](#)
- [81] P. Sacramento and P. Schlottmann. Thermodynamics of the n-channel Kondo model for general n and impurity spin S in a magnetic field. *Journal of Physics: Condensed Matter*, 3(48):9687–9696, 1991. [24](#)
- [82] E.-W. Scheidt, T. Schreiner, K. Heuser, S. Koerner, and G. R. Stewart. Low-temperature specific heat of  $UCu_{5-x}Pd_x$  a test for non-fermi-liquid theory. *Phys. Rev. B*, 58(16):R10104–R10106, Oct 1998. [22](#)
- [83] U. Schollwöck. The density-matrix renormalization group. *Rev. Mod. Phys.*, 77(1):259, 2005. [54](#)
- [84] J. R. Schrieffer and P. A. Wolff. Relation between the anderson and kondo hamiltonians. *Phys. Rev.*, 149(2):491–492, Sep 1966. [17](#), [60](#)
- [85] C. Seaman, M. Maple, B. Lee, S. Ghamaty, M. Torikachvili, J. Kang, L. Liu, J. Allen, and D. Cox. Evidence for non-fermi liquid behavior in the kondo alloy  $Y_{1-x}U_xPd_3$ . *Physical Review Letters*, 67(20):2882–2885, 1991. [21](#)
- [86] A. Shimoyamada, S. Tsuda, K. Ishizaka, T. Kiss, T. Shimojima, T. Togashi, S. Watanabe, C. Zhang, C. Chen, Y. Matsushita, et al. Heavy-fermion-like state in a transition metal oxide  $LiV_2O_4$  single crystal: Indication of kondo resonance in the photoemission spectrum. *Physical Review Letters*, 96(2):26403, 2006. [14](#)
- [87] Q. Si, S. Rabello, K. Ingersent, and J. L. Smith. Locally critical quantum phase transitions in strongly correlated metals. *Nature (London)*, 4:186, 2001. Enter text here. [4](#), [28](#)
- [88] Q. Si, S. Rabello, K. Ingersent, and J. L. Smith. Local fluctuations in quantum critical metals. *Phys. Rev. B*, 68(11):115103, Sep 2003. [4](#), [28](#), [107](#)
- [89] Q. Si, M. J. Rozenberg, G. Kotliar, and A. E. Ruckenstein. Correlation induced insulator to metal transitions. *Phys. Rev. Lett.*, 72(17):2761–2764, Apr 1994. [48](#)
- [90] J. L. Smith and Q. Si. Spatial correlations in dynamical mean-field theory. *Phys. Rev. B*, 61(8):5184–5193, Feb 2000. [28](#)
- [91] G. Sordi, A. Amaricci, and M. J. Rozenberg. Metal-Insulator Transitions in the Periodic Anderson Model. *Phys. Rev. Lett.*, 99(19):196403, 2007. [95](#), [98](#)

## BIBLIOGRAPHY

---

- [92] F. Steglich, J. Aarts, C. D. Bredl, W. Lieke, D. Meschede, W. Franz, and H. Schäfer. Superconductivity in the presence of strong pauli paramagnetism:  $CeCu_2Si_2$ . *Phys. Rev. Lett.*, 43(25):1892–1896, Dec 1979. [19](#)
- [93] G. R. Stewart. Heavy-fermion systems. *Rev. Mod. Phys.*, 56(4):755–787, Oct 1984. [19](#)
- [94] G. R. Stewart. Non-fermi-liquid behavior in  $d$ - and  $f$ -electron metals. *Rev. Mod. Phys.*, 73(4):797–855, Oct 2001. [3](#), [6](#), [7](#), [8](#), [21](#), [23](#), [28](#), [107](#), [119](#), [141](#), [144](#), [149](#)
- [95] A. N. Tahvildar-Zadeh, M. Jarrell, and J. K. Freericks. Protracted screening in the periodic Anderson model. *Phys. Rev. B*, 55(6):R3332–R3335, Feb 1997. [108](#), [126](#), [127](#)
- [96] A. N. Tahvildar-Zadeh, M. Jarrell, T. Pruschke, and J. K. Freericks. Evidence for exhaustion in the conductivity of the infinite-dimensional periodic Anderson model. *Phys. Rev. B*, 60(15):10782–10787, Oct 1999. [126](#), [127](#)
- [97] K. Umeo, H. Kadomatsu, and T. Takabatake. Non-Fermi-liquid behaviour at the pressure-induced antiferromagnetic to non-magnetic transition in a heavy-fermion compound,  $Ce\sim 7Ni\sim 3$ . *Journal of Physics Condensed Matter*, 8:9743–9758, 1996. [22](#)
- [98] N. S. Vidhyadhiraja. On the specific heat of heavy-fermion systems using the periodic Anderson model. *Europhysics Letters*, 77:36001–+, Feb. 2007. [72](#)
- [99] N. S. Vidhyadhiraja, A. N. Tahvildar-Zadeh, M. Jarrell, and H. R. Krishnamurthy. “Exhaustion” physics in the periodic Anderson model from iterated perturbation theory. *Europhys. Lett.*, 49(4):459–465, 2000. [126](#)
- [100] P. Werner and A. J. Millis. Doping-driven Mott transition in the one-band Hubbard model. *Phys. Rev. B (Condensed Matter and Materials Physics)*, 75(8):085108, 2007. [4](#), [95](#)
- [101] S. R. White. Density matrix formulation for quantum renormalization groups. *Phys. Rev. Lett.*, 69(19):2863–2866, Nov 1992. [53](#)
- [102] K. Yoshida and K. Yamada. Perturbation Expansion for the Anderson Hamiltonian. *Prog. Theor. Phys.*, 46:244–255, 1970. [44](#)
- [103] J. Zaanen, G. A. Sawatzky, and J. W. Allen. Band gaps and electronic structure of transition-metal compounds. *Phys. Rev. Lett.*, 55(4):418–421, Jul 1985. [80](#), [81](#)
- [104] F. C. Zhang and T. M. Rice. Effective Hamiltonian for the superconducting Cu oxides. *Phys. Rev. B*, 37(7):3759–3761, Mar 1988. [81](#), [95](#), [102](#)

- [105] X. Y. Zhang, M. J. Rozenberg, and G. Kotliar. Mott transition in the  $d = \infty$  Hubbard model at zero temperature. *Phys. Rev. Lett.*, 70(11):1666–1669, Mar 1993. [44](#), [45](#)

